BUILDING AND CHARACTERISATION OF A DUAL SPECIES QUANTUM SIMULATOR

Dissertation

zur Erlangung des Doktorgrades

des Department Physiks

der Universität Hamburg

vorgelegt von

Nadine Meyer

aus Wentorf bei Hamburg

Hamburg 2014

Für meine Familie

Abstract

Many interesting physical systems have one thing in common. Their complexity makes it impossible to simulate them on conventional computers. Feynman's idea of a quantum simulator for complex systems from 1982 [1] gives the possibility to study complex phenomena out of the reach of normal computers with tailored Hamiltonians. The world of ultra cold atoms offers a wide range of tunable parameters combined with a degree of control in unprecedented clean systems. Ultra cold quantum gases are the ideal tool for the realisation of quantum simulators and the study of phase diagrams of model systems.

This thesis presents a new setup for Bose-Fermi mixtures experiments with regard to quantum simulations in optical lattices and arbitrary light potentials with a high resolution for detection and atom manipulation. The setup was designed to be a low maintenance, robust tool box for quantum simulations incorporating new technology developments. Both fundamental quantum statistics can be observed and different interaction regimes can be investigated with the help of Feshbach resonances. From the beginning all decisions concerning the setup design take the implementation of optical lattices and a high resolution imaging system into account.

The magneto-optical trapping of Bose-Fermi mixtures with ^{87}Rb and ^{40}K and the Bose-Einstein condensation (BEC) of ^{87}Rb had been achieved. Another aim in the context of this thesis was the development and testing of new versatile technologies. A robust, flexible, miniaturised dual species laser system for laser cooling had been setup and tested. A new narrow coil design allowing for high magnetic fields with great optical access at a low power dissipation had been developed and used for the realisation of the BEC. One of the magnetic coil sets had been optimised for homogeneous magnetic fields for the application of Feshbach resonances. Furthermore an indium sealing technique for vacuum chambers had been realised. All these technology developments aimed for a compact and robust setup with high flexibility.

For the procedure the atomic sample was first laser cooled and trapped in a combined 2D-3D MOT complex before the atoms are magnetically trapped and transported with a linear rail over a macroscopic distance to the science chamber. In the science chamber the atoms were transferred to a different magnetic trap where forced RF evaporation cooled the atomic cloud further down. Loading the atomic cloud into an optical dipole trap and further evaporation lead to the Bose-Einstein condensate of ^{87}Rb.

The BEC contained $N_{BEC} = 3.5 \cdot 10^4$ ^{87}Rb atoms at $T_{BEC} = 100 nK$. The individual, separately loaded magneto-optical traps contained $N_{Rb} = 1.3 \cdot 10^9$ rubidium and $N_K = 1.4 \cdot 10^6$ potassium atoms. Hence, the setup reached the quantum regime necessary for quantum simulation for further studies.

Publications

The following research articles have been published in the course of this thesis.

- J. Rudolph, N. Gaaloul, Y. Singh, H. Ahlers, W. Herr, T.A. Schulze, S.T. Seidel, C. Rode, V. Schkolnik, W. Ertmer, E.M. Rasel, H. Müntinga, T. Könemann, A. Resch, S. Herrmann, C. Lämmerzahl, T. van Zoest, H. Dittus, A. Vogel, A. Wenzlawski, K. Sengstock, N. Meyer, K. Bongs, M. Krutzik, W. Lewoczko-Adamczyk, M. Schiemangk, A. Peters, M. Eckart, E. Kajari, S. Arnold, G. Nandi, W.P. Schleich, R. Walser, T. Steinmetz, T.W.Hänsch, J. Reichel, *Degenerate Quantum Gases in Microgravity*, Microgravity Sci. Technol. **23**, 3 (2010) [2]

- H. Müntinga, H. Ahlers, M. Krutzik, A. Wenzlawski, S. Arnold, D. Becker, K. Bongs, H. Dittus, H. Duncker, N. Gaaloul, C. Gherasim, E. Giese, C. Grzeschik, T. W. Hänsch, O. Hellmig, W. Herr, S. Herrmann, E. Kajari, S. Kleinert, C. Lämmerzahl, W. Lewoczko-Adamczyk, J. Malcolm, N. Meyer, R. Nolte, A. Peters, M. Popp, J. Reichel, A. Roura, J. Rudolph, M. Schiemangk, M. Schneider, S. T. Seidel, K. Sengstock, V. Tamma, T. Valenzuela, A. Vogel, R. Walser, T. Wendrich, P. Windpassinger, W. Zeller, T. van Zoest, W. Ertmer, W. P. Schleich, E. M. Rasel, *Interferometry with Bose-Einstein Condensates in Microgravity*, Phys.Rev.Lett. **110**, 093602 (2013) [3]

Zusammenfassung

Die Komplexität vieler interessanter physikalischen Systeme macht es nahezu unmöglich diese auf herkömmlichen Computern zu simulieren. Feynmans Idee eines Quantensimulators für komplexe Systeme von 1982 [1] bietet die Möglichkeit komplexe Phänomene ausserhalb der Reichweite eines normalen Computers mithilfe von maßgeschneiderten Hamiltonians zu studieren. Die Welt der ultrakalten Atomen bietet dafür mit unerreicht sauberen Quantengassystemen und flexiblen aber hoch präzise konrollierbaren Parametern hervorragende Eigenschaften. Ultrakalte Quantengase sind daher ein perfektes Werkzeug für die Realisierung von Quantensimulatoren und der Untersuchung von Phasenraumdiagrammen von Modellsystemen. Diese Arbeit stellt ein neues Experiment für Bose-Fermi-Mischungen im Hinblick auf Quantensimulationen in optischen Gittern und willkürlichen Lichtpotentialen mit hoher optischer Auflösung für Detektion und Manipulation vor. Der Aufbau einschliesslich neuer Technologieentwicklungen wurde auf hohe Wartungsfreiheit und Robustheit optimimiert. Beide Quantenstatistiken und verschiedene Wechselwirkungsregime werden mit Hilfe von Feshbachresonanzen untersucht werden können. Alle Entscheidungen bezüglich des Designs und des Aufbaus wurden hinsichtlich der Umsetzung von optischen Gittern und eines hochauflösenden Abbildungssystems getroffen. Das magneto-optische Fangen von Bose-Fermi-Mischungen mit ^{87}Rb und ^{40}K und die Bose-Einstein Kondensation (BEC) von ^{87}Rb wurde erstmals in dieser Arbeitsgruppe verwirklicht. Das Laserkühlen mit divergenten Strahlen wurde dabei erfolgreich demonstriert. Im Rahmen neuer Technologieentwicklungen wurde ein robustes, flexibles, miniaturisiertes Lasersystem für zwei unterschiedliche Spezies zur Laserkühlung designt, aufgebaut und getestet. Ein neues kompaktes Spulendesign mit hohem optischen Zugang und geringer Verlustleistung wurde entwickelt und für die Realisierung des BECs verwendet. Dabei ist einer der Magnetspulensätze für homogene Magnetfelder für die Anwendung von Feshbachresonanzen optimiert worden. Desweiteren wurde eine vielseitige Vakuumversiegelungstechnik mit Indium realisiert. All diese Technologieentwicklungen zielen auf einen kompakten und robusten Aufbau mit hoher Flexibilität ab. Die Atome werden zunächst in einem 2D-3D MOT Komplex eingefangen und lasergekühlt. Danach werden die Atome magnetisch gefangen und mithilfe beweglicher Spulen zur Science chamber transportiert. RF Evaporation in der magnetischen Quadrupolfalle kühlt das Ensemble soweit herunter, daß die Atomwolke in eine optische Dipolfalle geladen werden kann in welcher weitere Evaporation zur Bose-Einstein Kondensation von ^{87}Rb führt. Das BEC enthält $N_{BEC} = 3,5 \cdot 10^4$ ^{87}Rb Atome bei einer Temperatur von $T_{BEC} = 100 nK$. Die individuel geladenen magneto-optischen Fallen enthalten $N_{Rb} = 1,3 \cdot 10^9$ Rubidiumatome und $N_K = 1,4 \cdot 10^6$ Kaliumatomen. Der Aufbau hat somit das Regime der Quantengase erreicht, eine notwendige Vorraussetzung für Quantensimulationen mit ultrakalten

Atomen.

Publikationen

Im Rahmen dieser Arbeit sind die folgenden wissenschaftlichen Veröffentlichungen entstanden.

- J. Rudolph, N. Gaaloul, Y. Singh, H. Ahlers, W. Herr, T.A. Schulze, S.T. Seidel, C. Rode, V. Schkolnik, W. Ertmer, E.M. Rasel, H. Müntinga, T. Könemann, A. Resch, S. Herrmann, C. Lämmerzahl, T. van Zoest, H. Dittus, A. Vogel, A. Wenzlawski, K. Sengstock, N. Meyer, K. Bongs, M. Krutzik, W. Lewoczko-Adamczyk, M. Schiemangk, A. Peters, M. Eckart, E. Kajari, S. Arnold, G. Nandi, W.P. Schleich, R. Walser, T. Steinmetz, T.W.Hänsch, J. Reichel, *Degenerate Quantum Gases in Microgravity*, Microgravity Sci. Technol. **23**, 3 (2010) [2]

- H. Müntinga, H. Ahlers, M. Krutzik, A. Wenzlawski, S. Arnold, D. Becker, K. Bongs, H. Dittus, H. Duncker, N. Gaaloul, C. Gherasim, E. Giese, C. Grzeschik, T. W. Hänsch, O. Hellmig, W. Herr, S. Herrmann, E. Kajari, S. Kleinert, C. Lämmerzahl, W. Lewoczko-Adamczyk, J. Malcolm, N. Meyer, R. Nolte, A. Peters, M. Popp, J. Reichel, A. Roura, J. Rudolph, M. Schiemangk, M. Schneider, S. T. Seidel, K. Sengstock, V. Tamma, T. Valenzuela, A. Vogel, R. Walser, T. Wendrich, P. Windpassinger, W. Zeller, T. van Zoest, W. Ertmer, W. P. Schleich, E. M. Rasel, *Interferometry with Bose-Einstein Condensates in Microgravity*, Phys.Rev.Lett. **110**, 093602 (2013) [3]

Contents

iv

Chapter 1

Introduction

The invention of the laser for optical radiation in 1957 by *Schawlow* and *Townes* [4] did not just change our everyday life in the following decades enduringly, without it laser cooling of neutral atoms would simply be impossible. The discovery of the radiation force of resonant light acting on the atomic momentum by *Frisch* in 1933 [5] opened the doors towards laser cooling. Nowadays many inventions for the manipulation of neutral atoms based on the radiation force have been made, atomic lenses, beam splitters [6], mirrors with light sheets and optical tweezers [7] are just a few of them.

The laser cooling technique for neutral atoms in particular for alkali atoms down to the μK range [8, 9] paved the way for the achievement of the Bose-Einstein condensation (BEC) in dilute gases in 1995 [10, 11]. The Bose-Einstein condensation, a purely quantum statistical effect of indistinguishable particles governed by Bose-Einstein statistics, was proposed by *A. Einstein* in 1925 [12] influenced by the work of *S. Bose* [13]. It describes the situation where the atoms mainly occupy the same quantum mechanical state if the entropy of the system is far enough decreased. This only happens if the temperature is low and the density is high enough, so that the individual particle wave functions described by the *de Broglie* wave length start overlapping.

Another breakthrough in 1999 was the first realisation of ultra cold, degenerate Fermi gases (DFG) in dilute atomic gases [14]. Governed by the Fermi-Dirac statistic and the Pauli exclusion principle, it is impossible for the distinguishable fermions to occupy the same quantum state with two particles obeying the same quantum numbers. If the fermionic ensemble is cooled down below the Fermi temperature and enough entropy is extracted the system can be considered as a degenerate Fermi gas. It means that the atoms occupy successive energy states without any double occupation or unoccupied quantum states in between.

Both laser cooling and Bose-Einstein condensation were awarded with the Nobel prize in 1997 and 2001. Bose-Einstein condensation and degenerate Fermi gases

have been realised with many different atomic species in many laboratories all over the world [10, 15–22] [23–26] and the number is still growing mirroring the ongoing curiosity and progress in this field.

Ultra cold atom experiments deliver very clean systems with unique and outstanding properties. BEC experiments are reliable sources of coherent matter waves where the magnitude of the wave function $|\Psi|^2$ can directly be observed. In combination with optical lattices interdisciplinary insights into condensed matter phenomena like superconductivity and superfluidity can be given [27–30]. These many-body or few-body systems, where the parameters are under high control and precision but can dynamically be changed, permit the study of quantum phase transitions [27, 31]. Even the geometry and the dimensionality of the system can be adjusted with the optical lattice [30, 32, 33].
Not being limited to steady-state phenomena, Quantum coherent dynamics can be investigated. The exploration of different interaction regimes is possible due to Feshbach resonances altering the scattering length [24, 25, 34–38]. Strongly correlated and non-interacting gases have been realised. The transition between the macroscopic Fermi sea down to a few body system is under investigation [39]. Another exciting new regime covers far from non-equilibrium physics in ultra cold systems [40, 41].
Many interesting applications are subject to the field of ultra cold atoms like e.g. quantum sensors and optical clocks [42–44]. Also ultra cold quantum chemistry [45], quantum computers [46] and quantum simulations [47–50] are important implications.

Our main interest is the field of quantum simulation in order to gain a detailed understanding of quantum processes. Analogue to Feynmans vision of a quantum simulator [1] to uncover the key principles in nature, a well controlled model quantum simulator governed by a tailored and tunable Hamiltonian is prepared in a certain state of the system and evolves in time. The scaling problem on normal computers where the parameter space grows exponentially can be circumvented and the solution can be compared to existing theoretical models. For three dimensional problems the mean field approach has proven to be very successful, while many theoretical models for two dimensional systems prove to be unsolvable. This makes quantum simulation even more important.
For quantum simulation the field of ultra cold atoms has developed a huge toolbox for varying the Hamiltonians in many possible ways. First ultra cold bosons and fermions make it possible to study both fundamental statistics individually and Bose-Fermi mixtures together. With the help of Feshbach resonances the formation or destruction of molecules can be controlled and different interaction regimes

can be investigated. The strength, spacing, geometry and dimensionality of the simulated crystal structures is given by the layout of the optical lattice and can be amended. Even disorder effects can be studied by bringing "dirty" light potentials or disturbances into the system. Overall a quantum simulator realised with ultra cold atoms is the ideal toolbox for mapping out the quantum phase transitions of different systems in dependence of various parameters.

In the context of this thesis a new experimental setup for quantum simulation has been designed and build from scratch. The setup combines a compact 2D-3D MOT with magnetic transport to the science cell. Here optical lattices and Feshbach resonances in addition to an optical dipole trap can be applied. Microscope objectives and a spatial light modulator (SLM) will enable high resolution for detection and manipulation.
The setup aims for the investigation of phase diagrams of 2D Bose-Fermi systems in optical lattices. Solitons in 2D can be studied [51] and disorder phenomena like Anderson localisation [52,53], Bose glass phases [54], mobile impurities and polaron physics [55] can be investigated.
New technologies like a miniaturised two species laser system, a compact magnetic coil design with high optical access and a UHV sealing technique have been developed, improved and/or tested.

The state of the art for the realisation of ultra cold gases today is the following and used as such in this experiment. The atoms are pre-cooled in a magneto-optical trap and optical molasses before they are transferred to a magnetic or far detuned optical trap. Evaporative cooling [56, 57] cools the ensemble down to the quantum gas regime. In case for the fermionic ensemble the atoms will be sympathetically cooled by the bosons [58–60]. Although the all optical realisation of a BEC has recently been realised [61], this is still the usual procedure for many experiments.

Within this setup the realisation of a Bose-Einstein condensate and the dual species magneto-optical trap has been achieved. The thesis is organised as follows.

- **Chapter 2** gives a detailed overview of the experimental setup and its individual parts. The vacuum system with the compact 2D-3D MOT system, the magnetic transport on a linear rail and the science chamber including the magnetic coil layout is described. A detailed description on the vacuum system and the design process is covered in [62]. The magnetic coil design is discussed in chapter 4.

- **Chapter 3** contains a broad and detailed description of the miniaturised laser system with its outstanding stability, robustness and compactness. The miniaturised optical component design is based on [63].

- **Chapter 4** presents a detailed discussion of the narrow and versatile coil technology and the magnetic trap design in the experiment for both homogeneous and anti-Helmholtz fields.

- **Chapter 5** covers the magneto-optical trapping of both species ^{87}Rb and ^{40}K individually and as a mixture. The results of the 2D MOT and 3D MOT are discussed. For ^{87}Rb the magneto-optical trapping and the optical molasses with divergent beams is demonstrated.

- **Chapter 6** describes the experimental techniques used for magnetic trapping and transport of ultra cold atom clouds on a linear rail. Evaporative cooling with forced RF evaporation in a quadrupole trap is presented.

- **Chapter 7** gives an overview of the experimental setup and characteristics of the anisotropic dipole trap. Loading the dipole trap and forced evaporation to the BEC regime is achieved.

- **Chapter 8** summarises the results and discusses possible perspectives.

Part I

Experimental Setup

Chapter 2

Experimental overview

The vacuum system is the central piece in quantum gas experiments for isolating the ultra cold atom cloud against the environment. The work with ultra cold and dilute gases happens in vacuum regimes of 10^{-8} to $10^{-12} mbar$ in order to protect the ensemble against heating and particle losses.
The following discussion of the vacuum system for a versatile quantum simulator will show the individual parts of the vacuum system and point out occasionally the dependencies to other parts in the experiment due to the desired features of the experiment. The maximal possible optical access and high flexibility in the number of species have severe consequences on the design of the experimental setup. Hence some uncommon or new technologies need to be established. Two major examples for that are the magnetic coil design (see chapter 4) and the conception of the 3D MOT chamber (see section 2.2.2). A complete presentation of the design work can be found in [62].

Following a modular design approach the experiment is designed in such a way that dual species mixture experiments can be conducted in 2D optical lattices with large lattice spacing or in arbitrary optical potentials that are realised with a spatial light modulator (SLM). High optical resolution imaging and/or manipulation of atoms down to single site resolution will be achievable. Feshbach resonances tuning the atom-atom interaction will be exploited using magnetic coils that are optimised for the application of homogeneous magnetic fields.
The design of individual MOT systems allows for the implementation of other species. It also enables independent optimisation for high atom numbers and prevents possible disturbances in the magneto-optical trap performance like it is the case for ^{87}Rb and ^{40}K when trapped together (see section 5.3). One of these 2D-3D MOT systems has been realised in the context of this thesis.
The entire current vacuum setup is shown in figure 2.2, the optical setup for 2D and 3D MOT is not included in the picture but will be described later in section
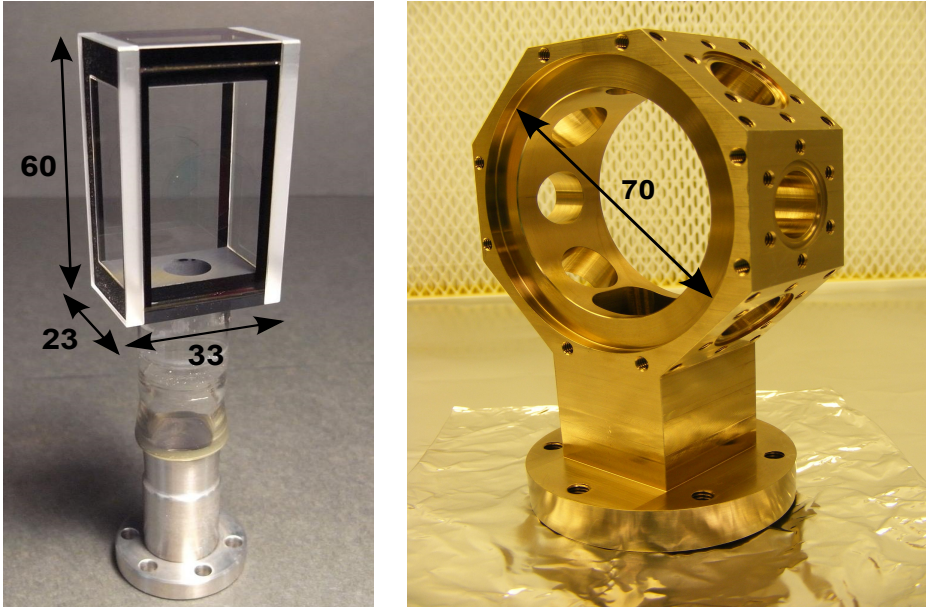
Figure 2.1: *Science chamber (left) and 3D MOT chamber (right):* The glass cell chamber, so-called science chamber, has black quartz in between the windows. It is $60mm$ long and the small window at the top measures at the outside $33 \times 23mm$ while the large window at the side is $23 \times 60mm$. The stainless steal 3D MOT is octagonally shaped and has two large recesses for $70mm$ diameter windows. The seven CF16 flange connections are used for the connection to the science chamber, to an optional 2D-3D MOT system and five view ports.

3.5. Further details on the vacuum system design can be found in [62]. The chapter is organised as follows. After a general overview over the individual parts of the vacuum system in section 2.1 we take a closer look on the 2D-3D MOT system and the different vacuum sealing techniques in section 2.2.

2.1   From the science to the MOT chamber

The experimental setup consists of three main parts: the science chamber, the magnetic transport and the 2D-3D MOT chamber.

Science chamber   The main experiments will be held in a glass cell that was specially designed for this experiment, the science chamber[1]. The science chamber is designed to be as small as possible whilst offering great optical access for the implementation of an optical lattice in addition to high resolution imaging and manipulation with the help of microscope objectives, see figure 2.1 on the left. The lattice configuration shall allow first for a beam pair entering horizontally, embracing an angle of minimum 90° through the larger side windows and second

---

[1]Manufactured by Japan Cell, Co. Ltd

through the smaller side window at an open angle of 30°.

Furthermore comparably inexpensive glass corrected microscope objectives, facing upwards and downwards, will be implemented for the high resolution imaging and manipulation system, in order to investigate the atom cloud in the horizontal plane. This demands a height of the science chamber of less then twice the working distance of the microscopes. Those minimum restrictions to the optical access determine the outer size of the science cell to $33 \times 23 \times 60mm$.

The glass cell windows show optical coatings for several wavelengths on both sides for optical imaging, trapping and manipulation and were glued together post coating. The vertices of the science chamber are made from black quartz that act as a beam dump for stray light reducing possible complication during fluorescence detection. More details on the design and features of the science chamber and the planned optical lattices can be found in [64].

The so-called Feshbach coils are placed around the science cell. They are used as magnetic trap but can also be used to modify the atom-atom interaction via Feshbach resonances [24, 34–36]. They were optimised for the generation of homogeneous magnetic fields with a minimum distance given by the science chamber width of $33mm$ as described in section 4.3. The optical access needed for optical lattice implementation of 90° through the large side window and 30° through the small side window is provided.

Linear rail and moving transport The atoms are transported to the science chamber with the aid of a moving magnetic trap placed on a linear rail[2] (see figure 2.2). The magnetic transport to a different chamber enables both for a better vacuum in the science chamber as well as the individual and simultaneous preparation of the magneto-optical trap during the experiment by implementing separate 2D-3D MOT systems. However, this system requires a positional accuracy and repeatability of a few microns over a distance of $50cm$ which is a technical challenge. The performance of the rail is analysed in detail in [64].

Our moving magnetic coils are designed for the highest magnetic field gradient whilst fulfilling the same optical restrictions as the Feshbach coils and a minimum distance given by the Feshbach coils as described in section 4.4. The moving magnetic trap collects atoms on the way from the MOT chambers to the science chamber. On each MOT chamber another magnetic trap is implemented that will be referred as the MOT coils since it is initially used for magneto-optical trapping. With the help of the MOT coils the collection of several clouds in one trip to the science chamber is possible by simultaneously trapping different atomic clouds in different magnetic traps that will be merged during transport to the science chamber. They are designed in the same way like the other magnetic traps but their
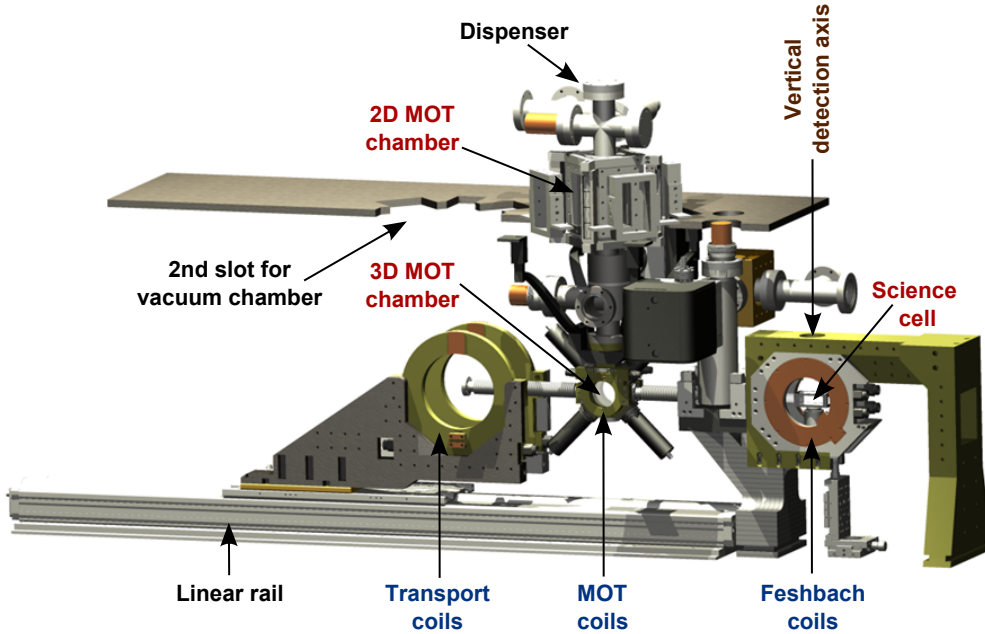
---

[2]Parker, 406XR-1200

Figure 2.2: *Vaccum chamber:* The vacuum chamber consist of three main parts: The science chamber, 3D MOT chamber and 2D MOT chamber, each individually pumped by ion and titanium sublimation pumps. The science chamber is located on the far right and shows the lowest vacuum in the setup of $10^{-12} mbar$. It is surrounded by the Feshbach coils. A high resolution imaging system with microscope objectives is planned in the direction of the vertical detection axis. The connection to the 3D MOT chamber in the middle of the picture is made with flexible bellows. A linear rail with moving transport coils serves to transport ultra cold atom clouds from the 3D MOT to the science chamber. The 3D MOT chamber is part of a combined 2D-3D MOT system. The two MOT chambers are connected via a differential pumping stage, allowing a differential pressure of two orders of magnitude. The self made vacuum seals for 2D and 3D MOT chambers are described in section 2.2. The dispensers are placed in a four way cross on top of the vacuum chamber. A second cut out in the bread board on the left indicates the place for the second 2D-3D MOT system for the implementation of an additional species.

dimensions are given by the MOT chamber. The detailed design and manufacturing process for all magnetic coil systems is presented in chapter 4. As aforementioned it is desirable to have separate MOT systems for higher atom numbers and therefore a magnetic trap design with two layers of magnetic coils is necessary. The three coil systems are depicted with the blue labels in figure 2.2.

The transport from the closest MOT chamber to the science chamber of about $0.4m$ takes approximately $0.9s$ and the maximal acceleration reached is $a = 6m/s^2$ and maximal velocity is $v = 0.875m/s$. An additional consequence to the individual MOT systems is the orientation of the moving magnetic trap. Whereas in other experiments the strong axis acts against gravity, in the setup here the weak axis of the magnetic trap is aligned with the direction of gravity. This is looked at in greater detail in chapter 6.

2D-3D MOT system Figure 2.2 also shows the 2D-3D MOT system consisting of a four way cross at the top, the 2D MOT chamber underneath, followed by the differential pumping stage and the 3D MOT chamber at the bottom. Inside the 2D MOT chamber the atoms are firstly pre-cooled and confined in a thin atom beam and sent through a a small tube, the so-called differential pumping stage, into the 3D MOT chamber where the atoms are recaptured and then transferred to the magnetic trap.

The vacuum seals of the windows for both 2D and 3D MOT chamber are self made. It will be discussed in more detail in the next section. The optical MOT beam layout at the individual MOT chambers is described in section 3.5.

2.2 Combined 2D-3D MOT system

The combination of 2D and 3D MOT systems became recently a common design in ultra cold atom experiments [26,65]. For a high loading rate a high background pressure is needed while low background pressure allows a long lifetime. By separating the trapping and storing of the atoms in the two different pressure regimes of 2D and 3D MOT, separated by a differential pumping stage, both requirements can be met and independently optimised [66,67].

The 2D MOT is based on the same technique as the 3D MOT but just in two dimensions, creating a bright, cold and directed beam from a hot background gas towards the 3D MOT where the atoms get recaptured (see section 5.1.1).

The combined 2D-3D MOT system is constructed as follows. At the top of figure 2.2 a four way cross can be seen holding the dispensers for Rubidium[3] and for Potassium[4] (enriched to 7% of ^{40}K). A view port at the top of the cross gives the opportunity to guide a laser beam through the system in order to push the confined atom beam from the 2D MOT chamber to the 3D MOT chamber.

The rectangular shaped 2D MOT chamber is directly connected to the four way cross. Four large windows give great optical access for pre-cooling the atoms.

The 2D MOT chamber is followed by the differential pumping stage. A graphite tube with an inner diameter of $6mm$ and length of $86mm$ leads to a differential pressure of two orders of magnitude in between 2D MOT and 3D MOT chamber [62]. The graphite acts as a getter material for alkali atoms in order to avoid contaminants creeping down the differential pumping stage.

Once through the differential pumping stage the atoms get recaptured in the 3D MOT chamber that connects with flexible bellows to another differential pumping stage. The bellow is followed by the science chamber or in case of two individual MOT systems by the second 3D MOT chamber. In figure 2.2 the cut out in the

---

[3]SAES
[4]Alvatec

top bread board on the left of the existing MOT system indicates the planned slot for the second MOT system aiming for the individual laser cooling and trapping of different species with high atom numbers.

In the context of the setup here a 2D MOT with lead sealed windows and a narrow 3D MOT chamber with initially epoxy glued optical windows and later indium sealed windows was created. The different chambers will be presented in more detail in the following section.

2.2.1 2D MOT chamber

The 2D MOT chamber is $120mm$ high and has an outer cross section of $110 \times 110mm$. There are four rectangular BK7 windows of $90 \times 45mm$ clear view for the elliptical laser cooling beams. For the magnetic field permanent magnets were installed.
At the top of the 2D MOT chamber the background gas from the dispensers and the pushing beam enter into the chamber. The opening at the bottom lets the cold atomic beam and the pushing beam pass through the differential pumping stage. The windows of the 2D MOT chamber are sealed with a lead solder ring similar to [68]. Lead alloy is less susceptible to oxidation than pure lead and can easily be renewed. The metal is softer than copper and decreases the risk of damaging the view ports during tightening due to lower compression forces.
The ring is compressed in between glass window and steel chamber at the inner sealing and respectively in between window and clamps at the outer vacuum seal. It is an easy way to realise the vacuum seals for large rectangular windows and has the advantage to indium of a higher melting temperature of $T \approx 320°C$ resulting in a higher maximum baking temperature in comparison to the softer indium. On the other hand lead has the drawback of reluctant wetting properties of glass and metal, therefore the use of permanent clamps is required. But since spatial restrictions at the top of the experiment are not present, it is not disadvantageous to use clamps permanently which is different for the 3D MOT chamber.

2.2.2 3D MOT chamber

The 3D MOT chamber has an octagonal shape with one CF35 flange connection at the top as can be seen in figure 2.1 on the right. The two horizontal openings are reserved for connections to the science chamber and additional 2D-3D MOT systems. From the 2D MOT passing through the differential pumping stage, the four openings allocated on the symmetry axes turned by $45°$ plus two large cut outs of a diameter of $70mm$ at the front and at the back are for the laser beams for magneto-optical trapping. The last opening is an optical view port at the bottom for the 2D MOT alignment and diagnostics of the atom cloud if necessary.

In order to prevent a high power dissipation in the transport coils, a large distance and therefore a wider 3D MOT chamber has unconditionally to be avoided. A desirable high optical access is realised by implementing the moving magnetic coils in a second layer further out from the transport axis for independent magnetic trapping. This makes it even more important that the shape of the 3D MOT chamber is very narrow.

On the other hand the 3D MOT vacuum chamber still needs to accommodate the necessary number of MOT beams at an adequate diameter. With the implementation of self made vacuum seals for the MOT beam openings, we achieved the realisation of a narrow 3D MOT chamber of only $33mm$ total width whilst having openings for a beam diameter of up to $25.4mm$.

2.2.2.1 UHV epoxy sealing

The initially realised vacuum seal for the 3D MOT chamber used an epoxy glueing technique. A detailed presentation of this technique can be found in [62]. The necessity of a very narrow vacuum chamber demanded to find a way to seal the vacuum without the use of commercially available view ports or brazing techniques. Possible sealing techniques are lead sealing like used in the 2D MOT chamber, indium and epoxy sealing. The fact that permanent clamps must be used with lead seal made this method infeasible due to limited space around the vacuum chamber. The Indium seal that has the advantage of sealing the vacuum permanently without clamps has the disadvantage of low melting temperatures and was therefore first condemned. In a second attempt, the indium sealing technique is used and is presented in greater detail in the next section.

The third option being epoxy glue combines higher baking temperatures of approximately $T = 175°C$ and seals without permanent external pressure.

Hence an epoxy glueing technique based on 353ND has been developed in order to realise a very narrow 3D MOT chamber design. The epoxy glue shows a low out-gassing rate [69] and has previously been used successfully in atom chip experiments [70]. As materials titanium and BK7 windows are used for two reasons. First they show more similar thermal expansion coefficients and second they are easier to machine than other material combinations.

Despite several promising pre-tests a continuous pressure increase on a long time scale made this kind of sealing technique unsuitable for this experiment without further testing and amendments. The pressure increases most likely due to water being dissolved in the glue layer and permeating the glue into the vacuum chamber. This hypothesis was corroborated by the fact that the increase in pressure can be decelerated if silica pearls are placed close to the vacuum chamber lowering the humidity in the direct environment [62].

Measurements of the MOT loading rate and lifetime of the magnetic trap in the 3D MOT chamber and science chamber showed a vacuum pressure unsuitable for this kind of experiments. The corresponding lifetime measurements in the magnetic trap are shown in figure 6.5.

A long term solution for the epoxy glueing technique is still under investigation but for the experiment a different sealing technique based on indium has been implemented. The indium fulfils the requirements of unnecessary external pressure but has also a lower melting temperature.

2.2.2.2 UHV indium sealing

In this section the indium sealing technique used for the 3D MOT chamber is presented in detail. The indium sealing technique was initially developed in [71] and further developed for UHV bakeable windows with permanent external clamping forces [72]. The indium sealing technique can also be used for fragile and oddly shaped windows since the applied force to achieve a sufficient vacuum seal is low for indium due to the Young's modulus of $E = 11GPa$ [73]. In comparison copper has a Young's modulus[5] of $E < 100GPa$ [74].

Without doubt and especially in comparison to the glueing technique, sealing the vacuum with indium is an easy way for UHV seals. The wetting properties of glass and metal are excellent and no permanent external pressure needs to be applied. Even venting the vacuum system and exposing it to atmospheric pressure and re-evacuating it again does not influence the quality of the seal.

The only drawback is the limited low baking temperature due to a lower melting point of indium in comparison to e.g. lead. The melting point for indium lies at $T_{melt} = 156°C$ allowing for baking temperatures of $T_{bake} = 130°C$ in this case.

For reasons of mainly cost and time consumption, we used a stainless steel vacuum chamber. The vacuum sealing surface should be cut out with the lathe rather than being milled to avoid scratches perpendicular to the seal [75]. The stainless steel vacuum chamber is pre-baked at high temperatures.

Due to time and spatial restrictions only the two big BK7 windows are sealed with indium, conserving the narrow shape of the vacuum chamber. The optical coating is only applied on the central region of $58mm$ diameter on the window, leaving a broad rim of $6mm$ on each side for the indium to spread.

The four small windows are replaced by CF16 view ports that result in further amendments in the 3D MOT telescopes which are looked into at a later point (see section 3.5).

An indium wire of a diameter of $1mm$ with 99.999% purity is used[6]. A viton ring

---

[5]The Young's modulus is an indication of the stiffness of an elastic material to describe its deformation under certain stress.

[6]Goodfellow IN005130
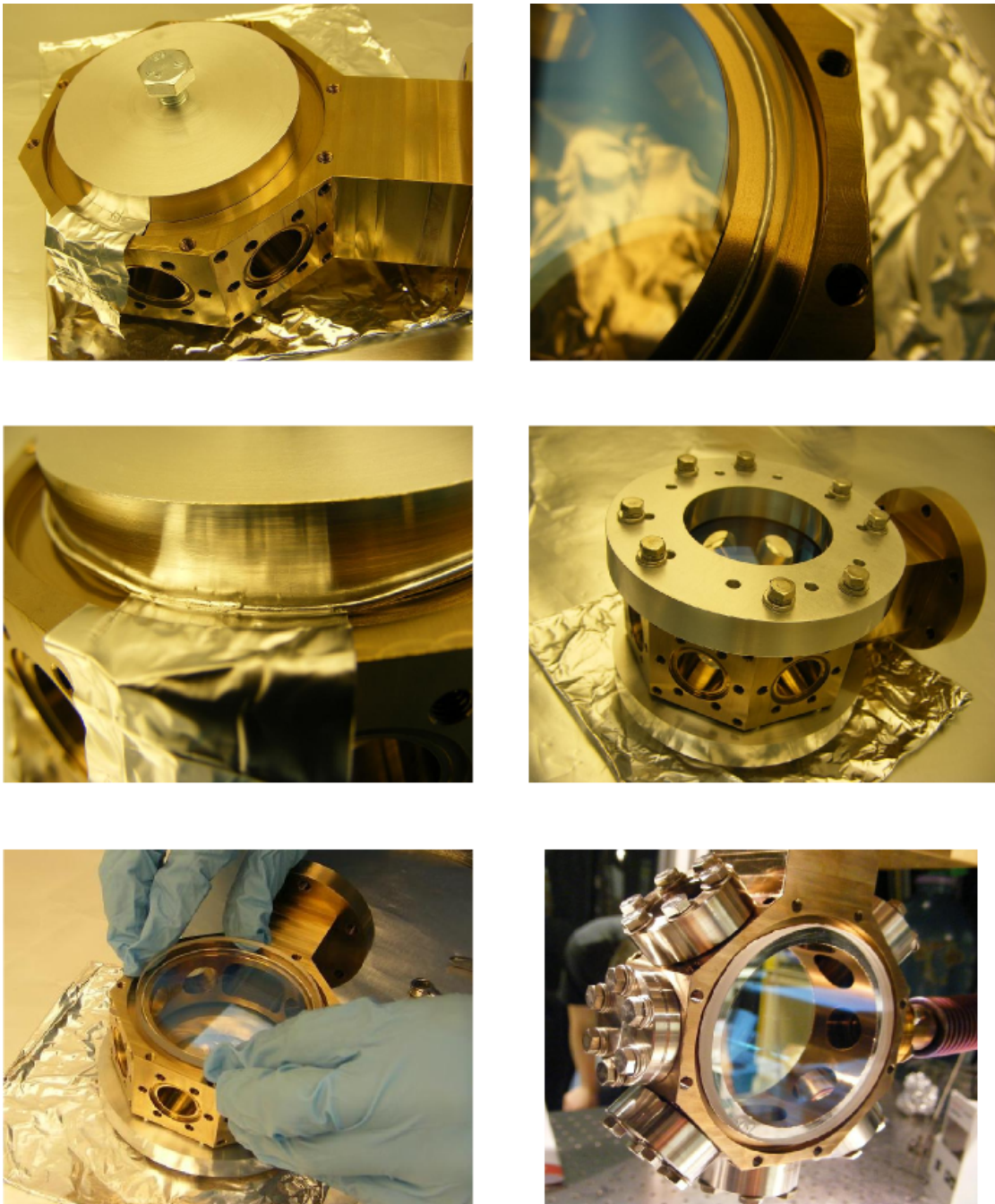
Figure 2.3: *Individual stages of creating an UHV seal with indium, from top to the bottom, from left to right:*
1) A jig is placed in the hole of the vacuum chamber to form a ring of indium wire. A piece of aluminium foil protects the sealing surface when the indium wire is cut. 2) In order to maximise the overlap in between the loose ends, the indium wire is cut at an angle. 3) & 4) The jig is removed and the indium ring is placed in the middle of the rim of the vacuum chamber. The window is carefully placed on top of the indium ring. A viton ring is placed on top of the window. 5) Aluminium clamps press on top of the viton ring with eight M6 screws and compress and flatten the indium ring underneath 6) Finished vacuum chamber without clamps and implemented in the experiment. It is clearly visible how the indium spread uniformly to form the seal over the entire surface.
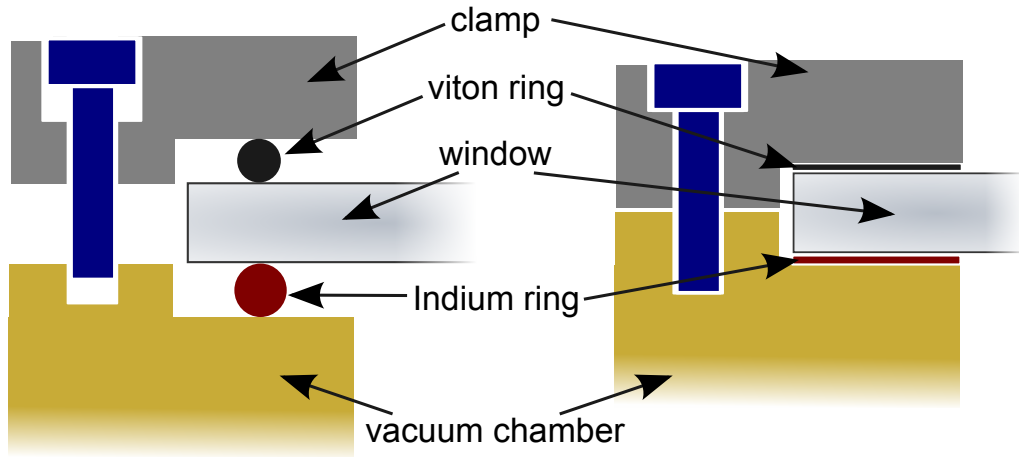
Figure 2.4: *Cross section of an UHV seal with indium:* The indium ring is placed centrally in between the window and the surface of the vacuum chamber's circumference. As a buffer between clamp and window, a viton ring of appropriate size is used. With the aid of the aluminium clamps the viton ring and the indium ring are compressed. The compressed indium forms the UHV seal.

of $1.5mm$ of approximately $67mm$ serves as buffer in between glass and aluminium clamp. For shaping the indium ring an aluminium jig is used.

All metal parts are cleaned in the ultrasonic bath in high grade acetone and liquinox water mixture for $15min$ each time. Afterwards they get soaked in distilled water and are further cleaned for $15min$ in isopropanol in the ultrasonic bath.

The individual stages of the process are depicted in figure 2.3 from top to the bottom and from left to right. First the jig is placed in the hole of the vacuum chamber, aluminium foil placed underneath preventing damage to the surface finish when the indium wire is cut.

In the second picture one can see how the indium wire is cut at an angle to maximise the overlap in between the loose ends without adding more material than in other places. The radius of the indium ring is $67mm$, situating the indium ring in the middle of the uncoated window rim.

The jig is removed and the window carefully placed on top of the indium which can be seen in the third and fourth picture. On top of the window a viton ring is placed with exactly the same radius as the indium ring. A schematic drawing of the arrangement is shown in figure 2.4.

The clamps press on top of the viton ring with eight M6 screws and compress and flatten the indium ring underneath, creating the seal as seen in the fifth picture.

The sixth picture shows the finished vacuum chamber without clamps implemented in the experiment. It is clearly visible how the indium spread uniformly over the entire surface. The vacuum chamber was pumped down to low $10^{-11}mbar$, vented

and afterwards pumped down successfully again.

Due to the change of the sealing technique from epoxy glueing to indium sealing combined with small commercial view ports it is impossible to fit the telescope length initially planned onto the 3D MOT chamber without restricting the linear rail to pass. The telescope lengths were reduced, letting the beams divergently expand (see figure 3.22). More details on that can be found in section 3.5 and the results are discussed in section 5.1. These amendments to the MOT beams do not hinder the performance of the experiment but gives moreover the possibility to optimise also the intensity and beam size in the future.

The entire system is pumped by three ion getter pumps with a pumping speed of $20 l/s$ and two titanium sublimation pumps. According to the ion pump readings the pressures reached are $10^{-9} mbar$ inside the 2D MOT chamber, low $10^{-11} mbar$ to $10^{-12} mbar$ range inside the 3D MOT chamber and $10^{-12} mbar$ inside the science chamber.

Hence we successfully implemented another vacuum sealing technique in our experiment but still conserving the main narrow features of the 3D MOT vacuum chamber needed for magnetic transport with high optical access. The ease and freedom of arbitrary shaped seals make this technique an interesting candidate for alternative vacuum seals.

This vacuum system can be used for a 2D simulation experiment for multiple species. The compact 2D-3D MOT system enables us to implement additional species with out amendments to the existing chamber. Separate 2D-3D MOT systems and a magnetic transport system based on a narrow vacuum chamber design have been designed. A two layer coils design retains a high optical access and transfers the cold atom clouds towards the science chamber with high optical access. Within the ultra high vacuum environment the atom clouds can be stored and cooled further in magnetic quadrupole and optical dipole traps where the atoms are directly observed with absorption imaging.

Chapter 3

A compact dual species laser system

For laser cooling and trapping of neutral atoms with discrete atomic transitions coherent laser light sources with comparable narrow line widths are needed. Given the species used two or more wavelengths are used.

In this section the miniaturised dual species laser system for ^{87}Rb and ^{40}K is presented. In the context of this thesis the laser system has been designed and set up. The alignment and testing in magneto-optical trapping experiments for two species has been completed. The design is ultra compact and highly modular and therefore shows outstanding flexibility. It stands out with high thermal and mechanical stability and robustness and very low maintenance.

The actual technique was first developed in the context of the QUANTUS collaboration project [3, 76] and is here realised for the first time for two species simultaneously and the first time for ^{40}K at a wavelength of $767nm$. A detailed description of the individual modules is presented.

This chapter is organised as the following, first an overview over the laser system and the conceptual idea is presented in 3.1. The different sections of the laser system frequency stabilisation (3.2), light amplification (3.3) and fibre preparation (3.4) will follow, guiding the reader step by step towards the experiment. The optical setup on the optical table is presented in section 3.5 followed by a brief overview of the detection system.

3.1 Laser system overview

The laser system setup used here fulfils all the functions of laser cooling, optical pumping for magnetic trapping and detection for the two chosen species. The entire setup is designed to provide the correct frequency, power and number of

fibres with all additional degrees of freedom needed for the dual species experiment with a combined 2D-3D magneto-optical trap. With the exception of a few smaller details the system is identical in construction for both species rubidium (^{87}Rb) and potassium (^{40}K) and gives even the flexibility to be adapted to other species in the future. Hence it will be discussed only once in the context of this thesis and as long as the two laser systems have not been stated to be different in design or operation, it can be assumed that in both cases it is the same setup.

The main difference to most of the usual laser system setups are the miniaturised mechanical optics (see figure 3.1) that were developed in the context of the QUANTUS collaboration project [3, 76], where the design has proven to withstand repeatedly decelerations of up to $50g$ where g is the gravitational force. During the deceleration the laser system often even stays locked without any damages [63]. Due to its miniaturised design it shows a higher stability against temperature drifts and mechanical stress on both short and long time scales. Furthermore it is ultra compact and needs less space in a laboratory experiment.
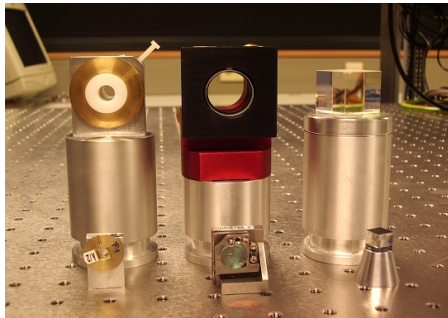

Figure 3.1: *Comparison of mechano-optical mounts:* The miniaturised version in front with commonly used mechano-optics in the back. The reduced size implicates a higher stability against temperature drifts and mechanical stress. The design was realised in the context of the QUANTUS collaboration project [3, 63, 76].

A highly modular approach for the laser system, enclosing the optics in separate aluminium boxes, reduces the space needed for the entire laser system even further. Instead of having the optics spread over the optical table, how it is often common practise in other laboratory setups, each section of the laser system is put in a separate module that is connected via optical fibres and can be stacked up. Each module fulfils one certain task and can be connected or added at arbitrary points in the system depending on the configuration of the experiment. In figure 3.2 one half of the dual species laser system is shown and in total it fills roughly one third of our optical table, leaving enough residual space for the vacuum setup.

Each of those individual modules serve one objective, e.g. amplification of the incoming laser radiation. Hence, the setup is very flexible meeting the experiment demands for the present and in the future.

The overall concept of the laser system is shown in figure 3.3 and can be divided in three different comprehensive sections. The first part is dedicated to frequency
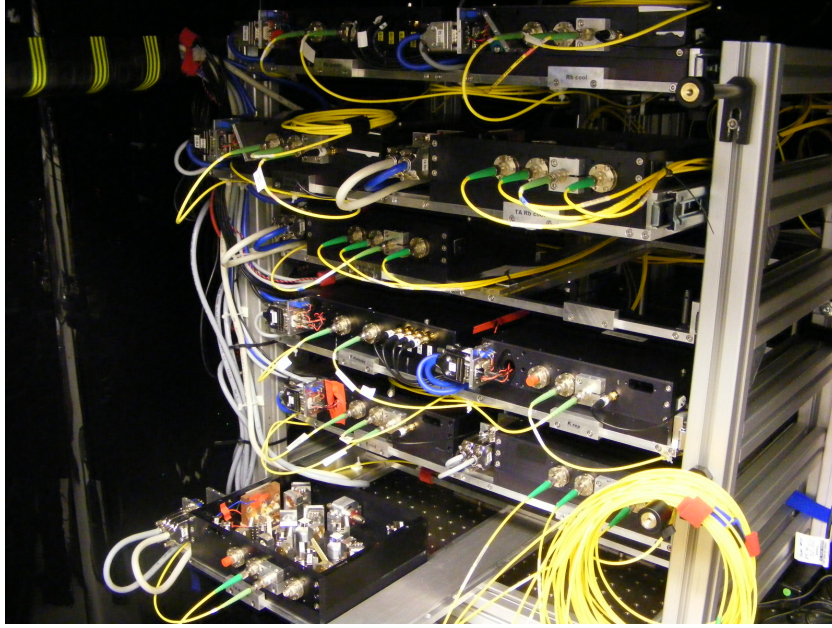
Figure 3.2: *Frequency stabilisation and power amplification section for both species:* Twelve individual boxes are stacked up and connected via optical fibres. The three top shelves are the modules for $780nm$, the bottom ones for $767nm$. Six laser diodes (ECDLs and DFB diodes) are frequency stabilised and the light is amplified with six tapered amplifiers (TA).

selection and stabilisation depending on the species used. This section itself is built by two distinctive modules (master and offset module) that use different methods for frequency stabilisation. Next comes the amplification stage where the incident power is amplified (amplification module). Splitting the light in the right number of beams and guiding the light through optical fibres to the experiment completes the last stage of the laser system for pre-cooling the atom clouds (three different splitting modules).

In the following paragraphs each of those sections and modules of the laser system is reviewed. Additionally the special features and the used transitions for rubidium and potassium are investigated.

3.2   Frequency stabilisation for ^{87}Rb and ^{40}K

3.2.1   Features of rubidium and potassium

Like in many more experiments in the ultra cold atom community rubidium and potassium are used in this setup. Since we are interested both in bosonic and fermionic statistics for quantum simulations, the atomic isotopes ^{87}Rb (boson) and
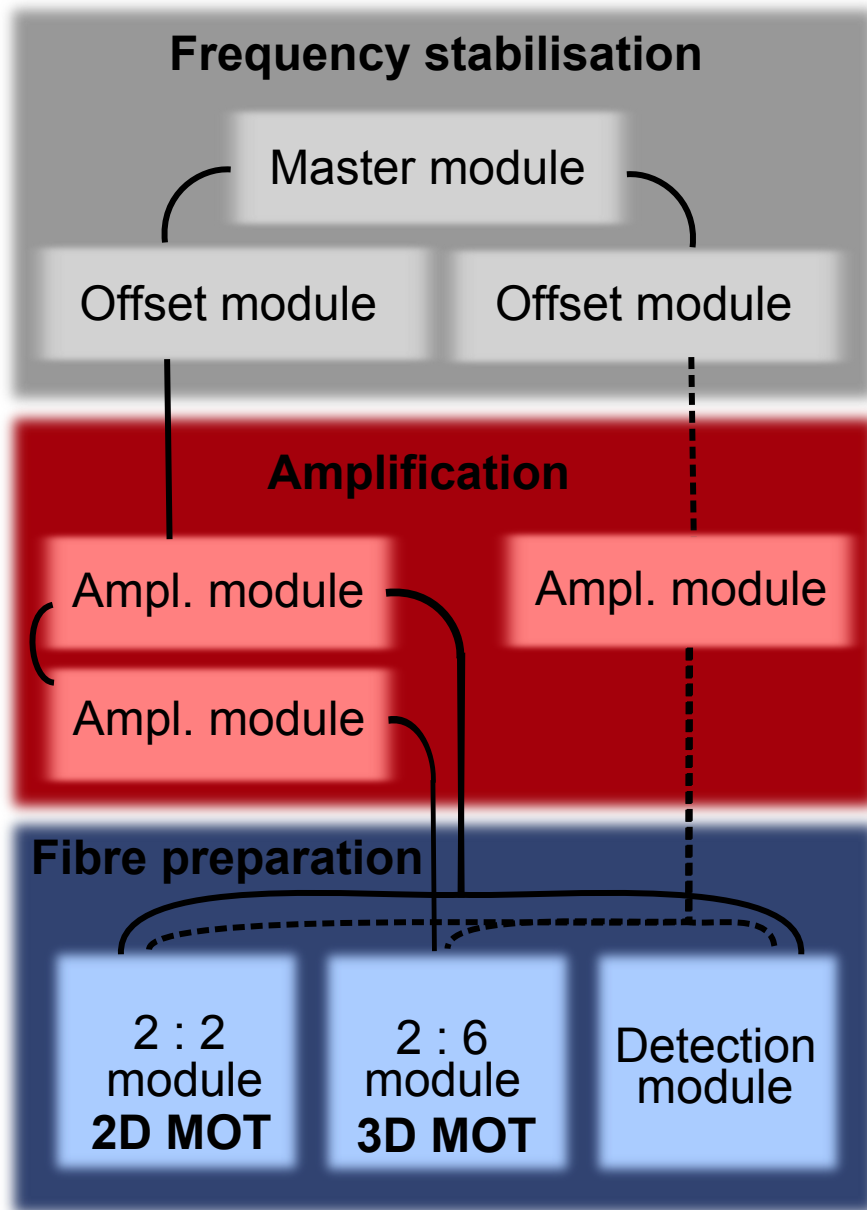
Figure 3.3: *Concept of the miniaturised laser system:* The laser system is separated into three different sections. The first one is dedicated to frequency stabilisation, including the master and offset lock module. Then follows the amplification stage and the preparation of the experiment fibres in the splitting modules by mixing the cooling and repumping light in different fibres. The solid line represents the cooling light and the dashed line the repumping light respectively.

^{40}K (fermion) have been chosen. For the future it will be possible to expand the system to other elements if necessary.

Both rubidium and potassium are alkali atoms with one single electron in the outer shell and are therefore chemically very reactive. But fortunately this makes the level scheme much easier in comparison to other elements and only a few transitions are needed to be taken into account for laser cooling what again makes the number of laser frequencies needed small.
A good summary of physical and optical properties for ^{87}Rb can be found in [77] and for all three existing isotopes for potassium ^{39}K,^{40}K and ^{41}K in [78] respectively. A few important properties for ^{87}Rb and the two isotopes of potassium ^{40}K (fermionic) and ^{39}K (bosonic) that will be needed through out this thesis are given in table 3.1. The isotope ^{39}K is taken here into account because due to the small natural abundance of ^{40}K of below 1% (s. table 3.1). It is needed for the frequency stabilisation of ^{40}K and besides it would be also possible to realise a cold atom cloud with this isotope with only small changes in the laser system.

Both elements rubidium and potassium, although having some severe differences, share quite a few common features. Both of them have no orbital momentum $L = 0$ in the ground state. Thus only the coupling in between the spin of the electron $S = 1/2$ and nuclear spin I of the nucleus occurs. Consequentially the hyperfine splitting of the ground state produces two non-degenerate ground states with $F = I + 1/2$ and $F = I - 1/2$. Exciting the electron to the orbital momentum $L = 1$, it can couple with the electron spin $S = \pm 1/2$ with $J = L + S$ to $J = 1/2$ or $J = 3/2$. The transition from the ground state $^2S_{1/2}$ to the excited state $^2P_{1/2}$ is called D_1-line. The transition from the same ground state to the excited state $^2P_{3/2}$ is called D_2-line.
Each of the excited states show a hyperfine splitting according to the coupling between J and I that is for all potassium isotopes very small and for ^{40}K inverted due to the high nuclear spin of $I = 4$. The level scheme of ^{39}K is very similar to ^{87}Rb since both atoms have the same nuclear spin of $I = 3/2$ (s. table 3.1).

In both cases ^{87}Rb and ^{40}K only the D_2-line is used that has a nearly closed transition for laser cooling in the hyperfine split manifold, a so called cycling transition. Since this particular transition is not entirely closed and there is a finite probability to loose the atoms to a "dark" state, a repumping transition is needed. Due to the fact that the probability to loose an atom to a different state that cannot be seen by the cooling laser is much higher for ^{40}K then for ^{87}Rb, the repumper acts in the previous case of ^{40}K more like a second cooling transition and will therefore be red detuned.

		^{87}Rb	^{40}K	^{39}K
Atomic Number	Z	37	19	19
Neutrons and Protons	N + Z	87	40	39
Nuclear spin	I	3/2	4	3/2
Rel. natural abundance [%]	η	27.83	0.0117	93.26
Mass [au]	m	86.91	39.96	38.96
Vapour pressure [$10^{-8}mbar$]	p	39.2 ($25°C$)	1.3 ($20°C$)	1.3 ($20°C$)
D_2 transition frequency [THz]	w_0	$2\pi \cdot 384.23048$	$2\pi \cdot 391.01629$	$2\pi \cdot 391.01617$
D_2 transition wavelength [nm]	λ	780.24121	766.70067	766.70092
D_2 transition lifetime [ns]	τ	26.23	26.37	26.37
D_2 transition line width [MHz]	Γ	$2\pi \cdot 6.067$	$2\pi \cdot 6.035$	$2\pi \cdot 6.035$
Saturation intensity [$\frac{mW}{cm^2}$]	I_s	1.67	1.75	1.75

Table 3.1: Physical and optical properties of ^{87}Rb, ^{39}K and ^{40}K (taken from [77] and [78])

For optical pumping, pushing and detection the cycling transition is used. The particular hyperfine transitions used for ^{87}Rb and ^{40}K are displayed in table 3.2 respectively table 3.3. The level schemes can be found in the appendix A.

In order to generate the laser radiation with exactly this specific frequency atomic spectroscopy is used like it is shown in the next section 3.2.2 where an external cavity diode laser is stabilised to an atomic transition.

3.2.2 Master module

The wavelength of a semiconductor laser diode is mainly determined by its energy band gap. Within this limitation a more precise tuning can be achieved by adjusting the temperature and the injection current. This will change the path length in the optical cavity and the carrier density in the active region that itself will also change the refractive index in the material. All those effects combined result in a change in frequency.

For actual laser cooling of a specific element the laser needs to be stabilised in respect to a certain atomic transition by constantly regulating the temperature, the injection current of the laser diode and if present the position of the piezo element

Purpose	Transition	Detuning	Power
Cooling light 2D	$\lvert F = 2\rangle \Rightarrow \lvert F' = 3\rangle$	red detuned	$\approx 49mW$
Repumping light 2D	$\lvert F = 1\rangle \Rightarrow \lvert F' = 2\rangle$	resonant	$\approx 11mW$
Cooling light 3D	$\lvert F = 2\rangle \Rightarrow \lvert F' = 3\rangle$	red detuned	$\approx 55mW$
Repumping light 3D	$\lvert F = 1\rangle \Rightarrow \lvert F' = 2\rangle$	resonant	$\approx 6mW$
Pushing light	$\lvert F = 2\rangle \Rightarrow \lvert F' = 3\rangle$	red detuned	$< 0.1mW$
Optical pumping	$\lvert F = 2\rangle \Rightarrow \lvert F' = 3\rangle$	resonant	$\approx 250\mu W$
Detection light	$\lvert F = 2\rangle \Rightarrow \lvert F' = 3\rangle$	resonant	$\approx 100\mu W$

Table 3.2: ^{87}Rb D_2-line transitions used: Detuning and laser power at the position of the atoms for different experimental stages are given.

Purpose	Transition	Detuning	Power
Cooling light 2D	$\lvert F = 9/2\rangle \Rightarrow \lvert F' = 11/2\rangle$	red detuned	$\approx 22mW$
Repumping light 2D	$\lvert F = 7/2\rangle \Rightarrow \lvert F' = 9/2\rangle$	red detuned	$\approx 6mW$
Cooling light 3D	$\lvert F = 9/2\rangle \Rightarrow \lvert F' = 11/2\rangle$	red detuned	$\approx 78mW$
Repumping light 3D	$\lvert F = 7/2\rangle \Rightarrow \lvert F' = 9/2\rangle$	red detuned	$\approx 23mW$
Pushing light	$\lvert F = 9/2\rangle \Rightarrow \lvert F' = 11/2\rangle$	blue detuned	$< 1mW$
Optical pumping	$\lvert F = 9/2\rangle \Rightarrow \lvert F' = 11/2\rangle$	resonant	$< 1mW$
Detection light	$\lvert F = 9/2\rangle \Rightarrow \lvert F' = 11/2\rangle$	resonant	$< 1mW$

Table 3.3: ^{40}K D_2-line transitions used: Detuning and laser power at the position of the atoms for different experimental stages are given.
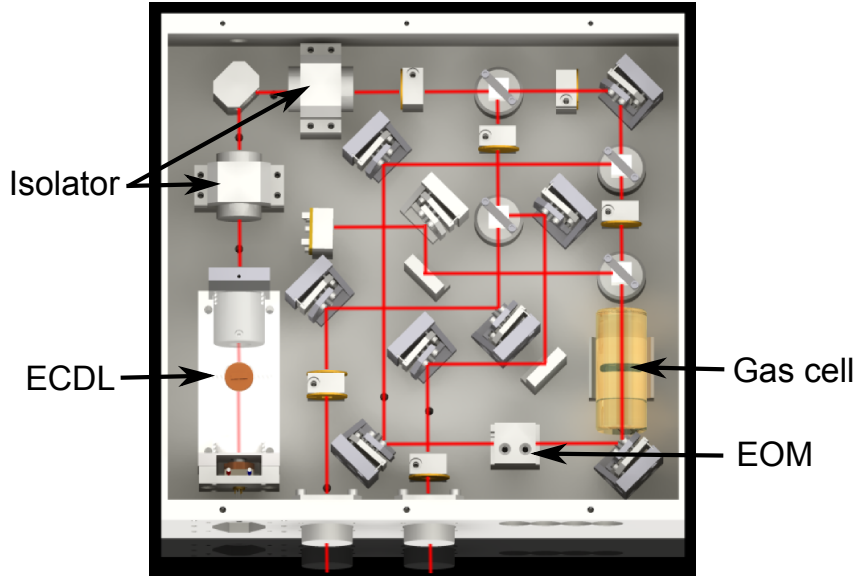
Figure 3.4: *Layout of the master module for frequency stabilisation of an ECDL with interference filter to an atomic reference in a gas cell:* FM spectroscopy is used as a locking scheme. In the bottom left corner the ECDL with interference filter and cats eye configuration is situated. The light passes through optical isolators before one part of the light is split on a polarising beam cube into the spectroscopy beam path. The residual light is fibre coupled. Two output fibres guide the locked reference frequency to the adjacent offset module. In the spectroscopy beam path the light is again split on a polarising beam cube into a pump and a probe beam that counter propagates through a gas cell for saturated spectroscopy. The probe beam is modulated by an electro-optical modulator (EOM) before passing through the gas cell and is then detected by a photo diode.

in the cavity. Therefore it is necessary to determine where the laser wavelength is positioned relative to the frequency of the atomic transition by performing spectroscopic measurements and then locking the laser onto one of these transitions. The locking scheme used here is frequency modulation (FM) spectroscopy [79]. The setup of the so-called master module is shown in figure 3.4.

The master module generates a stable reference frequency for a specific species by doing spectroscopy on an atomic gas cell. This frequency is then used within the entire part of the laser system for that species. All residual laser frequencies are locked in respect to that reference frequency.

Due to the low vapour pressure at room temperature for potassium (see table 3.1) the gas cell[1] needs to be heated to approximately $45°C$[2] in order to increase the signal by a significant factor. Non linear absorption phenomenon happening at high temperatures put a limit to the benefit of increasing the temperature much

---

[1]The length of the gas cell is roughly $5cm$.

[2]At $45°C$ potassium has approximately the same vapour pressure like ^{87}Rb at room temperature.

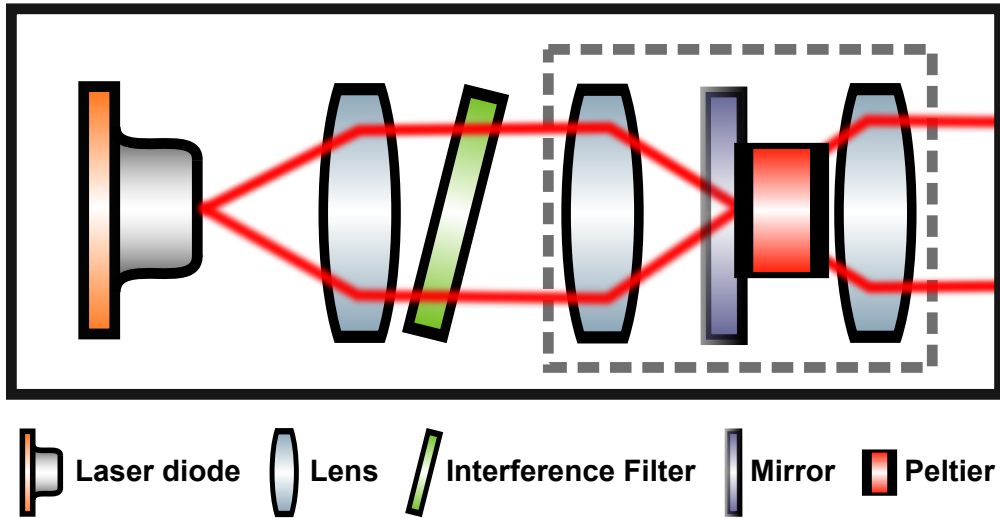| Laser diode | Lens | Interference Filter | Mirror | Peltier |

Figure 3.5: *The external cavity diode laser (ECDL) with interference filter* as a second order wavelength discriminator. The light of the laser diode is collimated, passes through the interference filter before being focussed down onto a partly reflecting mirror and being re-collimated by a cats-eye configuration. The partly reflecting mirror is situated on a piezo element. The feedback elements and wavelength selecting elements are fairly independent, resulting in a stable performance. The linear configuration makes it even more robust.

further [80]. The gas cell for potassium is wrapped in a film resistor heated with an approximate power dissipation of $4W$ and thermally shielded against room temperature.

The laser source in this module is an external cavity diode laser (ECDL)[3] with an interference filter as an additional wavelength discriminator. There has been no previous experience in the group with the miniaturised version of this particular ECDL. The next two paragraphs will concentrate first on the ECDL setup realised in this laser system and then very briefly on the FM spectroscopy to stabilise the ECDL to the atomic transition.

3.2.2.1 ECDL

The original design of an ECDL for telecommunication [81] was adapted for optical wavelength [82] and was even extended to tapered amplifiers for high power outputs [83]. Here we use exactly the same design from [84] for a miniaturised setup for a space interferometer.

---

[3]L785P090 (Thorlabs) for $780nm$ and EYP-RWE-0790-04000-0750-SOT01-0000 (eagleyard Photonics GmbH) for $767nm$.

The linear design of the ECDL with interference filter spares the grating that is replaced by a low loss interference filter. It is more robust in comparison to a fragile etalon that can turn out to be costly and be destroyed over time by ambient water [82].

The interference filter is basically a narrow band width filter for optical frequencies and serves as a second stage wavelength discriminator by reflecting the light multiple times within the dielectric coating similar to a thin Fabry-Perot Etalon and interfering the wave packets travelling in the cavity. By separating optical feedback and wavelength tuning elements and the linear design makes it more stable to mechanical disturbances and misalignment.

In figure 3.5 the ECDL with cats-eye configuration is shown. Two of these ECDLs, one for each species, have been built in the context of this thesis. The laser diode for $780nm$ $(767nm)$ is collimated with a collimation lens of $f = 4.51mm$ $(3.1mm)$, the light passes then through the interference filter (green). The following cats-eye configuration shown in the dotted framed box in figure 3.5 focuses the light with a lens of a focal length of $f = 18.4mm$ $(18.4mm)$ onto a partly reflecting mirror with a reflectivity of $R = 18\%$ that serves as feedback into the cavity. This arrangement of focussing it onto the mirror contributes significantly to the stability of the feedback of the ECDL. The divergent light gets collimated again behind the back reflecting mirror with the second collimation lens $f = 11mm$ $(11mm)$.

It is an easy and stable setup for a comparable narrow bandwidth radiation source where the collimation, feedback and wavelength tuning can be optimised individually. In the current setup it operates totally maintenance free. Even mounting it vertically should not cause problems in the performance of the laser. Furthermore it can also easily be adapted for other laser diodes.

As before mentioned the ECDL is depicted in the master module in the bottom left corner of figure 3.4. The light coming out of the ECDL passes through an optical isolator and splits then partly into the spectroscopy beam path for FM spectroscopy. The residual light is split into two beams of a few mW that are fibre coupled into the offset lock module as a reference frequency for further locking purposes (see section 3.2.3). The locking scheme used here to stabilise the master laser to an atomic transition is reviewed in the next section.

3.2.2.2 Frequency modulation spectroscopy

The most reliable and convenient frequency reference to lock a laser to an atomic transition is the atom itself. Usually a gas cell is used in which the spectral feature of interest is probed by a probe beam.

At room temperature the atomic transitions are significantly Doppler broadened
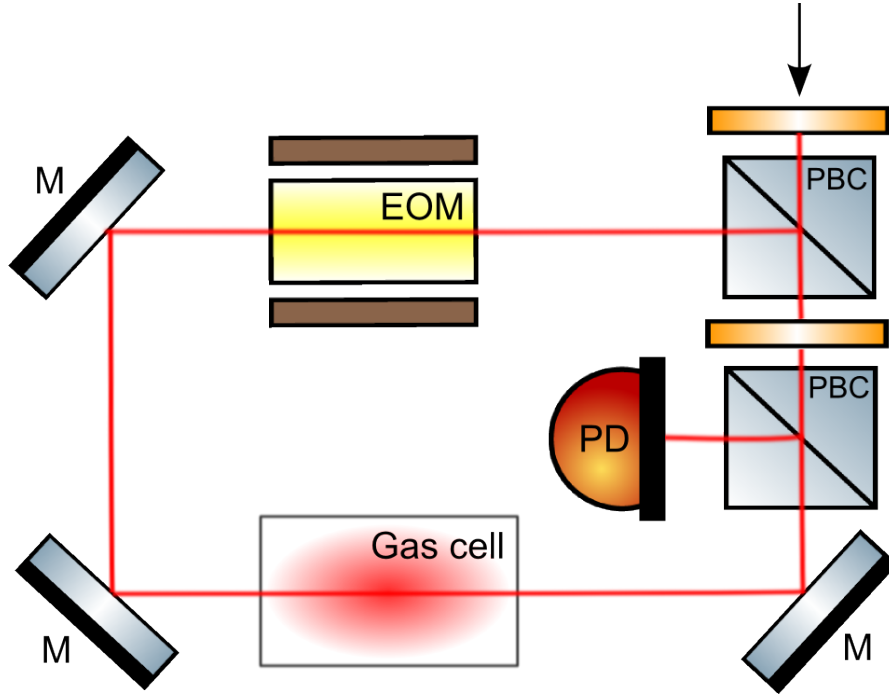
Figure 3.6: *Schematic of the FM spectroscopy for the master module:* A $\lambda/2$ wave plate splits the beam entering at the top on a polarising beam cube (PBC) into probe beam and pump beam. The linearly polarised probe beam goes through an eletro-optic modulator (EOM)(yellow) where the beam is frequency modulated (FM) with $10MHz$. For a good signal the amplitude modulation (AM) is minimised and the FM modulation index is chosen to be small. Shortly after the beam passes through the atomic sample (red) that has been optically pumped by the counter propagating pump beam. The probe beam produces a beat note signal on a fast photo diode (orange) due to the distortion by the atomic sample.

and most of the atomic frequency characteristics are washed out. By using a counter propagating pump beam at the same frequency, that is substantially stronger than the probe beam, atoms of the resonant velocity class v will be saturated. On the other hand the counter propagating probe beam is resonant to atoms of the velocity class $-v$. If the laser approaches the resonance atoms at $v = 0$ interact with the laser. But due to the much stronger pump beam the gas is saturated and becomes essentially transparent for the probe beam. The so called spectral hole burning sets in and in the absorption spectrum of the probe beam the spectral features of the atomic transitions start appearing.

However, the absorption spectrum shows more features than there are actual atomic transitions. This is due to so-called crossover resonances, half way between the actual transitions. They are rooted in the closely spaced hyperfine manifold of the atomic sample. The counter propagating beams react both with the same velocity class of atoms $v \neq 0$ but with opposite sign in frequency shift. This technique was first applied and initially limited to molecules [85] and gas laser transitions but

with the possibilities of organic dye lasers it was also extended to atomic transitions in sodium [86] and hydrogen [87].

A robust technique for generating good error signals out of spectroscopy measurements is the frequency modulation technique used here. It is a rapid and reliable technique using a hybrid optical and radio frequency approach [88, 89] that can use standard RF components. It relies on the occurrence of beat signals due to distorted optical signals. The distortion thereby can be generated even by a weak or narrow atomic transition. Although very sensitive to optical features the method is insensitive to e.g. power fluctuations of the laser beams. The RF frequency can be large in comparison to the optical line width where the laser noise has significantly decreased whilst conserving the laser's resolution.

Already applied successfully in other ultra-cold atom experiments and also on laser diodes with broader line widths [63] this locking scheme serves fully the demands of the experiment. The setup realised here follows reference [79]. A similar setup for potassium was investigated in [80].

The schematic in figure 3.6 displays the beam path for the spectroscopy setup. The beam enters at the top and gets split on a polarising beam cube by a $\lambda/2$ wave plate. The probe beam passes with linear polarisation through an eletro-optic modulator (EOM)(yellow) in such a way that the beam is frequency modulated (FM) with $10MHz$ and the amplitude modulation (AM) is minimised. Shortly after the beam passes through the atomic sample (red) that has been optically pumped by a counter propagating beam. The beam is then focused on a fast photo diode (orange) and produces a beat note signal.

The photo diode signal of the modulated beam would be a pure dc signal if the carrier and side bands beating with each other cancelled out completely. The distortion by an atomic sample will give rise of a non-vanishing rf beat signal, giving a zero crossing only if the two beat signals between carrier and each side band cancel out at resonance of the carrier with the atomic transition.

Here we use $\omega_m = 10MHz$ generating a good line shape and large slope size for locking a laser to a feature of $\Gamma \approx 6MHz$ [79]. The error signal therefore comes straight out of the spectroscopy signal. After the initial alignment procedure the setup operates maintenance free.

The FM spectroscopy technique produces an error signal that resolves the hyperfine splitting and the crossover transitions nicely in the case of ^{87}Rb and we lock stably to the crossover transition in between $|F = 2 \rightarrow F' = 2\rangle$ and $|F = 2 \rightarrow F' = 3\rangle$.

In case of potassium the hyperfine structure cannot be resolved with our setup since the transitions are very closely spaced, therefore its also advantageous to use a narrower line width laser like an ECDL.
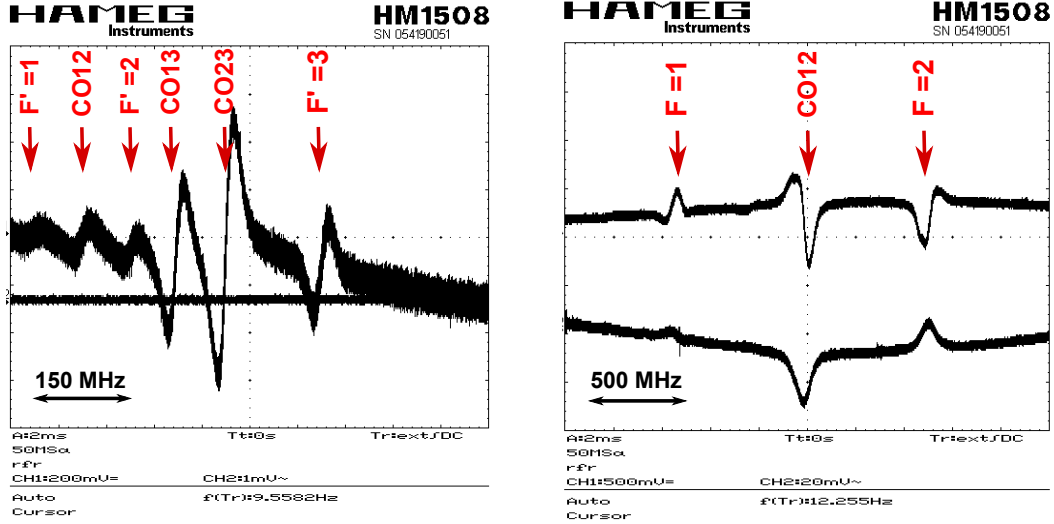
Figure 3.7: *Error signal rubidium and potassium master:* On the left the error signal of the rubidium master laser is shown. The strongest transition are from the ground state $|F = 2\rangle$ to $|F' = 2\rangle$ or $|F' = 3\rangle$. Due to the spectroscopy the clearest zero crossing is the cross over transition CO23 in between the two transitions. On the right the error signal of the potassium master laser is shown. The strongest transition are from the ground state $|F = 1\rangle$ or $|F = 2\rangle$ to the excited. In the case of ^{40}K the cross over transition CO12 is in between the two transitions from the ground states rather than the excited states like in ^{87}Rb. Both error signals are generated with frequency modulation spectroscopy and severe as reference frequencies through out the entire laser system.

The main features in the master error signal are the strongest transition in ^{39}K from the ground states to the excited manifold $|F = 1 \rightarrow F'\rangle$ and $|F = 2 \rightarrow F'\rangle$ and the crossover transition in between them. Since the crossover here is in between two ground states rather than two excited states like in rubidium the shape is inverted. The ^{39}K isotope has the strongest abundance (see table 3.1) and since additionally the wavelengths are so similar in between the three isotopes only the isotope ^{39}K can be seen in this spectroscopy setup. But since the frequency differences are so small locking to this isotope is sufficient. The master laser for potassium is locked to the strongest line, the crossover transition $CO12$.

Furthermore it makes it possible with small changes in the offset lock system to realise laser cooling and trapping of the other two isotopes of potassium as well.

All in all the FM modulation spectroscopy produces a stable and reliable lock for our reference frequency for both species ^{87}Rb and ^{40}K (also ^{39}K) that can be used in the offset lock module for locking the cooling and repumping laser diodes in respect to this frequency. The offset lock module is described in next section.

3.2.3   Offset lock module

The offset lock module is the part of the laser system where the laser diodes providing light for the cooling and repumping transitions and moreover for optical pumping and detection are locked to a reference frequency. This reference frequency is generated in the master module and guided in an optical fibre to the offset module.

The locking scheme used here is the offset lock technique that relies on the beat of two frequencies and enables locking independently to an atomic transition just by the mean of the difference of two wavelengths. Each module of this kind contains a laser diode, producing light used for either cooling or repumping purposes according to the species used. Consequentially there are four modules of that kind for two species.

Instead of using ECDLs as a source of laser radiation like in the master module case, this module realises an easier option, a distributed feedback diode (DFB). With the usage of distributed feedback diodes (DFB) the necessity of an additional external wavelength selecting element like gratings, interference filters and optical feed back can be avoided.

The module itself can be adapted to ECDL setups as well in case frequencies for elements are needed where no DFB diodes are available yet or a smaller line width becomes necessary.

But unfortunately the line width of DFB diodes are with approximately 2-10MHz [90] usually much larger than the line width of EDCLs that can be in the range of a few hundreds of kHz or even lower. The larger line widths of DFB diodes can be disadvantageous for ultra-cold atom experiments but turns out to be satisfying for laser cooling in this case here (see section 5.1).

The beat notes of an ECDL and a DFB diode for the two different wavelengths involved are shown in figure 3.9 and 3.10 and will be discussed later.

In case of rubidium ($\lambda \approx 780nm$) DFB diodes are well known and approved tools for generating light for laser cooling [63]. In case of potassium ($\lambda \approx 767nm$) the case lies different and at the time the experiment started, the status for potassium DFB diodes was still experimental.

The Ferdinand Braun Institute (FBH) investigates the possibilities of creating a DFB diode for $767nm$ and made some prototypes of their DFB diodes available in order to test their performance directly in an ultra cold atom experiment. Therefore it has been possible to achieve the frequency stabilisation of a DFB diode to a reference frequency and to test the performance in laser cooling experiments of ^{40}K as presented in section 5.1 in the context of this thesis.
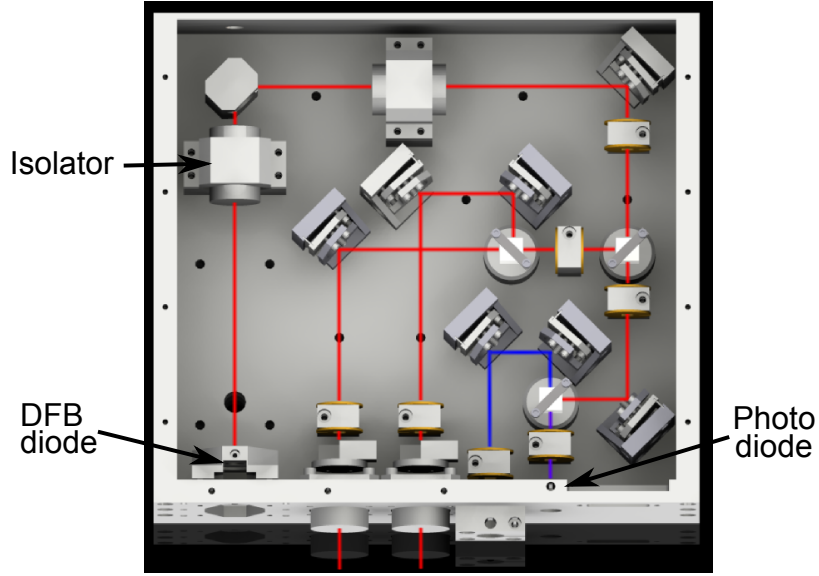
Figure 3.8: *Offset module for frequency stabilisation of cooling and repumping light in respect to a reference laser:* The collimated beam of a DFB diode passes through several optical isolators. The laser diode is positioned in the bottom left corner, followed by the optical isolators. The frequency stabilisation part is at the bottom right corner. It consists only of the superposition of the reference laser (blue) with the offset module beam (red) on a fast photo diode and is locked via an offset lock side filter technique [91]. To make the beams interfere, a polariser in front of the photo diode ensures the same polarisation of both incident beams. The beat signal generated by the photo diode is processed further by an electronic rf circuit. The residual light is coupled into optical fibres.

The DFB diodes for $767nm$ are mounted in a C-mount that itself is mounted on a copper block cooled by a peltier element placed underneath. The chip is $3mm$ long and the threshold current is approximately $I_{thres} \approx 80mA$ at a temperature of $T = 35°C$. According to the manufacturer the maximum output power at $I_{max} = 200mA$ is supposed to be $\approx 30mW$ leading to an efficiency slope of $0.25mW/mA$.

Unfortunately this could not be reproduced in our setup. The maximum output power lies by $P_{out} \approx 18mW$ at $I = 186.5mA$ and $T \approx 40°C$. The efficiency slope is then given by $0.097mW/mA$ which is far below previous expectations.

Furthermore the high temperature is unfavourable since it causes increased ageing in the laser diode [92] and degradation but cannot be avoided here since the wavelength for the D_2-line in ^{40}K (see table 3.1) needs to be reached.

But nevertheless the generated power and the line width of the DFB diodes are sustainable for laser cooling and trapping of ^{40}K.

The DFB for ^{87}Rb is mounted in a TO9 housing and has an integrated peltier element close to the chip. The housing is filled with a protective buffer gas to safeguard the diode at high optical power densities. But due to several failing

laser diodes, it was decided to open the housing and exchange the protective gas with ambient air and both diodes are performing with output powers above $P_{out} > 30mW$ faultlessly and maintenance free.

In figure 3.8 the layout of the offset lock module is shown. As afore mentioned the module is using the offset lock technique to stabilise the DFB diodes to a reference frequency obtained by spectroscopy of an atomic gas cell. The light from the DFB diode is collimated and travels through several optical isolators.
Since the modules are all fibre coupled with each other the alignment of the optical beam paths is optimised up to the point that the spontaneous emission travelling back from the following tapered amplifier (see section 3.3) couples back into the laser diodes. This causes instabilities and frequency jumps in the laser diode performance. In order to reduce this feedback to a level where the disturbances on the locking scheme are tolerable up to three isolators are used each isolating with a level of up to $-25dB$. One reason for the necessity of such a high isolation might be the high degree of amplified spontaneous emission (ASE) coupled back into the fibre from the following amplification module. The high level of ASE could be caused by low seeding power from the DFB diodes as mentioned above. This point will be picked up again at a later point (see section 3.3).
On the other hand the feedback effects could also be used to narrow down the line width of the DFB diodes from MHz to the kHz range [93, 94]. We have seen this narrowing effect of the line width for our laser diodes but did not investigate this effect further but it can be a possible future improvement of the performance of the laser system.

Once passed through the optical isolators the light is then split with polarising beam splitter cubes and $\lambda/2$ wave plates into beams that are then coupled into optical fibres for further usage in the amplification modules and a beam path for offset locking.
For the offset lock the beam (red) is superimposed with the reference beam (blue beam) on a high speed photo diode to measure the beat frequency of the two beams (purple beam). A polariser in front of the detecting photo diode ensures that the beams have the same polarisation on the photo diode.

The beat measurement [95] of the reference beam (blue) generated by the ECDL in the master module and the beam from the DFB diode (red) is shown in figure 3.9 for ^{87}Rb at $780nm$ and in figure 3.10 respectively for ^{40}K at $767nm$. Due to different broadening mechanisms the line width of a laser is a convolution of a gaussian and lorenztian shaped curve, a so-called Voigt profile [96]. The beat between two laser beams resembles the same shape.
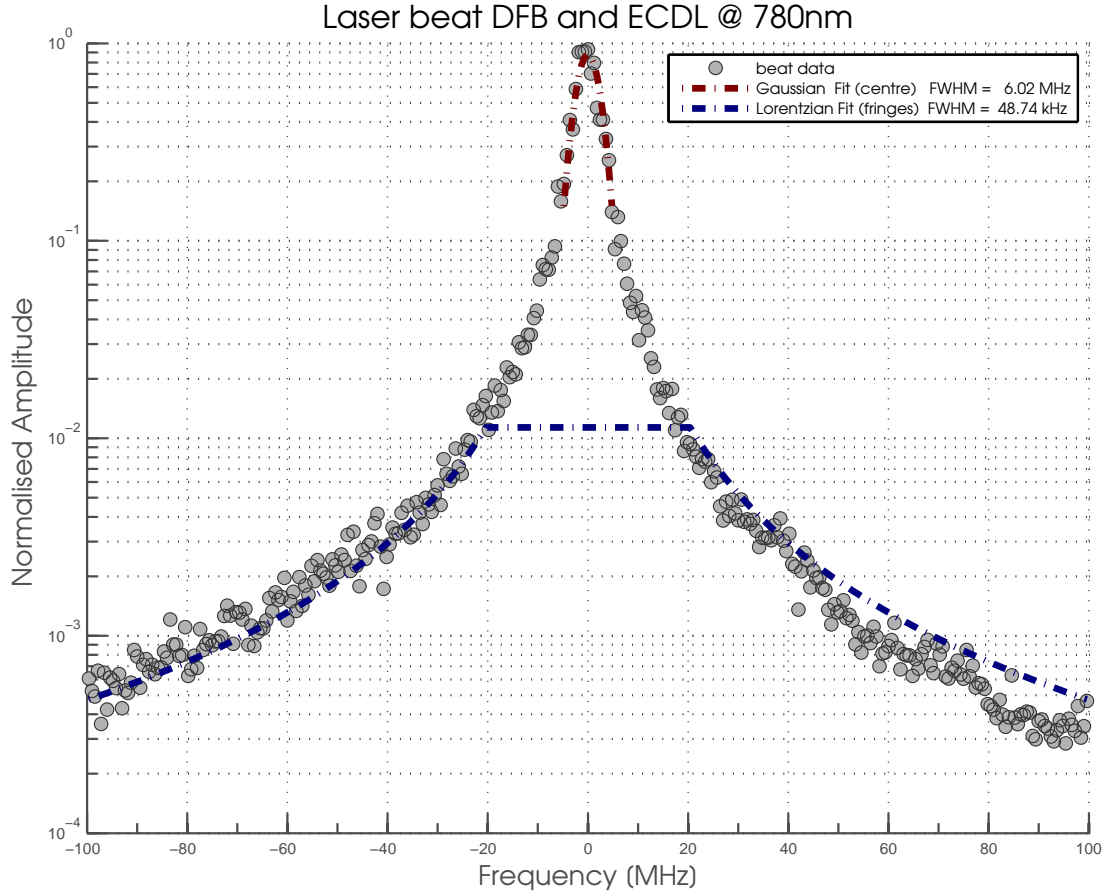
Figure 3.9: *The beat measurement of the reference master ECDL and the offset locked DFB diode for 780nm: The lorentzian line width is given by $\Gamma_L = 48.74kHz$ fitted to the wings of the beat and the gaussian line width is given by $\Gamma_G = 6.02MHz$ fitted to the central region of the beat note.*

The Gaussian line shape corresponds to fluctuation of charge carriers and technical noise in the laser diode emission [97] while the Lorentzian shape is due to noise from spontaneous emission depending on intrinsic features of the laser diode and in case for the DFB diode on design and operation [97, 98]. The line widths for the laser at $780nm$ was measured to $\Gamma_L = 48.74kHz$ for the Lorentzian line widths and $\Gamma_G = 6.02MHz$ for the Gaussian line widths. For the lasers at $767nm$ it is respectively $\Gamma_L = 38.55kHz$ for the Lorentzian line widths and $\Gamma_G = 1.91MHz$ for the Gaussian line widths.

In both cases the wider DFB diodes dominate the beat measurement. The nominal values for the line width given by the manufacturers are $\Gamma = 2$ -$10MHz$ for $780nm$[4]
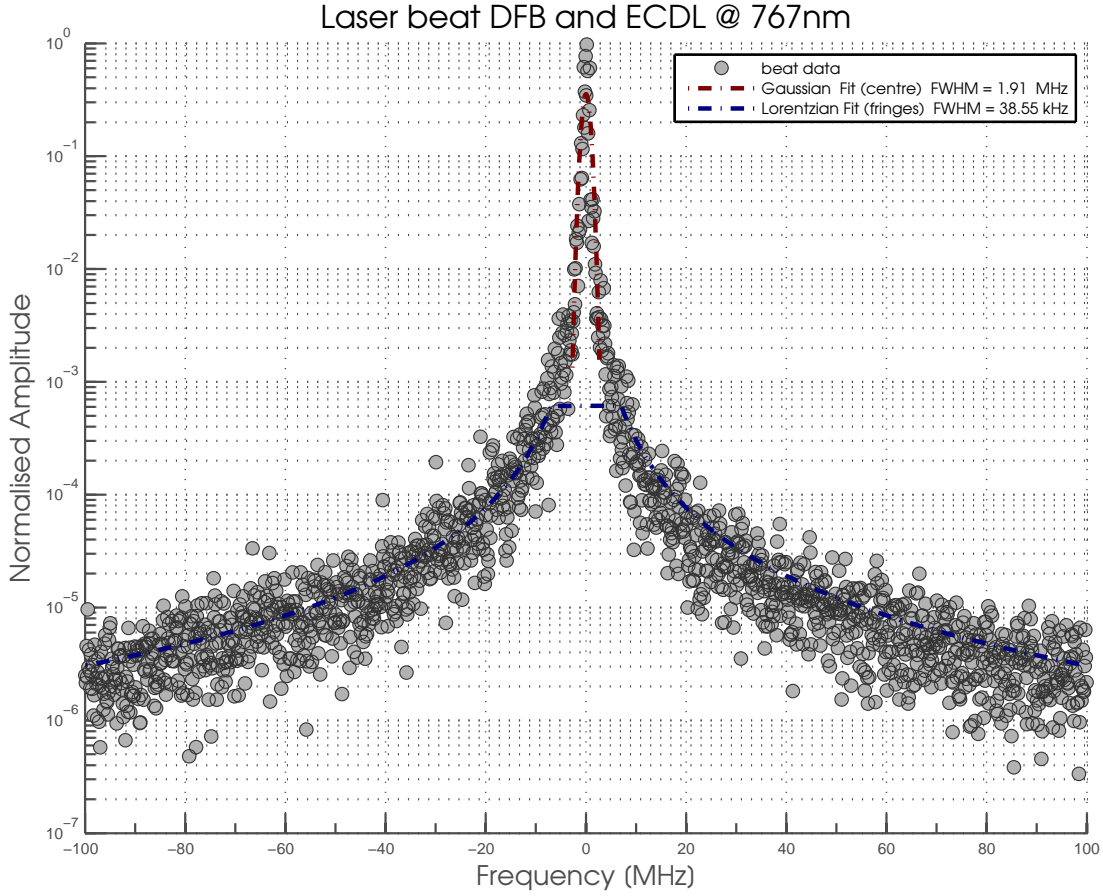
---

[4]eagleyard Photonics GmbH

Figure 3.10: *The beat measurement of the reference master ECDL and the offset locked DFB diode for 767nm: The lorentzian line width is given by $\Gamma_L = 38.55 kHz$ fitted to the wings of the beat signal and the gaussian line width is given by $\Gamma_G = 1.91 MHz$ fitted to the central region of the beat note.*

and $\Gamma = 1.0$ -$1.4 MHz$ for $767 nm$[5]. Both line width determinations are in the range of the manufacturers specifications.

3.2.3.1 Principles of the offset locking technique

Given our reference frequency from the master laser at a certain atomic transition, it will be necessary to frequency stabilise our repumping and cooling light in respect to that. Furthermore it is necessary that the frequency offset is flexible in magnitude for detuning purposes.
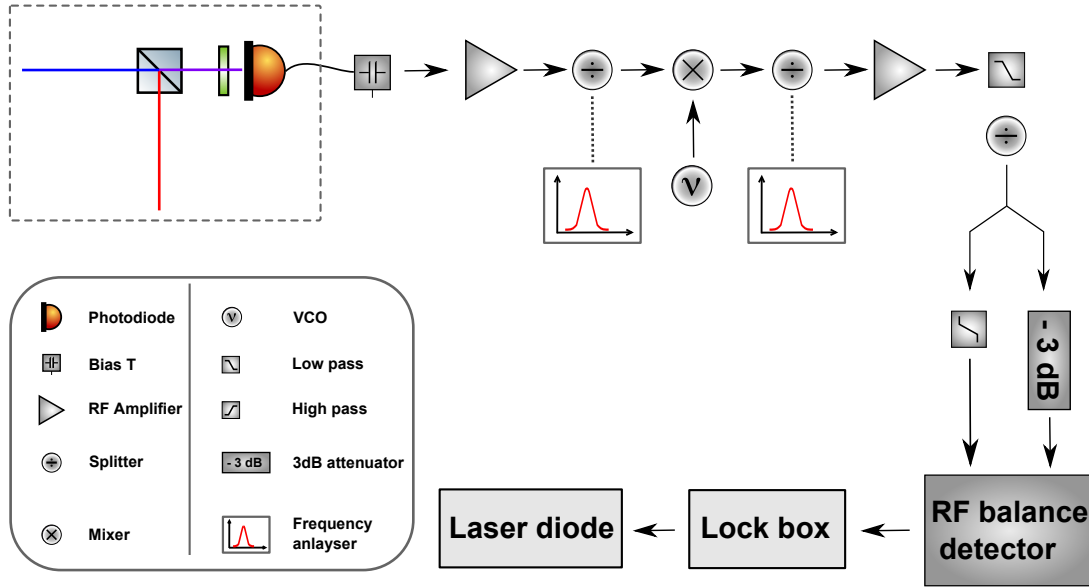
---

[5]Ferdinand Braun Institute FBH, Berlin, Germany

Figure 3.11: *Schematic of the principle of the offset lock using a side filter technique* [91]: The beat note in the range of several hundred *MHz* or *GHz* of two laser beams is detected by a fast photo diode. The beat note is amplified with up to 40-60*dB*. The following two power splitters are used purely for diagnostic reasons for checking the power spectrum of the signal. The signal is mixed down with a mixer and a voltage-controlled-oscillator (VCO) and a spectrum of several beats occurs. The beat spectrum is filtered with a low pass filter to minimise contributions of higher order beat notes. The beat spectrum can be further amplified if necessary. With the aid of another power splitter the signal is split in half. One part of the signal passes through a constant 3*dB* band pass attenuator for a wide frequency range. The other part of the signal passes through a high pass filter that has a 3*dB* attenuation point at a certain cut off frequency f_{cut}. Given that the frequency is above or below the cut off frequency, the signal experiences a larger or smaller attenuation. The amplitude response of the two signal paths is compared in the RF balance detector that gives out a voltage varying between positive and negative given which of the two signals is larger. At the cut off frequency the attenuation of the signal is equal for both parts so the output of the RF balance detector has a zero crossing that is used for locking purposes. The appearance of this zero crossing in relation to the offset laser frequency can be changed now by changing the frequency of the VCO. Its frequency range also determines the detuning range of the offset lock, independent from the lasers.

In the existing concept the light for cooling, detection, optical state preparation and pushing the atoms from the 2D MOT chamber through the differential pumping stage to the 3D MOT goes back to one laser diode. Thus a reliable way for variable detuning in respect to the reference frequency from the master module needs to be realised.

An easy approach for locking with variable detuning is the offset locking technique implemented in this setup. Before the invention of easy offset lock techniques it was necessary to phase lock [99] the laser that is in many cases a more complex setup than needed due to the unneeded phase relation between the two lasers. The error signal here is generated by the comparison of the amplitude response

of a high pass filter and a band pass filter. The setup is the same for all four DFB diodes implemented in the system. Only eventually the frequency range of components vary without effecting the overall setup or performance. Therefore this technique is a powerful and versatile way for frequency stabilisation to nearly arbitrary frequency differences.

The setup used here follows the approach of reference [91]. It is an easy technique independent from specific laser features that is used successfully for all DFB laser diodes in this experiment.

Despite all the advantageous characteristics there is one quite severe draw back of this technique. As it is currently realised, it shows a time delay of several *ms* to perform a frequency jump over a range of several tens of *MHz*. This might be due to the analogue electronics used in the setup. At the moment an improved setup based on digital electronics is realised in the context of a different project. This problem only shows influence on the detection sequence during the MOT optimisation but does not affect the magneto-optical trapping performance in a noticeable way.

The setup described in the following is the same for all four DFB diodes in use. Only the frequency range needs to be adapted.

In figure 3.11 the concept of this technique is shown. Once the beams with the same polarisation are superimposed on a fast photo diode[6] a beat signal of the two lasers occurs, the so-called laser beat. This beat consists of one part that oscillates with the sum of the two laser frequencies and one part that oscillates with the difference of the two frequencies. Since the laser frequencies are in the order of *THz* its impossible to detect those directly with a photo diode but luckily this is not the case for the difference that is in the range of up to several hundred *MHz* or low *GHz* in the specific case of the rubidium repumping laser.

The laser beat note is then amplified with up to 40-60 *dB*. The following power splitter is used purely for diagnostic reasons to check the laser beat signal. The signal is mixed down with a mixer and a voltage-controlled-oscillator(VCO) and the so-called beat spectrum (see figure 3.12) occurs. The wanted part of the signal is now in the range of a couple of hundreds *MHz*, independent of the frequency range of the laser beat note at the photo diode. At a second power splitter (figure 3.11) also the beat spectrum can be probed.

Ideally this beat spectrum contains only the beat of the laser beat and the VCO but as it can be seen in figure 3.12 there are also higher orders appearing at multiples of the contributing frequencies and only one beat is of actual interest for us. While scanning the offset locked laser all individual beat notes in the beat spectrum (see figure 3.12) move relatively to each other in different directions and at different

---

[6]Hamamatsu G4176-03

rates[7] and can thus pass through each other while detuning the offset lock laser to a different frequency. Since it will interfere with the locking of the laser it should be avoided by all means by choosing the frequency range of the parts used appropriately.

In addition the beat spectrum is filtered with a low pass filter to minimise contributions of higher order beat notes. The beat spectrum can be further amplified if necessary and passes the low pass filter.

The signal is then split in half with another power splitter and passes the frequency dependent part of the circuit. One arm of the signal passes through a constant $3dB$ attenuator specified for a wide frequency range so that the signal undergoes the same attenuation in the entire frequency range covered here. The other arm of the signal passes through a high pass filter that has a $3dB$ attenuation point at a certain cut off frequency f_{cut}. Frequencies above the cut off frequency experience a smaller attenuation and frequencies below the cut off frequency experience a larger attenuation.

The amplitude response of the two signal paths is compared in the RF balance detector that gives out a voltage varying in between positive and negative given which of the two signals is larger. At the cut off frequency the output has a zero crossing that is used for locking purposes. The appearance of this zero crossing in relation to the offset laser frequency can be changed now by changing the frequency of the VCO. Its frequency range also determines the detuning range of the offset lock, independent from the lasers detuning range.

When the offset lock laser is scanned from low to high frequencies due to symmetry reasons four zero crossings can be identified. The condition where the frequency that meets exactly the cut off frequency can be fulfilled in four different ways since the beat does not give any information about which beat partner has the higher frequency. Furthermore three different frequencies contribute: The two laser frequencies of the master laser f_{master} and the offset laser f_{offset} plus the VCO frequency f_{VCO}. Combining the three different frequencies, there are four possible combinations of addition and subtraction leading to the same frequency f_{cut}, the cut off frequency. Starting from the case where the offset laser has a smaller frequency f_{offset} than the master f_{master}, the offset laser scans to higher frequencies whilst the master and the VCO frequency remain constant. The four combinations can be summarised as the follwoing:

---

[7]The beats appear at the modulus of the difference of the contributing frequencies and can become smaller or larger by increasing the laser frequency ω_L or the VCO frequency ω_{VCO}.
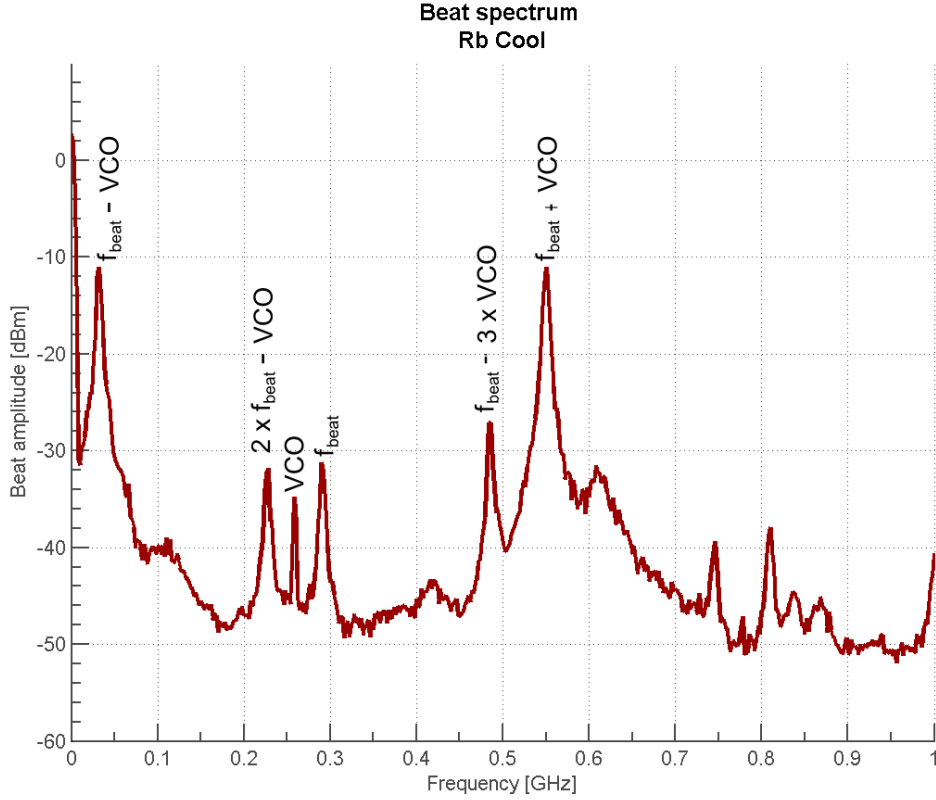
**Beat spectrum
Rb Cool**

Figure 3.12: *The beat spectrum of the offset lock (Rb cool)* is composed of several beat notes arising from higher order contributions.

$$1. \quad \underbrace{(\overbrace{f_{master}}^{\text{THz}} - \overbrace{f_{offset}}^{\text{THz}})}_{\text{MHz to GHz}} - \underbrace{f_{VCO}}_{\text{MHz to GHz}} = \underbrace{f_{cut}}_{\text{MHz}}$$
$$\underbrace{\phantom{(f_{master} - f_{offset}) - f_{VCO}}}_{\text{MHz}}$$

$$2. \quad (f_{master} - f_{offset}) + f_{VCO} = f_{cut}$$

$$3. \quad (f_{offset} - f_{master}) + f_{VCO} = f_{cut}$$

$$4. \quad (f_{offset} - f_{master}) - f_{VCO} = f_{cut}$$

For identifying the correct locking point one has to consult the level scheme of potassium and rubidium. The level schemes can be found in appendix A (see figure A.1 and figure A.2). As an example the case of the cooling frequency of ^{87}Rb is presented here. The considerations for the other three cases can be done in the same way.

The reference frequency of the master laser f_{master} is locked to the crossover

38

transition CO23. The cooling and repumping transition are both higher in frequency. The difference is obtained to $f_{master} - f_{cool} = 133MHz - \Delta$ where Δ is the detuning in the range of $\Delta = 0MHz \rightarrow 120MHz$. Furthermore the frequency shift due to an AOM placed at a later stage of $f_{AOM} = 160MHz$ needs to be taken into account. In total this gives a laser beat frequency range of $f_{offset} - f_{master} = 293MHz \rightarrow 173MHz$ if the -1. order of the AOM is used. The cut of frequency f_{cut} and the VCO frequency need to be chosen appropriately in order to ensure a stable lock with a wide detuning range. Especially higher order beat notes should not pass through the laser beat when the laser is detuned. At the same time the laser beat should not cross through zero. In case of the cooling light for ^{87}Rb a low cut off frequency of $f_{cut} = 50MHz$ is chosen, yielding a VCO range of $f_{VCO} = (f_{offset} - f_{master}) - f_{cut} = 243MHz \rightarrow 123MHz$. The offset laser is on resonance at a laser beat frequency of $(f_{offset} - f_{master}) = 293MHz$ and it is locked to the fourth slope (compare listing above, case 4.).

In both cases of the cooling and the repumping for rubidium its the fourth zero crossing, for potassium its the fourth zero crossing for the cooling light respectively the first zero crossing for the repumping light. A stable and robust lock in all cases is produced.

Frequency jumps of $\gtrsim 60MHz$ can be realised just by changing the related VCO frequency but as afore mentioned a time delay occurs[8]. This time delay is dependent of the amplitude of the frequency jump and is in the range of several ms [91]. Thus the experiment control includes a delay time slot of $10ms$ that shifts the detection frequency on resonance for time-of-flight times less then this delay time. This exhibits a problem for hotter atom clouds due to their fast expansion.

The four cooling and repumping lasers have been successfully locked to the desired transitions via a reference laser with the required degree of freedom for detuning. The locks are in all cases working reliably and stable, even under the occurrence possibly induced of thermal and mechanical instabilities.

However, the emitted power from those laser diodes in the range of $10mW$ is coupled into optical fibres guiding the light to the next module where the frequency stabilised light will be amplified.

3.3   Light amplification stage

In this section the light amplification stage based on self-made tapered amplifier setups will be considered. Since the output power directly from a laser diode is

---

[8]In principle the detuning is limited by the frequency range of the VCO and the speed of the analogue electronics.
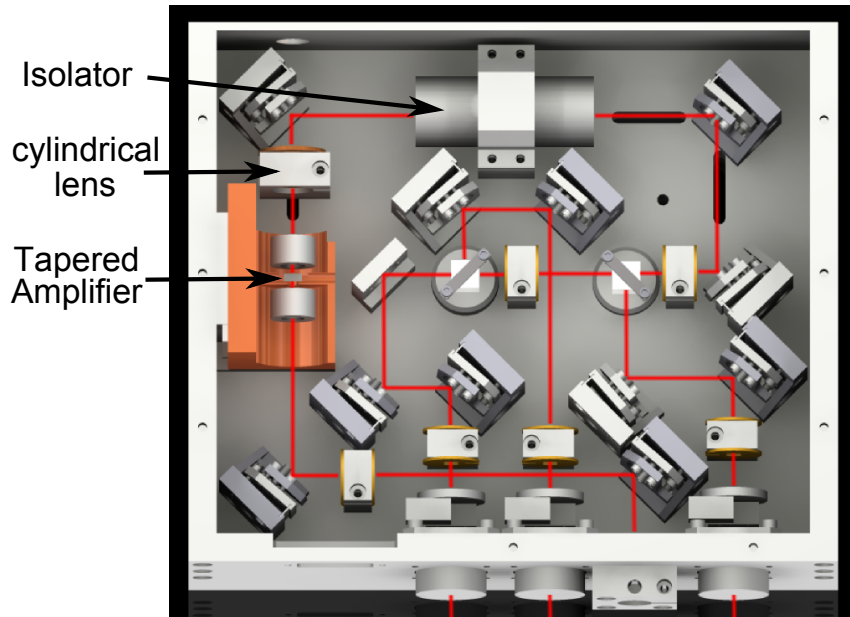
Figure 3.13: *The light amplification module* with the TA mount made of copper at the left. The tapered amplifier (TA) is seeded and the amplified light is collimated by a cylindrical lens and a spherical lens due to the prevailing astigmatism. The light passes through an optical isolator and is split into up to three beams and is re-coupled into optical fibres.

not sufficient for laser cooling of atomic gases a tapered amplifier (TA) is used to amplify the laser radiation by harvesting photons by stimulated emission from the inverted population within an optical active region.

One limitation for laser diodes to produce higher power output lies in the limited power density tolerable at the output facets. Tapered amplifiers circumvent this problem by having a broadening wave guide towards the output facet and are therefore a low cost alternative to a Titanium-Sapphire laser. The other facet on the opposite side resembles more of a Fabry-Pérot type laser diode for mode suppression. The facets are anti-reflection coated to suppress lasing on a different frequency competing with the input mode.

The output beam is divergent and shows an astigmatism that needs collimation with a lens system. The line shape characteristics is retained by the stimulated process but is slightly widened by amplified spontaneous emission (ASE) [100].

Each beam out of the offset lock modules gets amplified in one amplification module. Since the demand for cooling light power is higher than for the repumping light a part of the amplified cooling light is again amplified in an additional module. For this purpose and thanks to the modularity of the setup the amplification modules can be cascaded (see figure 3.3).
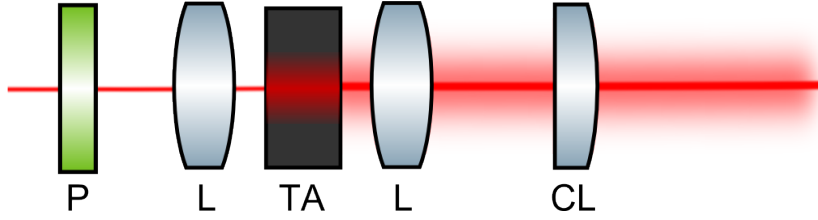
Figure 3.14: *Detailed setup of the tapered amplifier design:* The incoming seeding light passes through a polariser (P) from the left and is focussed down onto the tapered amplifier chip (TA) with a lens (L), the amplified light is collimated with the following collimation lens (L) and the astigmatism is compensated with a cylindrical lens (CL). The focal lengths for the two different TAs are given in the text (see section 3.3).

The light amplification stage consists of only one module type shown in figure 3.13 with the TA mount made of copper at the left.

The light feeds into the module with optical fibres and is then sent with the appropriate polarisation as seeding power into the TA chip. The TA chips used here are C-mounted and have a maximal output power of $1.0W$ for $780nm$ and $1.5W$ for $767nm$ at a maximal seeding power of $50mW$.

In figure 3.14 the light is focussed down with a lens (L) of a focal length of $4.6mm$ ($4.0mm$) in case of the TA for $780nm$ ($767nm$). The focal length of the seeding lens is optimised for high power output. For the alignment the seeding lens is fixed onto a xyz-translation stage and the spontaneous emission is coupled back into the input fibre [101, 102]. The seeding is then further optimised for maximum output power before the lens is permanently glued into place[9].

The output beam out of the tapered amplifier chip shows variable divergences in different axis combined with an astigmatism. In order to match the resulting beam size to the optical fibre, the output beam is collimated and shaped in both axes by a spherical lens (L) with a focal length of $3.1mm$ ($3.1mm$) followed by a cylindrical lens (CL) with a focal length of $20mm$ ($25mm$). The two collimation lenses serve as beam shapers for good fibre coupling efficiencies.

Back to figure 3.13 the collimated high power beam out of the TA passes through a Faraday isolator that protects the tapered amplifier from back reflection that are amplified in the chip and can lead to damage of the narrower front facet [101]. The beam then gets split up into maximal three output beams that are coupled into polarisation maintaining single mode fibres[10] that act both as a spatial and spectral filter [101]. The power in front of the out going fibre can reach up to several hundred mW but the fibres show a stable performance guiding the high power to the next section for fibre preparation. The beam profile from a tapered amplifier is known to be different from the TEM_{00} mode but the following single mode fibre acts like a spatial mode filter accompanied with related power losses. The coupling

---

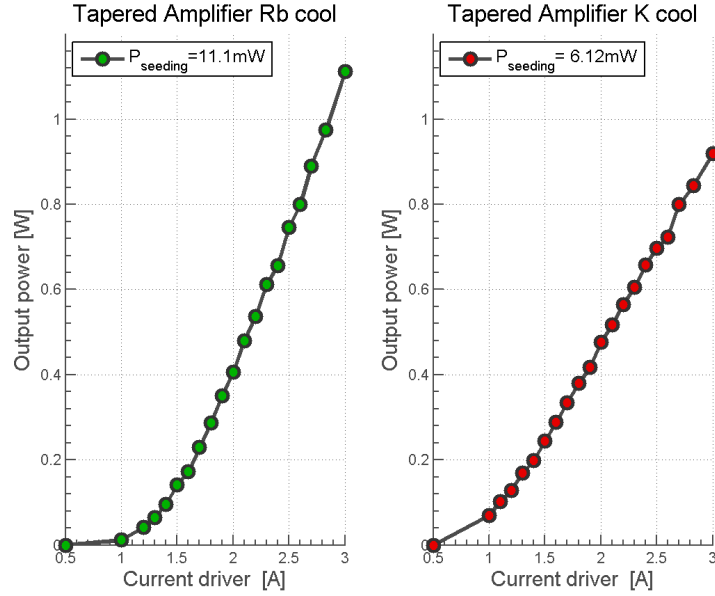[9]JB weld epoxy
[10]Thorlabs P3-780PM-FC-5

Figure 3.15: *The output power versus injection current* for the two different tapered amplifier. The maximum injection current in both cases is $3A$ and the seeding power is with $11mW$ for $780nm$ and $6mW$ $767nm$ well below the maximum seeding power. Unsaturated seeding can cause an increased level of ASE causing line broadening of the output spectra [100, 101]. The output power is measured right after the cylindrical lens. Both graphs show a non-linear rise in output power before going over into a linear slope till the maximum output power for the prevailing settings is reached. For the $780nm$ TA (on the left, green) the slope is $\eta_{780} = 0.71mW/mA$ and the maximum output power composed of stimulated and spontaneous emission is $P_{max} = 1.1W$. Respectively for the $767nm$ TA (on the right, red) the slope is $\eta_{767} = 0.44mW/mA$ and the maximum output power composed of stimulated and spontaneous emission is $P_{max} = 0.9W$.

efficiency lies between 40-45%. The optical fibres from the amplification modules are guided to the next stage where the repumping and cooling light is overlapped in the next modules in preparation for the experiment.

The output power versus injection current is displayed in figure 3.15 for the two different tapered amplifiers. The maximum injection current is for both $3A$. For the tapered amplifier at $780nm$ shown on the left hand side the maximum output power according to the manufacturer is $1.0W$, respectively $1.5W$ for the amplifier at $767nm$ shown on the right.

The seeding power of $11.1mW$ for $780nm$ and $6mW$ for $767nm$ is measured in front of the polariser and therefore even further reduced at the tapered amplifier (by $\approx$ 5-10 %). The output power is measured right after the cylindrical lens in front of the optical isolator where it is impossible to distinguish between ASE and the actual power of the output spectra due to stimulated emission.

Both graphs show a non-linear rise in output power before going over into a linear slope till the maximum output power for the prevailing settings is reached. The

threshold current increases with lower seeding power [101] what could give rise to the extended non-linear slope. In case for the $780nm$ TA (green) the slope is $\eta_{780} = 0.71mW/mA$ and the maximum output power composed of stimulated and spontaneous emission is $P_{max} = 1.1W$. Respectively for the $767nm$ TA (red) the slope is $\eta_{767} = 0.44mW/mA$ and the maximum output power composed of stimulated and spontaneous emission is $P_{max} = 0.9W$.

With $11mW$ and $6mW$ both tapered amplifiers are seeded well below the maximum seeding power specified by the manufacturer of $50mW$. This can result in an increased level of ASE that causes line broadening of the output spectra [100, 101]. Also an inappropriate temperature setting can lead to an increased level of ASE [101].
Indeed an increased line width has been observed after the amplification of the detection light for ^{87}Rb to $12.8MHz$ (FWHM) in a Gaussian fit (see figure 3.16) rather than the smaller line width of $6MHz$ measured before the amplification (see figure 3.9). The measurement in figure 3.16 shows the optical density while varying the detuning of the detection laser by changing the VCO frequency f_{VCO}.
Operating the tapered amplifier far away from the saturated seeding power could be a possible cause for a line broadening due to an increased level of ASE. It can also be a cause for the necessity of enhanced isolation in the offset module by several optical isolators [101].

In case of the cooling light there are two amplifier modules. The first amplifier guides the light to the 2D MOT module, the detection module and the second stage amplifier where the light gets re-amplified and the guided to the 3D MOT module. For the repumping light the fibres go straight to 2D MOT and 3D MOT module and detection module. Those three splitting modules are subject of the next section 3.4. All modules that have been discussed so far can be seen in the experiment setup in figure 3.2.

3.4   Fibre preparation for magneto-optical trapping

The last section of the laser system is dedicated to the actual fibre distribution for the experiment. This means the light for cooling and repumping will be superimposed and for switching and possible frequency shifting an AOM double path is installed. Fibres containing either repumping or cooling light are obtained from the amplifier modules.
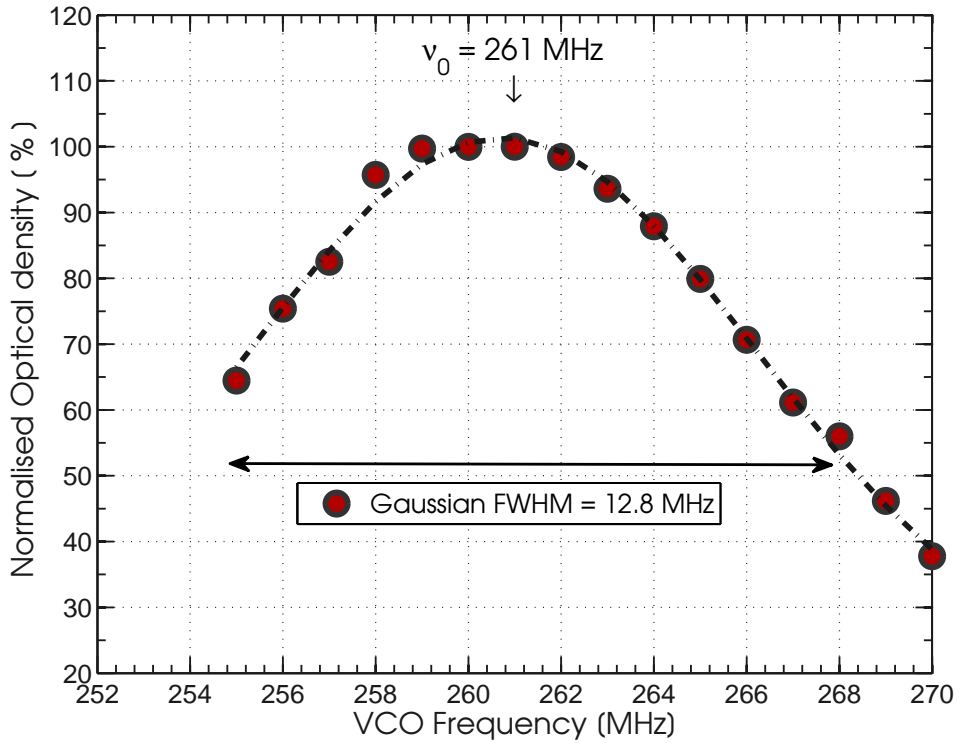
Figure 3.16: *Line width and resonance of detection laser vs. VCO frequency:* The optical density of an identically prepared atomic cloud in a magnetic trap measured while varying the VCO frequency and therefore the detection laser frequency for ^{87}Rb. The FWHM of an Gaussian fit results in $\sqrt{8\log 2}\sigma = 12.8MHz$.

At the experiment six beams for the 3D MOT chamber, two beams for the 2D MOT chamber and three beams for pushing the atoms from 2D MOT chamber to 3D MOT chamber, optical pumping and detection (in total 11 fibres per species) are needed. Due to the two species experiment this set of fibres will be needed twice. Most of these fibres need to carry both the cooling and repumping light in the same fibre.

For the mixing and splitting of the light there were three modules designed that all follow the same basic principle and then differ only in the number of output fibres towards the experiment. One example is the 3D MOT module shown in figure 3.17 that takes the two incoming fibres (red and blue), sends them through individual AOM double paths (see figure 3.18), superimposes them on a beam splitter (purple beam) and splits them into six outgoing fibres containing cooling and repumping light.
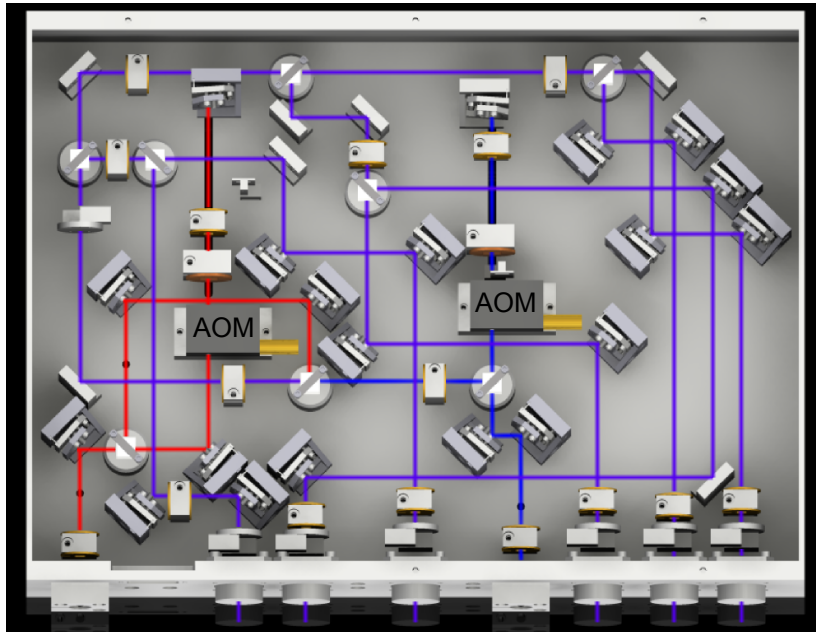
44

Figure 3.17: *The splitting module for the 3D MOT* Two incoming fibres (red and blue) pass independently through a double path AOM configuration (see figure 3.18) before they are superimposed on a polarising beam cube (purple beam). The beam is split into six outgoing fibres containing cooling and repumping light of the same polarisation.
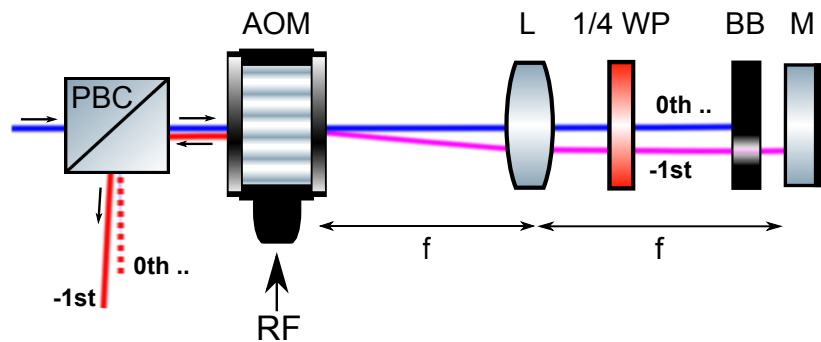
Figure 3.18: *The AOM double path:* The linearly polarised light (blue) passes through a polarising beam cube (PCB) through the AOM. A lens (L) with a focal length of $f_{AOM} =$30-60mm focuses the light onto a mirror. A beam block in front of the mirror blocks all orders except the -1. order. The light passes twice through a quarter wave plate (1/4 WP) picking up a total shift of $\lambda/2$ followed by the re-collimating lens (L) and the AOM for a second time. The beam gets then deflected onto the beam cube (PBC).

Figure 3.19: *Performance of the evanescent wave fibre splitter optimised at 780nm for different wavelengths:* The figure shows 780nm on the left and 767nm on the right. The graphs show the ratio of the out-coming power of the two out-coupling fibres versus 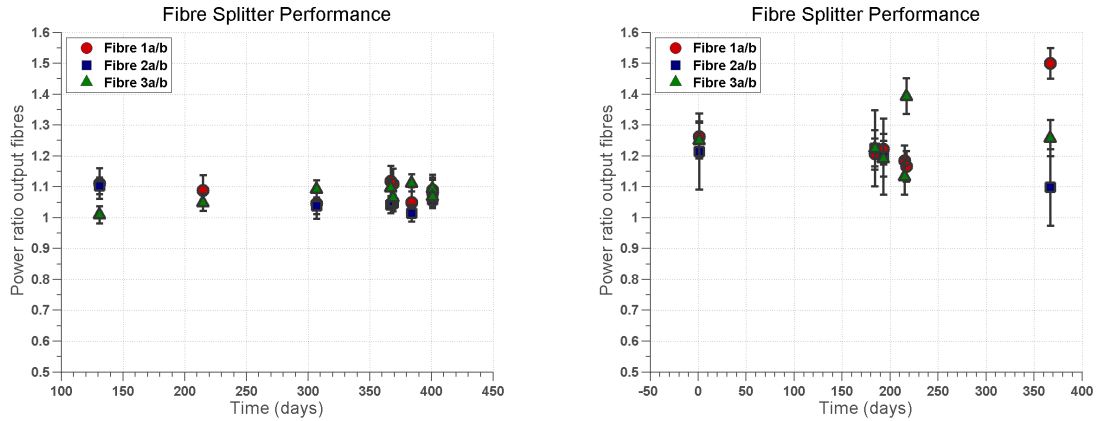time. In case of 780nm a ratio of $50:50=1$ is expected. For 767nm the expected ratio is $(50\%-4.23\%):(50\%+4.23\%)=1.18$ (see text). The measurement gives a constant average splitting ratio for fibre splitter 1-3 at 780nm of 1.07 ± 0.3, 1.05 ± 0.3 and 1.09 ± 0.3. Respectively for 767nm the splitting ratio started off with an imbalanced splitting ratio of 1.25 for all three 3D MOT fibre splitters. Additionally the imbalance seems to vary over to a maximum and minimum imbalance of 1.5 and 1.1 for different fibre splitters. The tendency of which fibre carries more output power is not stable and can change in between the fibres. The displayed error bars express an assumed accuracy of $\pm5\%$ in the power measurement with different power meters.

AOM double path In order to switch the light fast enough on the atomic time scale for the experiment sequence, acousto-optical modulators (AOM) with an applied rf frequency f_{AOM} were used. By emitting or absorbing phonons the beam is displaced and split in several orders. The efficiency is dependent on the alignment and the Bragg angle.

In the realised system the light passes through the AOM twice picking up one phonon on each round, a so-called AOM double path. The setup is shown in figure 3.18. The light from the left (blue) goes through the AOM following a polarising beam cube (PBC). An achromatic lens (L) with a focal length of $f_{AOM}=30\text{-}60mm$ focusses the light through a quarter wave plate (1/4 WP) onto a back reflecting mirror (M). All light is blocked by a beam block (BB) except the -1. order which passes through the quarter wave plate picking up a total shift of $\lambda/2$ followed by the lens (L) re-collimating the beam and the AOM for a second time. The beam then gets deflected by the beam cube (PBC).

Theoretically this setup enables to change the frequency f_{AOM} without changing the alignment of the beam path and therefore to change the detuning but a stable frequency of $f_{AOM}=80MHz$ is chosen. The detuning is changed with the VCO frequency for the offset lock (see chapter 3.2.3). The overall efficiency of the AOM double path is measured to $\approx70\%$ and is next to the fibre coupling the largest source for power loss of the laser system.

The fibres going out from the splitting modules (3D MOT, 2D MOT and detection module) contain both cooling and repumping light for laser cooling of two species ^{87}Rb and ^{40}K in two separate 2D-3D MOT systems. In this setup it was decided to realise a combined 2D-3D MOT system with both dispensers in the same chamber. In order to be able to realise a two species mixture it is necessary to combine the cooling and repumping light for two species that are currently split into 12 individual 3D MOT fibres into only six fibres for the 3D MOT chamber.
Similar issues arise from the 2D MOT beams which need to be reduced from four beams into two fibres each containing both cooling and repumping light for both species.
This is realised with polarisation maintaining evanescent wave fibre splitters. In total four fibre splitter take two incoming fibres each containing light for ^{87}Rb and light for ^{40}K and combine them into two outgoing fibres containing mixed light for both species. With this arrangement a two species 2D and 3D MOT for ^{87}Rb and ^{40}K is realised (see section 5.1).

The 2:2 fibre splitter[11] consists of two fibres that are partly polished down to the core of the fibre. The cores are merged together and the travelling light waves couple part of the evanescent wave field leaking out of the initial wave guide into the second wave guide. The ratio can be adjusted on demand during manufacturing. The fibre splitter is optimised for $780nm$ and produces a splitting ratio of 50:50. According to the manufacturer a deviation from the centre wavelength by 1% results in a 3% change from the 50:50 splitting. Assuming a linear relation between imbalance and wavelength deviation from the centre a coupling imbalance of $\pm 4.23\%$ is expected for $767nm$.
The result of the test for the cooling light for both species over a period of 400 days can be seen in figure 3.19 showing $780nm$ on the left and $767nm$ on the right. The graphs show the ratio of the out coming power of the two out coupling fibres versus time. In case of $780nm$ a ratio of $50 : 50 = 1$ is expected.
For $767nm$ the expected ratio is $(50\% - 4.23\%) : (50\% + 4.23\%) = 1.18$. The measurement gives a constant average splitting ratio for fibre splitter 1-3 at $780nm$ of 1.07 ± 0.3, 1.05 ± 0.3 and 1.09 ± 0.3. The result shows a slightly higher imbalance than expected.
Respectively for $767nm$ the splitting ratio started off with an imbalanced splitting ratio of 1.25 for all three 3D MOT fibre splitters. This is also a higher imbalance than expected. Additionally the imbalance seems to vary over time to a maximum and minimum imbalance of 1.5 and of 1.1 for different fibre splitters. The tendency of which fibre carries more output power is not stable and can change in between the fibres. The displayed error bars express an assumed accuracy of $\pm 5\%$ in the

---

[11]Evanescent Optics Inc.

power measurement with different power meters.

In context of a different experiment [103] a tuning of the splitting ratio with temperature was determined to $\approx 0.19\%/K$. Therefore, the temperature can not account as possible reason for such a high deviation from the expected splitting ratio. One possible reason can be insufficient quality of the specifications and the assumed linearity of the deviation in wavelength.

Despite the discouraging performance of the wave guide fibre splitters the stable operation of the magneto-optical traps both in 2D MOT chamber and 3D MOT chamber seem to be unaffected and the successful laser cooling of both species is performed (see section 5.1).

The fibre splitters only combine the 2D and 3D MOT fibres, the residual fibres like the pushing and detection beam for the two species ^{87}Rb and ^{40}K are superimposed in another module similar to the previous splitting modules without the AOM double path overlapping the beams on a polarising beam cube and re-coupling the light into a fibre that goes directly to the experiment. The light is switched by another AOM in a previous module.

The laser system for laser cooling of ^{87}Rb and ^{40}K in a combined 2D-3D MOT chamber is therefore completed and characterised. All modules have been designed, build and aligned in the context of this thesis including the frequency stabilisation. One of the major advantages of the laser system is the inbuilt modularity providing a high degree of flexibility. Nevertheless it also results in a high number of fibres connecting the individual modules. The consequential power loss is compensated with a relatively high number of optical amplifiers. Furthermore the initial alignment is more elaborate than for common optics setup but comes with an increased long term mechanical stability and reduced sensitivity against temperature drifts and hence it is nearly maintenance free.

In total is has been shown that this miniaturised dual species laser system fulfils all features mentioned in the beginning: Flexibility, robustness, low maintenance and high thermal and mechanical stability on long and short time scales. The single task, modular approach results in a high flexibility and versatility, giving the freedom to adjust the laser system to different necessities by cascading modules and also different species by simply duplicating the existing system.

For the first time the miniaturised technique has been successfully used for ^{40}K next to ^{87}Rb. The ECDL design for both species is a very robust and easy to use construction for frequency stabilisation and works maintenance free as well for $767nm$ as for $780nm$ using the same wavelength selecting interference filter and lenses.

The tested DFB prototypes for $767nm$ and the DFB diodes for $780nm$ show a promising performance during the magneto-optical trapping sequence. All diodes show are very stable long-term frequency stabilisation, no matter if FM or offset lock techniques were used.

Also the tapered amplifiers operated sufficiently even in the low seeding range. The broader line width of the cooling and possibly also repumping light due to a higher level of ASE has no noticeable effect on the magneto-optical trap (see section 5.1). The newly implemented and easy to use option of mixing light with the aid of evanescent fibre splitters has shown some weaknesses concerning the imbalance but performs still sufficiently in the experiment as the particle numbers prove. With this dual species laser system both samples of ^{87}Rb and ^{40}K atoms of $N_{Rb} = 1.3 \cdot 10^9$ and $N_K = 1.4 \cdot 10^6$ were realised (see section 5.1). The optical setup at the experiment preparing the beams is presented in the next section.

3.5 Beam preparation for 2D and 3D MOT

In this chapter the optical setup for the 2D-3D MOT system is presented. The beam path and parameters are discussed separately for 2D and 3D MOT systems, starting with the 2D MOT system. After the following discussion of the 3D MOT system. Finally a brief overview of the detection system is given.
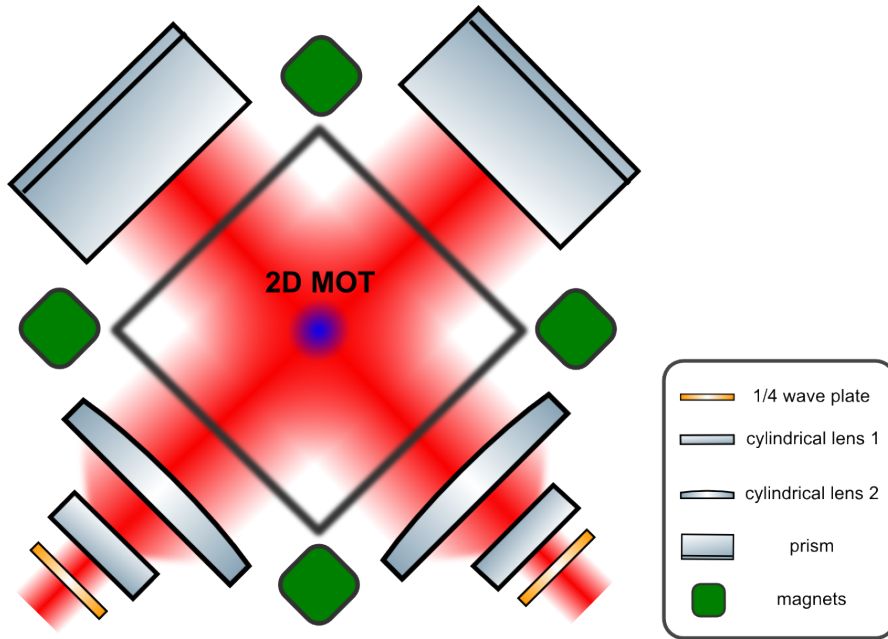
3.5.1 Optical setup 2D MOT

Figure 3.20: *The optical setup of the 2D MOT as seen from the top of the experiment:* Two linear polarised laser beams, containing both cooling and repumping light for both species ^{87}Rb and ^{40}K simultaneously, pass through a zeroth order $\lambda/4$ wave plate. The circular polarised beams are expanded by a lens system of two cylindrical lenses (1 and 2) of focal lengths $f_{focal_1} = -30mm$ and $f_{focal_2} = 150mm$. The elliptically expanded beams of approximately $80 \times 20mm$ are retro-reflected by large prisms at the back of the vacuum chamber. The expansion of the beam is depicted in the wrong direction but shall stress the fact that the expansion is due to the two cylindrical lenses. The two fold reflection on the tilted surfaces of the prism turns the polarisation appropriately. The light at the central part of the beam leaks out of the prism and is lost from the beam leaving a dark line in the counter propagating beam. At the region of this dark line the light fields are unbalanced but due to the small size of the unbalanced region no atom loss is expected. For details refer to text.

The optical setup of the 2D MOT is depicted in figure 3.20 as seen from the top of the experiment. It consists of two laser beams each containing repumping and cooling light for both species ^{87}Rb and ^{40}K simultaneously. The linearly polarised light out of an optical fibre is collimated by a lens with a focal length of $5cm$ (not depicted in figure 3.20) and sent through a zeroth order $\lambda/4$ wave plate

to create circular polarised light. The beams then pass through a lens system consisting of two cylindrical lenses (1 and 2) of focal lengths $f_{focal_1} = -30mm$ and $f_{focal_2} = 150mm$ resulting in elliptically shaped beams of approximately $80 \times 20mm$. In figure 3.20 the expansion of the beam by the cylindrical lenses is depicted in the wrong direction but serves to illustrate the fact that the expansion is due to the two cylindrical lenses.

The beam passes through the vacuum chamber and is retro-reflected by large prisms at the back of the vacuum chamber before being re-coupled into the fibre. The two fold reflection on the tilted surfaces of the prism turns the polarisation by half a wavelength like a $\lambda/2$ wave plate in relation to the atoms. Therefore a second macroscopic wave plate is unnecessary.

The light gets reflected twice on the prism, except the central part of the beam where the prism has its edge. The light here leaks out of the prism and is lost from the beam leaving a dark line in the counter propagating beam. At the region of this dark line the incoming beam is unbalanced and atoms entering that region are pushed to the side but most of them are not expected to be lost from the 2D MOT. A very simple picture is used to illustrate this statement. Atoms are considered to be lost from the trap if they get in contact with the vacuum chamber wall. Assuming the atom starts in the centre with zero transversal velocity entering the dark region of $d = 1mm$ length and scattering photons at the highest scattering rate possible of $R_{sc} = \Gamma/2$ [12]. The 2D MOT chamber is $2s = 110mm$ wide. The force F and acceleration a of the atom with mass m is then given by

$$F = m \cdot a = \frac{\Gamma \hbar \pi}{m \lambda} \tag{3.1}$$

The time t the atom needs to travel the distance s is given by

$$t = \sqrt{\frac{2s}{a}} = 0.98ms \quad (0.66ms) \tag{3.2}$$

The time t defines the upper limited for the vertical velocity $v_z = d/t = 1.02m/s(1.52m/s)$ for the ^{87}Rb (^{40}K) atom. Every atom that travels faster than the limit for v_z does not travel far enough transversally to touch the wall in the given time. This estimation neglects the fact that the atom will be shifted out of resonance, giving a higher limit on the velocity classes being lost.

The limitation on v_z is much smaller than the capture velocity of the 3D MOT of $56m/s$ for ^{87}Rb ($83m/s$ for ^{40}K) as seen in table 5.1. The pushing beam can reduce the effect even further by accelerating the slow atoms. Hence no significant effect on the loading rate of the 3D MOT is expected. This is reinforced by the fact that shielding the dark region already in the incoming beam has no effect on

---

[12]see table 3.1

the performance of the 2D-3D MOT complex.

For ^{87}Rb the power in the beams is $P_{2D\,cool} = 48mW$ and $P_{2D\,repump} = 11mW$ for the cooling and repumping light respectively. This results in an averaged intensity of the beam profile of $I_{2D\,cool} \approx 6mW/cm^2$ and $I_{2D\,repump} \approx 1.4mW/cm^2$ for the two 2D MOT both beams together. The cooling intensity is well above the saturation intensity of the D_2-line in rubidium (see table 3.1).
For ^{40}K the power in the beams is $P_{2D\,cool} = 21mW$ and $P_{2D\,repump} = 6mW$ for the cooling and repumping light respectively. The central intensity in the Gaussian beam profile therefore reaches the value of $I_{2D\,cool} \approx 2.6mW/cm^2$ and $I_{2D\,repump} \approx 1mW/cm^2$ for both beams together. In case of the cooling light this again is above the saturation intensity of the D_2-line for potassium.
The 2D MOT beams intersect in the middle of the vacuum chamber, trapping and cooling the atoms along the line of zero magnetic field (see blue indicated atom cloud). The atoms can move freely in the longitudinal direction. The pushing beam travels along the line of zero magnetic field, pushing the atoms towards the 3D MOT. The pushing beam diameter is approximately $r \approx 0.89mm$[13] with a power in the range of P_{push} several hundred μW. The detuning of the pushing beam are $\delta_{Push\,Rb} = -0.33\Gamma$ for ^{87}Rb and $\delta_{Push\,K} = +1.33\Gamma$ for ^{40}K where $\pm$ indicates blue and red detuning respectively. The pushing and 2D MOT beams need careful alignment and frequent optimisation on a day to day basis.
The magnetic field is generated by stacks of permanent magnets (see figure 3.20). The magnets, arranged in four stacks of twelve, generate a quasi 2D quadrupole field with a vanishing magnetic field along the central line. The gradient produced is of the order of $B'_{2D} = 20G/cm$ similar to [104].
The magnetic coils initially used cause birefringence in the rectangular windows of the vacuum chamber, induced by temperature gradients. This birefringence caused problems for the polarisation of the 2D MOT beams and is in particularly bad for rectangular windows due to the shape. Due to spatial limitations and easier implementation the permanent magnets were installed. There were no significant differences in the performance except the absence of the birefringence. The optical 3D MOT setup will be described in the next section.

3.5.2 Optical setup 3D MOT

In figure 3.21 the 3D MOT vacuum chamber with magnetic coils and MOT beams can be seen. In contrast to the 2D MOT magnetic field, the magnetic potential here is generated by magnetic coils. They are described in detail in section 4. On

---

[13]Beam diameter is given at the diameter where the intensity dropped to $1/e^2 = 13.5\%$ of the intensity level.
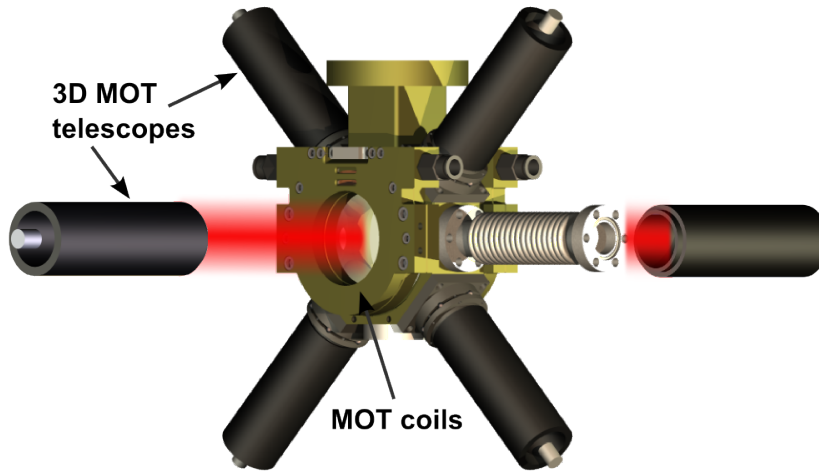
Figure 3.21: *Optical setup of the 3D MOT:* The six MOT beams are depicted as the black telescopes which pairwise counter-propagate through the centre of the 3D MOT chamber. Four of them intersect in the centre at an angle of 45° with respect to the bellows. They are connected directly to the 3D MOT chamber. The other two are detached from the vacuum chamber and run horizontally through the vacuum chamber. Each beam contains cooling and repumping light for both species ^{87}Rb and ^{40}K. In the centre, the 3D MOT vacuum chamber with MOT coils (see section 4) can be seen. On the right is the connection to the differential pumping stage going to the science chamber, realised with a flexible bellow.

the right, the figure also shows the connection to the differential pumping stage leading to the science chamber, realised with a flexible bellow.

The 3D MOT is operated with six beams depicted as the black telescopes that pairwise counter-propagate through the centre of the 3D MOT chamber. Four of them intersect at an angle of 90° but they are all rotated by 45° with respect to the bellows and are connected directly to the 3D MOT chamber. The other two are detached from the vacuum chamber and travel horizontally through the large windows of the chamber. Each beam contains cooling and repumping light for both species ^{87}Rb and ^{40}K.

Due to the occurrence of the 3D MOT vacuum chamber exchange as discussed in section 2, there are two different beam configurations that were realised in context of this experiment. The original plan works with collimated beams that are partially exchanged for partially divergent beams. This change becomes necessary due to smaller view ports restricting the beam size.
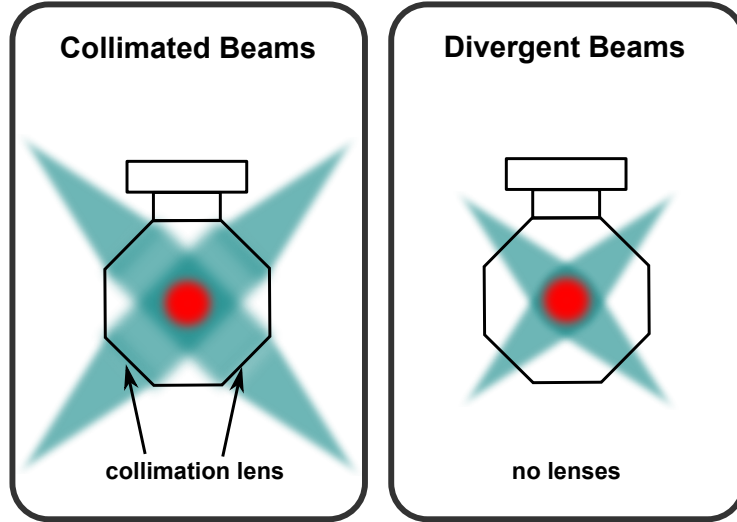
Figure 3.22: *Beam configurations at 3D MOT chamber:* On the left the beam layout for collimated beam is shown. On the right the collimation lenses have been removed and the beams can expand freely.

Collimated beams   Initially six collimated beams were planned. Each beam is passed out of an optical fibre through a lens of $100mm$ focal length and a zeroth order $\lambda/4$ wave plate, creating a beam of $d = 19.82mm$ diameter at the $1/e^2 = 13.5\%$ intensity level. They are overlapped in the centre of the chamber before coupling into the respective opposite fibre. The beam configuration is shown on the left in figure 3.22. In case of ^{87}Rb with a maximum total power in the 3D MOT in all beams of $P_{Cool\,Rb} = 47mW$ for the cooling light and $P_{Repump\,Rb} = 19mW$ for the repumping light a central intensity of $I_{Cool\,Rb} \approx 2.5mW/cm^2$ [14] and $I_{Repump\,Rb} \approx 1.0mW/cm^2$ in each beam is reached. For the cooling light this is a factor of approximately 1.5 times the saturation intensity of the D_2-line in ^{87}Rb.

For ^{40}K the maximum total power for all beams gives $P_{Cool\,K} = 78mW$ for the cooling light and $P_{Repump\,K} = 24mW$ for the repumping light in the 3D MOT. The average intensity for each beam is $I_{Cool\,K} \approx 4.2mW/cm^2$ and $I_{Repump\,K} \approx 1.2mW/cm^2$ for the cooling transition and for the repumping transition respectively. This is a factor of around 2.5 times the saturation intensity for the cooling light of the D_2-line in ^{40}K.

Divergent beams   Because of the exchange of the vacuum chamber for an indium sealed vacuum chamber with small commercial view ports, the telescopes

---

[14]Throughout the thesis perfectly collimated beams are assumed if not stated differently. The central intensity is given by $I(0, z) = \frac{2P_0}{\pi\omega_z^2}$ (see section C)

for collimated beams on the vacuum chamber needed to be replaced by shorter telescopes without restricting the movement of the linear rail passing underneath. The original collimation lens has been taken out without replacement, leaving the beam divergently propagate through the newly installed smaller view ports into the vacuum chamber. This enables for larger beams at the position of the atoms despite smaller commercial windows. The new beam configuration is shown on the right in figure 3.22. The two horizontal beams remain unchanged from the previous configuration. The maximum total power in the beams also remains unchanged. With a given distance from the fibre end to the MOT centre of $d = 100$-$112.7mm$[15] the intensity for each beam drops from 100% at $d = 100mm$ to 89% at $d = 112.7mm$. For ^{40}K the intensity also falls respectively.
The performance of the 3D MOT with divergent beam configuration is discussed in the chapter 5.4. The settings for the optimal detuning and gradient for the 3D MOT are also discussed in that section.

However, for both instances of collimated and divergent beams the splitting ratio between fibre pairs is fixed due to the use of 50:50 fibre splitters. Since the fibre splitters deviated slightly from their specifications as discussed in section 3.4 an unwanted imbalance in the 3D MOT beams is introduced that is larger in case of ^{40}K. It was attempted to counteract this by positioning the individual fibres carrying more light opposing the pushing beam at the 3D MOT chamber. The quantitative influence of the imbalance is unknown.
In later discussion the current configuration of divergent beams for the realisation of the 3D MOT is always assumed unless stated differently.

3.6   Detection system

In addition to the 2D MOT and 3D MOT optics described above there is also the detection system that will be presented very briefly in this section thus completing the experimental setup. It will be presented in more detail in [105].
In this experimental setup there are two different detection techniques implemented in the experiment: Absorption imaging and fluorescence detection.
Both techniques are well known in the community and not reviewed here in detail. For a better understanding it is referred to the literature e.g. [106]. The detection in the context of this thesis is always performed horizontally.

---

[15]The thickness of a commercial CF16 flange is $12.7mm$. They are used where the divergent beams are placed, displacing the fibres at a larger distance of the atoms than before.

3.6.1 Fluorescence technique for atom number determination

The fluorescence technique for obtaining atom numbers relies on measuring the spontaneous emission of an atom cloud. Some of the equations and more details can be found in [77, 107]. Assuming a two level atom, the probability to find an atom in the excited state with a detuning of Δ, a line width of $\Gamma = 1/\tau$, saturation parameter $S = I/I_s$ with the saturation intensity $I_s = \pi h c/(3\lambda^3 \tau)$ at a given total intensity I in the six beams is given by:

$$\rho_e = \frac{S/2}{1 + S + \left(2\frac{\Delta}{\Gamma}\right)^2} \tag{3.3}$$

The intensity of a Gaussian beam is given by equation C.6 in appendix C. Given the varying intensity depending on the position in the beam we can give a higher and a lower bound for the scattering rate and therefore also for the atom number. For the atom number lower and higher bound is inverted. The lower bound for the atom number N assumes the highest intensity $I(0, z)$ given by C.10. The higher bound for the atom number N assumes an averaged intensity over the beam profile $I_{aver} = P_0/(\pi(\omega_z)^2)$. Combined with the saturation intensity the corresponding saturation parameter S_{aver} and S_0 for equation 3.4 can be determined. The relation between S_{aver} and S_0 yields $2S_{aver} = S_0$.

The number of atoms is proportional to the total scattering rate of photons. The rate of photons scattered by a single atom R_{sc} is given by

$$R_{sc} = \Gamma \cdot \rho_e \tag{3.4}$$

The values for the line width Γ, saturation intensity I_s, wavelength λ and lifetime τ of ^{87}Rb, ^{40}K and ^{39}K are given in table 3.1.

The total power emitted by the atom cloud is then given by $P = N \cdot E_{phot} \cdot R_{sc}$ where N is the total number of atoms and $E_{phot} = h \cdot c/\lambda$ the energy of one photon. The photons are scattered isotropically in space into the full solid angle of 4π[16] but only a fraction of the solid angle is observed. The detection of a higher solid angle is restricted by optical access. The conversion factor to the full solid angle is given by

$$\Omega = \Omega_{frac}/\Omega_{tot} = \frac{\pi \cdot R_L^2}{4 \cdot \pi \cdot r^2} \tag{3.5}$$

with R_L being the lens radius and r the distance to the MOT. The measured power P_m converts then to the total power by using $P = P_m/\Omega$.

---

[16]Stimulated emission is neglected here.

In the context of this experiment both a photo diode and a CCD camera are used to detect the fluorescence signal.

Photo diode A photo diode for obtaining atom numbers is used for measuring the fluorescence of an atom cloud. The solid angle for the photo diode is given by the focal length of $f = 300mm$ and the radius $R_L = 1.5''$ of the lens. Hence the relative fractional solid angle is given by $\Omega = 4.03 \cdot 10^{-3}$. The photo diode[17] has a gain of $R = 500\,kOhm$ and a nominal quantum efficiency $qe \approx 70\%\,@\,767 - 780nm$. The voltage drop measured across the photo diode is given by $U = R \cdot I$ with $I = qe\,R_{sc}\,e^-\,N$. The total atom number is therefore given by:

$$N = \frac{U}{R\,R_{sc}\,e^-\,qe\,\Omega}$$

(3.6)

CCD camera The detected power on the camera is also only a fraction of the solid angle. The conversion factor to the full solid angle is again given by equation 3.5 with $R_L = 1$" being the lens radius and the focal length in the range of $r = 200$ - $400mm$. The measured power converts like above to the total power by using $P = P_m/\Omega$.

The camera[18] has a quantum efficiency of nominally ≈ 12 - $14\%\,@\,767$ - $780nm$ the A/D conversion factor of the camera is 3.8 e-/count giving the counts per pixel per photon. This is used to determine a conversion factor C for the number of counts per power and exposure time $[counts/(nW \cdot ms)]$. The total atom number N is then given by:

$$N = \frac{N_{counts}}{C \cdot \tau_{exp} \cdot E_{phot} \cdot R_{sc} \cdot \Omega}$$

(3.7)

The two different detectors agree within 40% in the atom numbers. One possible reason for this discrepancy can be the assumed quantum efficiencies.

3.6.2 Absorption technique for atom number determination

Absorption imaging is also used in this experiment for more accurate detection of cold clouds. Two CCD cameras are placed at the 3D MOT chamber and the science chamber, each with different magnification factor ranging from 1:4 to 2:3 but using the same CCD camera model[19]. The equations used follow [108].

---

[17]OSI100-V-500k (5kHz)

[18]pixelfly qe, PCO

[19]PCO, Pixelfly qe

Absorption imaging relies on imaging the shadow of an atom cloud. A resonant detection beam is directed onto the cloud and partly absorbed by the atoms. Another picture is taken without atoms and the difference of these two pictures gives the optical density $OD = ln(N_A/N_R)$ of the atom cloud. Possibly also a dark picture can be taken in order to subtract background and systematic noise but has not been done in the context of all measurements done here.

The total atom number is given by

$$N = -\frac{A\,\omega_0^2\,\alpha}{6\,\pi\,c^2}\,\left(1 + 4\frac{\Delta^2}{\Gamma^2} + \frac{I}{I_s}\right)\,ln\left(\frac{N_A}{N_R}\right) \tag{3.8}$$

where A is the area depicted by one pixel and ω_0, Γ and Δ are the atomic transition frequency, line width and detuning of the laser in respect to the transition. N_A and N_R are the brightness values of each pixel with atoms and without atoms respectively. The parameter α is the absorption coefficient that is dependent on the polarisation of the light and the state of the atoms. Here it is set to 1.
For the future objectives of different magnification at the top and the bottom of the science chamber are planned, allowing for detection and manipulation of the atoms [105].

3.6.3 Temperature determination of a thermal cloud

The thermal cloud can be described as a cloud of Gaussian shape for spatial and momentum distribution

$$\rho(r_0, p) \;\propto\; \exp\left(-\frac{p^2}{2mk_BT}\right)\,\exp\left(-\frac{r^2}{2\sigma_0^2}\right) \tag{3.9}$$

After time of flight and free ballistic expansion the distribution becomes independent of its initial momentum distribution. The distribution in space is now given by the position of the atoms either still in the same position as before or moving to a different position according to their kinetic energy.

$$\rho(r, t) = \int \rho(r_0, p)\,\delta\left(r - r_0 - \frac{pt}{m}\right)\,dr\,dp$$
$$\propto\; \exp\left(-\frac{mr^2}{2m\sigma_0^2 + 2k_BTt^2}\right) = \exp\left(-\frac{r^2}{2\sigma_{TOF}^2}\right) \tag{3.10}$$

If the size is defined as the standard deviation σ, the comparison of the last two expressions in 3.10 gives the following relation between the standard deviations,

$$\sigma_{TOF}^2 = \sigma_0^2 + \frac{k_BT}{m}t^2 \tag{3.11}$$

If the size of the cloud is defined as the $1/e^2$ radius equal to $\sqrt{2}\sigma$ the above equation changes to $2\sigma_{TOF}^2 = 2\sigma_0^2 + \frac{2k_BT}{m}t^2$. Therefore the temperature is independent from the definition of the size. The size is determined by absorption imaging and Gaussian fitting of the spatial atom distribution at different TOF times.

3.6.4 Density determination of a thermal cloud

Assuming a three dimensional Gaussian profile describing the normalised particle distribution

$$f(x,y,z) = \left(\frac{1}{\sigma\sqrt{2\pi}}\right)^3 \exp\left(-\frac{x^2}{2\sigma^2} - \frac{y^2}{2\sigma^2} - \frac{z^2}{2\sigma^2}\right). \qquad (3.12)$$

the peak density is then given by $n_0 = N\,f(x,y,z,) = N/(\sigma\sqrt{2\pi})^3$ and is used to determine the phase space density PSD.
Throughout the entire evaluation a Gaussian density distribution for a thermal cloud is assumed. Deviations in quadrupole traps are investigated in [105].

3.6.5 Phase space density determination of a thermal cloud

The temperature and density determine the phase space density (PSD). It expresses how many particles can be found in a cube with a length equal to the deBroglie wavelength Γ. It is the crucial parameter for Bose-Einstein condensation and is given by

$$PSD = n \cdot \Lambda^3 \qquad \text{with} \qquad \Lambda = \sqrt{\frac{\hbar^2 \cdot 2\pi}{mk_BT}} \qquad (3.13)$$

The phase space density of the atomic cloud can be increased by several orders of magnitudes [109] as will be shown later.

Chapter 4

Magnetic trap design

Despite the fact that optical cooling techniques are powerful tools for cooling, slowing and capturing neutral atoms, they still unavoidably meet their fundamental limitation in the recoil energy as long as photons are scattered by the atoms. Only recently the creation of a BEC only by laser cooling has been achieved [61] based on narrow transition cooling and optical dipole trapping. For most other elements other techniques for confinement and further cooling still need to be established, in order to reach temperatures and densities necessary for Bose-Einstein condensation and ultra cold Fermi gases.

Two trapping techniques are mainly used in ultra cold atom experiments, far detuned optical traps and magnetic traps. Combining both techniques by using the magnetic traps prior to the optical dipole trap we take advantage of each technique's features whilst compensating their weaknesses. The magnetic traps stand out with larger trapping volumes and depths and can capture larger and hotter atom ensembles while the optical dipole traps serve as a "leak free" trapping mechanism for very cold ensembles. The experimental results for magnetic and optical dipole trapping are discussed in section 6 and 7.

4.1 Overview of magnetic coil sets

Separate MOT vacuum systems for individual species give us the opportunity of adding other species on demand. It also prevents possible disturbances of different species onto each other during simultaneous loading in one chamber like experienced with ^{87}Rb -^{40}K mixtures (see chapter 5.1). For this purpose a narrow coil design with magnetic transport has been developed, providing the freedom of individual magnetic traps at the 3D MOT chambers for preparation and the collection of laser cooled atom ensembles with the magnetic transport system.

The realised horizontal magnetic transport system, as previously mentioned in

section 2, transfers the atoms from the 3D MOT chambers to the science chamber where the atoms are transferred to the Feshbach coils. Rather then having several overlapping coils with sophisticated current switching [110], we decided to realise a reliable but easier setup for the magnetic transport based on a linear rail with one pair of moving coils like implemented in many other experiments [111–115]. Magnetic transport thereby is in general not limited to quadrupole traps or adiabatic schemes but have also been realised in Ioffe-Pritchard type traps [116] and in non adiabatic regimes [117].

A quick investigation has shown that an overlapped coil approach similar to [110] with the same optical access available in this approach is probably impossible to realise. All three coil sets, MOT coils, moving coils and Feshbach coils, are designed to provide a gradient of $150\,G/cm$ at a current of $I = 100A$ for magnetic trapping. The Feshbach coils though can also be used to control and manipulate the inter-atomic interactions by using Feshbach resonances. Hence, they are optimised for homogeneous magnetic fields. The other two coil sets, MOT and moving coils, are optimised for a high gradient with outstanding optical access.

For the largest possible optical access for the implementation of optical lattices and beams for magneto-optical trapping, the Feshbach and MOT coils are placed as close as possible to the science and 3D MOT chamber. The design of a very narrow two layer coil system allows the moving coils to enclose the particular coil pair. The moving coils are displaced on the same horizontal axis with the help of the linear rail. They overlap fully with the Feshbach and MOT coils (see figure 2.2) whilst providing very good optical access.

The two layer coil system makes it important to reduce the extension of the coils. Especially the width is of special interest to reduce the distance of the moving coils to the atoms. For this purpose a narrow coil design based on flat wire is developed that delivers desirable gradients with small volume and high optical access.

At first this section concentrates on the basic working principle of magnetic trapping of neutral atoms (section 4.2). The optimisation of the wire layout for the generation of homogeneous magnetic potentials (section 4.3) and Anti-Helmholtz fields (section 4.4) are presented and finally the design, cooling and manufacturing process (section 4.5) are discussed.

4.2 Magnetic trapping of neutral atoms

Although magnetic traps show a much deeper trap depth than e.g. optical dipole traps, magnetic traps for neutral atoms with a typical trap depth of $k_B \cdot 1K$ can still only be used with prior laser cooling of the atoms. One of the main advantages of magnetic traps is the avoidance of optical heating due to light scattering and

the provision of a smooth, well defined potential that is not disturbed by light field fluctuations.

The interaction between neutral atoms and a magnetic field is based on the interaction between the relatively weak magnetic moment $\vec{\mu}$ of the neutral atom and the magnetic field $\vec{B}$, the so-called Zeeman effect for weak magnetic fields where the total angular momentum F couples to the magnetic field $\vec{B}$. At higher magnetic fields the Paschen-Back effect shifts the energy levels differently due to the fact that the coupling of the individual elements of the total angular momentum $F = J + I$ breaks up and couple separately to the magnetic field. For trapping atoms with electromagnetic forces only the Zeeman effect range is of interest.

Being trapped in a magnetic field the magnetic moment $\vec{\mu}$ precesses around the magnetic field vector $\vec{B}$. The projection of the total angular momentum F on the magnetic field axis gives the magnetic quantum number of the hyperfine splitting m_F. The number of possible different orientations is given by $m_F = \pm F, \pm(F - 1), ... 0$. The potential energy of the atom in a magnetic field E_{pot} is then given by

$$E_{pot} = -\vec{\mu} \cdot \vec{B} = g_F m_F \mu_B |\vec{B}| \tag{4.1}$$

with g_F being the hyperfine Landé factor and μ_B the Bohr magneton. From equation 4.1 it is obvious that an inhomogeneous magnetic field in coordinate space leads to a force $\vec{F} = -\nabla U$ where U is the potential given by the magnetic field. This force is used for spatial confinement of ultra cold atoms. It was first achieved by *Migdall et al.* [118] in a simple quadrupole trap.

4.2.1 Magnetic trapping of ^{87}Rb and ^{40}K

Atoms at a certain temperature T move in the magnetic trap with the velocity v corresponding to the total energy $3/2 k_B T = E_{kin} + E_{pot}$. The kinetic energy is converted in potential energy E_{pot} corresponding to a certain magnetic field strength. For the stretched state in ^{87}Rb at a temperature of $5mK$ the potential energy relates to a magnetic field of $112G$[1]. With a gradient of $150G/cm$ the radial extension of the cloud at this temperature yields $\approx 7mm$.

The easiest form of a magnetic trap is the quadrupole trap that was also used in the first experiment [118]. It is realised by two coils with equal but counter-propagating currents, also called Anti-Helmholtz configuration due to the analogue Helmholtz coils. In contrast to the Helmholtz coils that create a homogeneous field[2] the Anti-Helmholtz coils create a zero magnetic field in the centre of the trap and an

---

[1]$\frac{3}{2} k_B T = g_F m_F \mu_B |\vec{B}|$

[2]A homogeneous field is generated at a distance-to-radius-ratio equal to 1

increasing magnetic field with growing distance to the centre and can thus be used as an atom trap.

Due to the fact that no field maxima can be realised in charge and current free environments [119], the atoms can only be trapped in a magnetic field minimum. Combining this with equation 4.1 shows that only states with $g_F \cdot mF > 0$ lower the atomic potential energy with decreasing magnetic field and therefore experience a confining potential. These atomic states are called *low-field seeking* states. The *high-field seeking* states with $g_F \cdot m_F < 0$ on the other hand are accelerated away from the magnetic field minimum and expelled from the trap.

The trappable atomic states for both ^{87}Rb and ^{40}K are presented in table 4.1. The most stretched states $|F, m_F\rangle = |2, -2\rangle$ for ^{87}Rb and $|F, m_F\rangle = |9/2, +9/2\rangle$ for ^{40}K experience the largest energy shift and so the largest force in an inhomogeneous static field. Since in the optical molasses a mixture of all m_F is present, the stretched state is prepared by optical pumping with circular polarised light (see section 6.1).

^{87}Rb	F	2	2	1					
	m_F	+2	+1	-1					
^{40}K	F	9/2	9/2	9/2	9/2	9/2	7/2	7/2	7/2	7/2
	m_F	+ 9/2	+7/2	+5/2	+3/2	+1/2	-7/2	-5/2	-3/2	-1/2

Table 4.1: *Trappable atomic states for* ^{87}Rb *and* ^{40}K: Only the weak field seeking states can be trapped in a magnetic trap due to *Wings theorem* [119]. The most stretched states $|F, m_F\rangle = |2, -2\rangle$ for ^{87}Rb and $|F, m_F\rangle = |9/2, +9/2\rangle$ for ^{40}K experience the largest energy shift and so the largest force in an inhomogeneous static field.

Majorana losses   Although fulfilling a crucial feature for evaporation by generating the tightest confinement for the atoms and thus a high collision rate, the quadrupole trap design suffers from non-adiabatic spin flips in the centre of the trap, so-called Majorana losses. Here the magnetic field $\vec{B}$ is small and changes direction rapidly and the atomic magnetic moment might not be able to follow the magnetic field. The atom is 'transferred' to a different m_F state and is possibly lost from the trap. This effect is stronger for colder ensembles that spend more time in regions of low magnetic fields (compare 4.2 and 4.3 [120]).

Majorana losses in the trap centre not only cause atom loss but also heating of the atom cloud by removing the coldest atoms from the cloud. The loss region shrinks with the atom cloud temperature but slower than the cloud radius so that the loss mechanism increases with decreasing temperature and extension of the cloud. The loss rate can be estimated to [120]

$$
\begin{aligned}
\Gamma_M \quad &= \quad 1.85 \cdot \frac{\hbar}{m} \left(\frac{g_F m_F \mu_B B'}{k_B T} \right)^2 & (4.2)\\
&= \quad 0.061 \cdot \left(\frac{B' \, [G/cm]}{T \, [\mu K]} \right)^2 \quad \text{stretched state of } {}^{87}Rb & (4.3)
\end{aligned}
$$

A cloud of $T = 100\mu K$ in a trap with a gradient of $B' = 150G/cm$ along the strong axis experiences a loss rate of 0.137 atoms per second. The loss rate Γ_M increases quadratically with growing magnetic field gradient and with falling temperature since the atom cloud size decreases and the atoms spend more time in the loss region.

The effect of Majorana losses can be circumvented by introducing magnetic traps with non vanishing field minima. The most important examples are the Ioffe Pritchard trap [121], the baseball trap [122], the TOP trap with dynamic potentials [57], the cloverleaf trap [123] and the QUIC trap [124]. All these different approaches bring a smaller confinement strength, a more complicated setup and/or more complicated operation with them. Moreover, the non-vanishing magnetic field minimum preventing Majorana losses needs to be very well controlled during evaporation as a varying minimum field changes the resonance condition for RF induced spin flips. Due to simplicity and the fact that a moving magnetic trap is needed only quadrupole traps have been realised in the context of this experiment.

Another approach is a red detuned dipole trap to prevent Majorana losses during RF evaporation before finally transferring the atoms into the dipole trap (see section 6.4).

4.3 Simulation of homogeneous fields

The phenomena of Feshbach resonances is a unique and powerful tool in ultra cold ensembles for quantum simulations giving the freedom of arbitrarily tailoring inter atomic interaction potentials with magnetic fields. In order to access the resonances with high precision very homogeneous magnetic fields will be generated by magnetic coils that are designed based on the numerical simulations of magnetic field distributions of different wire layouts.

Feshbach resonances were initially realised in sodium [34] and for a given element it can be difficult to tune through a resonance with high precision due to magnitude of the magnetic field B where the resonance occurs and the ratio of the width to the magnitude $\Delta B/B$.

Luckily the Feshbach resonances for ${}^{87}Rb$ -${}^{40}K$ mixtures [35–37] and ${}^{40}K$ [24, 25, 38]

are within a range of $B_{Fesh} = 450\text{-}600G$ and typical widths of $\Delta B \approx 4G$ for the mixtures and with $B_{Fesh} = 202G$ for ^{40}K. These magnetic field magnitudes are easily accessible without extraordinary demands on the accuracy of the magnetic fields. Even for ^{39}K with $B_{Fesh} = 160\text{-}500G$ with widths of $\Delta B \approx 37\text{-}72G$ [125] the Feshbach resonances show very convenient features. Only the inter atomic resonance for ^{87}Rb [126] is a more demanding case with the widest Feshbach resonance at $B_{Fesh} = 1007G$ and width $\Delta B = 170mG$, requiring a relative accuracy of 10^{-4} to 10^{-5}. Meeting the required accuracy in homogeneity for the Feshbach resonances of 10^{-5} and still giving high optical access is the most crucial part in designing the magnetic coils.

In order to find the best coil design for the most homogeneous magnetic fields, several wire layouts are simulated and discussed. Other secondary optimisation aspects are high optical access, small volume, lower current and therefore power consumption.

The simulation is based on the *Biot-Savart* law [127] that describes the magnetic field $\vec{B}(\vec{r})$ at point $\vec{r}$ generated by an arbitrarily distributed current density $\vec{J}(\vec{r'})$ at point $\vec{r'}$. The magnetic field is then given by

$$\vec{B}(\vec{r}) = \frac{\mu_0}{4\pi} \int \vec{J}(\vec{r'}) \times \frac{\vec{r} - \vec{r'}}{|\vec{r} - \vec{r'}|^3} dV' \tag{4.4}$$

with μ_0 being the vacuum permeability. Equation 4.4 shows clearly that with a predetermined distance $\vec{r} - \vec{r'}$ given by the experimental setup the magnetic field $\vec{B}$ only depends on the current density $\vec{J}$. For a constant current I the current density translates directly into a copper density of the wire layout. Assuming a current limit given by the equipment, maximising the copper density translates into the maximal achievable magnetic field. Choosing the most compact and densest wire layout accordingly delivers the highest magnetic field magnitude.

But not only the magnetic field strength is of importance. Also the power consumption of the coil. With $B \propto N \cdot I/R$ the magnetic field strength B generated by a coil is proportional to the number of windings N with a radius R and the current I used while the power consumption P scales with $P \propto I^2NR/A_{cs}$. Both conditions together give $P \propto B^2R^3/(NA_{cs})$. The radius R and the cross section of the wire A_{cs} are directly connected due to the relative increase in radius with the height of the wire. Hence, a large width combined with a small height, leading to a small radius turn out beneficial for magnetic field strength and power consumption.

In order to find the best option for realising homogeneous potentials the magnetic field distribution for a certain wire layout is simulated in the following way: Each winding N_i is placed at a certain radius R_i and distance D_i depending on the position within the cross section of the coil and the coils central radius R and
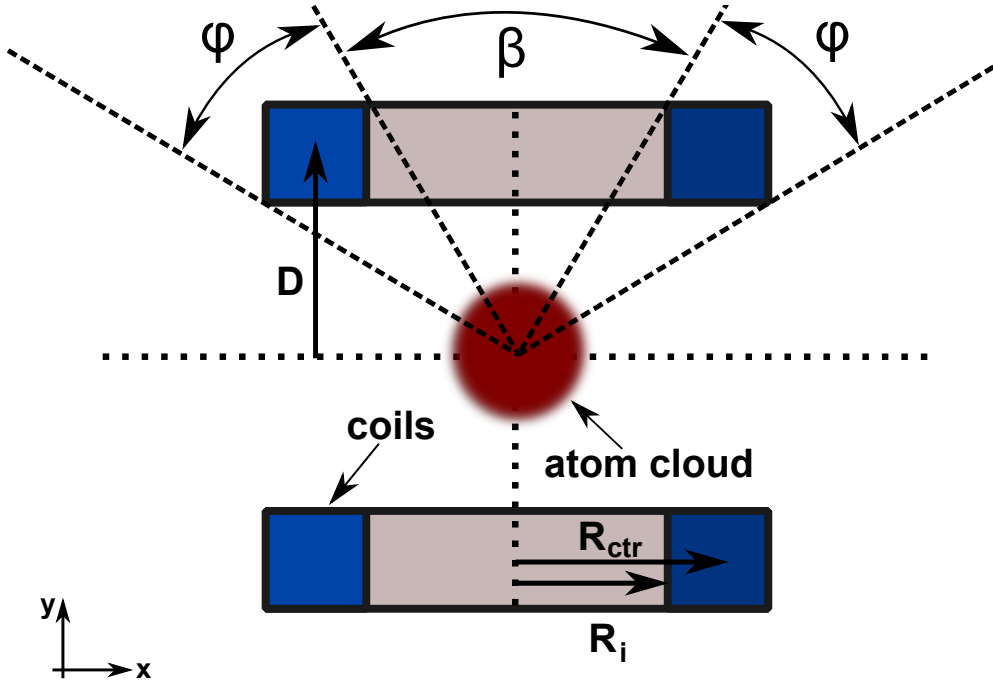
Figure 4.1: *Optical access definition for magnetic coils:* The optical access is given by the open angle β defined by the distance D and the inner radius R_i. The distance D, the central radius R_{ctr} and the extension of the coil body define the dead angle ϕ.

distance D (see figure 4.1). For a varying ratio of the central radius R and distance D with $\alpha = R/D$ the *Biot-Savart* law (see equation 4.4) is numerically integrated over the finite dimensions of a single winding N_i at a given distance D_i and radius R_i with a average current density $|\vec{J}| = I/A$ with I being the current flowing in the wire cross section A. The isolation and empty space for cooling purposes are included in the simulation as current free space and therefore not generating any magnetic field.

Since it is nearly impossible to design a perfect homogeneous field, a check point y is introduced where the deviation to the magnetic field in the centre $|B(y)| - |B(0)|$ is determined as an indicator for the homogeneity of the magnetic field. The check point is chosen to $y = 100\mu m$ and hence is comparable to the extension of a BEC. The distance D is a fixed parameter given by the experiment, leaving the radius R as the only free optimisation parameter, expressed as $\alpha = R/D$. The deviation $|B(y)| - |B(0)|$ at the checkpoint $y = 100\mu m$ is determined for a varying α. Interpolation of the results for the deviation at y gives a relation between α, the ratio of radius to distance, and the deviation of the homogeneity $|B(y)| - |B(0)|$. The optimum value α_{opt} is then defined as the interpolated point where the deviation is closest zero. It needs to be kept in mind that this numerical procedure does not
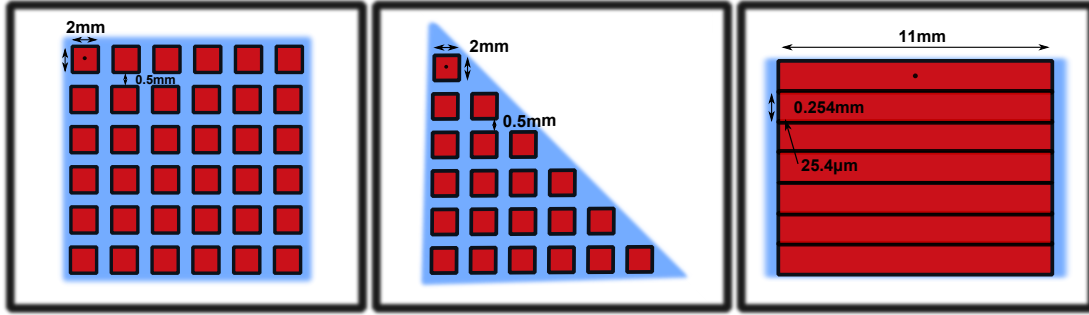
Figure 4.2: *Different wire layout for homogeneous magnetic fields:* From left to right, first the standard **rectangular** or square cross section where the small wires are stacked up. Second in the middle the **triangular** shape where the Helmholtz condition of equal radius to distance is imitated. The condition is not strictly fulfilled since the larger the radius and distance become the larger becomes the extension of the used wire cross section. In both cases rectangular wire of $2 \times 2mm$ cross sectional area with $0.5mm$ space for cooling purposes is assumed. Last on the right is the **flat** wire approach shown. The cross section is maximally filled by flat wire of $11mm$ width and $0.254mm$ height. The wires are separated by $25.4\mu m$.

give a value for α where the deviation is zero from the centre up to $y = 100\mu m$ but the deviation is close to zero at y for α_{opt}.

The optimised value for α_{opt} is then used to calculate the homogeneous field B_{HO} and the resulting anti-Helmholtz B_{AH} for N windings and a radius of $R = \alpha D$. For the anti-Helmholtz field considerations made in the following, the strong axis has been used.

We have chosen three easy wire layouts for rotationally symmetric coils, shown in figure 4.2, to be investigated. The black dot in each picture indicates the reference point for the individual wire distance D_i and radius R_i which are not identical with the overall coil distance D and radius R relating to $\alpha = R/D$.

First on the left the usually used and approved **rectangular** or square layout of stacked thin wires, where the cooling liquid flows in between the wires (blue area). Unfortunately the cross section for cooling is equivalent to current free volume not contributing to the magnetic field.

If the Helmholtz criteria is taken into account, saying radius and distance of the wire loop needs to be equal, then the wire's radial position should increase linearly to the distance. This layout results in a very large extension of the coil, having the windings allocated on a line going in 45° from the centre of the coils. But the idea can be followed in a less strict way by having the wires shaped as an isosceles triangle pointing at the centre of the coils. This layout will be the second approach and it will be referred to as the **triangular** shape shown in the middle of figure 4.2. The cooling fluid here will also need to flow in between the wires (blue area).

The third approach shown on the right in figure 4.2 is a **flat** wire configuration similar to Bitter electromagnets for plasma physics for high magnetic field generation [128, 129]. The flat wires can be stacked precisely and easily, leaving little current

free volume given by the isolation and a layer of adhesive. This will result in the highest copper density possible meaning also the highest current density at a given current that is defining the magnetic field. But as a result the cooling will happen only on the surface perpendicular to the current flow (blue area).

For each approach the same clear distance between the coils is assumed accounting for the science cell of $33mm$ width, a gap on each side of $3mm$ and $3mm$ for housing or support structures. The wire itself for the rectangular and triangular approach has a $2mm \times 2mm$ cross section and an isolation of a quarter of one millimetre thickness plus another quarter of one millimetre for cooling purposes on each side. The rectangular cross section approach has 10×10 windings while the triangular approach works with 55 windings. The flat wire approach uses 70 stacked windings, $11mm$ wide and $0.254mm$ thick with an isolation of $25.4\mu m$. The adhesives is not accounted for in the calculations but is determined to $\approx 22\mu m$ in the experiment. The requirements in all cases are the same with a homogeneous magnetic field of up to $B_0 = 1100G$ with a relative accuracy of 10^{-5} and a magnetic field gradient of $B' = 150G/cm$.

Out of the numerical integration the optimal radius can be determined from figure 4.3. In each graph the relative deviation of the magnetic field at the checkpoint $y = 100\mu m$ from the magnetic field in the centre $(\vec{B}(y) - \vec{B}(0))/\vec{B}(0)$ for different values of α, corresponding to different radii, is shown. Interpolating between the data points, gives the optimal value for α where the deviation is close to zero. At the top the result for the flat wire layout is shown. The optimal value for α yields $\alpha_{opt} = 1.019$. Below the results for the rectangular wire layout with $\alpha_{opt} = 0.95$ in the middle and for the triangular wire layout with $\alpha_{opt} = 0.77$ at the bottom respectively. As expected all values for α_{opt} are close to 1 due to the Helmholtz condition of equal distance and radius.

In case of the triangular wire layout the larger difference of the optimal value for the α parameter from 1 in comparison to the other two wire layouts is mainly due to a different definition of the α parameter for this approach (compare figure 4.1). For the flat wire and the rectangular approach we use the central radius R or R_{ctr} of all windings. While in case of the triangular wire layout we define the inner radius R_i in the parameter $\alpha = R_i/D$. But as it will be seen later the inner radius that is limiting the optical access is indeed smaller than it might promise from the α_{opt} value.

So far we have only investigated which value is best for α_{opt} for each individual wire layout by aiming for the smallest deviation at the check point y without actually comparing the different wire layouts. In order to make a meaningful statement, concerning which of the three wire layouts is fulfilling the requirements, the three
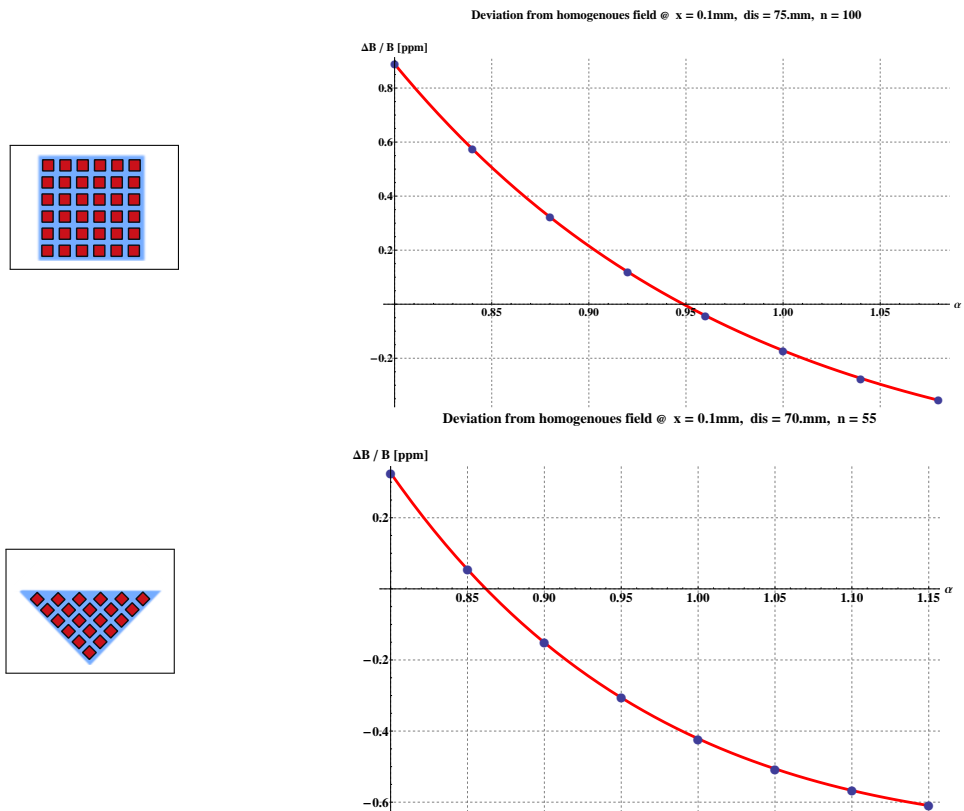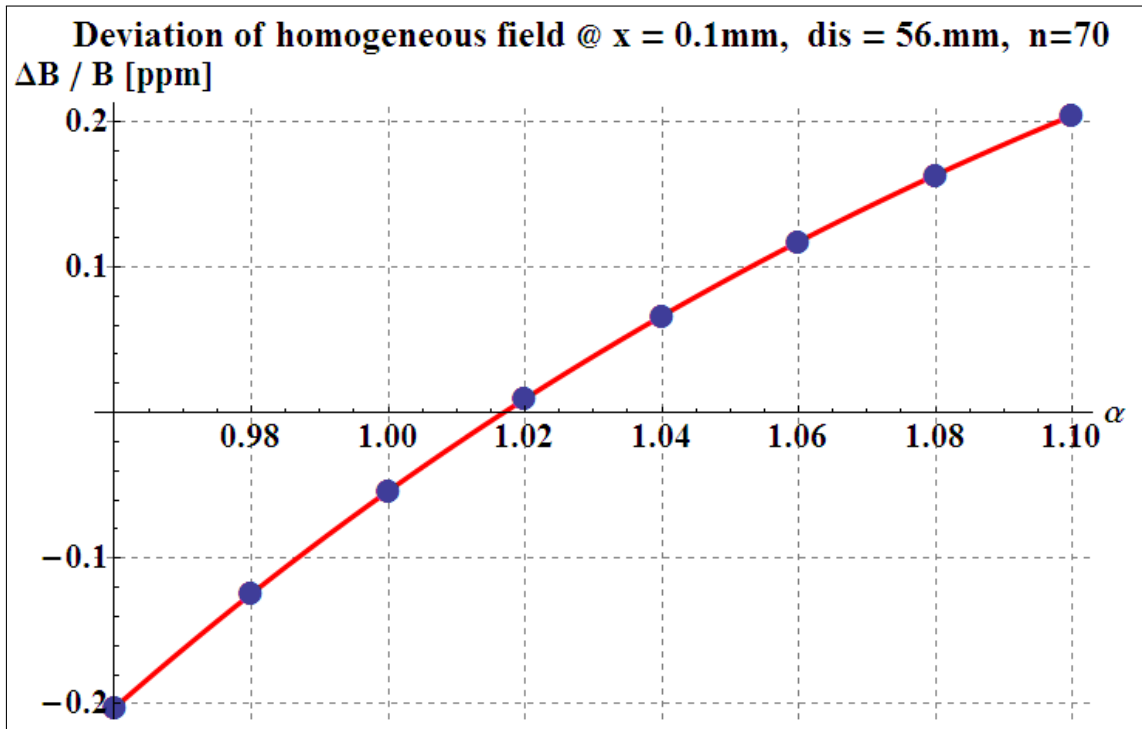
Figure 4.3: *Deviation of the magnetic field B from centre value versus α:* For a given value $\alpha = \frac{R}{D}$, a measure for the radius, is the difference between the magnetic field at check point $y = 100\mu m$ and $y = 0\mu m$ determined. The check point at $100\mu m$ is comparable to the extension of a BEC. Interpolation of the results gives a relation of distance to radius ratio α to the deviation $(\vec{B}(y) - \vec{B}(0))/\vec{B}(0)$. The optimum value α_{opt} is defined as the point where the deviation is closest to zero. At the top the results for the flat wire with $\alpha_{opt} = 1.019$ is shown. Below the results for the rectangular wire layout with $\alpha_{opt} = 0.95$ in the middle and for the triangular wire layout with $\alpha_{opt} = 0.77$ at the bottom are shown respectively.
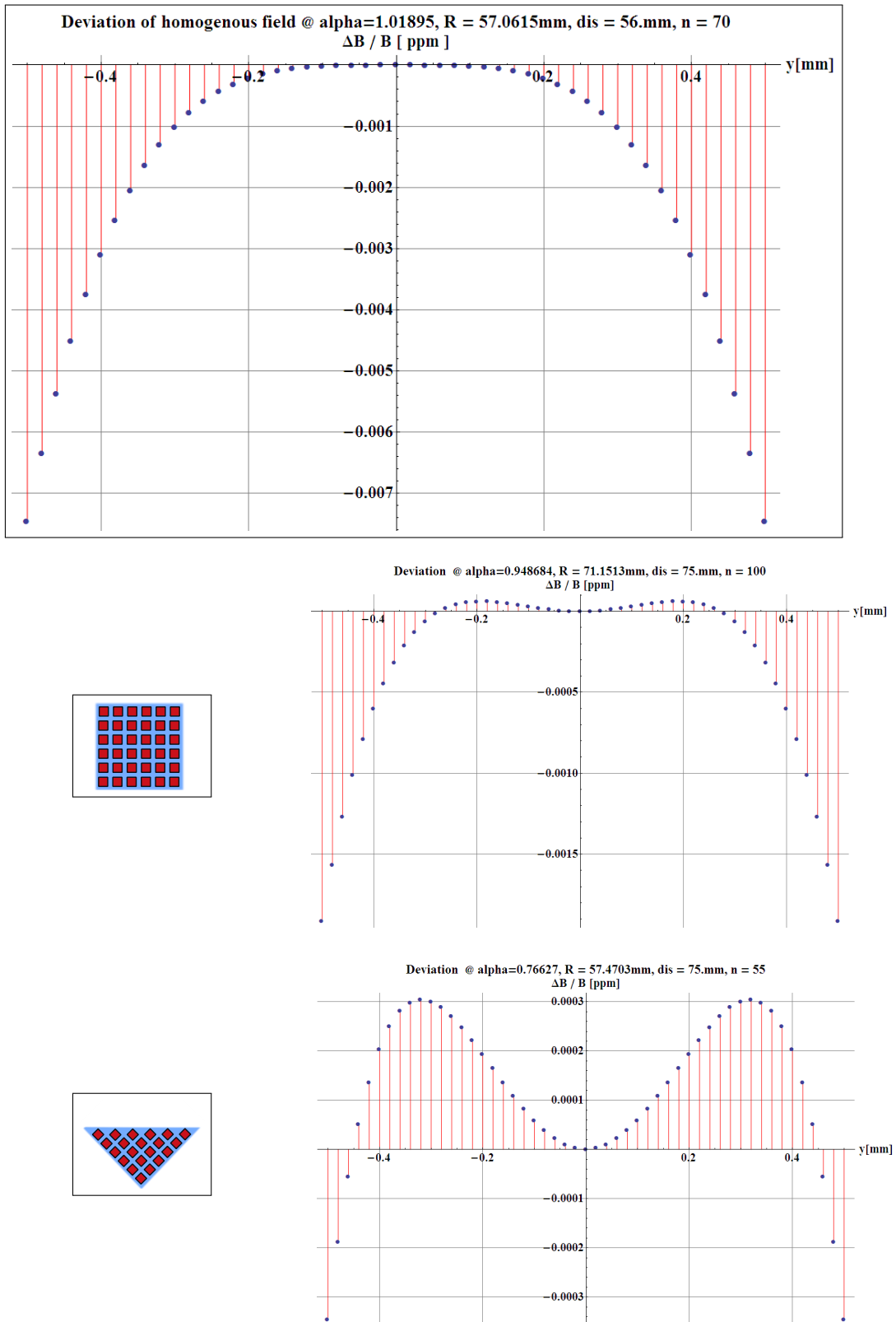
Figure 4.4: *Deviation of homogeneous field for different wire configurations:* At the top flat wire at $\alpha = 1.02$. The deviation shows a parabola like behaviour with a relative deviation at $y = 100\mu m$ of $1.7 \cdot 10^{-9}$. Furthermore the rectangular wire layout in the middle and the triangular wire layout at the bottom is shown. At the same distance from the centre of $y = 100\mu m$ the rectangular wire layout deviates by $0.5 \cdot 10^{-10}$ relative to the central magnetic field. The triangular wire layout deviates by $0.3 \cdot 10^{-10}$. All investigated layouts fulfil the requirement of the relative deviation of $\Delta B/B = 10^{-5}$.

different configurations need to be compared directly. Therefore the magnetic field distribution given by equation 4.4 is calculated and compared for each wire layout with its specific value for α_{opt} out of figure 4.3.

As expected all three wire layout show quite homogeneous fields in the centre. Hence, only the difference to the value in the centre of the magnetic coils is depicted in figure 4.4. The fact that in none of the cases the deviation is not equal to zero at the check point $y = 100\mu m$ is due to the numerical integration and interpolation procedure preformed before but the deviation in all cases is small enough to meet the requirements of a relative accuracy 10^{-5}.

Again at the top in figure 4.4 the flat wire layout is presented. The relative deviation at $y = 100\mu m$ yields $< 1 \cdot 10^{-10}$. The deviation evolves parabola like with increasing distance from the centre with a flat region in the centre. Below the rectangular wire in the middle and the triangular wire layout at the bottom is depicted. For the rectangular wire layout the deviation at the same distance from the centre is $0.5 \cdot 10^{-10}$ with two local maxima at $\pm 200\mu m$ The deviation is increasing rapidly towards the outside but less rapid then for the flat wire. On the left the deviation for the triangular wire layout is given by $0.3 \cdot 10^{-10}$. In all three cases the deviation has the same order of magnitude. The deviation is not constant over distance and increases more rapidly further out.

As it can be seen every investigated layout fulfils easily the requirement of the relative deviation of $\Delta B / B = 10^{-5}$. Therefore we have the opportunity to take secondary criteria into account.

The second most important features is the optically accessible angle to the science chamber β and the volume of the coils, creating a dead angle ϕ. In figure 4.1 the angles β and ϕ are illustrated. With the number and extension of the windings and the optimised α parameter the optical access is determined to $\beta = 109°$ for the flat wire, $\beta = 99°$ for the rectangular cross section and $\beta = 97°$ for the triangular cross section.

The volume is given by the cross section of the coil dominating the size of the dead angle ϕ since the α parameters are fairly similar for all three approaches. A smaller volume reduces the dead angle ϕ in the experiment. The ratio of the cross sections for the flat wire ($215mm^2$), rectangular ($625mm^2$)and triangular cross section ($344mm^2$) is given by $\approx$ 2:6:3. The corresponding filling factor[3] is 90% for the flat wire approach in comparison to 64% for the rectangular and triangular wire approach. The power consumption is within a factor of two fairly similar for all three approaches, especially for the rectangular and flat wire layout (see table 4.2).

---

[3]The filling factor is defined as the current carrying fraction of the total cross section
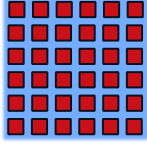
N	100	55	70
$D\,[mm]$	75	75	56
$R\,[mm]$	71.15	57.47	57.06
$\alpha_{opt} = \frac{R}{D}$	0.95	0.77	1.02
$A[mm^2]$	2×2	2×2	11×0.254
$\frac{|\vec{B}(0)| - |\vec{B}(y)|}{|\vec{B}(0)|}$	$0.5 \cdot 10^{-10}$	$0.3 \cdot 10^{-10}$	$< 1 \cdot 10^{-10}$
$\beta_{OA}\,[°]$	99	97	**110**
Total cross section $[mm^2]$	625	344	**215**
Filling factor $[\%]$	64	64	**90**
$I_H\,[A]$ @ $B_0 = 1100G$	88	149	**99**
$I_{AH}\,[A]$ @ $B' = 150\frac{G}{cm}$	71	115	**64**
$P_H\,[kW]$ @ $B_0 = 1100G$	1.5	1.9	1.5
$P_{AH}\,[kW]$ @ $B' = 150\frac{G}{cm}$	1.0	1.1	0.64
$R\,[m\Omega]$	200	85	155

Table 4.2: *Results of the simulation for homogeneous magnetic fields for different wire layouts:* The optimised parameters for rectangular, triangular and flat wire configurations for homogeneous magnetic fields of $B_0 = 1100G$ and a magnetic field gradients of $B' = 150G/cm$. For details on the simulation refer to text. The outstanding features for the flat wire configuration are the optical access β_{OA}, the total cross section and the filling factor.

Parameters of the Feshbach coils   The calculation of the magnetic field yield a 70 winding coil pair with flat wire at a centred distance of $56mm$ and a radius of $57.06mm$ with an α parameter of 1.019. The optical access granted by the coil to $109°$ which is amended to $99°$ because of the housing and other margins[4]. The smaller accessible angle through the small windows of the science chamber is given by $31°$ (see figure 4.6). The magnetic field is scaling linearly with the current so that the requirements of $B_{HO} = 1100G$ and $B_{AH} = 150G/cm$ are met at currents of $I_{HO} = 99A$ and $I_{AH} = 64A$. The resistance ρ per coil is given by

$$\rho = \frac{\varrho N 2\pi \alpha_{opt} D}{w\ h} = \quad 155m\Omega \tag{4.5}$$

and the inductance L for a short air core loop $[130, 131]$ by

$$L = \frac{\mu_0 N^2 (\pi \alpha_{opt}^2 D^2))}{w + 0.9\ \alpha_{opt} D} = \quad 0.64mH \tag{4.6}$$

The result of the inductance measurements can be found in section 6.2 and are in very good agreement.

In summary the flat wire is the best design option in terms of combining the best features. All three wire layouts show a convincing homogeneity and are comparable in power consumption. But the flat wire layout stands out with its high optical access of $99°$, filling factor of 90% and its small volume of the coils of $215mm^2$, leaving lots of accessible space around the experiment. Furthermore the required homogeneous field and anti-Helmholtz field are reached with convenient currents below $100A$. The moving and MOT coils will be fabricated with the same flat wire design.

Besides the Feshbach resonances the Feshbach coils are secondarily used as one set of quadrupole trap coils in order to store the atoms transported by the moving coils to the science chamber. Complementary to the design of the Feshbach coils, two additional pairs of coils are needed but those will serve only as magnetic traps and as long as the enclosure is strong enough to confine the atoms of a certain temperature, the precise linearity of the magnetic trap is neglected. The realisation of those traps is discussed in the next section.

Since the Feshbach coils are optimised for homogeneity, it is not clear how much this will influence the quadrupole trap features when the coils are used in anti-Helmholtz configuration. Therefore the field of the flat wire coils has been calculated with the parameters given in table 4.2. The result is shown in figure 4.5 and it can be seen that also the anti-Helmholtz field shows little deviation from the ideal linear potential as depicted at the top. The gradient at a current of $1A$ yields $B' = 2.4G/cm$. The deviation has with $\approx 1.8 \cdot 10^{-6}G$ a local maximum at $\pm 0.25mm$.

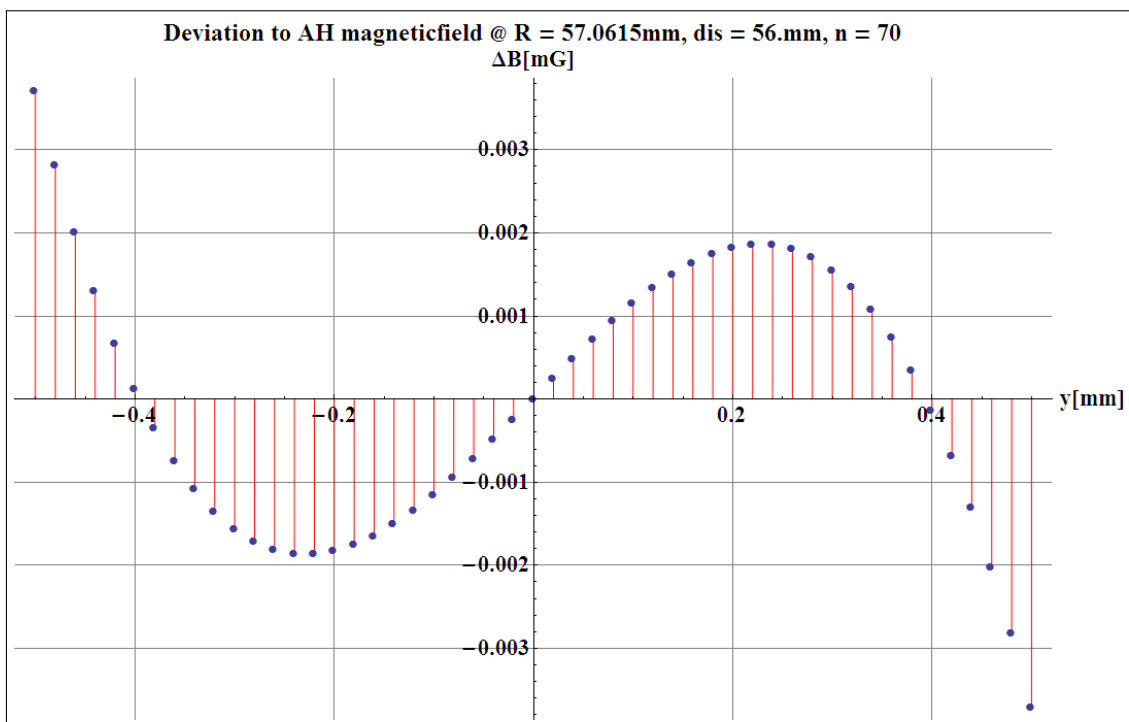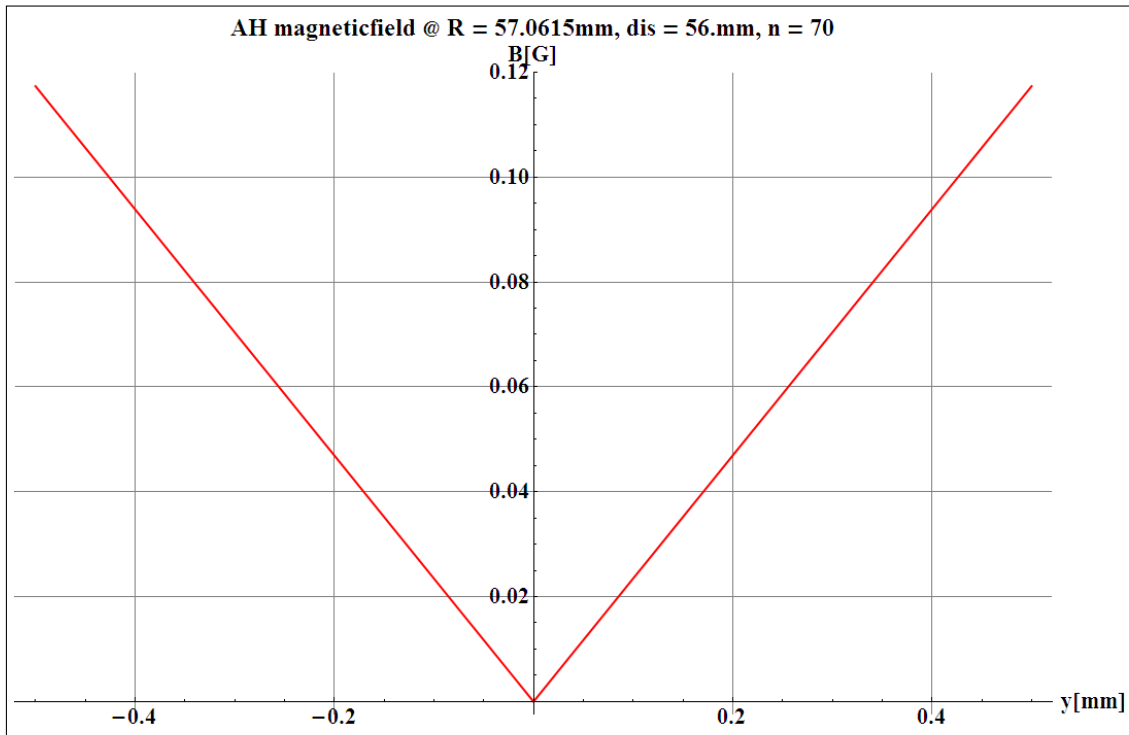[4]Housing and margins account for $4.5mm$ on the each side.

Figure 4.5: *Deviation of the magnetic field B from the ideal anti-Helmholtz field for flat wire:* At the top the anti-Helmholtz field generated by the Feshbach coils with parameters like for flat wire (table 4.2) is shown. At the bottom the deviation of the same field configuration from the ideal anti-Helmholtz field is shown. At a distance from the trap centre of $\pm 0.25mm$ the deviation yields at a local maximum $\Delta B = 1.8 \cdot 10^{-6}G$. The deviation increases further at larger distances from the centre than $\approx 0.5mm$.
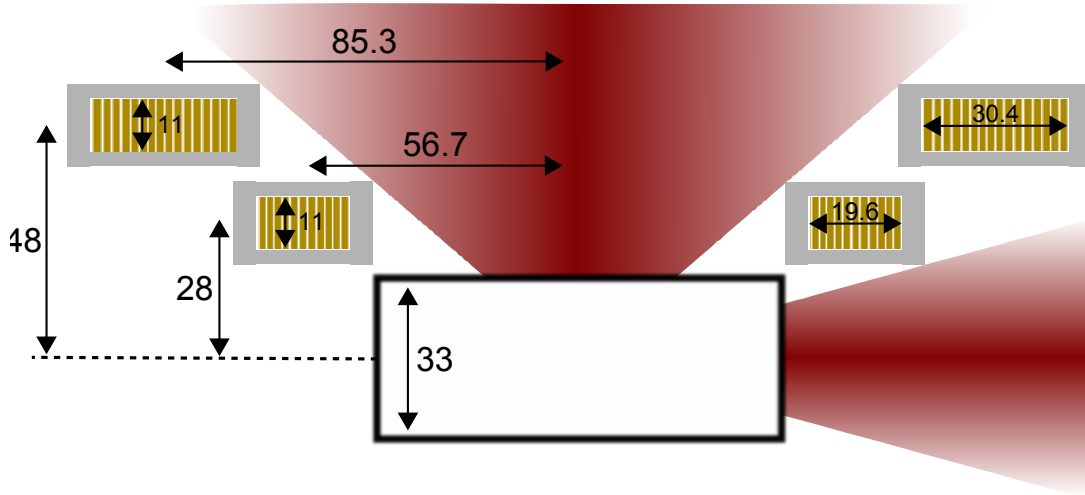
Figure 4.6: *Coil layout at science chamber:* In the centre the $33mm$ wide science chamber surrounded by the Feshbach coils at a distance of $56mm$ and a width of 19.6 without housing can be found. Further out at a distance of $96mm$ the moving coils with a width of $30.4mm$ can be found. The total cross section of the moving coil fits fully in the dead angle ϕ created by the inner Feshbach coils. The optical access β is given by the coils (illustrated as the red shaded areas).

But since the clouds that are confined in the magnetic trap can be larger than the distances of $\pm 0.5mm$, it can only be seen as an indicator how the deviation might evolve at larger distances from the centre. Still, this result indicates the high quality of the linear potential in anti-Helmholtz configuration even though the coils are designed for optimal homogeneity. However, the actual magnetic trap does not need to be perfectly linear because only the magnetic field magnitude determines the trap depth. Nevertheless the confinement strength that is the strongest in a perfectly linear trap potential determines the density which is important for the evaporation cooling. Hence, the other two coil sets, MOT coils and moving coils, are designed in respect of a high gradient combined with high optical access.

4.4 Compact magnetic traps with high gradients

In figure 4.6 the final coil layout at the science chamber with Feshbach coils and moving coils is shown. The moving coils and the magnetic coils at the MOT chamber use the same flat wire technology like the Feshbach coils but will be optimised concerning a high gradient.

For the design of magnetic traps with a high gradient at the 3D MOT and the moving coils a slightly different approach is taken than for the Feshbach coils. But in order to avoid an increasing dead angle ϕ (see fig. 4.1) created by the Feshbach

coils and also gaining greater compactness the flat wire with a width of $w = 11mm$, height $h = 0.254mm$ and an isolation of $25.4\mu m$ thickness will also be used here. It is questionable that any other approach is feasible if the same optical access shall be conserved. Commonly used hollow wire has a lower filling factor of maximal 88%[5] and has a higher current necessity combined with a large pressure drop for cooling.

In order to calculate the magnetic field gradient along the strong axis the equation 4.7 is used that has been derived in *Metcalf et al.* [122] out of an multi-pole polynomial expansion. The series expansion gives an estimation for the trap potential near to the origin and is helpful for the determination of derivatives of the potential for particle orbits. The quadrupole trap can then be expressed to the first order as equation 4.8.

$$b_1 = \frac{3\mu_0 I A R^2}{(R^2 + A^2)^{(5/2)}} = \frac{3\mu_0 I 4\alpha^2}{A^2(4\alpha^2 + 1)^{(5/2)}} \tag{4.7}$$

$$B(\rho, z) = b_1 \sqrt{\frac{\rho^2}{4} + z^2} \tag{4.8}$$

The gradient can be rewritten in terms of the parameter α giving the ratio of the coil radius R placed at $y = \pm A$ to the distance $D = 2A$ like used in the calculation in the previous section.
The extension of the individual winding will be neglected, assuming an infinitely small width and height (see appendix B)

4.4.1 Parameter finding for magnetic traps

The magnetic trap can be designed under different optimising aspects like e.g. the most linear gradient while minimising the curvature. Since here only the confinement of the atoms is important, the magnetic trap will be optimised for maximum gradient at a certain optical access. The resulting curvature will not be a design aspect. The power consumption is optimised for optical access and feasibility of the manufacturing process of the coils.

The maximum gradient at a certain distance $D = 2A$ and number of windings N is found by summing up equation 4.7 for N windings being separated by the width of the flat wire of $0.254mm + 0.0254mm$. The only two remaining free parameters are the number of windings N and the radius of the coil. The parameter $\alpha_{in} = R_i/D$ is a measure for the inner radius of the coil like shown in figure 4.1 and therefore

---

[5]Hollow wire with $3 \times 3mm^2$ out size and a cooling channel of $1 \times 1mm^2$

concurrently a measure for the opening angle for the optical access. α_{in} is varied from 0 to approximately 2.

If the optical access given by the Feshbach coils of 99° shall be conserved the radius is given by the minimum inner radius R_i and the number of windings N leaving the number of windings the only truly free parameter.

With fixed parameters like inner radius R_i and distance D and a chosen maximum gradient of $B' = 150G/cm$ (scaling with $\propto N \cdot I$) the power consumption (scaling with $\propto N \cdot I^2$) can now be minimised by choosing the number of windings N appropriately. Each additional winding N_i, placed at a larger and larger radius R_i, contributes less and less to the magnetic field reducing the average maximum achievable gradient b_{max} per winding but increasing the power consumption more and more. Another concern is the inductance of the coil determining the switch off time of the coil that increases linearly with the number of windings N.

Moving coils For the moving coils the distance is set by the Feshbach coils, the width of the wire and a gap of $3mm$ to $D = 96mm$. An inner radius of the moving coil of $R_i = 70.13mm$[6] leads to $\alpha_{in} = 0.73$ conserving the optical access angle of $\beta = 99°$.

In figure 4.7 the optimisation of the coil's power consumption depending on the number of windings with corresponding α parameters gives an optimum value of $N_{opt} = 156$. The gradient b_1 (see equation 4.7) generated at a current of $I = 1A$ (red dashed line) and the power consumed by one coil (blue solid line) are depicted in figure 4.7. The optimum power consumption and corresponding current are $P_{opt} = 2.9kW$ respectively $I_{opt} = 72.7A$. Nevertheless for a better winding accuracy we decided to limit the number of windings to $N = 100$, not far from the optimum power consumption where the requirements can still be fulfilled.

The generated gradient in the moving coils at the fixed number of turns $N = 100$ and distance $D = 96mm$, while varying the inner radius α_{in}, is shown in figure 4.8 on the left. The gradient peaks at $\alpha_{in} = 0.285$. At this point the maximum gradient generated at a current of $I = 1A$ is $b_{max} = 2.9G/cm$. But the corresponding inner radius at the optimal α_{in} is obstructing the optical access.

At $\alpha_{in} = 0.73$ corresponding to the optical access of 99°, the gradient is 53% of the maximum value b_{max}. The moving coils with $N = 100$ windings at a distance of $D = 96mm$ and an inner radius $R_{in} = 70.13mm$ generates a gradient of $b_{mov} = 0.53 \cdot 2.9G/cm = 1.54G/cm$ per $1A$ in the strong axis. A gradient of $B' = 150G/cm$ is reached at a current of $I = 98.3A$ with a corresponding power consumption of $P = 3.1kW$[7].

---

[6]The housing is accounted for with $4.5mm$ on each side.

[7]No heat related change in the copper resistance assumed

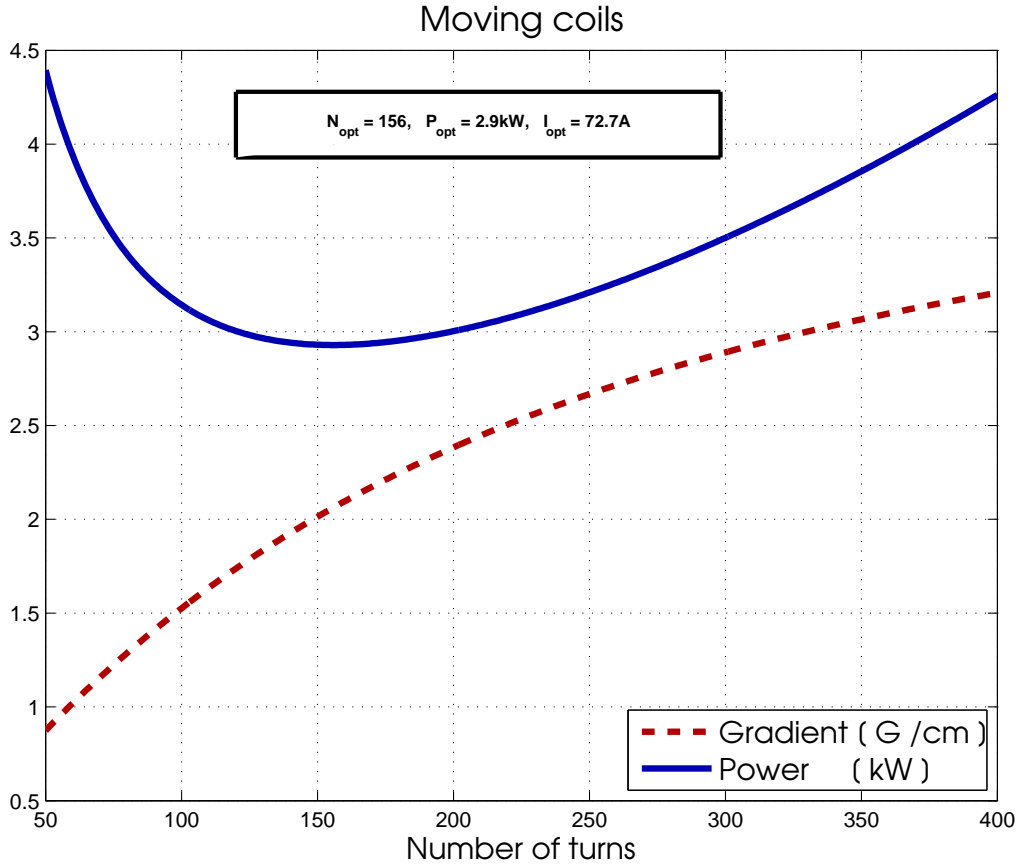**Figure 4.7:** *Power optimisation P concerning the number of windings N for the moving coils:* For one of the moving coils with an inner α parameter of $\alpha_{in} = 0.73$ at a distance of $D = 96mm$ and a current flow of $I = 1A$ the total gradient b_1 (red dashed line) and the power consumption P (blue solid line) with a changing number of turns N is shown. The power consumption P and the gradient b_1 according to equation 4.7 assume both an increasing radius from turn to turn. The optimum value concerning the power consumption is found at $N = 156$ with $P_{opt} = 2.9kW$ per coil and $I = 72.4A$ for a desired total gradient of $b_1 = 150G/cm$.

The resistance of one of the moving coil is given by $\varrho \approx \rho N(2\pi \cdot R_{ctr})/(w \cdot h) \approx 300m\Omega$ with $R_{ctr} = 85.32mm$ measuring the central radius, N the number of windings, ρ the specific resistivity for copper and $w \cdot h$ giving the cross sectional area of the flat wire.

The inductance L of the moving coil is given by equation 4.6 to $L = 3.3mH$. The result of the inductance measurements can be found in very good agreement in section 6.2.

The coil setup at the science chamber is shown in figure 4.6. It shows in the centre the $33mm$ wide science chamber surrounded by first the Feshbach coils at a distance of $56mm$ and a width of $19.6mm$ without housing. Further out at a distance of
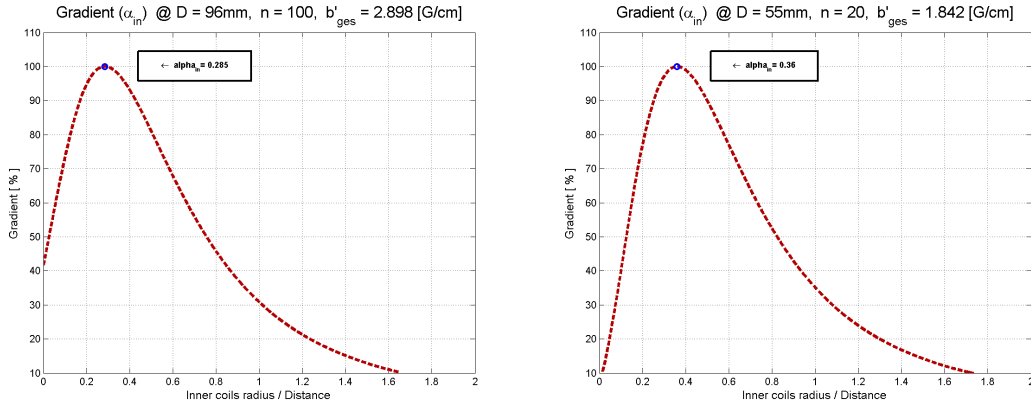
Figure 4.8: *Total gradient b_1 vs. α_{in} for moving and MOT coils:* On the left the gradient b_1 for the moving coils is depicted, contributed by $N = 100$ windings at a distance of $D = 96mm$ in dependence of the inner radius expressed by the α_{in} parameter. The gradient peaks at $\alpha_{in} = 0.285$, but for optical access reasons only a gradient of $\approx 55\%$ at $\alpha_{in} = 0.73$ is used. For the less critical MOT coils with $N = 20$ windings and a distance of $D = 55mm$ peaks the gradient at $\alpha_{in} = 0.36$. For large MOT beams coils with $\alpha_{in} = 0.51$ and a fraction of the maximum gradient of 90% have been built. In both cases a gradient of $150 G/cm$ with maximum current of $I = 100A$ can be reached.

$96mm$ the moving coils with a width of $30.4mm$ can be found. The red sections indicate the opening angle for the optical access. The total cross section of the moving coil fits fully in the dead angle created by the inner Feshbach coils.

In total a higher gradient could have been easily realised at the costs of the optical access. But since the requirements of the gradient and therefore the confinement of the atoms are met while still conserving the optical access we decided for a larger coil at the cost of higher power, number of windings and volume. Nevertheless the design is power optimised for the particular optical access.

MOT coils   The same procedure like for the moving coils can be done for the MOT coils. At the MOT chamber the optical access is less critical and the distance of $D = 55mm$ is given by the 3D MOT vacuum chamber. No particular attention is given to the power consumption because it is expected to be much smaller than for the other coil sets. The number of windings has been chosen to $N = 20$ and is due to the smaller distance of the coils not a critical parameter.

The gradient versus the inner α_{in} parameter is depicted on the right in figure 4.8. The general tendency of the graph is the same like for the moving coils but due to the smaller number of windings the position of the maximum gradient is slightly shifted outwards to $\alpha_{in} = 0.36$. The value for the central radius at the maximum gradient should coincide in both cases. A maximum gradient of $b_{max} = 1.84 G/cm$ at a current of $I = 1A$ can be achieved. In order to match the 3D MOT vacuum chamber's dimensions the inner radius for the MOT coils have been chosen to $R_{in} = 27.91mm$ leading to $\alpha_{in} = 0.51$ resulting in a fraction of the

	MOT coils	Feshbach coils	Moving coils
N	20	70	100
$D[mm]$	55	56	96
$R[mm]$	30.71	56.68	85.32
α	0.56	1.02	0.89
$b_1[G/cm]$ @ $100A$	165.6	234.4	153.7
$\varrho[m\Omega]$	22	155	300
$L[mH]$	0.039	0.64	3.3
$t_{off}[\mu s]$ @ $1000V, 100A$	4	64	330

Table 4.3: *Coil parameters:* The features of the three coil sets MOT coils, Feshbach coils and moving coils for the number of windings, central distance D, central radius R, optimised $\alpha = R/D$, gradient in strong axis at $I = 100A$, resistance ϱ, inductance L and the switch off time with an induced voltage of $U = 1000V$ given by the self inductance $U = L \cdot \frac{dI}{dt} \rightarrow t = \frac{L \cdot I}{U} = L\frac{100A}{1000V}$. The result of the inductance measurements can be found in section 6.2 and are in very good agreement.

maximum gradient of 90%. At a current of $I = 100A$ the coils generate a gradient of $b_{MOT} = 100A \cdot 0.90 \cdot 1.84G/cm = 165.6G/cm$ in the strong axis.

The resistance of one of the MOT coils is given by $\varrho = \rho N(2\pi \cdot R_{ctr})/(w \cdot h) = 22m\Omega$ with $R = 30.71mm$ measuring the central radius and $w \cdot h$ giving the cross sectional area of the flat wire. The inductance L of the MOT coil is given by equation 4.6 to $L = 39\mu H$.

The dimensions and other properties of the coil systems are summarised in table 4.3.

In order to determine the trap depth of the magnetic trap designs the magnetic field generated by coils of N windings at a given distance D and radius R can be approximated by two one-loop coils with a current weighed by the number of turns N [122]. The approximated absolute magnetic field along the two axis ρ (blue) and z (red) of one loop coils in anti-Helmholtz configuration are shown in figure 4.9, where z is the axial direction along the coil separation.

From left to right the MOT coils are depicted first, followed by the Feshbach coils in the middle and last the moving coils on the right. For the approximation the distance and radii were taken from table 4.3. The current is assumed to be $I = N \cdot 1A$ for each coil pair. The coil sets have different distance to radius ratios $\alpha = 0.56, 1.0$ and 0.89 for MOT coils, Feshbach coils and moving coils respectively.
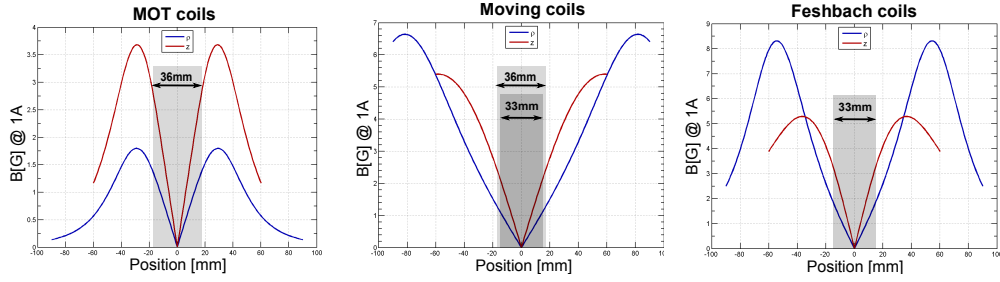
Figure 4.9: *Absolute magnetic potential of magnetic traps:* Approximation of N winding coils with a one loop coil [122] along the radial direction ρ (blue) and the axial direction z (red) in the anti-Helmholtz configuration. From left to right: MOT coils, Feshbach coils and moving coils (see table 4.3). The current is assumed to be $I = N \cdot 1A$ for each coil pair. The thresholds in the MOT coils along different directions are $B_{thres} = 1.8G/3.68G$ but at the same distance of $29mm$ from the centre. The Feshbach coils show threshold values of $B_{thres} = 8.32G/5.27G$ at a distance of $54.5mm/36.5mm$ from the centre. For the moving coils the situation is quite similar with threshold values of $B_{thres} = 6.64G/5.4G$ at a distance of $82mm/59mm$ from the centre.

The x-axis scaling along the distance from the coils is kept constant for all three graphs in order to give a better impression of the potential. In the centre the radial gradient along ρ is in all cases as expected half as strong as in the axial direction along z.

For the MOT coils with $\alpha = 0.56$ the two maxima in different directions are found to be quite different with $B_{max} = 1.8G/3.68G$ but at the same distance of $29mm$ from the centre.

The α parameter of the Feshbach and moving coils are nearly twice as large and therefore close to 1. This fact exchanges the relative positions of the maxima in different directions. The maximum in axial direction lies now further inside than the maximum in the radial direction, leading in total to a more similar magnitude in the axial direction as in the radial direction. The Feshbach coils show maximum values of $B_{max} = 8.32G/5.27G$ at a distance of $54.5mm/36.5mm$ from the centre. For the moving coils the situation is quite similar with maximum values of $B_{max} = 6.64G/5.4G$ at a distance of $82mm/59mm$ from the centre. The grey shaded areas indicate the size of the respective vacuum chamber in the axial z-direction.

The lowest magnetic field maxima for each of the three magnetic traps are the following $B_{max} = 1.8G, 5.27G, 5.4G$. With $\frac{3}{2}k_BT = g_F m_F \mu_B |\vec{B}|$ yields a corresponding temperature scale of $81\mu K, 236\mu K, 241\mu K$ at $I = 1A$. The trap depth scales as the magnetic field linearly with current I. For three magnetic traps with the same depth the current scaling of MOT to Feshbach to moving coils needs to be like the following $3 : 1 : 1$.

In figure 4.9 it can also be seen that for Feshbach and moving coils the deviation from a perfect anti-Helmholtz field is larger. The orientation of this curvature has different directions for axial and radial directions.
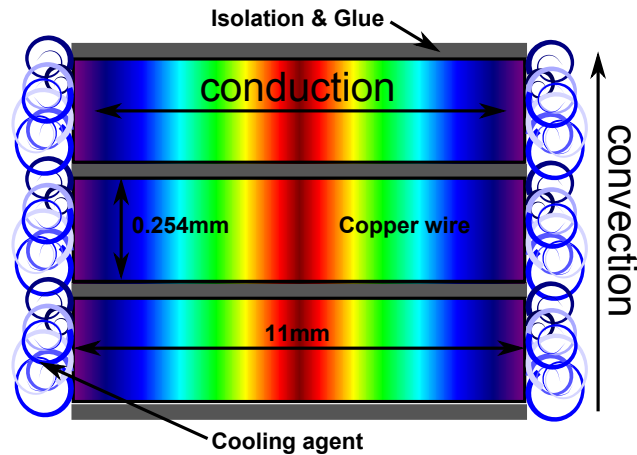
Figure 4.10: *Cooling principle of the coil design:* The heat generated within the coil is conducted perpendicular to the current flow towards the sides of the wire. Heat transport in between individual layers and along the wire is not assumed. On the surface the heat is transferred to the cooling agent.

4.5 Mechanical design for a compact coil design

The previous sections focussed mainly on the theoretical design of the coil sets, deciding the wire type and the geometry given by the distance D, the radius R, and the number of windings N. For a summary see table 4.3.

The new approach with the usage of flat wire also necessitates a new approach to cool, manufacture and mount the coils as the main reason to use flat wire, the compactness minimising the unused space within the coil, would be obsolete with conventional designs. The cooling, winding, design and manufacturing process is described in the following section.

4.5.1 Heat transfer and cooling procedure

Conduction within the copper The heat transport mechanism in the copper wire is based on heat conduction where the heat is displaced by energy transfer similar to the electrical resistance.

Assuming a steady state situation with a uniform heat generation due the current flow, the heat flux travels only perpendicular to the electrical current through the small cross section on both cooled sides of the flat wire. The two-sided cooling generates a temperature gradient in the copper wire. The situation is depicted in 4.10. Furthermore no heat transfer is presumed along the current flow direction, since the cooling predominately occurs perpendicular to the current flow due to negligible temperature differences along the wire in the direction of the current flow. The heat transfer rate on the surface of the coil is down to convection and

will be discussed in more detail in the next section.

The heat conduction in the flat wire is due to reasons given above assumed to occur only in one dimension, but being bi-directional and symmetric about the centre. Following *Fouriers law* for heat conduction [132] in steady state conditions the temperature difference on the coil surface and its centre ΔT_{cop} is governed by

$$P = -k_{cop} A_{sa} \frac{\Delta T_{cop}}{\Delta x} \qquad (4.9)$$

where P is the generated power in the coil, $k_{cop} = 401 \frac{W}{Km}$ the thermal conductivity of copper, A_{sa} the total coil surface along the wire and $\Delta x = 5.5mm$ the distance from the centre of the wire to the surface. With the parameters given later in table 4.4 the temperature difference from the centre across the wire is given by $\Delta T_{cop} = 3K$. In order to determine the temperature in the centre of the wire, the coil surface temperature given by the convection cooling needs to be determined first. This will be done in the next sections and later equation 4.9 is used to determine the temperature in the centre.

Convection by a cooling agent   The heat transfer from the coil to a flowing liquid is based on heat convection, where the heat is transferred by moving a liquid or gas and must not be confused with heat conduction. The heat transfer efficiency strongly varies with the type of flow and is in case of turbulent flow by a manifold larger than in case of the laminar flow.

The important thermo-physical properties determining the overall heat transfer efficiency of a liquid are a high specific heat, a high thermal conductivity, a low viscosity and a low density of which all of them show a thermal dependence.

Newtons second law of cooling given by equation 4.10 expresses the energy conservation during the cooling process. The thermal energy transfer rate q is equal to the product of the heat transfer coefficient h, the cooled surface area A_{sa} and the temperature difference between the fluid and the surface ΔT.

$$q = h A_{sa} \Delta T \qquad (4.10)$$

In a thermal steady state situation the generated electrical heat is equal to the transferred energy and the temperature difference between cooling agent and surface stabilises at a certain value ΔT. The magnitude of the temperature difference depends on the heat transfer rate. The surface area A_{sa} is given by the coil design while the heat transfer coefficient h is given by the cooling agent's properties, the cooling channel dimensions and the flow rate Q. The following estimations follow closely [133].

The heat transfer coefficient h is given in equation 4.11 by the Nusselt number

Nu and the thermal conductivity k. The parameter l is a characteristic length scale of the problem. Here the hydraulic diameter for non-circular tubes is used $D_H = 4A_{cs}/u$ with $A_{cs} = w \cdot l$ being the flow cross section and $u = 2(w + l)$ the wetted perimeter of the cooling channel [134].

$$h = \frac{Nu\,k}{l} \tag{4.11}$$

The Nusselt number is the ratio of convection to conduction heat transfer and can be averaged for turbulent flow in a tube with a finite length to

$$Nu = 0.0023\,Re^{4/5}\,Pr^{0.4} \tag{4.12}$$

The two parameters in equation 4.12 are the Reynolds number Re that determines the regimes of laminar and turbulent flow due to the ratio of inertia and viscous forces and the Prandtl number Pr that gives the ratio between momentum and thermal diffusiveness [135]. The Reynolds number Re will be one of the two major criteria for the evaluation of the cooling agent's efficiency and is given by

$$Re = \frac{\rho\,v\,l}{\mu} = \frac{\rho\,Q\,l}{\mu\,A_{cs}} \tag{4.13}$$

where ρ is the fluid density, v the volume velocity, μ the viscosity. The l parameter is again the hydraulic parameter used for the heat transfer coefficient h. An universally valid range of the Reynolds number Re indicating laminar or turbulent flow cannot be given but in the most common cases the transition is assumed to be in the range of $Re \geq 2000$. From equation 4.13 it can be seen that an irregular shaped flow cross section acts beneficial in consideration of the turbulent flow.

The outstanding Prandtl number is only determined by features of the fluid and is given by

$$Pr = \frac{\mu c_p}{k} \tag{4.14}$$

With a fixed cooling channel geometry, the cooling agent's dynamic viscosity μ, specific heat c_p, thermal conductivity k and density ρ and equation 4.10 to 4.14, the heat transfer coefficient h becomes a function of the fluid flow Q only.

$$h = 0.0023\,\frac{\left(\frac{\rho\,Q\,l}{\mu\,A_{cs}}\right)^{4/5}\left(\frac{\mu c_p}{k}\right)^{0.4} k}{l} \tag{4.15}$$

The heat transfer coefficient for different cooling liquids will be investigated in the next section.

Feshbach coil dimension		
Power [kW]	P	1.5
Channel height [mm]	l	1
Channel width [mm]	w	19.56
Channel length [cm]	L	35.61
Channel cross section [mm^2]	A_{cs}	19.56
Coil Surface [m^2]	A_{sa}	0.007
Surface roughness [μm]	e	70

Table 4.4: *Feshbach coil parameter for cooling*

Different cooling agent properties   In order to evaluate the quality of different liquids as cooling agents the heat transfer coefficient in a certain environment (see table 4.4) is determined. Thereby, in order to verify the regime of turbulent flow the Reynolds number Re will also be checked.

In the context of this thesis nearly 35 different commercially available cooling liquids have been compared of which only the best ten including water will be presented here. The cooling liquids are based on water, glycol and hydrocarbon fluids or mixtures of these. Their thermo-physical properties of interest are summarised in table 4.5 together with the Reynolds number Re and the relative heat transfer rate h normalised in comparison to water.

For the Reynolds number a liquid flow of $Q = 1 l/min$ in the cooling channel of the Feshbach coils, described in table 4.4 is used. The cooling channels are in all coils given by two manifolds of $1mm$ high slots whilst the width varies with the coil width. If the height of $1mm$ is much smaller than the width of the cooling channel the hydraulic parameter becomes comparable to twice the height $D_H \approx 2mm$. The cooling channel is realised with spacers in the cooling body as shown in figure 4.11. As can be seen from equation 4.13 and table 4.5 the Reynolds number is in all cases well above $Re = 2000$ and therefore verifies the turbulent regime. The heat transfer rate h scales linearly with the flow Q and is given by equation 4.15.

The heat transfer efficiency for all cooling liquids will always be inferior to water. But in order to prevent corrosion and electrolysis liquids based on water or glycol are disregarded although these show the highest heat transfer rate efficiencies of up to 84% due to their similarity to water.

	Material	$\rho\,[\frac{kg}{m^3}]$	$c_p\,[\frac{J}{kgK}]$
Water	Water	1000	4181
Dynalene EG 10%	Ethylene Glycol	1017	3969
Dynalene HC-20	Water based	1237	3212
Dynalene PG 10%	Propylene Glycol Inhibitors	1009	4078
Dynalene BioGlycol 20%	BioGlycol+DI water+corr inhibitor	1020	4145
Dynalene BioGlycol 70%	BioGlycol+DI water+corr inhibitor	1053	3182
Paratherm CR	**Hydrocarbon Blend**	**828**	**1920**
Dynalene MV	Hydrocarbon Blend	845	1796
Dynalene PG 80%	Propylene Glycol Inhibitors	1054	2885
Dynalene EG 80%	Ethylene Glycol	1126	2604

	$k\,[\frac{W}{Km}]$	$\mu\,[mPa\,s]$	$Re[10^5]$	$h[\%]$	Reference
Water	0.6	0.9	18.1	100	[136]
Dynalene EG 10%	0.547	1.18	16.5	84	[136]
Dynalene HC-20	0.523	2.10	9.56	70	[136]
Dynalene PG 10%	0.545	1.38	11.9	79	[136]
Dynalene BioGlycol 20%	0.493	1.99	8.31	65	[136]
Dynalene BioGlycol 70%	0.291	10.60	1.61	22	[136]
Paratherm CR	**0.140**	**0.81**	**16.6**	**27**	**[137]**
Dynalene MV	0.133	1.07	1.28	23	[136]
Dynalene PG 80%	0.261	19.79	0.86	16	[136]
Dynalene EG 80%	0.298	9.62	1.9	23	[136]

Table 4.5: *Parameter for cooling fluids:* The thermo-physical properties for water and other cooling liquids based on water, glycol and hydrocarbon. The Reynolds number *Re* and the heat transfer coefficient *h* are determined with equation 4.13 and 4.15 respectively assuming the geometry of the Feshbach coils in table 4.4.

Figure 4.11: *Cooling channel design:* A 1*mm* high cooling channel is realised with peek and rubber spacers, leaving the cooling fluid in direct contact with the coil surface. On the left the slotted design of the moving coils is shown. In the middle the cooling channel is blocked with rubber tube between inlet and outlet. On the right a distance spacer for an unslotted cooling body design with slots for the cooling fluid can be seen.

The best cooling agent of the ones considered here that is not based on water or glycol is the hydrocarbon liquid *Paratherm CR* with a heat transfer efficiency of 27% in comparison to water. *Paratherm CR* is 100% synthetic with a transparent appearance. It can be used in a temperature range of $T = -100°C$ to $200°C$.

After looking for the best cooling agent apart from water based liquids it still needs to be proven that the provided cooling effect is indeed sufficient for the demands given by the coil system here.

In the steady state situation where all power generated in coils P is transferred to the cooling liquid the temperature difference between the cooling agent and the coil surface ΔT (equation 4.10) saturates at a constant value. With the given parameters of table 4.4 and 4.5 and equation 4.10 to 4.14 the heat transfer coefficient h (equation 4.11) becomes as already mentioned before a function of the fluid flow only. The result of the expected cooling performance for *Paratherm CR* is displayed in figure 4.12 but will be discussed later. For comparison also the results for water are displayed in figure 4.12.

In order to gain a sufficient heat transfer coefficient h also the generation of an appropriate flow rate Q is a crucial factor in the cooling system design. The pressure drop across the coils is subject of the next section.

Pressure drop across cooling channel The pressure drop across a tube for laminar and turbulent flow is given by the *Darcy-Weissbach* equation [138–140]

$$\Delta P = f_{DF/M} \frac{L \, \rho \, Q^2}{2 \, A_{cs}^2 \, D_H} \tag{4.16}$$

where L is the length of the tube, ρ the fluid density, Q the fluid flow rate, A_{cs} the cross section of the wetted perimeter and D_H the hydraulic diameter. This equation is generally valid and the specific resistance of the tube is given by the Darcy or Moody friction factor $f_{DF/M}$. A analytical equation for the friction factor is given in [140] as a function of the diameter D_H and the roughness of the pipe ϵ.

For the roughness of the sandblasted surface a value of $\epsilon = 70\mu m$ is assumed [141]. The results depicted in figure 4.12 show the heat transfer coefficient (red circles) for the Feshbach coils against the fluid flow for both Paratherm CR (left) and water (right). Furthermore the expected temperature difference ΔT between coil surface and fluid (blue triangles), the according pressure drop ΔP(green squares) and the Reynolds number Re (yellow stars) versus fluid flow are shown. The calculations assume a homogeneous field of $B' = 1100G$ at a current of $I = 99A$ and a power dissipation of $P = 1.5kW$ (see table 4.2). The two fold cooling channel is $2 \times 1mm$ high and provides cooling from both sides. The estimations are valid for one cooling channel transferring half the energy to the oil.

Comparing the two graphs it can clearly be seen that water is without doubt the far better cooling agent but *Paratherm CR* is with a 3.5 times smaller heat transfer coefficient still in the same order of magnitude. Important features that make hydrocarbon fluids good heat transfer agent are mainly the moderate specific heat and thermal conductivity for synthetic hydrocarbon fluids. The low density and viscosity on the other hand assists the low pressure drop in comparison to fluids with higher viscosity which enables for higher heat transfer due to higher flow.

Already for very small flow rates of $1l/min$ the Reynolds number of above 2000 indicates the inset of turbulent flow. This is due to the asymmetric and small design of the cooling channel.

In the left-hand graph a pressure drop of $\Delta P = 2.5bar$ per coil leads to a temperature difference of $\Delta T = 17.5K$ between the heated oil and the coil surface and a *Paratherm CR* flow of ca. $Q = 2 \times 6l/min$. These are feasible conditions for the experiments.

With a temperature difference between the fluid and the coil of $\Delta T = 17.5K$ and a temperature increase of the cooling fluid by

$$\Delta T_{heat} = \frac{P}{Qc_p\rho} = \frac{57K}{Q[\frac{L}{min}]} = 9.5K \quad @ Q = 6l/min \tag{4.17}$$

yields the surface temperature of the coil of $T = 47°C$ if the oil starts at room temperature of $20°C$. With the results of section 4.5.1 the temperature at the centre of the flat wire is then reasonable $50°C$.

Similar considerations for pressure drop, flow rates and temperatures can also be done for the other coils. The estimated parameters show that hydrocarbon fluids can be used as cooling agent as an alternative to water even within the limited possibilities of an laboratory experiment.

Details on the other parts of the cooling cycle like fluid pump, external heat exchanger, flow meters and pressure regulators can be found in [64].
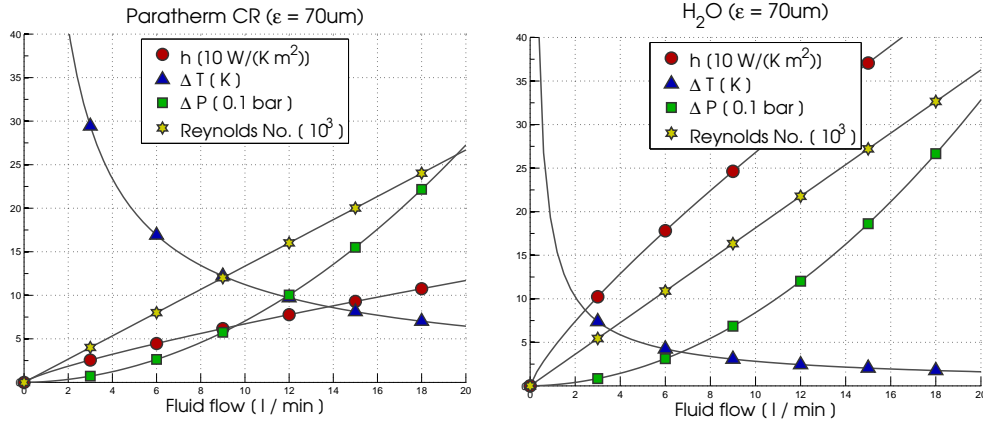
Figure 4.12: *Heat transfer calculation for water and hydrocarbon fluid:* The graphs display the heat transfer coefficient h (red circles), the temperature difference between coil surface and oil ΔT (blue triangles), the pressure drop ΔP (green squares) and the Reynolds number Re (yellow stars) versus increasing fluid flow. On the right for the hydrocarbon fluid Paratherm CR and the on right for water. For Paratherm CR a pressure drop of $\Delta P = 2.5bar$ per coil leads to a temperature difference of $\Delta T = 17.5K$ between the heated oil and the coil surface and a flow of ca. $Q = 2 \times 6l/min$. The calculations assume a homogeneous field of $B' = 1100G$ at a current of $I = 99A$ and a power dissipation of $P = 1.5kW$ (see table 4.2).

4.5.2   Manufacturing of narrow coils with flat wire

After the discussion of the design process of the wire type, size and number of turns of the individual coils and the cooling procedure in the preceding sections, the manufacturing of the new coil design is presented in this section.

The developed process for making a narrow coil with flat wire is depicted in figure 4.13 showing the individual steps from left to right and top to bottom for one of the Feshbach coils.

In the first picture the winding process is shown. Flat wire[8] of $0.254mm$ thickness are isolated one-sided with Kapton foil of $25.4\mu m$ thickness. During winding special care needs to be taken of accurate winding. Each coil must be wound accurately over N number of windings within the limits of $\pm 0.85mm$[9]. Individual windings are then glued with a thin layer of the low viscosity epoxy resin *RT151*[10] while winding the coils. It easily wets the surface and balances out gaps left during applying the glue, creating evenly spread thin layers of epoxy. The glue promises good impact and thermal shock resistance what makes this resin an ideal candidate for this purpose. This glueing technique also ensures a highly compact design of the coil with still easy manufacturing process and avoids the necessity of clamps to hold the windings in place during handling and mounting.

---

[8]Alpha Core

[9]The initial width of the flat wire is $12.7mm$ and is machined down to $11mm$. This leaves a margin of $1.7mm/2$ on each side.
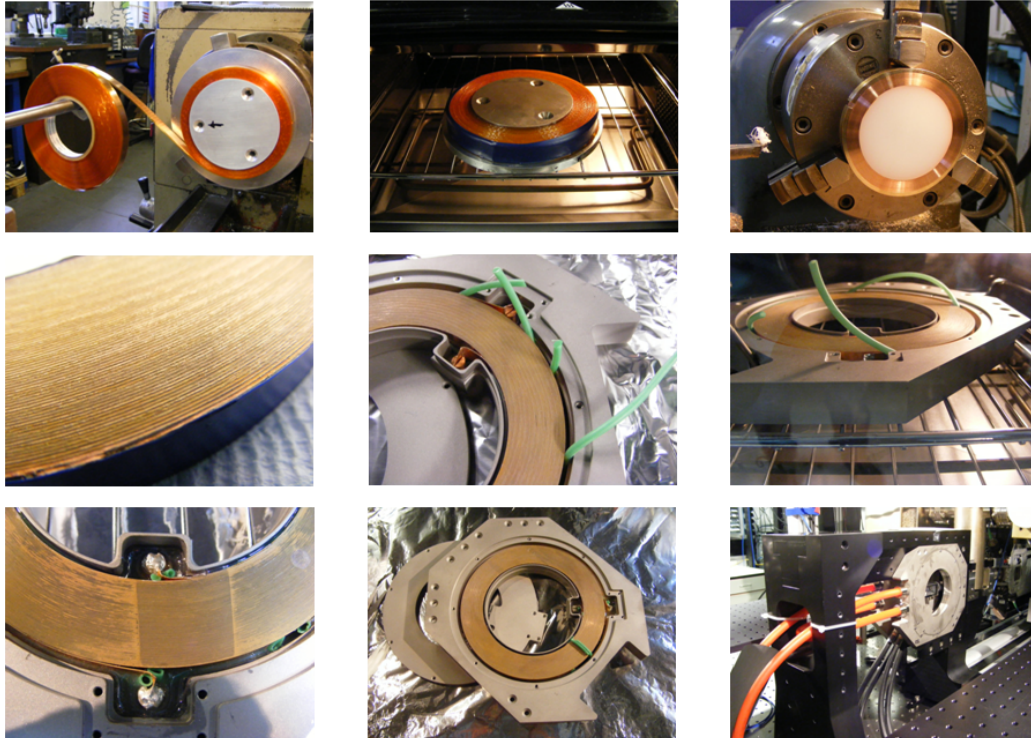
[10]Resintech Ltd

Figure 4.13: *Coil Manufacturing:* From left to right, top to bottom. The first picture shows the winding process for flat wire. Individual windings are glued with a low viscosity epoxy resin. In the second picture the coil is cured at $60°C$. In order to optimise the heat transfer the surface is mechanically cleaned from the epoxy in picture three. Afterwards the coil is etched to remove short circuits introduced by the surface machining in picture four. In the middle the coil is placed within the cooling body that is optimised first for minimising the housing's volume and secondly optimising the joint strength for the adhesive seal. The green rubber is used to separate cooling channel from the glue fixing the coil inside the housing. At the bottom left the electrical connections are shown where electrically conductive epoxy is realising the connection between copper rod and flat wire. The last two pictures show the finished coil without lid and implemented in the experiment around the science chamber.

The second picture shows the coil in the curing phase at 60 $°C$. The curing must happen rather quick but gently since little air bubbles can stay trapped in the epoxy layer. As mentioned before due to the compact design it is necessary to cool the coil from the side rather than between the windings (see figure 4.10) but the heat transfer efficiency orthogonal to the current flow will be hindered by the cured *RT151*.

Hence, in order to optimise the heat transfer that only occurs now through the small cross section of the wire at the side the surface is mechanically cleaned from the epoxy. This phase is depicted in the third picture on the right. In order to prevent damage to the wires the windings need to be mechanically supported from the inner and outer radius (winding mandrel in white and aluminium ring on the
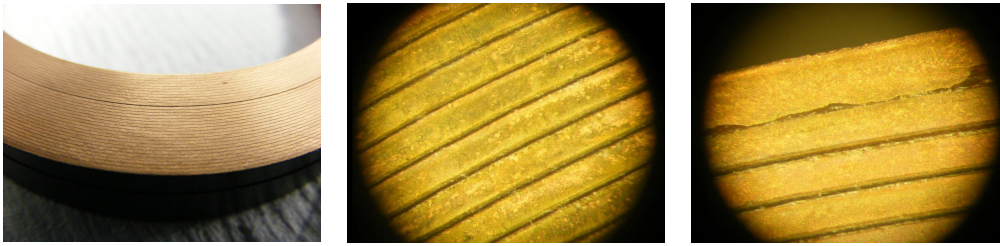
Figure 4.14: *Etching process:* In order to remove electrical shorts on the surface of the coils the area is carefully treated with sandpaper before immersing it in a Ferric Chloride solution to etch the residual short circuits. On the left the sanded coil before etching is shown. The result is shown in the middle. A faulty section with smeared out copper can be seen on the right. Here the etching time needs to be increased. The Kapton isolation can be seen as dark lines between the windings.

outside). Support from the back prevents a breakdown of the glued wire structure during the constant mechanical stress of this process.

The occurrence of little areas of smeared out copper on the cleaned surface creating little contacts and short-circuits with neighbouring windings demands for further post processing of the coil by etching the surface. Foregoing surface sanding removes the largest imperfections before immersed in a Ferric Chloride solution to etch the residual short circuits. A layer of 50-$70\mu m$ is etched within 20-$40min$. The figure 4.14 shows the sanded coil before and after etching. In the middle an adequate section of the coils surface is shown in comparison to a faulty section with smeared out copper on the right. The Kapton isolation can be seen as dark lines between the windings. In figure 4.13 the finished etched coils is shown in the fourth picture. In the middle of figure 4.13 in the fifth picture the coil within the cooling body is shown. The cooling body design concentrates on two aspects. First the housing's volume minimises the outer dimensions of the coils and secondly optimises the joint strength for the adhesive seal.

The green rubber showed in figure 4.13 is used for several purposes. First it separates the cooling channel from the glue fixing the coil inside the housing, leaving a $1mm$ deep cooling channel above and underneath. Secondly, it isolates the coil from the metallic housing. Furthermore it also blocks the channel between the forward and backwards flow for the cooling liquid (figure 4.13 bottom middle).

Although, the rubber is a flexible and easy to use solution for this purposes recently we found it swelled up and got detached from the glue in the long term. Alternative solutions for future amendments will be discussed in [142].

At the bottom left of figure 4.13 the electrical connections are shown where electrically conductive epoxy is realising the connection between copper rod and flat wire. In the experiment it stands $100A$.

The last two pictures of figure 4.13 show the finished coil without lid and implemented in the experiment around the science chamber.

4.5.3 Joint design

As aforementioned the cooling body design has two main aspects. First the minimisation of the volume and second the optimisation of the joint strength for the adhesive seal. Nowadays adhesive joints are used in many engineering areas like aerospace, aircraft and automotive industry, withstanding stress for many years of usage.
In the context of this project the adhesive seal is a space-saving alternative to bolted structures and it also gives the freedom of material choice unlike welding without introducing located points of high thermal stress. The realisation of a mechanical strong and liquid sealing joint requires an appropriate choice of materials including adhesives and an adequate joint design.

Since the housing structures are desirably narrow in design, heavier materials like metals were preferred to certain type of plastics. Here aluminium has been chosen for the moving coils in order to reduce weight and costs while titanium has been chosen for the MOT and Feshbach coils.
In order to avoid eddy currents in the housing structure of the moving coils (aluminium) are slotted, loosing some of the stability. The other housings made of titanium have a lower electrical conductivity than other metals and remain unslotted.
For isolating structures mainly peek is used. Alternative solutions like macor are investigated in [142].
Hence the multifarious material spectrum demands for an exceptional adhesive to bond to all different and possibly complex shaped surfaces with sufficient strength and good chemical and environmental resistance. A suitable adhesive that also stands out with easy handling and curing is *RT111*[11].

For sealing between cooling liquid and environment the joint has to be designed carefully. There are four different stress types that are used for the characterisation of adhesives: Shear stress, tension stress, cleavage and peel stress. For structural adhesives most often the properties suggest the strongest bonds for shear stress followed by tension stress. Poor qualities appear for peel and cleavage joints [143]. Therefore it is desirable to base the joint design mainly upon sheared areas reinforced by surfaces put under tension. The tension stress can be compensated by screws.

These considerations lead to a stepwise design (see figure 4.15 on the right) alternating tension and shear stresses and avoiding peel and cleavage as much as possible rather than a simple surface joint (see figure 4.15 on the left). A recommendable
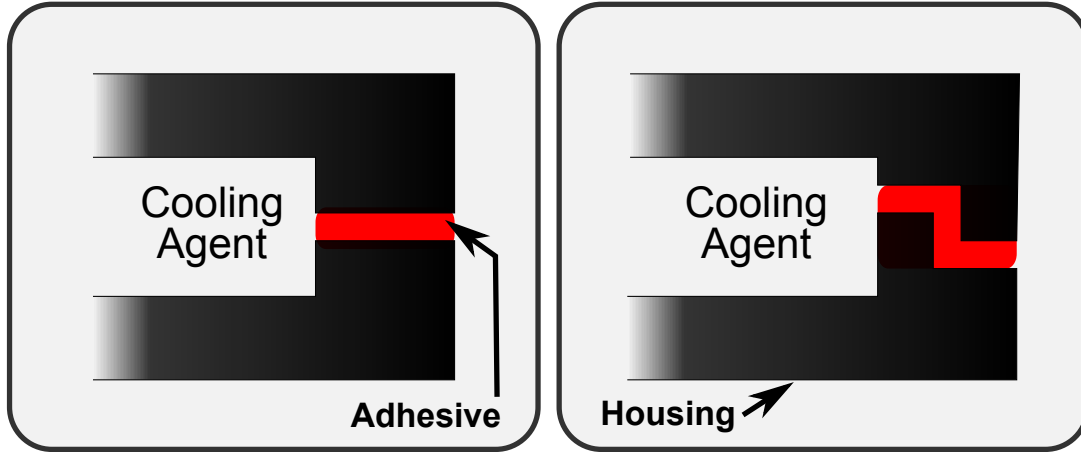
---

[11]Resintech LTD

Figure 4.15: *Joint design* for sealing the cooling agent inside the cooling body against the environment. On the left a simple surface joint, relying only on tension stress. On the right a stepwise joint, combining tension and shear stress.

surface treatment is sandblasting and ultrasonic cleaning for the metal surfaces. The adhesive used here has a shear strength of $20MPa$[12] and a tensile strength of $47MPa$. Balanced forces and assuming the cooling liquid pressure acts only on a surface as big as the coil a liquid pressure of $1bar$ can be held in shear stress by an area of

$$\frac{P_{liquid}}{\tau_{shear}} \cdot A_{coil} = \frac{10^5 Pa}{20MPa} \cdot 70cm^2 = 0.35cm^2$$

With an expected pressure drop in the range of $\gtrsim 2bar$ and a glued surface area given predominately by the perimeter and the width of the flat wire in the range of $A = 2\pi R \cdot h = 2\pi \cdot 56.7mm \cdot 11mm = 39cm^2$ this adhesive exceeds the requirements by a factor of more than 50.

After some iterations the mechanical design of the electrical connections also uses a similar step shape for sealing the cooling channel. Figure 4.16 shows different versions of the electrical connections displaying the initial approach of clamped wires for the MOT and moving coils at the top and the improved version for the Feshbach coils at the bottom. The electrical connections are the weakest point of the design due to large thermal stress and smaller sealing surfaces. The initial seal is only based on the sealing strength of $RT151$ applied on a long slot. Its weakness is mainly due to mechanical stress when the flat wire connections are bend in tight angles.

---

[12]Aluminium to aluminium

The second approach avoids any clamping and bending of the contacts by having a step shaped screw in connector. The performance showed much better behaviour than the previous design but has still two main weaknesses. First the connector is covered in glue decreasing the cooling efficiency by the cooling agent. This leads to higher temperatures and gradients. Secondly, the force works against the seal due to the orientation of the connector resulting in a force pushing the connector out of the peek isolation. Both features combined lead to leakage but can with the gained knowledge now easily be re-designed. The next iteration aims to solve this issue by creating a seal that is increasing in strength when pressure is applied rather than weakening it and uses slightly different materials. It will be discussed in [142].
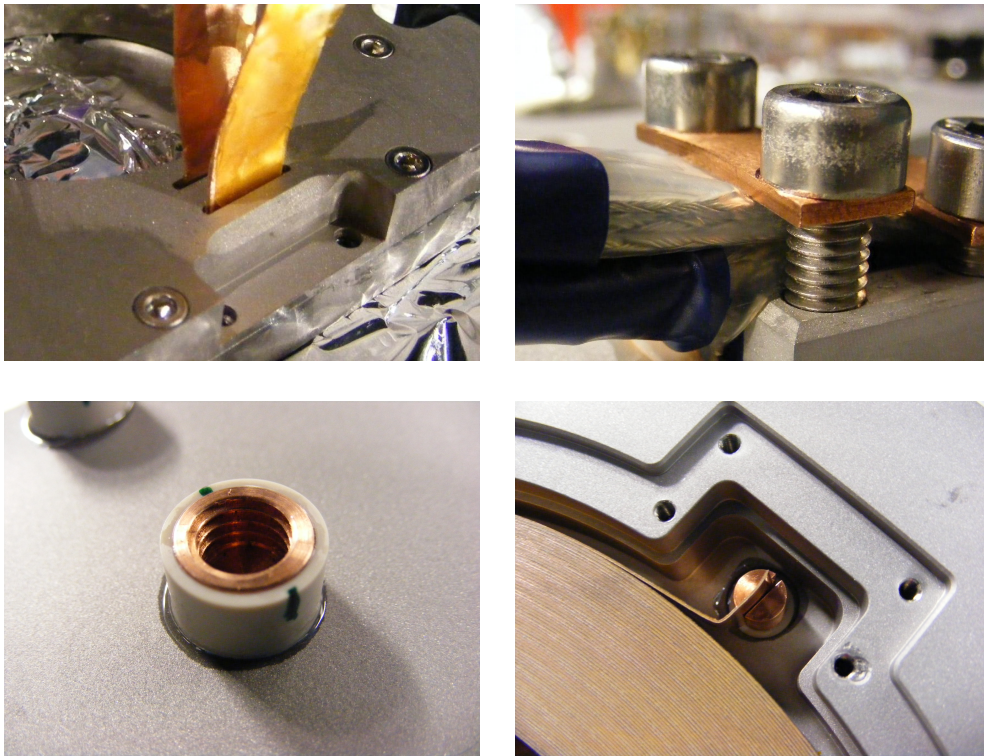
Figure 4.16: *Electrical connection at the coils:* On the left the initial approach of clamped wires for the MOT (left) and moving coils (right) at the top. The improved version for the Feshbach coils at the bottom, seen from out side (left) and inside (right).

Thus far the system of magnetic traps consists of three sets of coils. All of them are designed with the flat wire technique and can produce a gradient of $150G/cm$ or higher. The Feshbach coils have been optimised with the help of magnetic field simulation to generate a highly homogeneous magnetic field in order to tune atomic interaction with the aid of Feshbach resonances. The entire coil system has been built, satisfactorily tested and has been used successfully for the realisation of a ^{87}Rb BEC.

A cooling system using oil was installed. It has been estimated that the parameter range is suitable for laboratory experiments and is used on a daily basis in the experiment.

Overall the narrow design is a suitable candidate for any experiment that seeks high optical access and a compact, more precisely a narrow coil design.

Part II

Creating a Bose-Einstein condensate

Chapter 5

^{87}Rb and ^{40}K in magneto-optical traps

5.1 Introduction

After the detailed description of the experimental setup in part I the following part is devoted to the first experiments of magneto-optical trapping of ^{87}Rb and ^{40}K performed in the context of this thesis. The species are successfully trapped both individually and collectively as a Bose-Fermi mixture representing the first step towards the exciting regime of quantum gas experiments in three and two dimensions.

The investigation of the optimised parameter range is presented and the loading rates and cloud sizes achieved are given in this chapter. The chapter is organised as follows. After a brief introduction of the concept of the magneto-optical trapping and laser cooling within a combined 2D-3D MOT system and the expected temperatures in the following optical molasses phase in section 5.1.1 and 5.1.2, the characterisation of the magneto-optical traps for ^{87}Rb and ^{40}K operated separately in 2D and 3D MOT is discussed in the next sections 5.2.1 and 5.2.2. The performances are compared and peculiarities for the fermionic ^{40}K in comparison to ^{87}Rb are emphasized. Furthermore the influence of both species onto each other during simultaneous magneto-optical trapping is investigated in section 5.3.

In the following section 5.4 the magneto-optical trap with divergent beams is compared to the performance of the same setup with collimated beams. The last laser cooling step, the optical molasses, is presented in section 5.5. The last two sections are operating with divergent beams and only with ^{87}Rb.

The detection method for from section 5.2 to section 5.4 is fluorescence measurements with the CCD camera. For section 5.5 absorption imaging is used. For details on the different techniques refer to section 3.6.

5.1.1 Combined 2D-3D MOT

The technique of optical cooling and trapping atoms as the first cooling step on the way from a hot background gas to quantum degenerate gases is a powerful tool used in many experiments. The so-called magneto-optical trap (MOT) is based on the energy exchange between the moving atom and the laser light field and was first demonstrated by *Raab et al.* [9].

The working principle of laser cooling relies on a spatially varying resonance condition of the atom moving in a light field produced by near resonant counter-propagating or reflected laser beams. Superimposed is a quadrupole magnetic field shifting the atomic energy level according to the linear magnetic field gradient, the so-called Zeeman effect.

The working principle is discussed for the one dimensional case. The atom is moving along the detuned laser beam at a frequency ω_L close to but below the atomic resonance ω_0. Due to the Doppler effect the atom sees a shifted laser frequency by $\Delta_{Dopppler} = \vec{k} \cdot \vec{v}$ in comparison to the atomic transition ω_0. Thereby $\vec{k}$ is the laser light's wave vector and $\vec{v}$ is the atomic velocity. The sign of this additional detuning is dependent on the relative direction of $\vec{k}$ and $\vec{v}$. If the atom is situated in two counter-propagating laser beams of the same frequency the probability of an atom absorbing a photon is higher for the beam propagating against the atom's velocity. This so-called radiation force acts only in momentum space.

The atom is also confined in coordinate space by using the magnetic quadrupole field B. The atomic energy levels are shifted depending on the spatially varying magnetic field strength B. In total this gives a overall resonance condition of $\Delta = (\omega_0 - \omega_L) \mp \vec{k} \cdot \vec{v} \pm \mu' B \hbar$ resulting in a force in both momentum and coordinate space[1].

If the polarisation and the detuning of the light beams are chosen appropriately the force will push and confine the atom in the quadrupole centre. When the atom scatters a photon the momentum of the atom will change due to the fact that the momentum transfer by the stimulated absorption of a photon is directed towards the trap centre. The following momentum transfer due to the spontaneous re-emission of the photon has an isotropic probability distribution. This leads to a vanishing average momentum transfer by spontaneous emission and a directed momentum transfer by the absorption process if many photons have been scattered. For more details about this technique refer to [107, 144].

The following optical molasses works without a magnetic field gradient. The purely velocity dependent damping force does not confine the atoms in coordinate space

---

[1]The factor μ' is related to the hyperfine level transition used.

but can reach lower temperatures than the magneto-optical trap. The reachable temperature range will be discussed in more detail in section 5.1.2.

In many cases the 3D magneto-optical trap confines the atoms directly from a hot back ground gas. The capture range of the Maxwell-Boltzmann velocity distribution and therefore the number of atoms being trapped is limited to a very small velocity range of the total velocity spectrum. A high background pressure of the desired species can increase the number populating the trappable velocity classes and therefore the loading rate of trapped atoms but at the same time the higher back ground pressure increases the number of collisions with the background gas decreasing the lifetime in the trap. Whilst the lifetime

Figure 5.1: *Maxwell-Boltzmann distribution for ^{87}Rb and ^{40}K:* The velocity distribution at an oven temperature of $T = 298K$ for ^{87}Rb (blue) and for ^{40}K (red). The small inlet shows the atom fraction of roughly 1%, which can be captured directly in the 3D MOT with the present experiment parameters, as the red and blue surface.

might not be of importance during the laser cooling process it becomes of great importance during magnetic trapping and evaporative cooling later on in the experiment sequence and therefore is a crucial parameter. If the magneto-optical trap is loaded from a background gas the total atom number N loaded into the magneto-optical trap will be independent to some approximation of the background pressure and depends on other parameters like beam size, light intensity I and detuning Δ [145, 146].

In figure 5.1 the velocity distribution at room temperature of $T = 298K$ for ^{87}Rb (blue) and for ^{40}K (red) [107] is shown. The average velocity of the freely moving atoms for ^{87}Rb and ^{40}K is $v_{rms} = 292m/s$ (Rb) and $v_{rms} = 431m/s$ (K) due to different mass assuming a Maxwell-Boltzmann distribution (see figure 5.1 and equation C.1 in the appendix). The small inlet illustrates the atom fraction that can be captured with the present experiment parameters in a purely 3D magneto-optical trap as the red and blue areas. The graph shows a capture velocity of $v_{cap\,Rb} = 47m/s$ for ^{87}Rb and $v_{cap\,Rb} = 70m/s$ for ^{40}K. Those velocities follow from estimations later on. In both cases the fraction of atoms that travel with velocities below the capture velocity is approximately 1%. The residual atoms leave a background pressure around the cold atom cloud limiting the lifetime inside the trap.
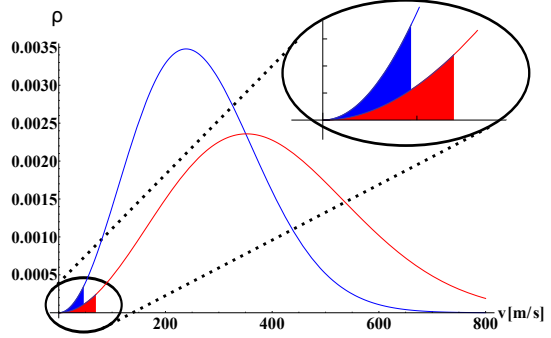
Therefore, it would be beneficial to capture a large range of velocity classes at a constant background pressure and to decouple the loading rate and total atom number from the lifetime of the atomic cloud.

One approach for a better MOT performance with high atom numbers at high loading rates and the high lifetimes of the atom ensemble is a robust combined 2D-3D MOT system like implemented in this experiment here (see figures 2.2 and 5.2) [62].

This combined 2D-3D MOT setup decouples exactly the important parameters of high loading rate and high atom numbers from the lifetime of the system. The loading rate is dominated by the 2D MOT parameters while the total atom number N is given by the 3D MOT parameters. The lifetime in the 3D MOT chamber is given by the vacuum conditions in the 3D MOT chamber and is significantly higher than in e.g. the 2D MOT chamber.

The 2D magneto-optical trap works in the following way. It produces a bright atomic beam with low divergence [66, 67, 147, 148] and can be exploited for every atomic species that can be laser cooled. It compresses the atom beam in two dimensional phase space and can be realised in a compact setup in comparison to the alternative of a Zeeman slower [149]. A small setup is specifically necessary in this arrangement due to the extension to separate 2D-3D vacuum compartments for different species. Furthermore the 2D MOT technique promises a lower beam divergence than the Zeeman slower technique [67].

In the 2D MOT an atomic beam is collimated within a high background pressure regime aiming for high atom flux through the differential pumping stage to the 3D MOT chamber. Here the atoms are re-confined within better vacuum conditions for better lifetimes. Large atom ensembles with long lifetimes and therefore smaller loss rates are a necessary starting point for the following evaporation on the way to the realisation of a Bose-Einstein condensate or a quantum-degenerate Fermi gas.

A schematic picture of the 2D MOT is shown in figure 5.2. The 2D MOT technique exploits the same physics as the 3D MOT technique but only in two dimensions. The light beams and the magnetic field zero are elongated in the longitudinal direction compressing the atoms in coordinate- and momentum space into an elongated atomic beam as shown as red cloud in figure 5.2. This atomic funnel cools and slows down the atoms transversely v_x and conserves the longitudinal component of the velocity v_z. Due to the an-isotropic selection of the atoms the original velocity distribution is distorted in the transverse and conserved in the longitudinal direction. After passing through the 2D MOT beams the atoms are then transferred to the 3D MOT through the differential pumping stage placed at the bottom of the 2D MOT chamber.
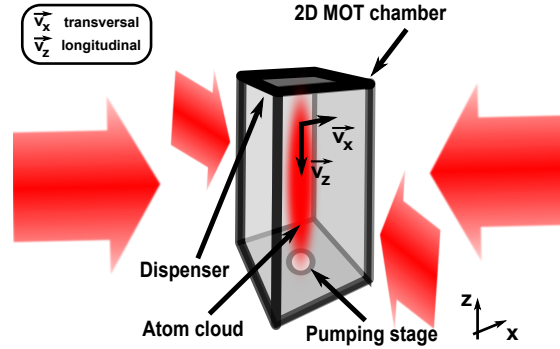
Figure 5.2: *Working principle of the 2D magneto-optical trap:* Four beams or two counter-propagating beams aligned in the horizontal plane with appropriate $\sigma^{\pm}$ light polarisation laser cool and compress the atoms in momentum and coordinate space forming a cold directed atomic beam with low divergence as a high atom flux source for the 3D MOT. The atoms are only laser cooled in the transverse direction and move freely in the longitudinal direction. The dispenser is placed at the top of the 2D MOT chamber and the differential pumping stage with a diameter of $D = 6mm$ and a length of $L = 86mm$ at the bottom.

Nevertheless the 2D MOT and 3D system together are a coupled structure and those atoms that will finally be captured in the 3D MOT need to comply three conditions [66, 67].

1. The longitudinal velocity component v_z needs to be smaller than the velocity capture range of the 3D MOT.

2. The initial transverse velocity component of the atom v_x needs to be smaller than the velocity capture range of the 2D MOT.

3. Given by the geometry of the differential pumping stage the transverse velocity component v_x right before entering the differential pumping stage needs to be low enough in comparison to the longitudinal velocity component v_z in order to pass through to the 3D MOT chamber without collision with the wall (see equation 5.1).

In order to get a rough estimate of the performance of the 2D and 3D MOT the capture velocities for the MOT will be determined in a very simple picture. Those considerations will be done for ^{87}Rb and ^{40}K. The parameters used for the following estimations can be found in table 3.1 and most of the equations in appendix C and [107].

In the 2D MOT chamber a dispenser (see figure 5.2) generates a background gas of a certain temperature and pressure. A background pressure of $P = 1 \cdot 10^{-8} mbar$ given by the highest ion pump reading observed leads to a mean free path of
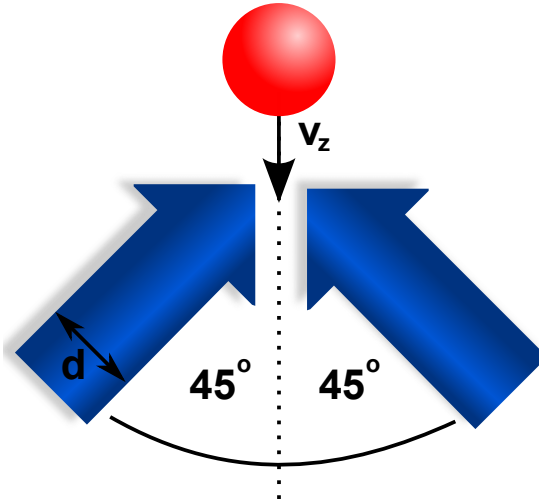
Figure 5.3: *Schematic of capture range of 3D MOT:* Atoms being transferred through the differential pumping stage with a longitudinal velocity of v_z need to be slowed down by the two beams opposing the atom's velocity at $45°$.

$l = 4.2km$ [2] for rubidium and a comparable order of magnitude for potassium (see equation C.2). The mean free path therefore is much larger than the largest dimension of the 2D vacuum chamber of $d = 120mm$. Hence, collisions between the atoms are suppressed and the pre-cooled atoms mainly interact only with the light field. The flow of undesired hot background atoms is purely determined by the vacuum design of the differential pumping stage realised by a graphite tube of $86mm$ length and $6mm$ inner diameter at the bottom of the chamber (see figure 5.2). This leads to a maximum opening angle of $\alpha = 4°$ (see equation 5.1). In comparison a trajectory starting from the top corner of the vacuum chamber and reaching the edge of the differential pumping stage at the bottom of the vacuum chamber has an angle of $\tan((55mm - 3mm)/120mm) = 23°$. This is much larger than the opening angle allowed by the differential pumping stage α.

Assuming that mainly only pre-cooled atoms will contribute to the atomic flux in the 3D MOT chamber ensuring a cold atom source we will determine the capture ranges of the 2D and 3D MOT by assuming a very simple picture neglecting any kind of random walk movement due to spontaneous emission. Furthermore it will be assumed that each scatter event slows the atom by the recoil velocity v_{rec} (see equation C.3) at the highest scattering rate possible of $R_{sc} = \Gamma/2$. This gives a

---

[2]As the scattering cross section a particle diameter of $470pm$ is assumed for rubidium [150]

rather optimistic result concerning the number of photons needed to decelerate and trap the atom but will demonstrate the order of magnitude of the velocity classes contributing to the cold ensembles.

The overall limiting parameter is the capture range of the 3D MOT and hence will be discussed first. The longitudinal velocity component of the atomic beam arriving in the 3D MOT is due to geometrical design of the differential pumping stage much larger than the transversal components. With the geometric constraints of the differential pumping stage of length l and radius r the maximum divergence of the atom beam in the 3D MOT and therefore the ratio of the transversal and longitudinal velocity components is given by

$$\tan \alpha = \frac{2r}{l} = 0.07 \geq \frac{v_{x,y}}{v_z} \tag{5.1}$$

Atoms that do not fulfil the condition given by equation 5.1 will collide with the differential pumping stage. Therefore the limiting velocity component for the capture range in the 3D MOT is the longitudinal component v_z. The transverse components v_x and v_y will be pre-cooled in the 2D MOT.

Like shown in figure 5.3 the v_z component is cooled by the crossed beams of diameter d at the 3D MOT chamber and is opposed to the bottom beams at 45° to v_z (blue arrows). In a very simple picture one can assume that the atom is trapped in the 3D magneto optical trap if it scatters N photons while travelling through the beam cross section area $\sqrt{2}d$ so that the accumulated recoil velocity v_{rec} of the scattered N photons equals the longitudinal velocity v_z. The photons are spontaneously and isotropically emitted yielding a vanishing momentum transfer. In this picture the maximum scattering rate along the beam of $R_{sc} = \Gamma/2$ is assumed for the time t the atom spends in the beam at a velocity v_z[3]. The atoms' deceleration is also neglected.

$$t = \frac{\sqrt{2}d}{v_z} \tag{5.2}$$

$$v_z = N \cdot v_{rec} \tag{5.3}$$

$$N = t \cdot \frac{R_{sc}}{\sqrt{2}} = t \cdot \frac{\Gamma}{\sqrt{8}} \tag{5.4}$$

With equation 5.3 to 5.4 and C.3, the maximum capture velocity yields

$$v_z = \sqrt{\frac{d}{2} \frac{\Gamma h}{m \lambda}} \tag{5.5}$$

Therefore, the maximum capture velocity is given with the atomic parameters from table 3.1 and the beam diameter $d = 19.82mm$ (see table 5.1) given to

---

[3]The resonance condition is for simplicity neglected

$v_z = 47m/s$ for ^{87}Rb and $v_z = 70m/s$ for ^{40}K. These values were used in figure 5.1 as capture range. This is the maximum value of the velocity component that can be captured in the 3D MOT. The total velocity that can be trapped in the 3D MOT is then given by $v = \sqrt{3}v_z$. If one velocity component exceeds the maximum value of the capture velocity the atom can not be trapped in the 3D MOT.

For the 2D MOT a similar approach can be taken to determine the capture velocity $v_{x,y}$ in the transversal direction. The longitudinal velocity component v_z is conserved in the 2D MOT cooling process. Therefore only atoms travelling with $v_z = 47m/s$ for ^{87}Rb respectively $v_z = 70m/s$ for ^{40}K or less are worth considering in the 2D MOT. The active cooling area is larger in the 2D MOT due to the fact that the limiting geometry is the width of the chamber. The beam diameter d from before is replaced by the width of the 2D MOT beam of $W = 20mm$. For the time the atoms passes through the 2D MOT beam again for simplicity a maximum scattering rate $R_{sc} = \Gamma/2$ is assumed. The transversal capture velocity is then similar to equation 5.5 determined by

$$v_{x,y} = \sqrt{\frac{W\,\Gamma\,h}{2\,m\,\lambda}} \tag{5.6}$$

A comparison with of equation 5.6 with 5.5 gives

$$\frac{v_{x,y}}{v_z} = \sqrt{\frac{W}{d}} \approx 1 \tag{5.7}$$

The results of this calculation for the two species ^{87}Rb and ^{40}K are summarized in table 5.1. The capture velocities for the 2D MOT match the 3D MOT estimations due to similar beam sizes. Hence, the numbers are only given for completeness and as an indication that the 2D MOT capture range is not limiting the capture process. The differences in the velocity values between the two species are due to different masses. Therefore the have different recoil velocities. High capture velocities like $v_z = 70m/s$ for ^{40}K are likely to be overestimated since the assumptions initially made break down at high capture ranges.

All considerations so far neglected the pushing beam for the sake of simplicity. The pushing beam is a collimated beam close to resonance that is superimposed in the longitudinal z-direction with the 2D MOT. The atomic motion in longitudinal direction is unaffected by the cooling properties of the 2D MOT and leaves the atoms able to drift up- or downwards. The pushing beam is implemented to guide as many atoms as possible along the line of zero magnetic field into the trapping region of the 3D MOT. The atoms added by the pushing beam to the atomic flux are accelerated so that the ratio of the longitudinal velocity and transversal velocity

		^{87}Rb	^{40}K
Temperature	$T[K]$	298	298
Velocity	$v_{rms}[\frac{m}{s}]$	292	431
Recoil velocity	$v_{rec}[\frac{m}{s}]$	0.59	1.3
Max. Scattering rate	$R_{sc}[10^7\frac{1}{s}]$	1.91	1.90
Maximum divergence	$\alpha[°]$	4	4
Max. 3D capture velocity	$v_z[\frac{m}{s}]$	47	70
Max. 2D capture velocity	$v_{x,y}[\frac{m}{s}]$	≈ 47	≈ 70194
Beam size 2D	$L \times W[mm \times mm]$	80×20	80×20
Beam diameter 3D	$d[mm]$	19.82	19.82

Table 5.1: 2D-3D MOT: Initial conditions, limitations and beam parameters. For high capture velocities the assumption made before become invalid and lead to overestimation.

matches the geometrical constraint given by the differential pumping stage (see equation 5.1). As mentioned before the divergence of the atomic beam needs to be less than $\alpha = 4°$. This way the atoms are transferred without collision with the wall of the differential pumping stage. But the atoms are only trapped in the 3D MOT if the longitudinal velocity matches the capture range of the 3D MOT.

The pushing beam detuning lies typically slightly to the red or blue close resonance. Like this it accelerates the lowest longitudinal velocity classes in the atomic beam in such a way that the atoms travel through the differential pumping stage rather than colliding at its walls.

In summary the combined 2D-3D MOT is expected to decouple lifetime and loading parameters in comparison to a normal 3D MOT setup so that a long lifetime can be combined with fast loading rate for large atom clouds. The most important parameter for the magneto-optical trap will be the total atom number while the following optical molasses concentrates on low temperatures accompanied with high phase space densities *PSD*. The reachable temperature ranges of the so-called polarisation cooling in the molasses phases will be reviewed in the next section.

5.1.2 Temperature in the optical molasses

The first three dimensional molasses was done by *S. Chu et al.* [151] and uses pure laser cooling processes without magnetic field in a six beam configuration. The temperatures reached are well below the initially thought Doppler limit of $T_D = 140\mu K$ (see equation C.4) for ^{87}Rb [152] due to polarisation gradient cooling mechanisms [153].

The Doppler limit theory uses a two-level atom that neglects polarisation dependent optical pumping processes and light shifts of internal energy levels. Furthermore the counter-propagating beams create a lattice of changing polarisation introducing a polarisation gradient field. The cooling mechanism is more efficient due to preferred optical pumping processes depending on the atom's position in the polarisation gradient field [153]. In general the polarisation gradient cooling mechanism shows a very low capture velocity meaning that the atoms need to be pre-cooled by the magneto-optical trap to experience this cooling mechanism. Moreover the optical molasses is not a trap since there is no restoring force towards the trap centre. Theoretical derivation suggest preferably a reduced intensity I and an increased detuning of the cooling light Δ_{RbCool} for low temperatures. However, the intensity reduction in comparison to the MOT parameters has no large beneficial consequence in this experiment as it will be shown later in figure 5.9 but the detuning Δ has a large influence.

In order to get an impression of the expected parameter range in the optical molasses the equations in [153, 154] are used to calculate the temperature in case of the classical optical molasses and the polarisation gradient cooling mechanism.

The **classical** molasses is thereby based on a two-level system in a low intensity field of non interacting counter-propagating electromagnetic waves. Stimulated emissions are neglected throughout the entire chapter. The detuning is $\Delta = \omega_0 - \omega_L$ where ω_0 and ω_L are the atomic transition frequency and the laser frequency. The minimum theoretical temperature for this model is the Doppler temperature where heating and cooling rate balance. But the Doppler temperature $T_D = \hbar\Gamma/2$ is only reached for a certain detuning Δ and intensity I. Due to the similar natural life time of the specific atomic level (see table 3.1) for ^{87}Rb and for ^{40}K the Doppler temperature is given by $T_D = 140\mu K$ for both species. The more general expression for the temperature for this model is given by equation 5.8. The expression also takes higher dimensions j and a moderate intensity I/I_s into account.

$$T_{classical} = \frac{\hbar\Gamma}{4k_B} \cdot \frac{1 + 2j\frac{I}{I_s} + (\frac{2\Delta}{\Gamma})^2}{\frac{2|\Delta|}{\Gamma}} \tag{5.8}$$

The recoil momentum should not shift the atom out of resonance in order to scatter enough photons for cooling. The ratio between Doppler shift due to the recoil energy $\vec{k}\vec{v}_{rec}$ and the natural line width Γ is 0.0012 and therefore many photons can be scattered for efficient cooling before the atom is shifted out of resonance.

The **polarisation gradient** cooling mechanism on the other hand predicts a smaller temperature for the same parameters. The polarisation of the counter-propagating light beams create a varying polarisation field. The kind of the polarisation field is determined by the polarisation used in the beams. Therefore the expression for the temperature in the sub-Doppler regime varies with the light polarisation. In this experiment the σ^+-σ^- configuration is used leading to a rotating linear polarisation in space. The temperature for this scenario is given by equation 5.9 [153, 154]. It is valid again for moderate intensity I/I_s but only for one dimension.

$$T_{polgrad} = \frac{\hbar\Gamma\frac{I}{Is} \cdot \left[\frac{29}{300} + \frac{254}{75} \cdot \frac{1}{1+(\frac{2\Delta}{\Gamma})^2}\right]}{k_B \frac{2|\Delta|}{\Gamma}} \tag{5.9}$$

The temperatures reached within a few ms in the magneto-optical trap are below the mK range, even when the sample is initially at room temperature. This is far beyond the limitations of cryogenic cooling methods. But still down to this temperature regime quantum statistical effects for bosons and fermions are negligible and in both cases ^{87}Rb and ^{40}K the clouds will be treated fully as classical thermal clouds.

5.2 Characterisation of individual MOTs for ^{87}Rb and ^{40}K

5.2.1 Individual 2D MOT results

The first 2D laser cooled potassium samples were realised in [155] for the bosonic species ^{39}K and in [156] for the fermionic ^{40}K that is also investigated in this experiment. The optical setup used here has been described in section 3.5 and only collimated MOT beams are used for the characterisation of the individual and the mixed MOT.

The highest loading rate of the 3D MOT in combination with the 2D MOT is determined out of the loading curve depicted in figure 5.6. For ^{87}Rb the loading rate yields $1.15 \cdot 10^9$ atoms/s on the left of figure 5.6. The detuning of the 2D MOT beams are $\Delta_{Cool\,Rb} = -2.5\Gamma$ and the repumping light on resonance. The pushing beam is red detuned by $\Delta_{Push\,Rb} = -0.33\Gamma$ with a power $P_{Push\,Rb}$ of several

		^{87}Rb	^{40}K
Loading rate $[\frac{1}{s}]$	$\frac{1}{\tau_{Load}}$	$1.15 \cdot 10^9$	$9.0 \cdot 10^5$
Cooling light intensity $[\frac{mW}{cm^2}]$	$I_{2D\,Cool}$	7.7	3.4
Cooling light detuning $[\Gamma]$	$\Delta_{2D\,Cool}$	-2.5	-1.5
Repumping light intensity $[\frac{mW}{cm^2}]$	$I_{2D\,Repump}$	1.7	1
Repumping light detuning $[\Gamma]$	$\Delta_{2D\,Repump}$	0	-1.5
Gradient $[\frac{G}{cm}]$	B'_{2D}	≈ 20	≈ 20
Pushing beam detuning $[\Gamma]$	Δ_{Push}	-0.33	+1.33
Pushing beam power $[\mu W]$	P_{Push}	$\gtrsim 120$	$\gtrsim 200$

Table 5.2: Optimised Parameters for ^{87}Rb and ^{40}K 2D MOT

hundred μW. The pushing beam enhances the atom cloud size by a factor of ten. For ^{40}K the highest loading rate out of the 2D MOT of $9 \cdot 10^5$ atoms/s has been realised at $\Delta_{Cool\,K} = -1.33\Gamma$ and $\Delta_{Rep\,K} = -1.5\Gamma$. The pushing beam is blue detuned by $\Delta_{Push\,K} = +1.33$. The results for both species are summarised in table 5.2.

The achieved loading rates are comparable to other experiments in rubidium [66,67, 104] and potassium [104]. The higher atom numbers in some other experiments are due to slightly more complicated setups e.g. by implementing an optical molasses in the third direction. However, for both species the 2D MOT offers a bright source of atoms with low divergence for the 3D MOT. The 3D MOT will be described in the next paragraph.

5.2.2 Individual 3D MOT results

In this section the performance of the individually loaded magneto-optical traps for ^{87}Rb and ^{40}K is reviewed. Preceding the individual characterisation and the results of the optimisation process the estimated phase space density in the background gas and 3D MOT is compared for both species.

As already mentioned in the beginning laser cooling and trapping are powerful tools increasing the atomic sample's phase space density *PSD*. There are mainly two parameters of the magneto-optical trap to be optimised: First a high atom number N and second a low temperature T that together with the density n determine the phase space density *PSD* (see equation 3.13).

The reachable atom number limit in the MOT is given by the MOT's capture and loss rate and the atom flux from the 2D MOT. The highest reachable atom number in steady state is reached where both capture and loss rate balance [145, 146]. For the capture rate the intensity, detuning and beam size are determining parameters. The cross section for background collisions and the trap depth play a dominant role for the loss rate in lower quality UHV conditions. In better vacuum conditions light assisted Rb-Rb collision leading to losses take place in larger ensembles [157–160]. Typically atom clouds of the size of $N = 10^9$-10^{10} for ^{87}Rb and $N = 10^6$-10^7 for ^{40}K are realised but this depends critically on the experimental setup.

The fundamental temperature limit of laser cooling processes lies in the spontaneous emission. The spontaneous emission is needed to carry the entropy change away from the isolated system being a crucial ingredient for cooling. Nevertheless, the temperatures reached here are orders of magnitudes larger.

Assuming an ideal gas the density of the thermal background gas at the given temperature of $T_{BG} = 298K$ for ^{87}Rb (^{40}K) at the pressure $P \approx 1 \cdot 10^{-8} mbar$ is the density $n = P/(k_B T) = 2.4 \cdot 10^8 cm^{-3}$. The phase space density (see equation 3.13) yields therefore $PSD = 3 \cdot 10^{-19}$ ($1 \cdot 10^{-18}$) as a starting point.

For typical values in a magneto-optical trap with the Doppler temperature T_D and a typical density of $n = 10^{10} cm^{-3}$ the phase space density in the laser cooled and trapped cloud can reach $PSD = 4 \cdot 10^{-8}$ ($4 \cdot 10^{-8}$). The gain of that many orders of magnitude in phase space density shows how powerful the tool of magneto-optical trapping is [109].

Nevertheless there are several cooling steps following the magneto-optical trap, hence it is more beneficial preferable to gather as many atoms as possible rather than optimising for temperature and particle number in one step. Consequentially the performance of the magneto-optical traps was optimised for highest atom number only.

The restoring force of the 3D MOT as mentioned before needs to counteract the velocity of the arriving atoms. The restoring force itself depends on the magnetic gradient, detuning, beam size and intensity. The beam size is fixed by the experimental setup and the intensity is controlled by an AOM double path. Very easily controllable parameters are the detuning and the gradient. For optimal loading performance of the 3D MOT the detuning of both 2D and 3D MOT need to be adapted.

Within the following discussion of the results the peculiarities of potassium will be emphasized which arise from a small and inverted hyperfine splitting of the relevant levels (see figure A.1 and table A.1).

The first magneto-optical traps for potassium were realised with the bosonic isotopes ^{39}K and ^{41}K [161]. Initially observed temperature limits higher than the

Doppler limit have been successfully circumvented [162–164].

The first 3D MOT for ^{40}K [165] did not experience these cooling problems [166]. This is due to the fact that the hyperfine splitting of the fermionic isotope is larger but more importantly inverted. Therefore, the closely spaced hyperfine levels are further detuned and do not interfere with the optical pumping. Large detunings can be used without additional heat generation.

In the following the results of the 3D MOT characterisation are presented. The setup and the experiment sequence is the same as for the 2D MOT measurements described in the previous section. The atoms trapped and pre-cooled in the 2D MOT get through the differential pumping stage and are re-trapped in the 3D MOT beams. The trapping parameters defining the restoring force of the trap and the kinetic energy of the atoms are varied individually and the number of atoms is recorded. For the optimisation process the atom numbers were determined with the aid of fluorescence measurements with the CCD camera. The measurements are depicted in figure 5.4 to 5.6 each displaying two curves. The difference between those data sets is the intensity assumed to determine the photon scattering rate in the data evaluation process (see section 3.6.1). Hence the triangles (red) show the lower bound and the circles (blue) show the higher bound for the atom number. The lines in the graphs are only to guide the eye.

Unless stated differently the trapping sequence described in the following is used to capture the atoms. For the ^{87}Rb MOT the atoms are loaded for $\tau = 4s$ into the 3D magneto-optical trap. The cooling light intensity is maximised and red detuned to $\Delta_{cool\ Rb} = -3\Gamma$ with Γ being the natural line width. The repumping light intensity is maximised and on resonance of the repumping transition. The pushing beam is slightly red detuned to $\Delta_{push\ Rb} = -0.33\Gamma$. The MOT coils are operated at $B' = 14G/cm$. The exposure time of the camera is set to $t_{exp} = 100\mu s$. On the other hand for the ^{40}K MOT the atoms are loaded for $\tau = 15s$ into the 3D magneto-optical trap. The cooling light intensity is maximised and red detuned to $\Delta_{cool\ K} = -1.33\Gamma$. The repumping light intensity is maximised and detuned to $\Delta_{repump\ K} = -1.5\Gamma$. The pushing beam is blue detuned to $\Delta_{push\ K} = +1.33\Gamma$. The MOT coils are operated at $B' = 4.3G/cm$ generating a relatively low gradient for better stability of the magneto-optical trap. The exposure time of the camera is set to $t_{exp} = 1ms$.

This is the initial parameter range; parameters are changed during the characterisation process. The parameters are summarised in table 5.3. Changes to the parameters will be stated through out the discussion. For both measurements the light of the other species is not present.

The measurements show atomic samples in the range of $N_{Rb} \approx 1 \cdot 10^9$ atoms for ^{87}Rb and $N_K \approx 1 \cdot 10^6$ atoms for ^{40}K but it strongly depends on the loading time of the 3D MOT.

Atom number vs magnetic field gradient   The gradient of the magnetic field is varied by changing the current of the MOT coils. At the top of figure 5.4 the behaviour of the atom number in dependence of the magnetic field gradient for ^{87}Rb (left) and ^{40}K (right) is shown. The findings are quite different from each other. While for the ^{87}Rb MOT the number of atoms increases first linearly with higher gradient up to $B' = 5G/cm$ it starts saturating for higher gradients and only grows very slowly. The MOT is saturated at $B' \approx 15G/cm$ and a further increase of the magnetic field has no beneficial influence. The gradient for the ^{87}Rb MOT will be kept unchanged at $B' = 14G/cm$ for following measurements.
For the fermionic ^{40}K MOT the situation lies differently. With increasing gradient the number of atoms decreases linearly till the loss mechanisms are too high. The loss is approximately $4.5 \cdot 10^4$ atoms per $1\ G/cm$ gradient change suggesting a density loss mechanism. The highest atom number is reached with a gradient of $B' = 2.5G/cm$ but the magneto-optical trap becomes unstable. For better stability the MOT is operated at $B' = 4.3G/cm$.

Detuning of cooling light and pushing beam   The detuning of the cooling light is changed with the VCO frequency in the offset lock. This means that in addition to the detuning of the cooling light in the 2D and 3D MOT also the frequency of the pushing beam is changed by the same amount. This is due to the fact that one laser diode delivers both cooling, pushing and detection light (see section 3). The change in the pushing beam frequency is compensated for by changing the AOM frequency.
The ^{87}Rb MOT shows a maximum atom number at an optimal setting for the cooling light detuning of $\Delta_{cool\,Rb} = -3\Gamma$. This is consistent with a Doppler shift of $14m/s$. The optimum pushing beam detuning is $\Delta_{push\,Rb} = -0.33\Gamma$.
For ^{40}K the highest atom number is reached at $\Delta_{cool\,K} = -1.2\Gamma$ which is consistent with a Doppler shift of $6m/s$. This is significantly smaller in comparison to the case of ^{87}Rb and might be due to stronger optical pumping to other hyperfine levels that are closer spaced than in rubidium. The optimum pushing beam detuning is $\Delta_{push\,Rb} = +1.33\Gamma$.

Atom number vs power of push beam   The dependency of the atom number on the pushing beam power is depicted at the bottom of figure 5.4. Other before optimised parameters used are presented in table 5.3. For ^{87}Rb shown on the left the atom number increases rapidly with increasing pushing beam power.
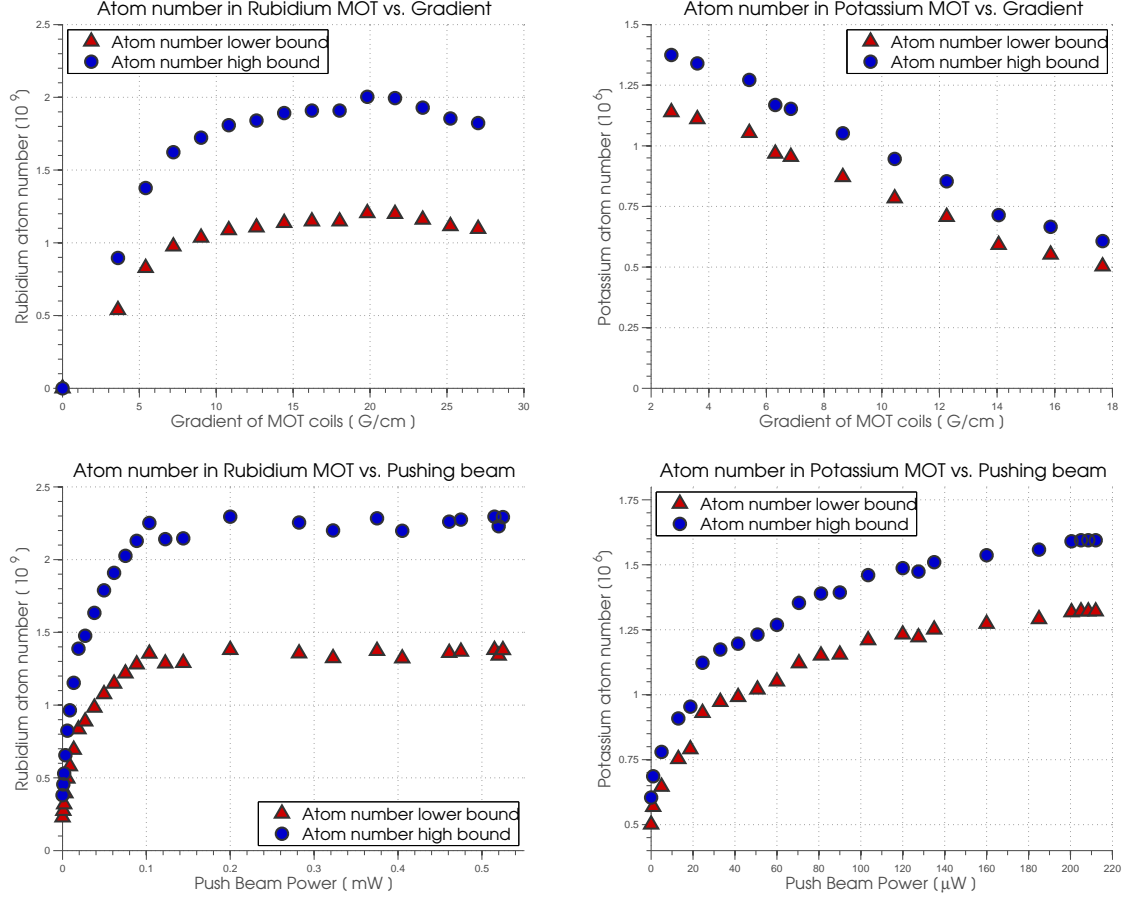
Figure 5.4: *Number of atoms in the 3D magneto-optical trap for* ^{87}Rb *and* ^{40}K: From top to bottom is the dependency of the atom number of magnetic field Gradient B' and the power of the pushing beam P_{push} for ^{87}Rb and ^{40}K depicted. The cooling light and pushing beam detuning have an optimal setting at $\Delta_{cool\,Rb} = -3\Gamma$ and $\Delta_{push\,Rb} = -0.33\Gamma$ for ^{87}Rb respectively $\Delta_{cool\,K} = -1.2\Gamma$ and $\Delta_{push\,K} = +1.33\Gamma$ for ^{40}K. Thereby is the left column showing the results for ^{87}Rb and the right column for ^{40}K.
Magnetic field gradient: For ^{87}Rb the number of atoms increases with higher gradient till $B' = 15G/cm$. For ^{40}K MOT number of atoms decreases linearly with increasing gradient B' as approximately $4.5 \cdot 10^4$ atoms per $1G/cm$.
Pushing beam power: For ^{87}Rb the atom number increases with increasing pushing beam power. Already at very low power of approximately 20-30μW the atom number starts to saturate. At $120\mu W$ the cloud is saturated. ^{40}K shows an increase in atom number for increasing pushing beam over the observed range. A detailed description is found in the text.
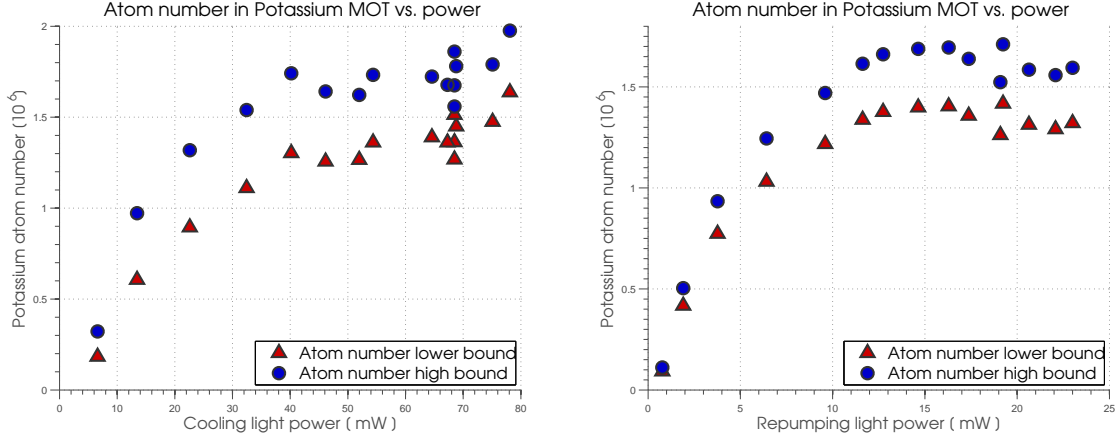
Figure 5.5: *Number of atoms in the 3D MOT for ^{40}K in dependence of the power of cooling and repumping light:* On the left the results for the cooling light (with maximum repumping power) and the right for the repumping light (with maximum cooling power) are depicted. Other parameters can be found in table 5.3. Both graphs show a generally increase in atom number with increasing power. While for the repumping light the atom number starts saturating at $P_{rep} = 16.7mW$ a saturation with increasing cooling light can not be observed. The power translates into intensity as $P = 10mW \rightarrow I = 0.5mW/cm^2$. A detailed description can be found in the text.

Already at very low power of approximately 20-30μW the atom number starts already to saturate. At 120μW the cloud is saturated and a more powerful pushing beam does not result in a higher atom number. The pushing beam is red detuned by $\Delta_{push\,Rb} = -0.33\Gamma$ which is consistent with a Doppler shift of $1.4m/s$. This means the pushing beam interacts with and accelerates mostly the atoms close to being at rest or moving slightly towards the 2D MOT. In the 3D MOT for ^{87}Rb the pushing beam enhances the atom number by a factor of ten.

On the other hand for ^{40}K the pushing beam has only a factor of three enhancement and the cloud saturates at higher power. The smaller hyperfine splitting or density related losses also observed at higher gradients might play a role there. For ^{40}K the graph is shown on the bottom right of figure 5.4 using a different scale. Also here the atom number increases rapidly with increasing pushing beam power. The saturation effect like in ^{87}Rb is not observed here but the power range investigated is a factor of 2.5 smaller and might appear at higher power. The highest pushing beam power is used further on. The pushing beam is slightly blue detuned by $\Delta_{push\,K} = +1.33\Gamma$ which is consistent with a Doppler shift of $6m/s$. The pushing beam interacts with atoms mainly travelling away from the 3D MOT and accelerates the slowest atoms towards the 3D MOT.

For the further investigation the maximum power for the ^{40}K pushing beam is used and for ^{87}Rb the pushing beam power is picked to be close to the saturation point.

Atom number vs power of cooling and repumping light in ^{40}K   In figure 5.5 the influence of the intensity on the atom number for both cooling (left) and repumping light (right) is displayed. The power and hence the intensity is varied by changing the current in the appropriate tapered amplifier (see section 3). In both cases the relevant cooling or repumping power is kept at the maximum value while the other parameter is varied. This does not affect the pushing beam power. Other parameter settings can be found in table 5.3.

The maximum power used for cooling respectively repumping light is $P_{Cool\,K} = 78mW$ and $P_{Repump\,K} = 24mW$. This relates to a maximum intensity of $I_{Cool\,K} \approx 4.2mW/cm^2$ and $I_{Repump\,K} \approx 1.2mW/cm^2$. The beam reaches the saturation intensity at $31mW$ for the cooling light and half the saturation intensity[4] of the atomic transition at $16.7mW$ for the repumping light. In both cases the atom number is initially rising with increasing power.

In case for the repumping light (right) the atom number reaches its maximum at 15 - $17mW$ after a quick rise of $2.5 \cdot 10^5$ atoms per $1mW$ at low power that slows down to approximately $4.6 \cdot 10^4$ atoms per $1mW$ before saturating. If the power is increased even further than $17mW$ the atom number decays slightly. Due to the small hyperfine structure in potassium the optical pumping and depletion of desirable states is quite high and therefore the repumping transition acts more like a second cooling transition. The fact that the MOT is operated with a repumping detuning of $\Delta_{repump\,K} = -1.5\Gamma$ reinforces this impression. The sensitivity of the atom number on the repumping power is also quite high.

On the other hand for the cooling light (left) the atom number steadily rises but seems to show a smaller growth rate over the entire investigated power range than the repumping power. A higher increase in atom number can be seen for a lower power range up to $30mW$ of $5 \cdot 10^4$ atoms per $1mW$ power increase. In the middle range the growth rate decreases to $1 \cdot 10^4$ atoms per $1mW$ power increase. Due to the quality of the data the slowing down and increasing growth rate could be just an artefact of the varying data points. However a saturation can not be observed which is in disagreement with some other experiments [26] but might be due to different magnetic field gradients affecting the density.

Loading curves of ^{87}Rb and ^{40}K   After finalising the optimisation of the two magneto-optical traps individually the loading curves for both species are shown in figure 5.6. The parameters for the optimal operation of the MOT are given in table 5.3. As before ^{87}Rb is depicted on the left and ^{40}K on the right. Both curves show the expected exponential growth. The lines are an exponential fit to the data points. The largest clouds reached are $N_{Rb} = 1.3 \cdot 10^9$ (lower bound) for a loading time of $4s$ and $N_K = 1.4 \cdot 10^6$ (lower bound) after $6s$. The $1/e$ time is slightly
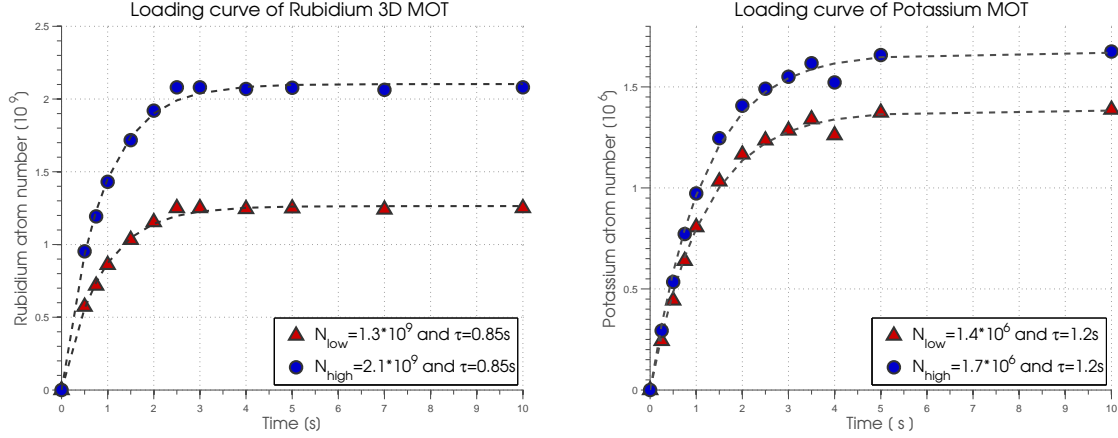
---

[4]$I_{sat} = 1.67mW/cm^2$

Figure 5.6: *Loading curves of the 3D magneto-optical traps for ^{87}Rb and ^{40}K: For ^{87}Rb the result is depicted on the left and ^{40}K on the right. Both curves show the expected exponential growth. The lines are an exponential fit to the data points. The largest atom numbers achieved are $N_{Rb} = 1.3 \cdot 10^9$ (lower bound) for a loading time of $4s$ and $N_K = 1.4 \cdot 10^6$ (lower bound) after $6s$. The 1/e time is slightly different for both species due to a different loading rate for each species of $1.15 \cdot 10^9 s^{-1}$ for ^{87}Rb and $9 \cdot 10^5 s^{-1}$ for ^{40}K*

different for both species due to a different loading rate for each species. From section 5.2.1 the loading rates are $1.15 \cdot 10^9 s^{-1}$ for ^{87}Rb and $9 \cdot 10^5 s^{-1}$ for ^{40}K.

Overall the bosonic MOT with ^{87}Rb does not show any unexpected behaviour. For the red detuned pushing beam the resonance of the atomic transition lies in reach of the uncertainties of the laser locking scheme of ± 1-$2MHz$. However, the atom number is comparable to other experiments [23, 26, 167].

For the fermionic MOT with ^{40}K the atomic cloud is an order of magnitude smaller than in other experiments for example [23, 26, 166] but these experiments have occasionally a dark spot MOT [168] and other extra experimental efforts implemented that were for simplicity so far avoided here.

Furthermore a density induced loss has been observed like in other experiments too. But the surprising result for the ^{40}K MOT is that the expected loss due to light assisted collisions [23, 104] in a similar intensity range from $I_{Cool\ K} = 0 \rightarrow 4.2mW/cm^2$ has not been observed. In other experiments even higher intensities seem to be beneficial [165]. As far as this experiment is concerned the ^{40}K MOT does not show any peculiar behaviour in comparison to ^{87}Rb if it comes to the beam intensity. The atom number is generally increasing with intensity for both repumping and cooling light.

After optimising and characterising the magneto-optical trap individually the clouds will now be loaded simultaneously in order to realise Bose-Fermi mixtures. The next section will discuss the results.

		^{87}Rb	^{40}K
Atom Number	N	$1.3 \cdot 10^9$	$1.4 \cdot 10^6$
Loading rate $[\frac{1}{s}]$	$1/\tau_{Load}$	$1.15 \cdot 10^9$	$9.0 \cdot 10^5$
Loading time $[s]$	t	4	6
Cooling light intensity $[\frac{mW}{cm^2}]$	$I_{3D\,Cool}$	2.5	4.2
Cooling light detuning $[\Gamma]$	$\Delta_{3D\,Cool}$	-3	-1.33
Repumping light intensity $[\frac{mW}{cm^2}]$	$I_{3D\,Repump}$	1.0	1.2
Repumping light detuning $[\Gamma]$	$\Delta_{3D\,Repump}$	0	-1.5
Gradient $[\frac{G}{cm}]$	B'_{3D}	14	4.3
Pushing beam detuning $[\Gamma]$	Δ_{Push}	-0.33	+1.33
Pushing beam power $[\mu W]$	P_{Push}	$\gtrsim 120$	$\gtrsim 200$

Table 5.3: Optimised Parameters for ^{87}Rb and ^{40}K 3D MOT

5.3 Magneto-optical trapping of ^{87}Rb -^{40}K mixtures

The procedure for creating Bose-Fermi mixtures in magneto-optical traps is similar to individually loading the magneto-optical traps. As it will be seen the potassium and rubidium atoms are both disturbed by the presence of the other species. That is in discrepancy with other experiments [104]. Here the potassium is loaded fully for $5s$. The cloud contains $N_K = 2.6 \cdot 10^6$ atoms. As soon as the ^{40}K cloud has reached its full size the ^{87}Rb MOT loading is started. The number of atoms in each cloud are detected individually at certain times after starting to load the ^{87}Rb MOT.

The measurement is depicted in figure 5.7. The potassium cloud starts at $N_K = 2.6 \cdot 10^6$ atoms and decays down to $N_K = 1.5 \cdot 10^6$ atoms. This is a decrease of 40%. The decay stops as soon as the ^{87}Rb MOT is fully loaded. The ^{87}Rb cloud shows a loading in the beginning of $\approx 6.7 \cdot 10^8$ atoms per second and grows to its full size of $N_{Rb} = 6.75 \cdot 10^8$. The ^{87}Rb cloud is therefore only half as large and the loading rate decreased also by a factor of two in comparison to the individually loaded MOT (see table 5.3). The disturbing effect of the MOT onto each other is significant in this setup.

The strong influence on the ^{87}Rb MOT loading is not in consistency with some
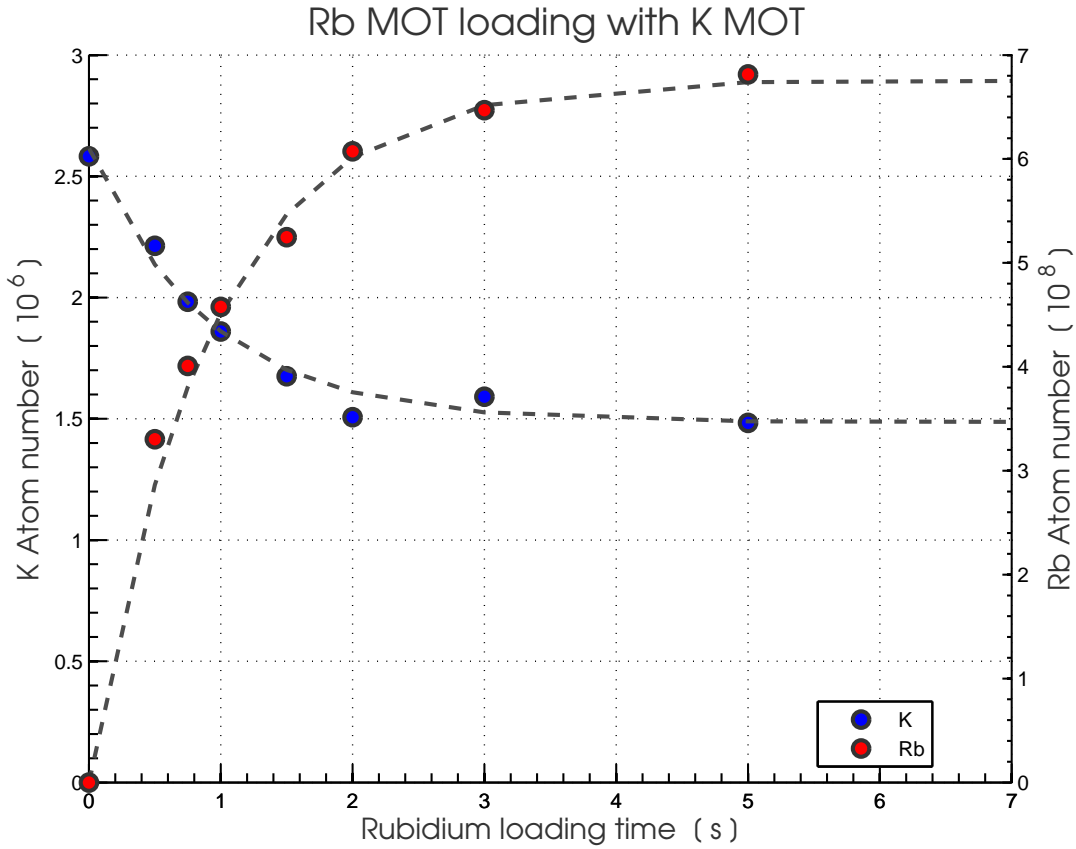
Figure 5.7: *Magneto-optical trap of a Bose-Fermi mixture with* ^{87}Rb *and* ^{40}K: *The potassium is fully loaded in 5s. The* ^{87}Rb *MOT loading is started once the* ^{40}K *MOT is fully loaded. The potassium cloud starts at* $N_K = 2.6 \cdot 10^6$ *atoms and decays by 40% down to* $N_K = 1.5 \cdot 10^6$ *atoms until the* ^{87}Rb *MOT is fully loaded. The* ^{87}Rb *cloud shows a full size of* $N_{Rb} = 6.75 \cdot 10^8$.

other mixture experiments [23, 104] where ^{40}K had basically no influence on the number of ^{87}Rb atoms in the MOT. The absolute loss of ^{40}K increases with an increasing ^{87}Rb density due to assumed mediated collisions. The ^{40}K loss rate in dependence of the ^{87}Rb atom number is $K/Rb = 1.63 \cdot 10^{-3}$. For each 1000 ^{87}Rb atoms is approximately 1.6 ^{40}K atoms lost. This behaviour has been observed in other experiments.

The loss mechanism motivated the twofold 2D-3D MOT vacuum setup with magnetic transport in order to generate samples with higher atom numbers. The twofold 2D-3D MOT system avoids the loss mechanism due to interspecies interaction during the magneto-optical trapping phase. Another approach with the help of the realised magnetic transport is the sequentially loading of the different species.

All the experiments up to here were conducted in the glued vacuum chamber at a

point of lower vacuum quality than desirable. For the next section the collimated beams were exchanged to divergent beams in order to compare the two different beam configurations. This is necessary due to even higher spatial restrictions with the new indium sealed vacuum chamber which will be used for all experiments in section 6 and 7. For the following quick discussion of the optical molasses the divergent beam configuration in the new vacuum chamber was used.

5.4 Magneto-optical trap with divergent beams for ^{87}Rb

Normally collimated beams are used in experiments with magneto-optical traps. There are a few unusual beam configurations around like magneto-optical traps using four beams [169] and one beam pyramid funnels [170, 171] but usually those experiments work with collimated beams.

Due to the exchange of the vacuum chamber in this experimental setup the beam setup used for magneto-optical trapping has been modified (see section 3.5). The magneto-optical trap is therefore operated with four divergent and two collimated beams shown in figure 3.22.

The effect on the magneto-optical trap size with the collimated and divergent beams is investigated. First the direct comparison of the loading time with collimated (red circles) and divergent beams (blue squares) is presented in figure 5.8. The loading time of the 3D MOT remains unchanged with divergent beams in comparison to collimated beams. Both data sets have been recorded in fluorescence detection with a CCD camera.

The sequence used is described in table 5.2 and 5.3. For the divergent beams the fibre end is situated $10cm$ away from the 3D MOT centre. This is the same distance like the focal length of the collimation lens resulting in a comparable intensity in the centre of the beam at the centre of the MOT.

The measurements in the next part 6 and 7 are exclusively conducted with divergent beams in the magneto-optical trap. But due to the size of the CF16 flanges for the small windows the fibre end is further away from the MOT centre which leads to a decrease in intensity to 89% of the collimated beam.
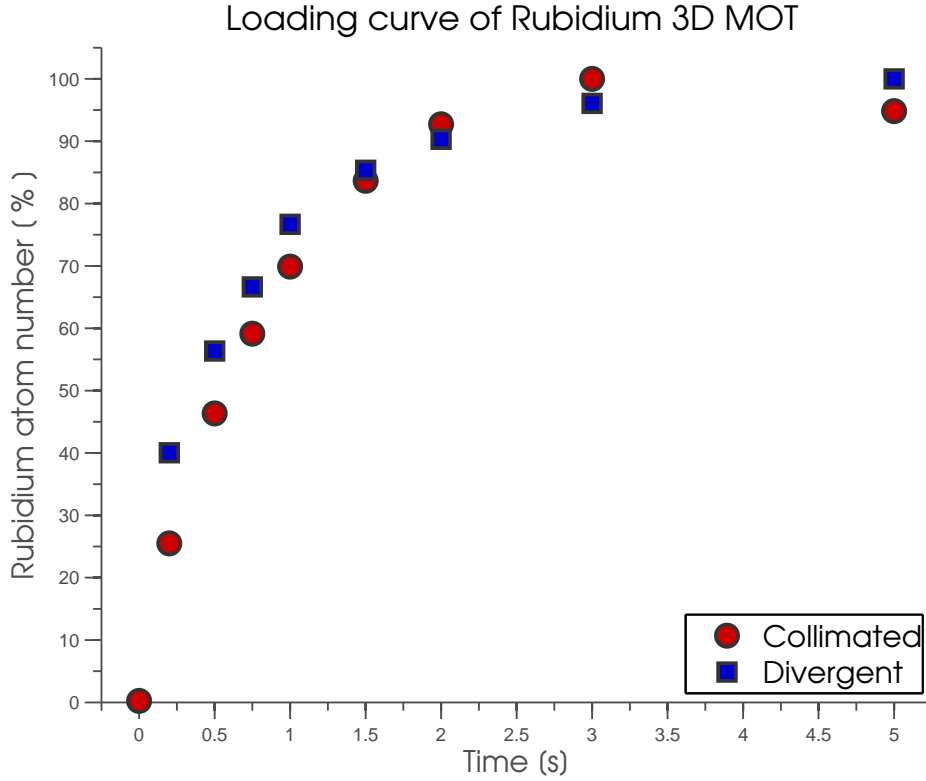
Figure 5.8: *MOT loading with collimated and divergent beams:* The two different beam configurations with six collimated or with four divergent and two collimated beams are shown in figure 3.22. The parameter settings can be found in table 5.2 and 5.3. For the divergent beams the fibre end is situated $10cm$ away from the 3D MOT centre equal to the focal length of the collimation lens resulting in a comparable intensity in the centre of the beam at the centre of the MOT in both cases.

5.5 Further cooling in the optical molasses for ^{87}Rb

In this section the optical molasses for ^{87}Rb only will be discussed. So far the atom cloud of $N_{Rb} = 1.3 \cdot 10^9$ atoms is trapped in the magneto-optical trap and cooled down to several hundred μK. In order to reach even lower temperatures and higher phase space densities *PSD* the atoms are confined for a short time in an optical molasses.

The parameters of $I = 6 \times 2.2 mW/cm^2$ for the intensity[5] and $\Delta_{cool} = -10\Gamma$ give the following expected temperatures. For the classical optical molasses a temperature of $T_{classical} = 1.5mK$ (see equation 5.8) is expected. The temperature for the polarisation gradient cooling is $T_{pol\,grad} = 4.6\mu K$ (see equation 5.9) but this is one

---

[5]Six divergent beams at 89% of the collimated power.

dimensional and is expected to be higher for higher dimensions. The difference between the two temperatures is three orders of magnitudes.

A fundamental limitation for the polarisation gradient cooling is the recoil momentum. As long as the atom scatters photons the temperature can not be lower than the recoil temperature of $0.36\mu K$. Those theoretical temperatures will be compared later to the temperature measured in the optical molasses and it will be seen that the measured temperature is much higher then $T_{pol\,grad}$ (see figure 5.10).

The optical molasses is realised by switching off the magnetic field and laser beams and then switch the laser light back on in order to prevent undesired forces on the atoms during the switching of the magnetic field.

Eventual residual magnetic stray fields and unbalanced laser intensities of counter-propagating laser beams can change the resonance condition for the atom. This can influence the performance of the optical molasses leading to higher temperature or atom loss.

Three sets of compensation coils situated on all three axes are compensating the stray magnetic fields and eventual unbalanced laser intensities by generating homogeneous offset fields in the centre of the cloud.

Furthermore a fourth set of small coils in the vertical z-direction is used to apply a homogeneous offset field before the magnetic trap is ramped up. More details will be discussed in section 6. All four coil sets have ten windings and are situated at the MOT coils in x-, y- and two in the z-direction.

The measurements for the optical molasses are exclusively done with divergent beams. The detection method is absorption imaging after a certain *time-of-flight* time t_{TOF} of free expansion. The atomic density n is determined by a 2-dimensional Gaussian fit. For optimising the optical molasses the dependency on the cooling light intensity and duration is investigated. Furthermore the temperature and phase space density is studied in dependence of the detuning Δ_{Cool}.

In favour of reaching the lowest temperature with the lowest atom number loss during the molasses phase it is important to use a short time for the optical molasses. The figure 5.9 on the left shows the size of the Gaussian distributed atom cloud σ in dependence of the duration of the optical molasses after a certain *time-of-flight* time. The size is a coarse measure of the temperature of the cloud[6]. The temperature scales with $\propto (\sigma^2 - \sigma_0^2)$, where σ_0 is the initial size of the cloud at $t_{TOF} = 0$. The intensity is $I_{Rb\,cool} = 1.75mW/cm^2$ at a detuning of $\Delta_{Cool\,Rb} = -10\Gamma$. The TOF-time for both measurements in figure 5.9 is $t_{TOF} = 20ms$.

A rapid reduction in size of the atom cloud with increasing time is observed. The decrease in size slows down at $t_{Mol} = 7.5ms$ and further reduction in size and

---

[6]Neglecting the initial size of the cloud
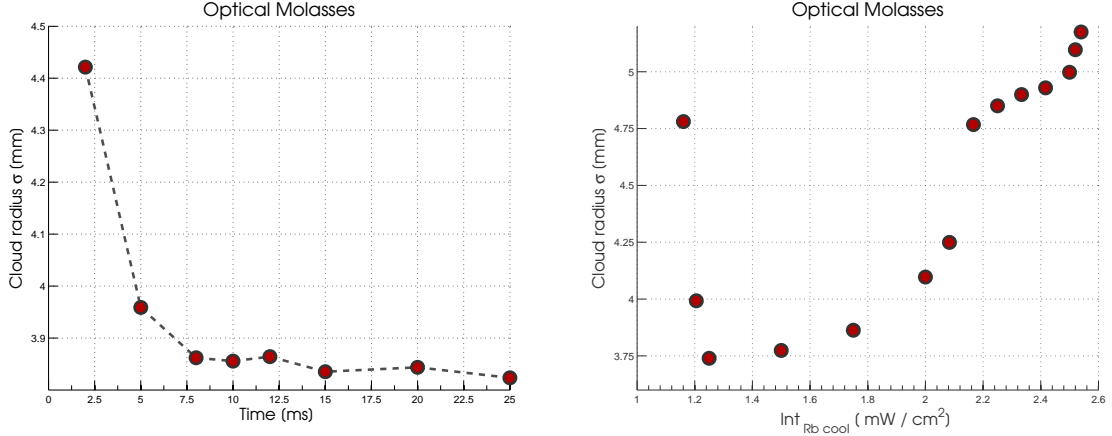
Figure 5.9: *Optimisation of molasses time and intensity for ^{87}Rb:* On the left the size of the atom cloud σ in dependence of the molasses duration. The intensity is $I_{Rb\,cool} = 1.75mW/cm^2$ at a detuning of $\Delta_{Cool\,Rb} = -10\Gamma$. A rapid reduction in size with increasing time is observed but slows down at $t_{Mol} = 7.5ms$. The size was reduced to 87% between $t_{Mol} = 2ms$ and $t_{Mol} = 12ms$. The cooling light intensity dependence shows a steadily increasing atom number with higher intensity. The size σ shows a minimum around $I_{Cool\,Rb} = 1.25mW/cm^2$. The detuning is $\Delta_{Cool\,Rb} = -10\Gamma$ at a $t_{Mol} = 12ms$. The measurements were performed with $t_{TOF} = 20ms$.

therefore temperature reduction is unnoticeable without taking the initial size of the cloud into account. The size was reduced to 87% between $t_{Mol} = 2ms$ and $t_{Mol} = 12ms$. But it must be stressed this is not related to the reduction from the size of the magneto-optical trap or its temperature. In the following a optical molasses phase of $t_{Mol} = 12ms$ will be used giving better results in the later stage of the experiment. This is most likely due to the fact that neglecting the initial size falsifies the results slightly.

The cooling light intensity dependence within the optical molasses phase on the size is depicted on the right in figure 5.9. The detuning is set to $\Delta_{Cool\,Rb} = -10\Gamma$ for a molasses phase duration of $t_{Mol} = 12ms$. The size σ shows a minimum around $I_{Cool\,Rb} = 1.25mW/cm^2$ of $\sigma = 3.6mm$. With the intensity decreasing from the maximum intensity used in the magneto-optical trap phase to the minimum to still observe a reasonable result, the size σ first decreases steadily from its maximum of $\sigma = 5.2mm$ down to its minimum of $\sigma = 3.6mm$ before it increases rapidly again. In between $I_{Cool\,Rb} = 1.25mW/cm^2$ and $I_{Cool\,Rb} = 2.0mW/cm^2$ the size reduction slows down. The relative decrease from its maximum to minimum is 40%. Although the cloud has a smaller size and therefore temperature at $I_{Cool\,Rb} = 1.25mW/cm^2$ we use most often higher intensities up to $I_{Cool\,Rb} = 2.0mW/cm^2$ for the molasses phase since a higher robustness and stability over the entire experimental sequence has been achieved.

121
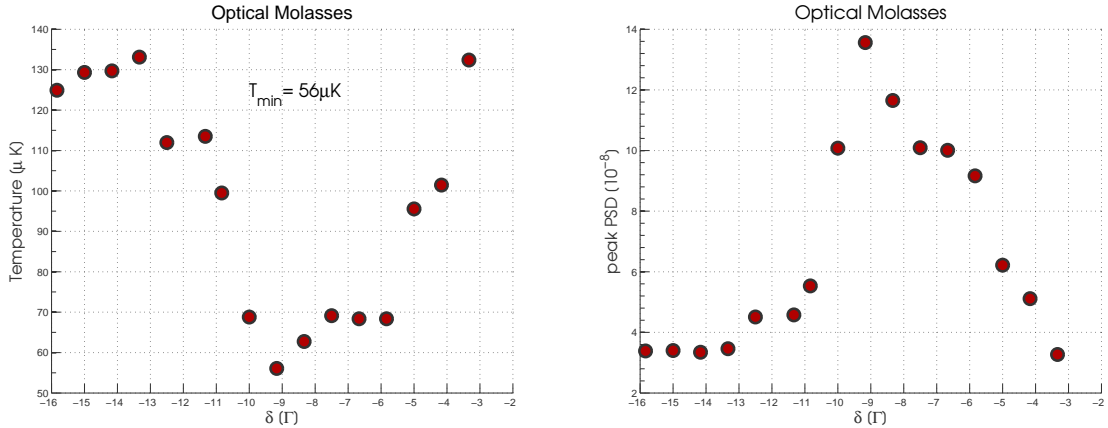
Figure 5.10: *Temperature and phase space density versus cooling light detuning in the optical molasses:* On the left is the temperature T and on the right is the peak value of the phase space density PSD against the cooling light detuning Δ_{Cool} displayed. Both plots show a distinct minima for the temperature respectively maxima for the phase space density. The temperature minimum is $T_{Mol\,min} = 56\mu K$ corresponding to a phase space density of $PSD = 13.6 \cdot 10^{-8}$. Its position at $\Delta_{Cool\,Rb} = -9.2\Gamma$. The temperature varies over a detuning range of $\pm 6\Gamma$ by a factor of ≈ 2.3 up to $T_{Mol} = 130\mu K$. The phase space density varies over the same detuning range by a factor of ≈ 4 down to $PSD = 3.4 \cdot 10^{-8}$. The TOF-time for both measurements is $t_{TOF} = 15ms$.

With the molasses time of $t_{Mol} = 12ms$ and an intensity of $I_{Cool\,Rb} = 1.75mW/cm^2$ per beam the temperature and phase space density against the cooling light detuning is measured.

The results are depicted in figure 5.10. On the left the temperature T and on the right the phase space density PSD against the detuning $\Delta_{Cool\,Rb}$ is displayed. The phase space density is given by equation 3.13 where the peak density on the centre of the Gaussian cloud has been used[7] (see section 3.6.4). The temperature and initial size is determined out of several datasets at different TOF-times and is given by equation 3.11. In both cases the $t_{TOF} = 15ms$ dataset is depicted. The detuning is controlled with the VCO frequency in the offset lock scheme.

Both plots show a distinct minima for the temperature respectively maxima for the phase space density. Its position at $\Delta_{Cool\,Rb} = -9.2\Gamma$ is related to each other since the phase space density is dependent on the temperature by $PSD \propto \sqrt{T}^3$ (see equation 3.13). The temperature minimum is $T_{Mol\,min} = 56\mu K$ corresponding to a maximum phase space density of $PSD = 13.6 \cdot 10^{-8}$. The temperature varies over a detuning range of $\pm 6\Gamma$ by a factor of approximately 2.3 up to $T_{Mol} = 130\mu K$.

The temperature of $T_{Mol} = 56\mu K$ is by a factor of > 25 smaller than the expected value for the classical molasses theory mentioned above. But it is also much larger than the temperature expected for the polarisation gradient cooling

---

[7]Peak density $n_0 = N/(\sqrt{2\pi}^3 \sigma^3)$ where N is the atom number and σ the initial cloud size at $t_{TOF} = 0$

of $T_{pol\,grad} = 4.6\mu K$. The deviation yields a factor of > 12. The deviation of the classical molasses theory was expected since the theory neglects the internal structure of the atom, multiple photon scattering and the interference effects of the laser beams. For the polarisation gradient model it is needed to mention that the model is 1-dimensional and therefore not fully suitable for direct comparison but rather gives the expected order of magnitude for the temperature T. The temperature observed in the molasses is a factor of approximately 2.5 smaller than the Doppler temperature of $T_D = 145\mu K$ and therefore well below the Doppler limit suggested by the Doppler theory.

The phase space density varies over the same detuning range by a factor of approximately 4 down to $PSD = 3.4 \cdot 10^{-8}$. The peak density in the centre of the cloud at a detuning of $\Delta_{Cool\,Rb} = -9.2\Gamma$ is $n_{Mol} = 8.9 \cdot 10^{15} m^{-3}$. The density varies in the detuning range of $\pm 6\Gamma$ by -14% and is therefore much smaller than the variation in temperature and phase space density.

For the measurements in part 6 and 7 the molasses parameters for intensity, detuning and molasses time are as follows $I_{Cool\,Rb} = 1.75\text{-}2.00 mW/cm^2$, $\Delta_{Cool\,Rb} = -9$ to -10Γ and $t_{mol} = 12ms$.

Starting from a background gas of several hundred Kelvin in temperature and a density in the range of $n_{BG} = 10^8 cm^{-3}$ the magneto-optical trapping and cooling of ^{87}Rb and ^{40}K in a combined 2D-3D MOT has been successfully used for cooling and compressing the atoms. The experiment sequence was optimised for high atom numbers and samples $N_{Rb} = 1.3 \cdot 10^9$ and $N_K = 1.4 \cdot 10^6$ were prepared.

In case of ^{87}Rb the sample has been cooled further down in the optical molasses phase. Temperatures of $T_{Mol} = 57\mu K$ and densities of $n_{Mol} = 8.9 \cdot 10^{15} m^{-3}$ has been achieved. This corresponds to a phase space density of $PSD = 1.4 \cdot 10^{-7}$. Comparing this to the initial PSD of the background gas the increase in PSD yields twelve order of magnitudes. The PSD reached here is 3.5 times higher than the typical value for the magneto-optical trap estimated earlier.

In order to achieve Bose Einstein condensation the phase space density needs to be increased by several orders of magnitudes. This is impossible to accomplish with laser cooling. Hence the atoms will be confined in a magnetic trap and transported to the science chamber where the application of evaporation in magnetic quadrupole and optical dipole traps yield the desirable phase space density for the realisation of a Bose-Einstein condensate. These steps to further increase the phase space density are described in the next two sections.

Chapter 6

Magnetic trapping and transport - From the MOT to the science chamber

Due to the limitations of laser cooling techniques it is necessary to change the trapping and cooling technique. Standing out with a smooth, well defined potential and the lack of optical heating magnetic traps are the ideal candidates for trapping of ultra cold ensembles. Forced RF evaporation in magnetic traps is used for cooling the atoms to degeneracy.

As discussed in section 4 the easiest magnetic trap design with the strongest confinement, a quadrupole trap, is preferred in this experiment over the more complicated trap geometries. The magnetic transport is realised with a quadrupole trap on a linear rail.

When the atoms are transferred in between traps, irrespective of magnetic or optical traps, heating and particle losses need to be avoided. Important are adiabadicity and spatial mode matching of the traps. The experimental sequence has been optimised for minimised particle loss and heating.

In this section the experimental sequence from the magneto-optical trap in the 3D MOT chamber to the first evaporation step in a magnetic trap in the science chamber will be presented. In the process the atom cloud will be transported from the 3D MOT vacuum chamber to the neighbouring science chamber. The time line of the complete sequence to reach a Bose-Einstein condensate is depicted in figure 6.1.

The top part corresponds to all sequential steps in the 2D-3D MOT complex, at the bottom the steps that take place in the science chamber are presented. Each box stands for one part of the sequence e.g. laser cooling in the 2D-3D MOT. The duration is displayed underneath each box.

The process of magneto-optical trapping and laser cooling up to the red line is
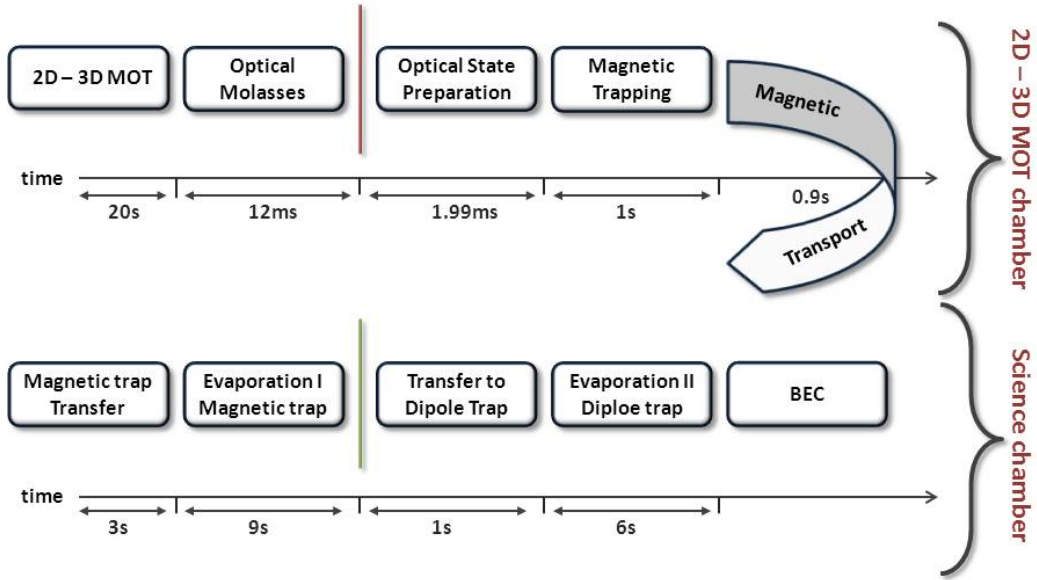
Figure 6.1: *Time line of the BEC sequence:* Top part corresponds to steps in the 2D-3D MOT complex, at the bottom the steps take place in the science chamber. Each box stands for one part of the sequence. The duration is presented underneath each box. The laser cooling process (up to the red line) is described in section 5.2 and 5.5. From red to green line: Optical state preparation (section 6.1), loading of the magnetic trap (section 6.2), transport and the transfer to the Feshbach coils in the science chamber (section 6.3), first evaporation ramp with forced RF evaporation (section6.4). Beyond the green line will be covered in section 7

described previously in section 5.2 and 5.5. The settings can be found in table 5.2 and 5.3. The experimental results from the red line to the green will be the subject of this section. Beyond will be covered in section 7.

The last step of optical state preparation is discussed in 6.1. The loading of the magnetic trap and its characterisation in the MOT chamber and the science chamber is presented in 6.2 followed by the description of the transport and the transfer to the Feshbach coils in the science chamber in section 6.3. At last the experimental results for the first evaporation ramp with forced RF evaporation in the magnetic trap is discussed in section 6.4. The atoms are then loaded into the optical dipole trap in order to prevent Majorana losses at the centre.

All results from now on only concern ^{87}Rb atoms and the atoms are trapped in a magneto-optical trap with four divergent beams at 89 % of the central intensity of the original collimated beams. The results are solely obtained in absorption imaging (see section 3.6).

6.1 Preparing the atomic cloud: Optical pumping

The magneto-optical trap is occupied by a mixture of possible hyperfine states but not all of them are weak field seeking and therefore the untrappable states will be lost during the loading process. In order to maximise the number of atoms in the weak field seeking states optical pumping is used. By choosing circular polarised light $\sigma^{\pm}$ the atoms will be repeatedly transferred from one m_F state to the neighbouring one at $m_F \pm 1$ into the stretched state and can then be confined in a magnetic field minimum. A weak magnetic offset field of $\approx 1G$ serves as quantisation axis and an appropriate choice of circularised light maximises the atom number being transferred from the optical molasses to the magnetic trap.

The duration and intensity used in the optical pumping process are thereby a crucial parameter because of possible heating of the atomic cloud. In $1.99ms$ a resonant beam[1] at an intensity of $130\mu W/cm^2$ transfers ≈ 3.5 times more atoms in a trappable m_F state. The heating of the optical pumping increases the temperature inside the magnetic trap from $590\mu K$ by $100\mu K$ that corresponds to a rise of approximately 17%. Temperature estimation assumes an infinitely small initial cloud size overestimating the temperature. The increase in atom number contributes linearly to the PSD. The PSD decreases with temperature like $\frac{1}{T^{3/2}}$ resulting in decrease of the *PSD* by $\approx 20\%$ due solely to temperature rise. Overall the phase space density *PSD* increases roughly by a factor of 3 due to optical pumping and also gives a better starting point for evaporation processes due to a higher atom number.

6.2 Magnetic trapping of neutral atoms

As described in section 4.2 the magnetic trapping of neutral atoms relies on the interaction of the magnetic moment of the atom $\vec{\mu}$ and the magnetic field vector $\vec{B}$. But in order to successfully load the atoms into a magnetic trap a small and cold atom cloud needs to be prepared with the help of laser cooling techniques described in section 5.2. The volume of the cloud shall match as close as possible the occupied trapping volume of the magnetic trap. This process is called mode matching.

For the loading procedure of the magnetic trap out of the optical molasses the laser light and magnetic fields are switched off and the atoms find themselves in free fall. In order to minimise particle loss the trapping field needs to be switched on

---

[1]The frequency is set to resonance at the beginning of the optical pumping slot, sweeping towards resonance during $1.99ms$.

quickly acting against gravity. But if the trapping fields are switched on too fast the atom cloud is heated. It is important to find a compromise to accomplish the minimisation of particle loss and heating processes by first levitating the atoms as quickly as possible at a magnetic field gradient balancing the gravitational force followed by a slow and therefore adiabatic increase of the magnetic field.
The levitating gradient is $B' \approx 15 \frac{G}{cm}$[2]. For the magnetic trap realised with MOT or moving coils this corresponds to a current of $I_{MOT} = 18A$ or $I_{Mov} = 19A$[3]. The ramping time is expected to be roughly 1-2ms. A longer levitation time has not turned out to be beneficial.

In many experiments that use quadrupole traps the strong axis of the magnetic gradient is aligned with the direction of gravity. But due to the combination of a preferred orientation of the 2D-3D MOT chamber along gravity and the implementation of the magnetic transport horizontally from the MOT chamber to the science chamber is it necessary to align the magnetic traps with the weak axis along the direction of gravity (z-direction).
In figure 6.2 the magnetic field in the three trap dimensions x, y and z is depicted at a vanishing magnetic field gradient at the top and at the levitating magnetic field gradient at the bottom. The z and x-direction are the weak gradient axes.
In case of no trapping field only the linear gravitational potential $U(z)$ acts onto the atoms in z-direction. In the other two directions the atom moves freely.
As depicted at the bottom the levitating magnetic field of $B' = 15 \frac{G}{cm}$ in the direction of gravity z is applied. Because of the trap geometry the magnetic field gradient in the x-direction is of the same magnitude while the gradient in the y-direction is twice as high.
Due to the fact that the atom only sees the magnitude of the magnetic field the gravity is balanced for atoms below the centre of the trap and the atoms move freely but for atoms above the centre the potential slope is twice as steep as before. Hence, the atoms above the magnetic trap centre experience a kick by the magnetic field B once it is turned on suddenly. This kick accelerates and heats the atoms and if the field is not ramped up quickly enough the atoms will also be lost from the trap. In the other two directions the atoms experience an asymmetric confinement, twice as strong in the y-direction than in the x-direction.
In order to prevent the kick to the atoms during the switch on process the centre of the magnetic trap is shifted outside of the atom cloud for a limited amount of time resulting in a colder ensemble confined in the magnetic trap. This is accomplished by quickly discharging capacitors applying a magnetic offset before ramping up the trapping fields.

---

[2] $E = mgz = g_F m_F B' z \rightarrow B' \approx 15 \frac{G}{cm}$
[3] Gravity acts on the weak axis of the trap.
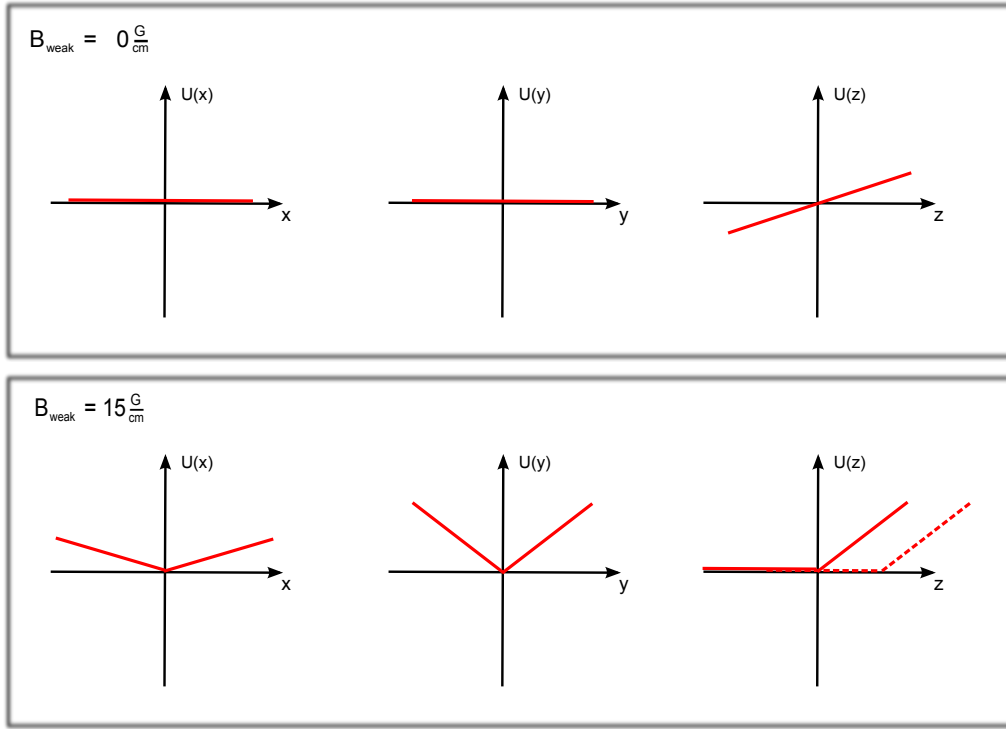
Figure 6.2: *Magnetic Offset:* Magnetic field components in x-,y- and z-direction at zero magnetic field flow at the top and levitating magnetic field at the bottom. Due to the chosen orientation of the coils is the direction of gravity aligned with the weak axis of the trap. If the magnetic field is $B_{weak} = 0G/cm$ the atoms only see the gravitational potential in z-direction depicted at the far right. At the bottom: If the magnetic field reaches the gravitational field strength at $B_{weak} = 15G/cm$ the gradient in y-direction is twice as high as in the x-direction. In the direction of gravity the magnetic field is compensated below the trap centre and doubled above the trap centre. If the magnetic field is switched on suddenly the atoms above the trap centre experience a kick and are heated and in worst case lost from the trap if the magnetic field does not ramp up quickly enough. The dotted line in z-direction indicates a shifted magnetic field zero due to a magnetic offset field where the levitating region is extended preventing the kick of the atomic cloud by the magnetic field.

The process is indicated by the dotted line in the bottom far right of figure 6.2. The shift is realised by capacitors generating a homogeneous bias field in one of the compensation coils while the capacitors discharge. The measurements done in the following are conducted with two or four capacitors in parallel with a capacity of $C = 47000\mu F$ each. Each of them is charged at a voltage of $U = 24.5V$ and discharge at a time constant of $\tau = RC$ equal $0.288s$ for two and $0.451s$ for four capacitors starting at an initial current of $I = V_0/R = 24.5V/2.4\Omega = 10.2A$ where R is the resistance of the compensation coil.

The compensation coil has 10 windings at a radius of $r = 9.5cm$ and at a distance of $D = 12.5cm$. The magnetic field yields

$$B_{offset} = \frac{\mu_0 N I R^2}{(R^2 + D^2/4)^{3/2}} = 7.87G \tag{6.1}$$

128

At a levitating gradient of $15\frac{G}{cm}$ this corresponds to a shift of the magnetic trap centre of $\frac{7.87G}{15G/cm} = 5.25mm$. The atomic cloud is expected to be smaller so that the entire cloud is placed in the levitating region once the magnetic trap is switched on.

The magnetic offset is applied simultaneously with the onset of the magnetic trap and with an approximate conductivity of the compensation coils of $L \approx 60\mu H$ is the maximum current of $10.2A$ reached within $\Delta t = 24.5\mu s$ [4] which is much faster than the magnetic trap coils. The capacitor discharges slow enough to ensure the build up of the trapping potential before the trap centre is back in its original position.

For the switch on procedure the main limitation for the moving and the Feshbach coils is given by the power supply. A nominal current of $I = 80A$ is reached after $\gtrsim 15ms$ for both coil sets. On the other hand the switching off behaviour is governed by the voltage across a varistor of $U = 1000V$, the inductance of the coil and the current of $I = 80A$. Measured switching off times for the current are $330\mu s$ for the moving coils and $50\mu s$ for the Feshbach coils. The inductances given by that measurement yield $L = 3.28mH$ for the moving and $L = 0.64mH$ for the Feshbach coils. That is in good agreement with the estimation out of equation 4.6 and table 4.3.

The effect of both optical pumping and magnetic offset has been measured. The results are presented in figure 6.3. Displayed are four measurements with and without optical pumping and magnetic offset. Both temperature T (blue, dotted line, on the right) and particle number N (red, solid line, on the left) have been calculated. The temperature assumes a point like initial cloud overestimating the result.

The first dataset is a pure magnetic trap without optical pumping or magnetic offset trapping. The current is switched on rapidly to $I = 50A$ and then ramped up to $I \rightarrow 83A$ within $3s$. These settings stay the same through out the data sets taken for figure 6.3. The cloud contains $N = 5.7 \cdot 10^7$ atoms at a temperature of $T = 590\mu K$.

For the second data set a magnetic offset as described earlier is applied shifting the magnetic zero out of the cloud centre reducing the heating of the atomic cloud. The temperature reached is just below $T = 500\mu K$ with a slightly higher atom number[5] of $N = 6.3 \cdot 10^7$. The magnetic offset clearly suppresses heating.

---

[4] $\frac{dI}{dt} = \frac{U}{L} = \frac{24.5V}{60\mu H} = 4.08 \cdot 10^5 \frac{A}{s} \rightarrow \frac{10.2A}{4.08 \cdot 10^5} = 24.5\mu s$

[5] Statistical variation can reach $\pm 5\text{-}10\%$
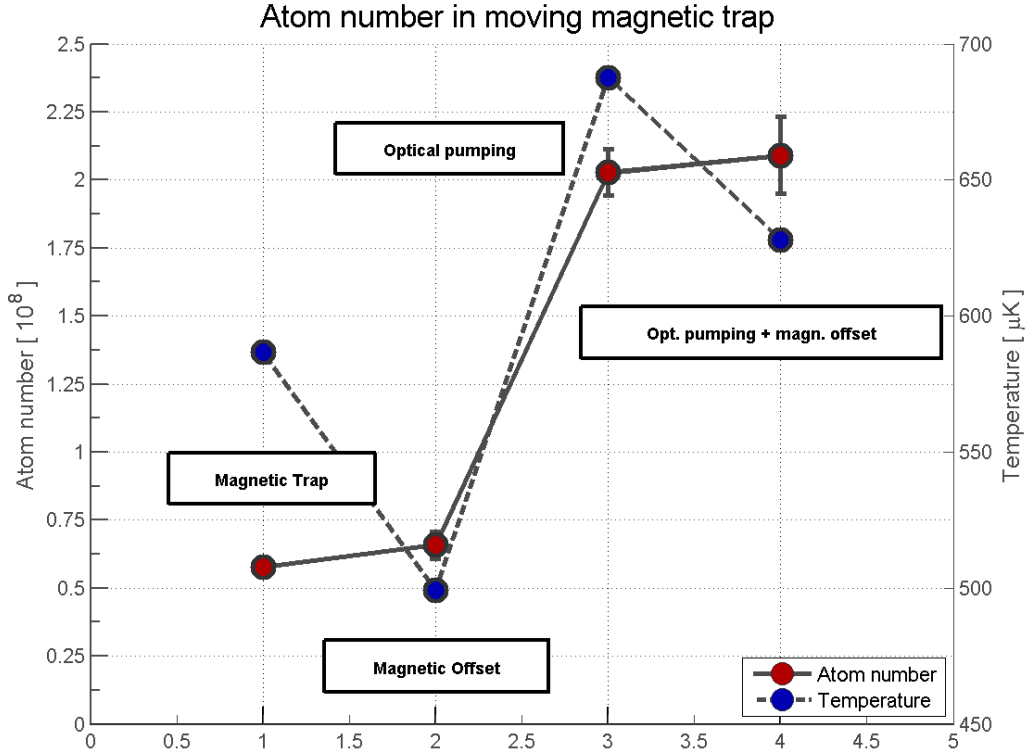
Figure 6.3: *Effect of magnetic offset and optical pumping on temperature T and atom number N in the magnetic trap:* Pure magnetic trap without optical pumping and magnetic offset, just with magnetic offset or optical pumping or both optical pumping and magnetic offset together. The magnetic trap switches on as quick as possible to $I = 50A$ and ramped further up to $I \to 83A$ in $t = 3s$ and is kept unchanged for all four data sets. For the details on the settings of the loading procedure, the optical pumping and the magnetic offset refer to the previous text. While the magnetic offset prevents heating of the atomic cloud and slightly increases the atom number, the optical pumping increases both temperature T and atom number N. Both techniques combined result in a large and cold cloud of $T = 630\mu K$ assuming an infinitely small initial cloud size and $N = 2.1 \cdot 10^8$ atoms.

The third data set does not apply a magnetic offset but optically pumps the atoms as described in section 6.1 in a weak field seeking state. The atom number increases by a factor of 3.5 to $N = 2 \cdot 10^8$ atoms but the cloud is heated by $100\mu K$ to $T = 690\mu K$.

Combining both methods in the fourth data set combines the benefits of both. The optical pumping increases the atom number while the magnetic offset reduces the heating in the atomic cloud. Atom numbers of $N = 2.1 \cdot 10^8$ at a temperature of $T = 630\mu K$ is reached. In comparison to the first data set is this an increase of 7% in temperature and of 370% in atom number.

Due to the limitations of the current setup it is impossible to realise currents in the range of $80A$ or higher within less than 15-20 ms. After the initial switch on of the magnetic trap the current is ramped up adiabatically to the final setting. The initial trap can be realised with the MOT or the moving coils but if not stated differently the atoms are transferred from the optical molasses into the moving coils.
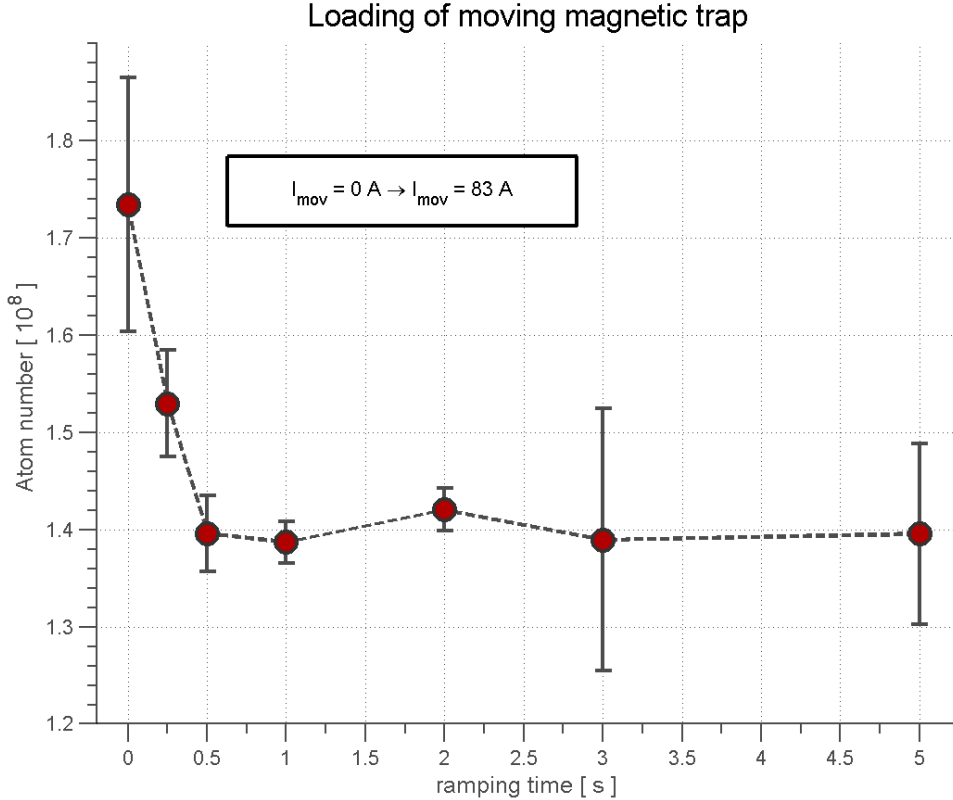
Figure 6.4: *Atom number N versus the ramping time of the coil current $I = 0A \rightarrow 83A$. The atom number decreases rapidly in the first $0.5s$ but stabilises in the time region of $1s$ to $5s$. Unavoidable losses due to lifetime losses are compensated by more gentle ramping of the magnetic field.*

In figure 6.4 the particle number N during the loading procedure is depicted for varying ramping times of the current in the moving coils up to $I = 83A$.
The highest atom number of nearly $N = 1.75 \cdot 10^8$ is trapped at short ramping times but this also generates heat in the atomic ensemble. If the ramping time is increased the number of particles decreases but settles at a value of $N = 1.4 \cdot 10^8$ at times of $t = 1s$ and longer. Unavoidable losses due to lifetime losses are compensated by more gentle ramping of the magnetic field. The temperature T on the other hand is expected to decrease with increased ramping time. Longer ramping times than

$3s$ have not turned out to be beneficial concerning higher PSD at later points in the experiment and the corresponding time regimes have not been investigated here.

For future measurements the magnetic trap loading is conducted with the moving coils. The current is set to $I = 50A$ and the ramped from $I = 50A$ to $83A$ in $t = 1s$ or $3s$. Previously the atoms are optically pumped for $1.99ms$ with a beam set to resonance at a power of a few hundreds of μW. The magnetic offset is realised with four capacitors of $C = 47000\mu H$ each and a voltage of $U = 24.5V$ and is triggered at the same time as the magnetic trap current. From the $4.85 \cdot 10^8$ atoms in the magneto-optical trap are $N = 1.4 \cdot 10^8$ atoms transferred to the magnetic trap. This corresponds to an efficiency of 30%. The low atom number is due to different parameter settings in the MOT and shorter MOT loading times.

6.2.1   Lifetime measurements in the magnetic trap

Once confined in the magnetic trap the atoms need to stay long enough in the trap for further cooling and manipulation. The most important loss mechanisms are background collisions, three body recombination and heating processes. Here the loss mechanism with the residual gas in the background is the dominant limitation in the life time of the atom in the magnetic trap.

The life time has been characterised in different places of the vacuum system (3D MOT chamber and science chamber) and also for the different vacuum setups with different 3D MOT chambers (epoxy seal in section 2.2.2.1 and indium seal in section 2.2.2.2). Due to an additional differential pumping stage the lifetime in the science chamber is expected to be significantly higher.

For determination of the trap lifetime the atoms are held in the magnetic trap for various lengths. The residual atom number is fitted with an exponential decay of the form

$$N(t) = N_0 \, e^{-t/\tau} \tag{6.2}$$

where τ is the magnetic trap lifetime and N_0 is the initial atom number at $t = 0$.

Magnetic trap lifetime in the epoxy sealed vacuum system   In figure 6.5 the magnetic trap lifetime for the epoxy sealed vacuum chamber is presented. On the left the measurement in the MOT chamber and on the right the measurement for the science chamber can be seen. The lifetime in the MOT chamber yields $\tau_{3D} = 2.15s$ and in the science chamber $\tau_{GC} = 8.8s$. This is by far too small for the experimental requirements.
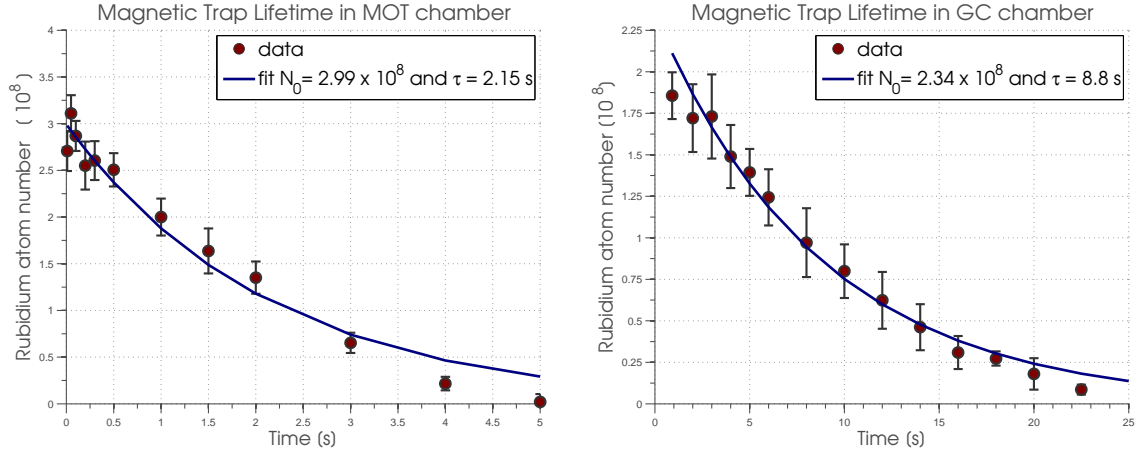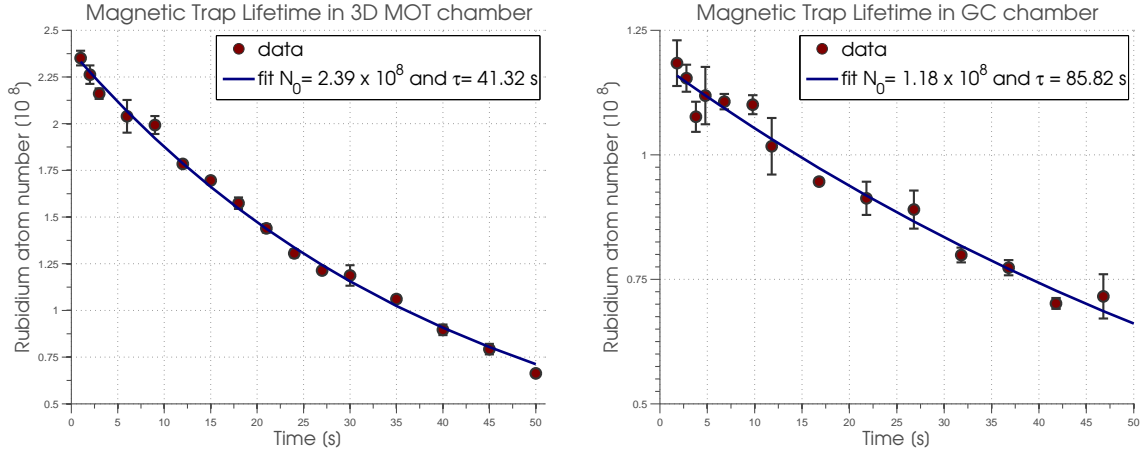
Figure 6.5: *Magnetic trap lifetime in epoxy sealed chamber:* Exponential decay of atom number N versus time t following equation 6.2. The lifetime in the 3D MOT chamber is $\tau_{3D} = 2.15s$ (left) and in the glass cell $\tau_{GC} = 8.8s$ (right).

Magnetic trap lifetime in the indium sealed vacuum system   The replacement of the epoxy sealed MOT chamber with an indium sealed chamber very much improved the lifetime in both the MOT chamber and the science chamber. In figure 6.6 is the result of the very same measurement depicted. The lifetime in the MOT chamber yield $\tau_{3D} = 41s$ and in the science chamber $\tau_{GC} = 86s$. This is an sufficient improvement of a factor of approximately 20 in the MOT chamber and a factor of 10 in the science chamber.
Hence the magnetic trap lifetime in MOT and science chamber with the indium sealed vacuum chamber is sufficient.

Flooding the vacuum chamber with argon without repeated baking reduced the lifetime of the magnetic trap in the science chamber to $\tau_{GC} = 52s$ as shown in figure 6.7. All following measurements in the science chamber will be conducted with this magnitude of magnetic trap life time.
The varying atom number N_0 in the various measurements is due to different loading times and optimisation levels of the experiment when the life time measurements have been performed.

Thus far the loading procedure of the magnetic trap including optical pumping for higher particle numbers and magnetic offset for reduced heating has been optimised. The next step is the optimisation of the magnetic transport in order to realise the largest and coldest cloud possible in the science chamber. This will be reviewed in the next section.

Figure 6.6: *Magnetic trap lifetime in indium sealed chamber:* Exponential decay of atom number N versus time t following equation 6.2. The lifetime in the 3D MOT chamber is $\tau_{3D} = 41.32s$ and in the glass cell $\tau_{GC} = 85.82s$.

6.3 Magnetic transport along a macroscopic distance

As discussed in section 2 and 4 a magnetic transport along a macroscopic distance is necessary due to the modular approach of the vacuum system. The transport rail collects the atoms at the 3D MOT chamber and carries them to the science chamber where they are later transferred to the Feshbach coils. Further details on the linear rail and its operation can be found in [64].

This setup is simple, reliable, maintenance free and easy to use. The maximum transport speed of $0.875m/s$ is quite high in comparison with other experiments with maximum velocities of $5cm/s$ - $68cm/s$ [110, 113–115].

The optimised settings correlate with the fastest transport possible. A slower and more gentle transport with a significant decrease in acceleration and/or velocity does not act significantly beneficial on the atom number or temperature.

Therefore for all future references the fastest settings of $v_{max} = 0.875m/s$ and $a_{max} = 6m/s^2$ are used.

On the way to the science chamber the atoms need to pass through a differential pumping stage with a diameter of $d = 16mm$. The magnetic trap has a gradient of $132\frac{G}{cm}$ at $I = 83A$ in the strong axis and $66\frac{G}{cm}$ in the weak axis. Assuming a prefect aliment right through the centre of the differential pumping stage the hottest atoms in the cloud can have a temperature of

$$T = \frac{2\mu_B|\vec{B}|}{3k_B} = 1.8mK \qquad (6.3)$$
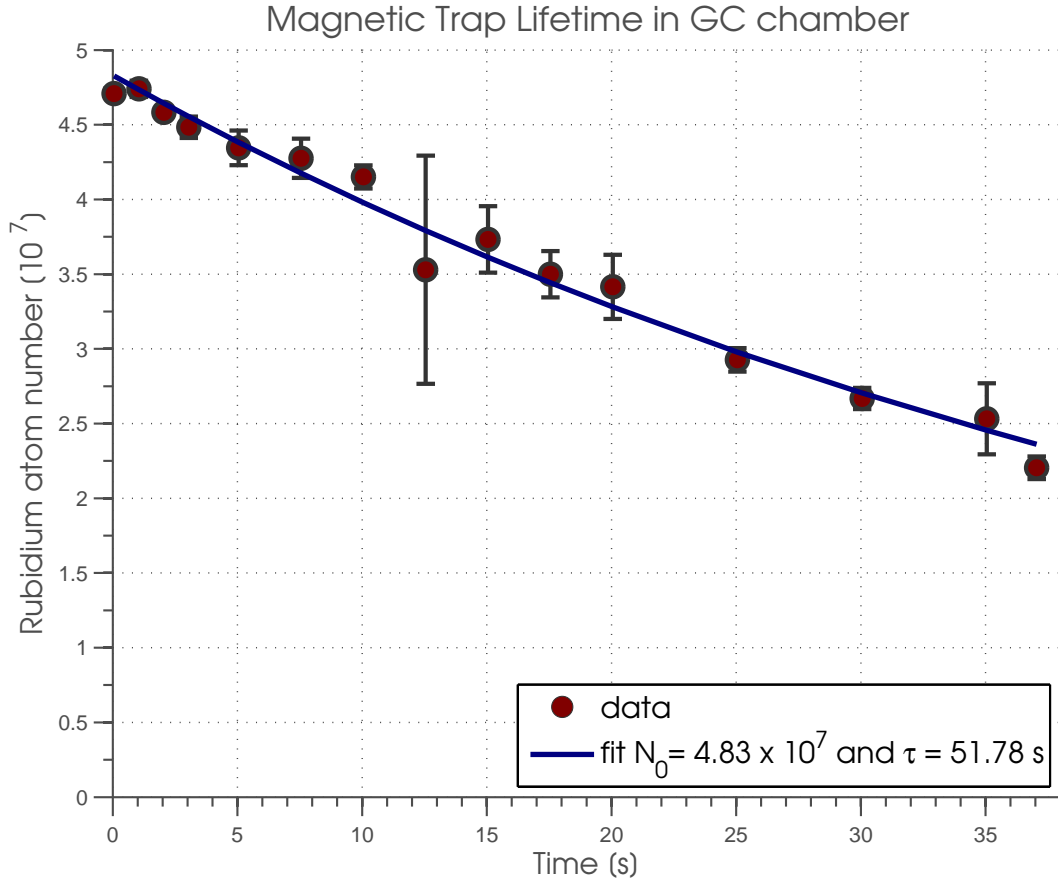
Figure 6.7: *Magnetic trap lifetime in indium sealed chamber after flooding the vacuum chamber with argon: Exponential decay of atom number N versus time t following equation 6.2. The lifetime in the glass cell is measured to $\tau_{GC} = 52s$.*

If the atoms are hotter and eventually get in contact with the wall they will be removed from the trap instantly. This is the first unintended evaporation step at a hot surface [172, 173] and therefore careful alignment of the linear rail position is demanded. Measurements have shown that the cloud temperature remains unchanged during transport from the MOT chamber to the science chamber. The atom number loss is in the range of 5% higher than due to background collisions. This can be explained by a marginal heating effect by the transport that is compensated by surface evaporation during the transport. Due to the temperature of the atoms in the magnetic trap of $T \leq 500\mu K$ the losses because of the cloud extension is not expected to be high.

After successful transport the atom cloud will be transferred to the Feshbach coils at the science chamber and later to an optical dipole trap (see section 7). This

135

enables on one hand to collect an additional atomic cloud with the aid of the moving coils and on other hand the atomic cloud can be further compressed due to a larger gradient in the Feshbach coils. Forced evaporation to the BEC transition is performed by combining both the advantages of magnetic trap and the far detuned optical trap and simultaneously eliminating both traps drawbacks.

6.4 RF evaporation in the magnetic trap

Evaporation is a natural effect in every day life occurring in hot tea cups or oceans and it is also in the form of forced evaporation a standard technique in BEC experiments [106, 174]. Except of specific cases [61] it is not just being so far the main method to realise a BEC in dilute atomic gases it is also a very successful technique for sympathetic cooling of mixtures where one of the constituents might be impossible or harder to cool solely by evaporative cooling like for the fermionic isotope of potassium ^{40}K [59, 60, 175]. Evaporative cooling was suggested by *Hess et al* [176] and demonstrated for hydrogen [177]. It was quickly adapted for alkali atoms [56, 57] leading to the first creation of a BEC [11].

The basic concept relies on constantly removing the hot tail of the Boltzmann distribution while the atoms rethermalise by performing elastic two body collisions. The net cooling effect is based on the fact that the removed atom carries more than the average energy and therefore the new thermal equilibrium will be at a lower temperature[6].

In the magnetic trap forced RF evaporation is used in contrast to the evaporation process in the optical dipole trap that is discussed later. Initially proposed by *Pritchard et al.* [121] the advantage of RF evaporation is the well defined RF cutting edge transferring the atoms in untrapped or even repelled m_F states and the unchanged strong confinement during the RF ramp conserving the density and collision rates at their highest possible values.

A linear trapping potential like in a quadrupole trap has the strongest confinement and therefore high density and collision rates. The elastic two body collision rate is together with the magnetic trap lifetime the most important parameter in forced evaporation. The ratio of collision rate to background losses determines all dynamics in the evaporation process and decides if a BEC can be reached at certain initial conditions. Other losses are present but can be neglected till the very end of the evaporation process as will be shown later.

Before the loss rates during the evaporation process are investigated. The transfer to the Feshbach coils will first be presented briefly.

---

[6]It takes only a few collisions to find a new equilibrium [178].
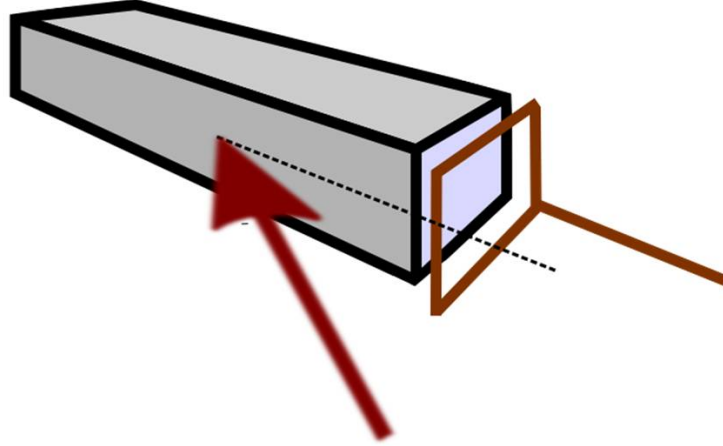
Figure 6.8: *Science chamber setup* with RF antenna. The arrow indicates the direction of the later described dipole trap.

6.4.1   Transfer to the Feshbach coils

In order to free the moving coils the atoms are transferred to another magnetic trap formed by the Feshbach coils. The overlap of the two coils can be dynamically controlled only in the horizontal position with the linear rail. Its stability and repeatability of it set position is very important [64]. The procedure for the loading of the trap is due to the same potential form done by just ramping the currents in the coils during the same amount of time linearly up or respectively down.
The transfer is done in a $3s$ slot ramping the moving coil current from $I_{mov} = 83A \rightarrow 0A$ and the current in the Feshbach coil accordingly $I_{Fesh} = 0A \rightarrow 50A$[7]. The gradient only changes slightly from $132G/cm$ to $117G/cm$. The transfer efficiency is 83% from $N_{mov} = 2.9 \cdot 10^8$ to $N_{Fesh} = 2.5 \cdot 10^8$ atoms. The temperature decreases from $T_{mov} = 420\mu K$ to $T_{Fesh} = 340\mu K$. During the transfer mainly hot atoms are lost. Straight after the transfer the RF evaporation is started.

6.4.2   RF Evaporation

The setup for the evaporation process is depicted in figure 6.8. The arrow indicates the direction of the optical dipole trap. The one loop RF antenna in the vicinity of

---

[7]Higher currents in the Feshbach coils were avoided to minimise thermal stress on the electrical connections.

the science chamber is connected to a DDS that performs linear RF ramps of chosen length, power and frequency range. The evaporation sequence is summarized in table 6.1

		$f_{ini}[MHz]$	$f_{end}[MHz]$	$t[s]$	$A[dBm]$	$B'_{Fesh}[\frac{G}{cm}]$	$DT[\%]$
①	Transport	-	-	0.9	0	0	0
②	Transfer I	-	-	3	0	$0 \rightarrow 117$	0
③	1. Ramp	40	10	5	1	117	100
④	2. Ramp	10	2	4	0.75	117	100
⑤	Transfer II	2	2	1	0	$117 \rightarrow 28$	100
⑥	3. Ramp	-	-	3	0	0	$100 \rightarrow 30$
⑦	4. Ramp	-	-	3	0	0	$30 \rightarrow 8$
⑧		-	-	0.25	0	0	8

Table 6.1: *Evaporation sequence:* Parameters for evaporation in the Feshbach coils and the dipole trap.

The main drawback despite the strong confinement in the quadrupole trap is the zero crossing of the potential in the centre of the trap. Here Majorana spin flips can occur [179] where the atomic moment looses its orientation with the magnetic field direction $\vec{B}$ and can enter a repellent spin state. The loss rate Γ_m depends on temperature T and gradient B' and is given by equation 6.4.

$$\Gamma_m = \chi \frac{\hbar}{m} \left(\frac{g_F \, m_F \, \mu_B B'}{2 \, k_B \, T} \right)^2 \tag{6.4}$$

The proportionality constant is measured to $\chi = 0.15$ in [16, 180]. For atoms in the $|F = 2, m_F = 2\rangle$ state in the moving and Feshbach coils at similar gradients the Majorana losses behave like shown in figure 6.9. The loss rate is normalised to the losses due to background collisions $1/\tau_{BG} = 1/52s$ and become comparable to the background loss rate at a temperature of $29.7\mu K$ for the Feshbach trap and $33.6\mu K$ for the moving trap. This is the latest point in the evaporation process where the hole in the trap needs to be plugged.

Therefore the optical dipole trap is running at full power from the start of the evaporation in order to prevent atom loss due to Majorana spin flips. The dipole trap captures atoms expelled from the magnetic trap similar to [120]. In other experiments blue detuned optical plugs have been realised [11, 16, 180]

138

Additionally to Majorana losses there are other loss mechanisms that cannot be prevented on the way to reach the necessary phase space densities. These are background collisions $1/\tau_{BG}$, inelastic two body collisions $1/\tau_{2b}$ and three body recombinations $1/\tau_{3b}$ [181]. As it will be seen later on the predominant process for losses throughout the longest part of the evaporation is due to background collisions that are given by the vacuum system's pressure. The back ground losses therefore set the upper time scale for the evaporation.

These bad collisions need to be put in relation to the good elastic two body collisions needed for re-thermalisation. The ratio of good to bad collisions R is ultimately given by the density n depending on the form of the trapping potential, the number of atoms N and the temperature T. It is defined as

$$R = \frac{\frac{1}{\tau_{el}}}{\frac{1}{\tau_{BG}} + \frac{1}{\tau_{2b}} + \frac{1}{\tau_{3b}}} \tag{6.5}$$

Ideally one wants to enter the regime of runaway evaporation. During evaporation the elastic collision rate needs to grow faster than the loss rates. The elastic collision rate $1/\tau_{el}$ is given by the scattering cross section σ, the density n and the average velocity $\bar{v}$ of the atoms at the temperature T to

$$\frac{1}{\tau_{el}} = n\sigma\bar{v}\sqrt{2} \quad with \quad \bar{v} = \sqrt{\frac{8\,k_B\,T}{\pi\,m}} \tag{6.6}$$

The scattering cross section $\sigma = 8\pi\,a^2$ is dominated at low temperatures by the s-wave scattering length $a = 5.24nm$ [181, 182]. The elastic scattering rate determines a lower time scale for the evaporation since it is the time scale on which the re-thermalisation takes place. The loss mechanisms are determined by

$$\frac{1}{\tau_{2b}} = G_{2b}\,n \quad \to G_{2b} = 6.0 \cdot 10^{-15} cm^3 \tag{6.7}$$

$$\frac{1}{\tau_{3b}} = G_{3b}\,n^2 \quad \to G_{3b} = 4.3 \cdot 10^{-29} cm^6 \tag{6.8}$$

with G_{2b} being the inelastic two body collision rate[8] [185] and G_{3b} being the three body recombination rate [183].

For the evaporation sequence performed here (see table 6.1) the collision rates in a magnetic trap according to equations 6.6 - 6.8 are depicted in figure 6.10 on the right. On the left the individual contributions to the ratio of good to bad collisionsare shown, combining to the parameter R.
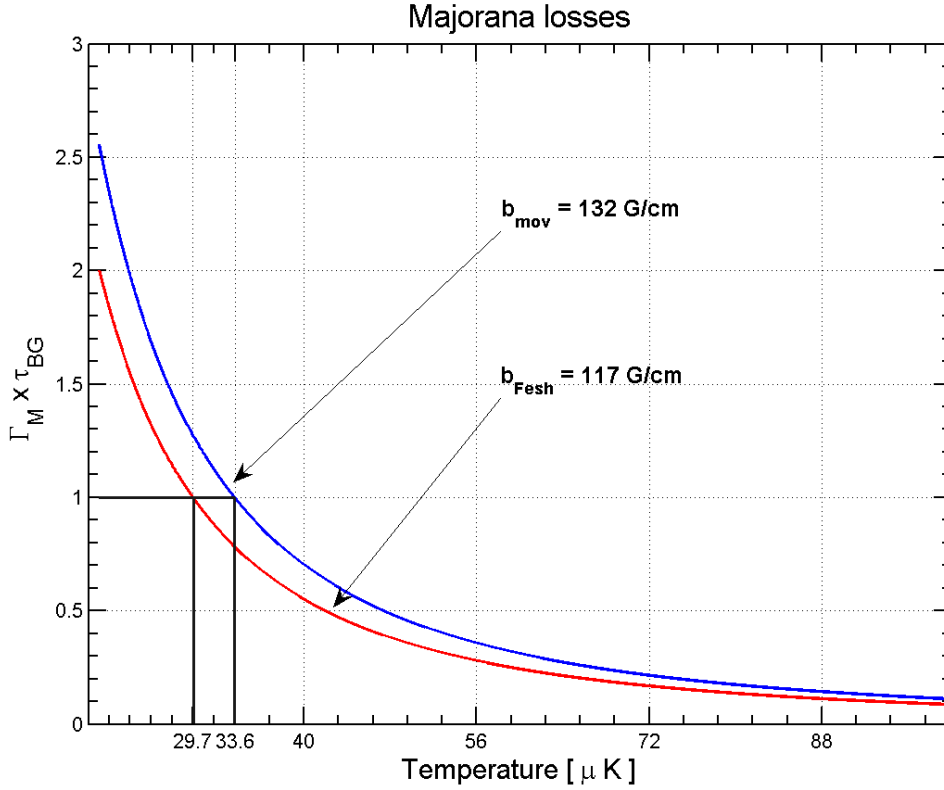
Figure 6.9: *Majorana Losses* per background loss $1/\tau_{BG}$ in the moving coils and the Feshbach coils in dependence of the temperature T. In the moving coils the Majorana losses equal the background losses at $T_{mov} = 33.6\mu K$ and respectively at $T_{Fesh} = 29.7\mu K$ for the Feshbach coils. The gradients according to the experiment parameters are $b_{mov} = 132G/cm$ and $b_{Fesh} = 117G/cm$.

In parallel to that, figure 6.11 depicts how the phase-space density evolves during the evaporation process with decreasing atom number at the top (blue) and temperature at the bottom (red).

Each point in all four graphs in figure 6.10 and 6.11 corresponds to the same point in the experimental sequence of which all of them correspond to one entry in table 6.1. For figure 6.10 only the first points ① - ⑥ going from right to left are depicted. The ⑦ and ⑧ are represented as the last point (right to left) in figure 6.11.

The starting point for evaporation after laser cooling and magnetic transport in the moving coils into the science chamber (①) with a parameter R of ≈ 400 is not great and keeps constant after the transfer to the Feshbach coils (②) even though the temperature is reduced by $\approx 20\%$ from $420\mu K$ to $340\mu K$. Only when the trap

---

[8]The inelastic two body collision rate G_{2b} for the $|F = 1, m_F = -1\rangle$ state is an order of magnitude smaller [183, 184]
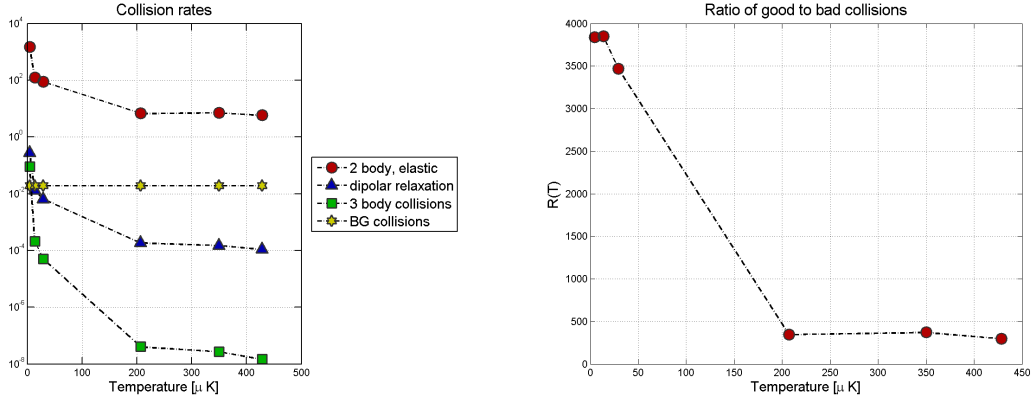
Figure 6.10: *Loss rates and collisional parameter R during evaporation:* On the left the different loss rates for background collisions (yellow stars), 3-body collisions (green squares), dipolar relaxation (blue triangles), elastic 2-body collisions according to equation 6.7 (red circles). The experimental parameter coincide with the evaporation steps ① - ⑥ in table 6.1. On the right the ratio of good and bad collisions is shown according to equation 6.5 to 6.8 for the same evaporation steps ① - ⑥ in table 6.1.

is truncated down from $f_{ini} = 40MHz$ to $f_{end} = 10MHz$ in $5s$ (③) and then to $2MHz$ in $4s$ (④) the ratio of good to bad collisions R starts increasing from below 500 to 3500.

The transfer from the magnetic trap to the pure optical dipole trap in $1s$ by ramping down the current to a gradient in the weak axis of $14G/cm$ just below levitating the atoms against gravity acts as an additional evaporation step by only loading the coolest atoms into the dipole trap (⑤) and the parameter R increases further to 4000.

The further evaporation process to the BEC in the optical dipole trap is discussed in chapter 7.

At point ⑤ the parameter R seems to saturate. This is due to the fact that other loss mechanisms than just the background collisions become important due to the increased density n in the atomic ensemble. On the left in figure 6.10 the individual collision rates for different mechanisms are depicted. The valuable elastic collision rate (red circles) shows an accelerated increase with decreasing temperature. The loss mechanism due to background collisions (yellow stars) is constant and the dominating loss rate for the major range of temperatures covered. Only at temperatures below $T < 30\mu K$ the other loss rates due to inelastic two body collisions (blue triangles) and three body recombinations (green squares) become comparable. Up to the point ⑤ in table 6.1 where the atoms are loaded into the dipole trap only the background collisions need to be taken into account. Beyond that will be discussed in chapter 7.
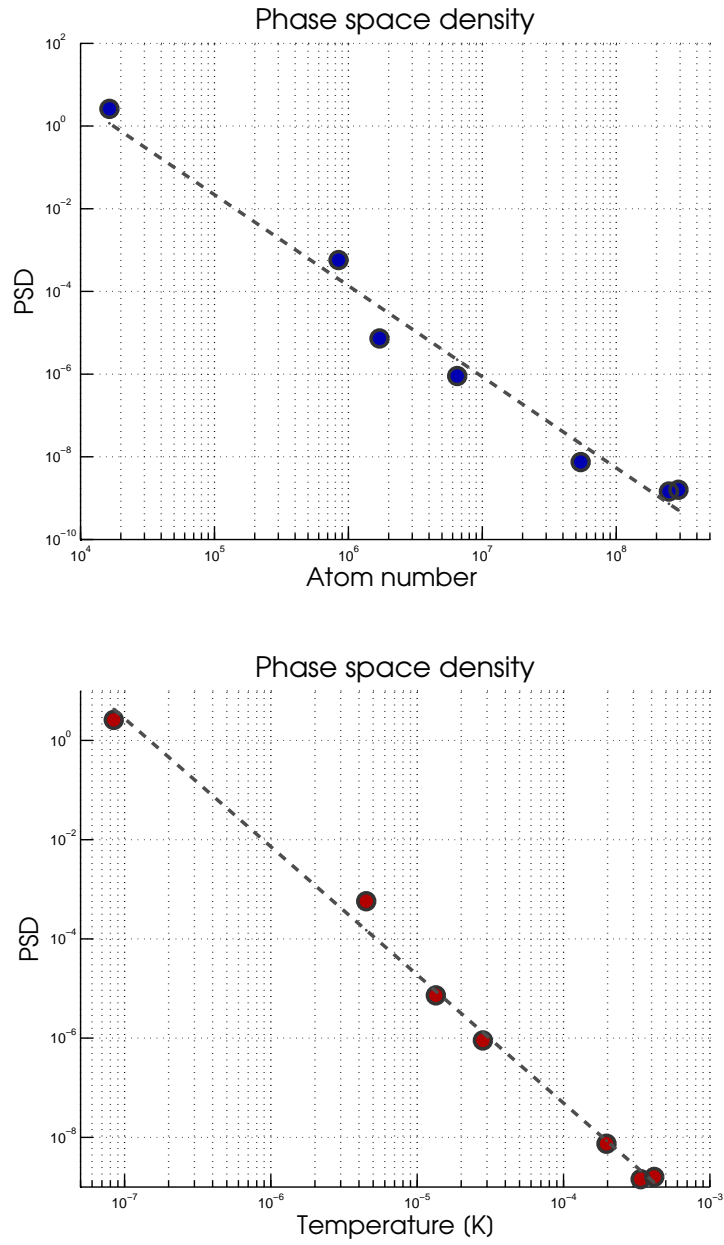
Figure 6.11: *Phase space density PSD against atom number N and temperature T during the evaporation process* described in table 6.1. Each point corresponds to one entry in table 6.1 going from right to left, except ⑦ and ⑧ that are represented as one point.

The figure 6.11 anticipates already some of the results of the next chapter by showing the behaviour of atom number (left) and temperature (right) for the entire evaporation sequence from the arrival of the moving trap in the science chamber to the appearance of the BEC. On a logarithmic scale the slope of the fitted curve yields $\alpha = \frac{dln(PSD)}{dln(N)} = -2.2$ for the atom number and $\gamma = \frac{dln(PSD)}{dln(T)} = -2.58$ for the temperature.

In order to determine if we are in the runaway regime experimental parameter's tendency like atom number and temperature can be expressed in power laws and their exponents [186]. The requirements for runaway evaporation are very different for different trap geometries. Following the arguments given in [186] the power laws ruling the runaway evaporation process while accounting for trap losses in a spherical quadrupole trap are given as

$$\tau_0 \quad = \frac{\tau}{\nu^{1+\gamma/2}} \quad \geq 4.7 \tag{6.9}$$

$$\tau \quad = \frac{\tau_{BG}}{\tau_{step}} \tag{6.10}$$

$$\nu \quad = \frac{N'}{N} \tag{6.11}$$

$$\gamma \quad = \frac{log(\frac{T'}{T})}{log(\frac{N'}{N})} \tag{6.12}$$

with N' and T' being atom number and temperature in the truncated trap at a step duration of τ_{step} and N and T the precedent values.

The condition changes for a parabolic trap to $\tau_0 \geq 29$. The condition is well fulfilled during the entire evaporation process with $\tau_{0\,exp} \geq 1.5 \cdot \tau_0$. Overall this corresponds to a theoretical value of the R parameter of

$$\frac{\left(\frac{1}{\tau_{el}}\right)}{\left(\frac{1}{\tau_{BG}}\right)} \quad \geq 25 \quad \text{spherical quadrupole trap} \tag{6.13}$$

$$\frac{\left(\frac{1}{\tau_{el}}\right)}{\left(\frac{1}{\tau_{BG}}\right)} \quad \geq 150 \quad \text{parabolic trap} \tag{6.14}$$

which is also always well fulfilled in the evaporation sequence and hence the evapotation sequence is in the runaway regime.

6.4.3 Notes on the "wrong" coil orientation

A quick estimation in order to determine the effect of the different orientation of the moving coils concerning gravity is following. Different to other magnetic
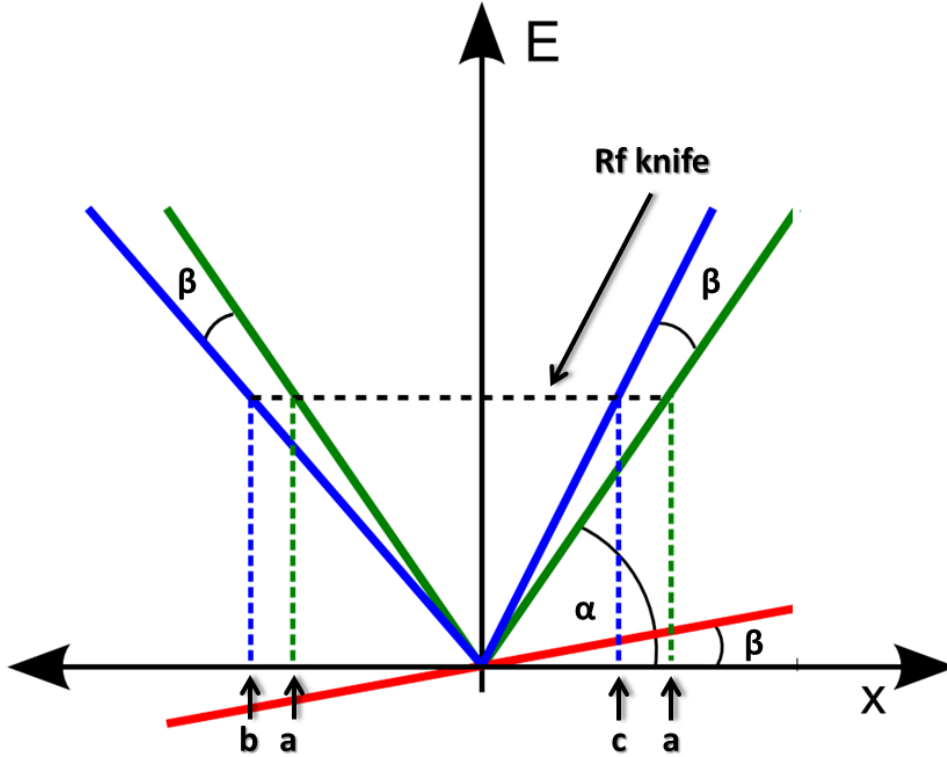
Figure 6.12: *Effects on potential in magnetic trap due to gravity during the evaporation process:* Energy in dependence of the position in a pure quadrupole trap (green), gravity (red) and quadrupole trap combined with the gravitational potential (blue). The pure quadrupole potential is slightly tilted against its original position due to gravity, changing the position x where the atom is resonant to the RF knife from being symmetric around zero at position a to position b and c. The change in time the atom needs to travel within the trap to the resonant position is dependent on the gradient of the quadrupole trap. For details refer to text.

traps [187] the changed orientation of the quadrupole trap is expected to have no or little effect on the evaporation process by reducing the frequency marginally when the atoms are resonant with the Rf knife inside the trap.

In figure 6.12 the quadrupole trap along gravity is depicted. The actual trap potential (blue) is composed of the unperturbed trap potential (green) and gravity (red). The gradient on each side of the centre of the trap can be expressed by an angle and the position where the atom in a certain state $|F, m_F\rangle$ with a certain energy $E = E_{pot} = E_{kin}$ is resonant with the applied RF knife (black dotted line). It is assumed that the atoms are in equilibrium.

Assuming the atom has a velocity $v = 0$ at the position where it is resonant with the Rf knife $E_{RF} = \hbar\omega_{RF} = E_{pot}$, the potential gradient acts as an accelerating force on the atom and after passing the centre of the trap it decelerates the atom

again till it stands still when it reaches the other resonant position.

The question now to be asked is if the timing going from one side of the trap to the other side changes under the influence of gravity and if yes by how much it depends on the strength of the trap. For this the time t_0 the atom takes travelling from $x = -a \rightarrow a$ is compared to the time t_g it takes to travel from $x = b \rightarrow c$ in the particular potential. The force is given by

$$\vec{F} = \nabla U \quad with \quad U = g_F \, m_F \, \mu_B \, B' \, |x| + m \, g \, x \qquad (6.15)$$

but also $\vec{F} = m \cdot \vec{a} = m \frac{d\vec{v}}{dt}$. The atomic state parameters are assumed to $g_F = 1/2$ and $m_F = 2$.

$$\frac{dU}{dx} = -\mu_B B' + m \, g \quad \text{perturbed trap (blue) for x} < 0 \qquad (6.16)$$

$$\frac{dU}{dx} = \mu_B B' + m \, g \quad \text{perturbed trap (blue) for x} > 0 \qquad (6.17)$$

$$\qquad (6.18)$$

The time the atom needs to travel from $x = a \rightarrow 0$ and similar for $x = b$ or $c \rightarrow 0$ yields therefore

$$t(a) = \frac{m \, v}{\mu_B B'} \quad \text{unperturbed trap (green) for x} \gtrless 0 \qquad (6.19)$$

$$t(b) = \frac{m \, v}{|-\mu_B B' + m \, g|} \quad \text{perturbed trap (blue) for x} < 0 \qquad (6.20)$$

$$t(c) = \frac{m \, v}{\mu_B B' + m \, g} \quad \text{perturbed trap (blue) for x} > 0 \qquad (6.21)$$

$$\qquad (6.22)$$

where in all cases the velocity is given by $v = \sqrt{\frac{2 \hbar \omega_{RF}}{m}}$. The trap frequencies $f_0 = 1/t = 1/(2 \, t(a))$ for the unperturbed trap and $f_g = 1/(t(b) + t(c))$ for the perturbed trap are given at a gradient of $B'_{Fesh} = 117 \frac{G}{cm}/2$ at the start of the evaporation with $\hbar \, \omega_{RF} = \hbar \, 2\pi \, 40 MHz$ as $f_0 = 31 Hz$ and $f_g = 29 Hz$. This is a relative difference of $f_0/f_g = 1.07$ in trap frequencies of approximately 7%. The effect decreases if the strong axis is aligned with the direction of gravity to 1.7%. The estimations show that the effect becomes stronger with lower trap confinement but should not affect the evaporation process in any way due to high enough gradients so that the effect becomes completely negligible as it has been observed in the experiment.

Magnetic trapping, transport and forced evaporation has been successfully demonstrated in this section. Majorana losses in the quadrupole trap at low temperatures

make a change of trapping mechanism unavoidable. A combined trap of magnetic and optical dipole trap combine all advantages while simultaneously compensating the disadvantages like low trapping volume of the optical dipole trap and the Majorana losses for the quadrupole trap [120]. The optical dipole trap and the realisation of the Bose-Einstein condensate are discussed in the next section.

Chapter 7

Creating a BEC in an astigmatic optical dipole trap

The occurence of unavoidable Majorana spin flips in a quadrupole trap make it necessary to circumvent the losses by changing the trapping mechanism from being magnetic to a far detuned optical dipole trap. The use of dipole traps first realised in [188] is by now a well established technique in ultra cold atom experiments [189] and relies on the induced *AC Stark* shift of the atomic energy level in an electromagnetic wave. The small trapping volume of optical dipole traps is one of the main disadvantages but can be used as an additional evaporation step.

The realised setup of a combined quadrupole trap and a far detuned optical trap combines all advantages of both trap designs like e.g. large trapping volume for the quadrupole trap and the spin independence for the dipole trap but also compensates the drawbacks of the individual traps [120]. Many different trap geometries like with one or two or more beams being red or blue detuned have been realised in different experiments while in this setup a single red detuned beam trap has been chosen [64].

The chapter is organised as follows. The working mechanism of optical dipole traps will be briefly discussed in section 7.1 before the special features of our setup and the trap frequencies are discussed in section 7.2. The BEC part of this chapter starts in section 7.3 with the evaporation process after the loading procedure and the final result of the BEC.

7.1   Dipole trapping of neutral atoms

The dipole force on an atom relates to the interaction of an induced electric dipole and the intensity gradient of a laser field. Thereby only the absolute detuning, not the sign, and the intensity gradient determine the strength of the force. The sign

on the other hand determines the direction of the dipole force. After the radiation pressure force and the force experienced by an atom in an inhomogeneous magnetic field it is the weakest of the three mechanisms. But in contrast to the magnetic force it can be atomic state independent so that spin mixtures and their Feshbach resonances can be be easily be investigated without changing the actual trapping potential [34]. The following considerations are based on [189] and more details specifically on this project can be found in [64].

The dipole force was first investigated by *Bjorkholm et al.* [190] and later used as an optical trap by *Chu et al.* [188]. A special case of optical dipole trap FORT implemented here was first realised by *Miller et al.* [191]. Due to the negligible scattering of photons it resembles a nearly ideal conservative trap. In case of a far detuned optical dipole trap with a detuning Δ much larger than the fine splitting of a multilevel atom the system can be approximated by a semi-classical approach of a two-level atom in a classical light field. The polarisation has no effect in this scenario.

Following [64, 189] for large detunings $\Delta = \omega_0 - \omega$ at low saturation the dipole potential U_{dip} and the scattering rate Γ_{sc} are given by

$$U_{dip} = -\frac{3\pi c^2}{2\omega_0^3} \left(\frac{\Gamma}{\omega_0 - \omega} + \frac{\Gamma}{\omega_0 + \omega} \right) I(\vec{r}) \tag{7.1}$$

$$\Gamma_{sc} = \frac{3\pi c^2}{2\hbar\omega_0^3} \frac{\omega}{\omega_0}^3 \left(\frac{\Gamma}{\omega_0 - \omega} + \frac{\Gamma}{\omega_0 + \omega} \right)^2 I(\vec{r}) \tag{7.2}$$

The rotating wave approximation for detunings closer to resonance simplifies the connection between potential, scattering, detuning and intensity to

$$U_{dip} \propto \frac{\Gamma}{\Delta} I(\vec{r}) \tag{7.3}$$

$$\Gamma_{sc} \propto \left(\frac{\Gamma}{\Delta}\right)^2 I(\vec{r}) \tag{7.4}$$

and yields a simple relation of scattering rate and dipole potential

$$\hbar\Gamma_{sc} = \frac{\Gamma}{\Delta} U_{dip} \tag{7.5}$$

The two main points that should be taken from equation 7.3 and 7.4 here is first depending on the sign of the detuning the force is repellent (for blue detuning $\Delta > 0$) or attractive (for red detuning $\Delta < 0$) and second the scattering rate Γ_{sc} and the trapping potential U_{dip} scale differently with the dipole trap parameters Intensity $I(\vec{r})$ and detuning Δ. Given that the potential and therefore the trap depth scales like I/Δ whereas the scattering rate leading to heating in the trap scales with I/Δ^2 it is beneficial to work with far detuned and high intensity dipole traps.

The scattering of photons is the fundamental heating source in optical dipole traps where each photon absorption and spontaneous emission heats the atom in total by $2E_{rec}$ in the time of $1/\Gamma_{sc}$. At large detuning the scattering rate and therefore the heating by photons becomes negligible. The overall increase in temperature dT/dt in a 3D harmonic trap is given by [189]

$$\frac{dT}{dt} = \frac{T_{rec}\Gamma_{sc}}{3} \qquad (7.6)$$

The second source for heating is given by technical noise due to instabilities in the experimental setup [192]. Technical noise will be neglected in these considerations. Another problem in optical dipole traps can become density related particle losses. As previously discussed there are three loss mechanisms due to background collisions, two-body collisions and three-body collisions of which the later two are negligible for a wide density range covered in these type of experiments and only play a role in the last part of the evaporation (see figure 6.10 on the left).

The most popular way to create red detuned optical dipole traps are a focussed laser beam, a standing wave trap or two crossed beams. The easiest solution is the focussed, single beam trap that also has been realised in the context of this experiment.

The potential is then given by the intensity distribution of a Gaussian beam with w_0 being the beam waist, z_R the Rayleigh range and P the laser beam power (see section C).

At the bottom of the harmonic trap the particle distribution follows a Gaussian distribution with a standard deviation of σ_i and the temperature T of an atomic cloud in thermal equilibrium can be linked to the trap frequencies w_i inside the trap as

$$k_B T = m\sigma_i\omega_i \qquad (7.7)$$

The parameters of the actual setup are given in the following section. The scattering rate and the heating rate will be determined with the aid of the afore given equations.

7.2 Astigmatic setup

A detailed review of the dipole trap setup and characterisation is given in [64] and will only be discussed briefly in this section. For reasons discussed in [64] a red detuned focussed single beam trap has been realised here. Due to the desired two dimensional trap geometry a cylindrical lens produces an astigmatic effect resulting in two asymmetric foci.

A $1.55\mu m$ commercial $10W$ fibre amplifier[1], seeded by a laser diode, passes through

---

[1]PSFA-1550-15-10W-2-Z, Nufern
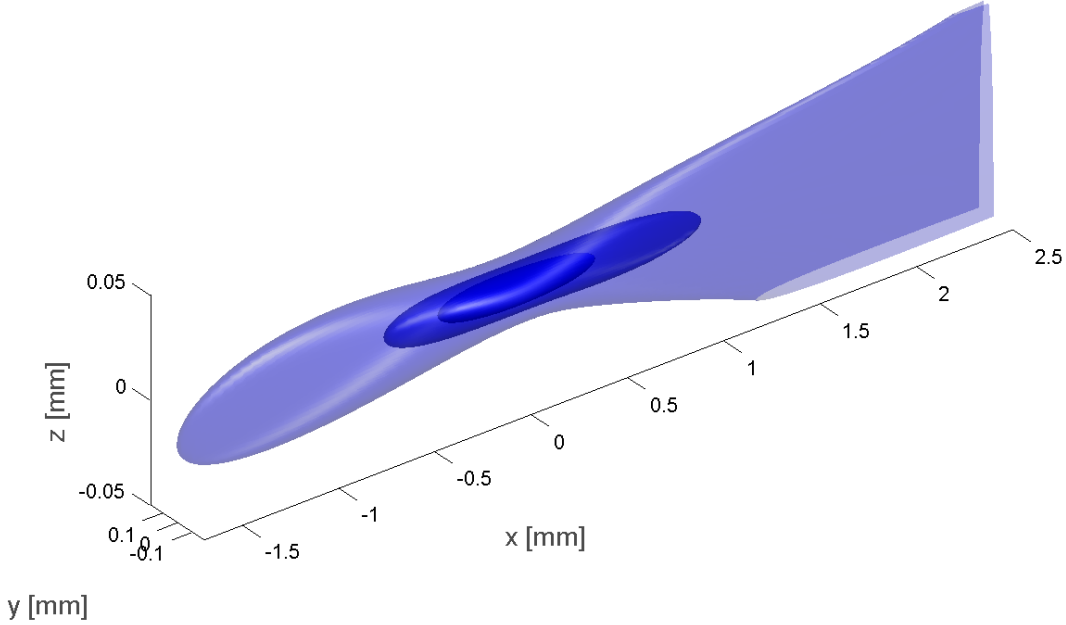
Figure 7.1: *Dipole trap potential:* Equipotential surface at 50%, 75% and 100% of the trap depth minimum. The total power is $P = 3.5W$ at $\lambda = 1550nm$ with a corresponding peak intensity in the trap centre of $I = 113kW/cm^2$. The trap depth minimum yields $E = 1/2k_B \, 93\mu K$.

a high power AOM and is then guided via an optical fibre towards the experiment. The optical setup at the experiment consists of a collimation lens of $f_{coll} = 100mm$, followed by a lens complex of a cylindrical lens with $f_{cyl} = 10m$ and the focussing lens of $f_{foc} = 200mm$. The high power AOM serves only fast switching purposes. The resulting two foci situated $4mm$ apart at $19.4cm$ and $19.8cm$ are elongated vertically and horizontally. The atoms are loaded into the second horizontally elongated focus with a beam waist of $w_{vert} = 11.4\mu m$ and $w_{horz} = 197.6\mu m$. The trap design fulfils the criteria for the investigation of 2D physics [64].

Equipotential surfaces of the dipole trap are depicted in figure 7.1. The displayed potential values are at 50%, 75% and 100% of the trap depth minimum of $E = 1/2k_B \, 93\mu K$ at a total power of $P = 3.5W$ and a corresponding peak intensity in the trap centre of $I = 113kW/cm^2$. In figure 7.2 the cut through the trap centre is shown. The x-direction is the propagation direction of the beam. The anisotropic trap geometry shown in figure 7.1 also helps with preventing heating
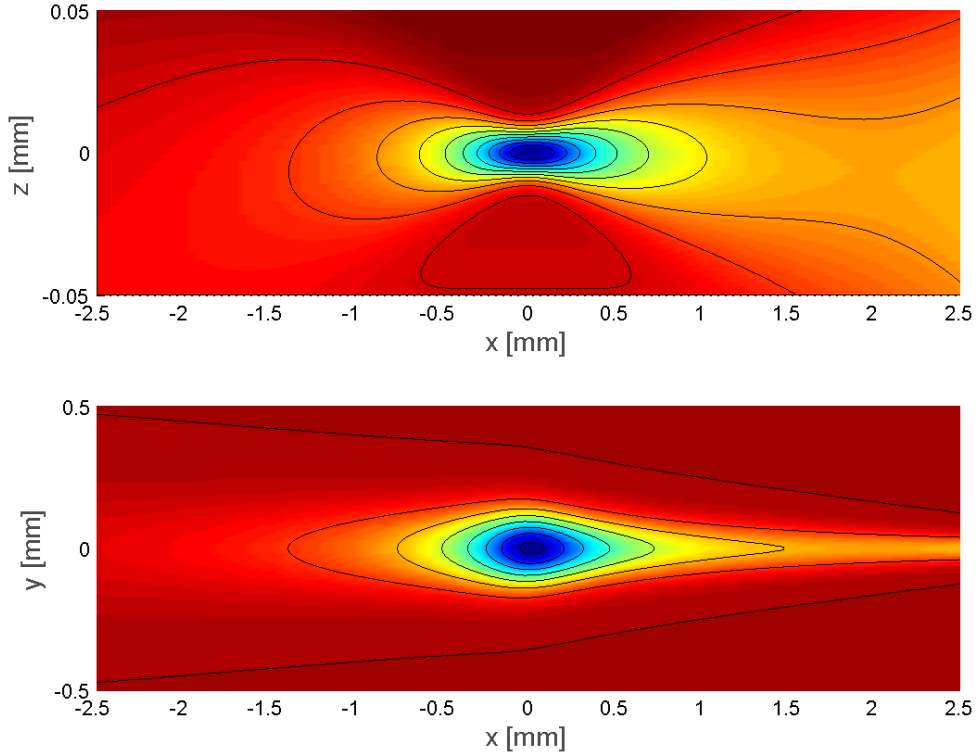
Figure 7.2: *Cut through dipole trap centre:* The x- axis is the direction of beam propagation. The anisotropic shape of the trap is clearly visible. The total power is $P = 3.5W$ at $\lambda = 1550nm$ with a corresponding peak intensity in the trap centre of $I = 113kW/cm^2$. The scattering rate $R_{sc} = 0.075s^{-}1$.

by reducing the escape distance of a scattered photon and therefore decreasing the probability for re-scattering events. The scattering rate Γ_{sc} given by equation 7.2 at a total power of $P = 3.5W$ with weighted Γ and ω_0 for the $D1$- and $D2$-line in ^{87}Rb yields $0.075s^{-}1$. The temperature increase over time (equation 7.6) with a recoil temperature of $T_{rec} = 362nK$ (see equation C.4) amounts to $dT/dt = 9nK/s$.

The trap depth given by the potential (see equation 7.1) at maximum power of $P = 3.5W$ is $T = 105\mu K$ and the expected trap frequencies are $f = 60Hz$ across the beam, $185Hz$ along the beam and vertically $f = 2.795kHz$. At the lowest confinement at minimum power of $P = 50mW$ the trap depth is $T = 1.6\mu K$ and the expected trap frequencies are $f = 6Hz$ across the beam, $f = 21.1Hz$ along the beam and $f = 288Hz$ vertically.
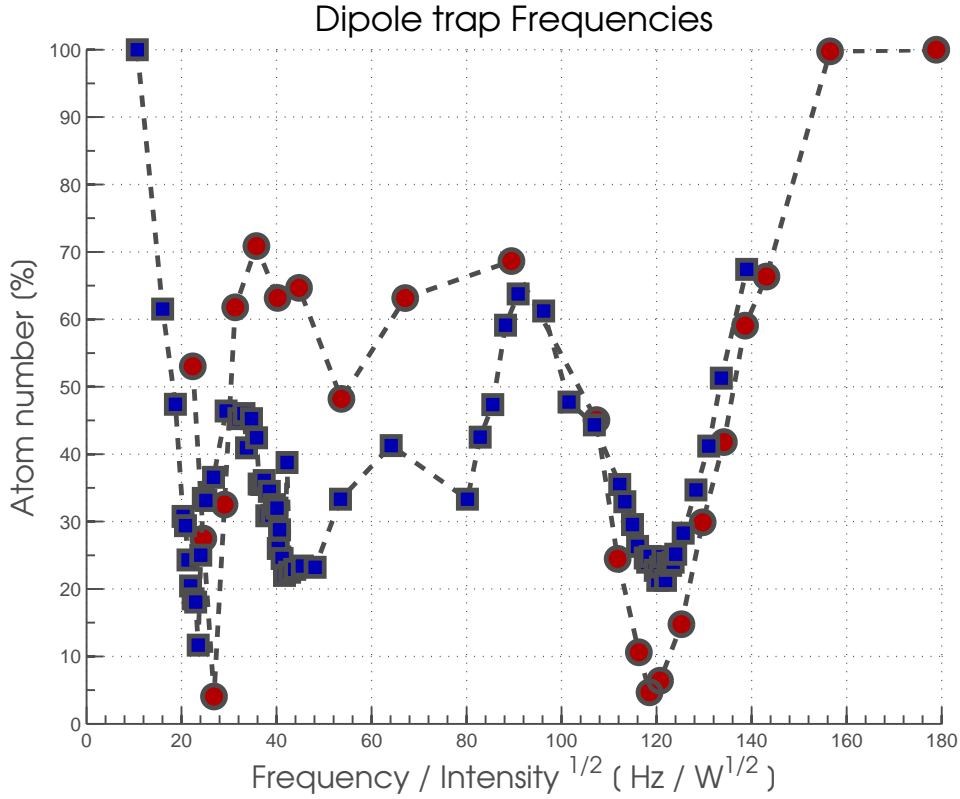
Figure 7.3: *Dipole trap frequencies:* Remaining atom number N against the modulation frequency f over intensity I of the dipole trap. The losses maximise at $28Hz/W$ and $120Hz/W$. These are expected to be related to the trap frequencies in the horizontal plane. For the details on the measurement refer to the text.

Experimentally the two lower trap frequencies have been measured in the strongest $(P = 3.5W)$ and the weakest $(P = 50mW)$ dipole trap by applying a modulation of a constant peak-to-peak value during a constant holding time. The frequency of the modulation varies but the number of cycles is held constant. The result for both cases is depicted in figure 7.3, in blue the strong confinement and in red the weak confinement. The frequency is rescaled over the square root of the intensity showing two overlapping minima at $\approx 26Hz/\sqrt{W}$ and $\approx 120Hz/\sqrt{W}$. The according frequencies for the individual measurements are $44Hz$ and $226Hz$ for the strong confinement, and $6Hz$ and $26.5Hz$ for the weak confinement.

This is in reasonable agreement with one time the theoretical trap frequencies but not twice the value as expected from parametric heating. Possible reasons might be optical imperfections or the anisotropic shape of the dipole trap.

The lifetime of a thermal cloud at the end of the third evaporation ramp is $\tau = 12.7s$.
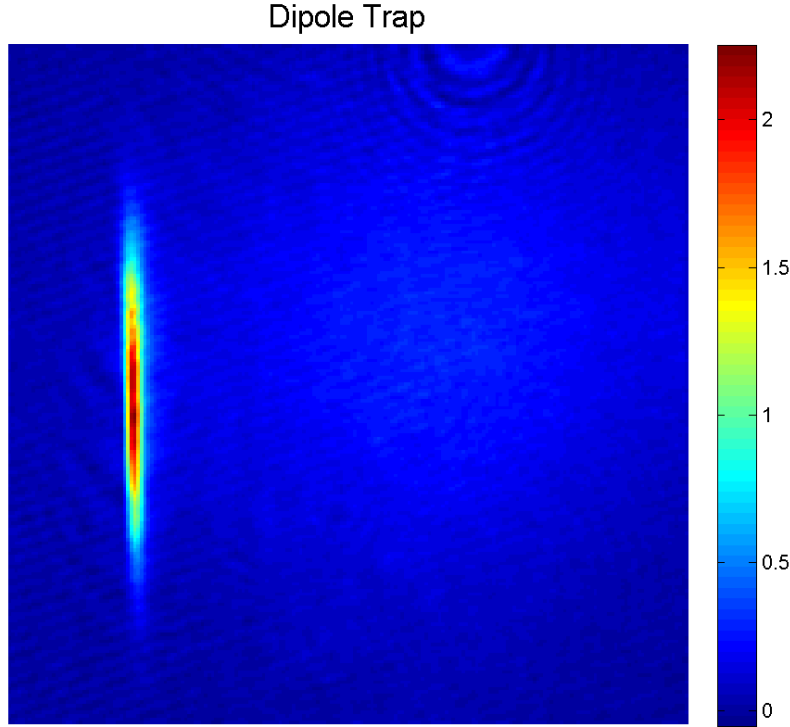
Figure 7.4: *Loaded dipole trap* The optical density at $t_{TOF} = 0s$. The elongated shape is clearly visible.

7.3 Reaching the BEC

As described before the dipole trap setup is focussed and aimed at an angle of approximately 45° towards the centre of the science chamber and of the magnetic trap formed by the Feshbach coils (see figure 6.8). For the evaporation it is important that the individual trap centres are aligned to each other, in order to avoid heating during the transfer of the magnetic trap to the dipole trap. If the centres of the two traps are misaligned the atoms can get heated or even lost by sloshing into the dipole trap.

The transfer efficiency yields 26% with $N_{Fesh} = 6.5 \cdot 10^6$ atoms in the Feshbach coils and $N_{DT} = 1.7 \cdot 10^6$ atoms in the dipole trap. Only the coolest atoms are transferred resulting in a decrease in temperature from $T_{Fesh} = 28 \mu K$ to $T_{DT} = 13 \mu K$ in the dipole trap. This can be seen as another evaporation step yielding a $PSD = 7.2 \cdot 10^{-6}$ as shown in figure 6.11.

The transfer from the magnetic trap to the dipole trap is not a compression of the atomic cloud since the overall trapping geometry and volume changes adiabatically. The entropy is conserved and the atoms keep in the thermal equilibrium while the population of different states changes and therefore a PSD density change can occur [193, 194].
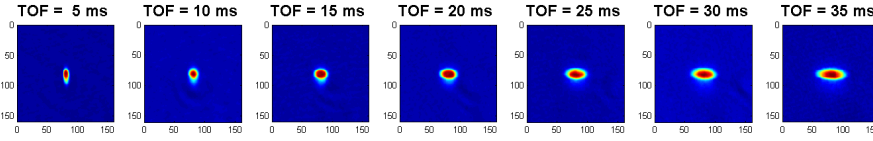
Figure 7.5: *BEC at different TOF times $t_{TOF} = 5ms$-$35ms$:* The aspect ratio of the BEC is changing over time from vertically elongated to horizontally elongated. The BEC contains $N_{BEC} = 3.5 \cdot 10^4$ atoms at a temperature of $T_{BEC} = 100nK$.

The initial atom distribution in the dipole trap at $t_{TOF} = 0s$ is shown in figure 7.4 and the asymmetric trap geometry is clearly visible. This is the starting point for further evaporation by lowering the trapping potential. The confinement is decreasing during the evaporation process and so does the density n. This procedure can turn out beneficial due to increasing three and two body losses at higher densities (see figure 6.10). The losses become important at the end of the sequence and therefore a fast evaporation is wanted.

The two evaporation ramps in the dipole trap can be found in table 6.1. The trap depth is ramped in $3s$ from initially 100% to 30% and the ensemble temperature decreases from $T = 13\mu K$ to $T = 4.5\mu K$ (⑥). The corresponding particle number changes from $N = 1.7 \cdot 10^6$ to $N = 8.5 \cdot 10^5$. In the successive and last $3s$ ramp down to $T_{depth} = 1.6\mu K$ (⑦) the cloud temperature decreases to $T = 100nK$ with $N_{BEC} = 3.5 \cdot 10^4$ atoms in the BEC and $N_{therm} = 2.2 \cdot 10^4$ residual thermal atoms. The PSD increases during step ⑥ to ⑧ from $PSD = 5.7 \cdot 10^{-4}$ across the needed PSD density for the creation of a BEC. The following holding time of 0.25s at the same potential strength serves re-thermalisation purposes (⑧).

In figure 7.5 the atomic ensemble is shown at different *time-of-flight* times developing the characteristic change of its aspect ratio from vertically to horizontally elongated during the expansion, rather than the typical ballistic expansion of thermal clouds. The smallest TOF time on the left is $5ms$ going in $5ms$ steps up to $35ms$ on the right. The temperature of the $N \approx 3.5 \cdot 10^4$ atoms in the BEC is around $T_{BEC} = 100nK$. The BEC fraction yields around 60%.

In figure 7.6 the lifetime measurement of the BEC (blue circles) next to the BEC fraction (red triangles) and BEC production rate (green squares) is depicted. The atom number in the BEC is fitted to an exponential decay yielding a lifetime of $\tau = 7s$. In the beginning the atom number is still growing. This is most likely due to ongoing collisions re-thermalising the atoms and a larger number of atoms populating the ground state. The BEC fraction is growing from 25% to stably above 75-90% with a 100% chance to create a BEC. The BEC lifetime might be limited due to heating of the dipole trap with $1.3nK/s$ at the lowest confinement of $50mW$ enabling atoms to leave the condensate but still stay in the trap. A
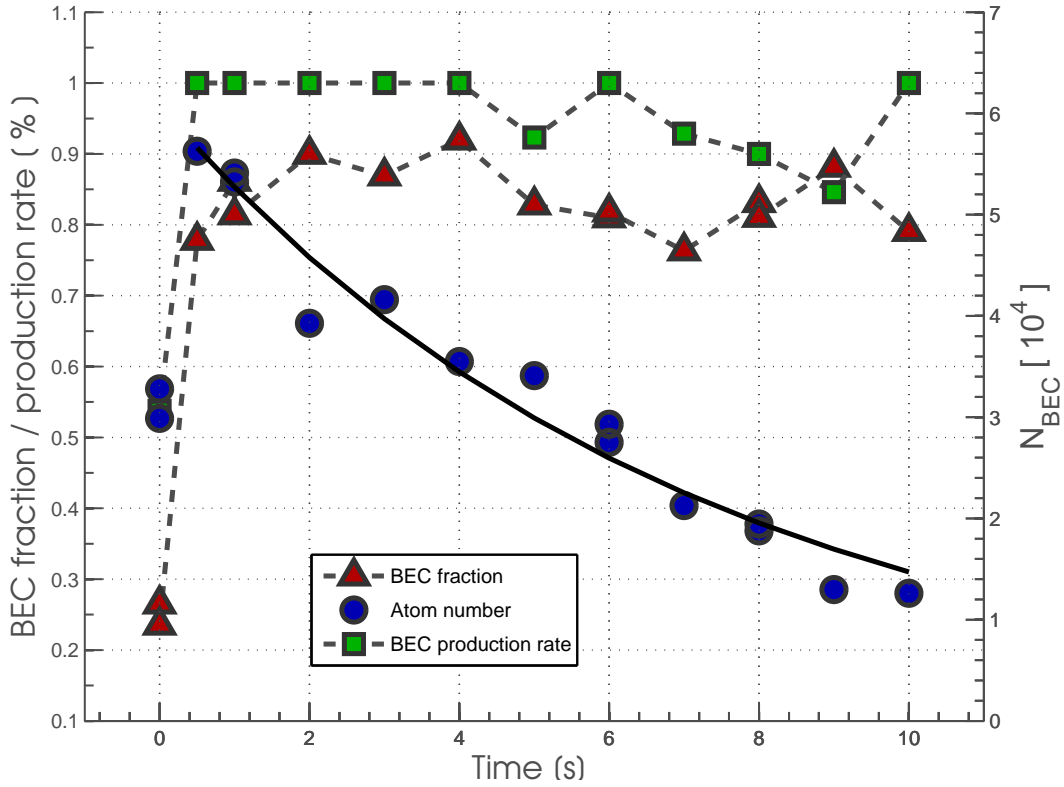
Figure 7.6: *BEC lifetime* in the dipole trap. In the beginning the absolute size and fraction of the BEC is growing due to ongoing collisions. The BEC fraction stays at high values above 75% with a production rate of 100%. The atom number in the BEC decays exponentially due to background collisions and heating in the dipole trap. The lifetime is $\tau \approx 7s$

tendency of a smaller BEC fraction strengthen the indication.

A constant RF field could lengthen the lifetime of a condensate by constantly removing thermal atoms and therefore encountering the heating effect of the atomic ensemble [123].

Heating due to background collisions at a rate of $1/\tau = 1/52s = 0.019$ can be neglected since the energy transfer E per collision assuming that all atoms stay trapped can correspond maximal to the temperature of $T = 1.6\mu K$ due to the according trap depth, otherwise the atom will be lost. The energy transfer is distributed in the entire cloud of $N = 5.7 \cdot 10^4$ atoms resulting in a heating rate of $0.5pK/s$.

Chapter 8

Summary and outlook

The main concern of this thesis is the construction and characterisation of a quantum simulator. In the progress a reliable creation of Bose-Einstein condensates at a temperature of $T_{BEC} = 100nK$ with $N_{BEC} = 3.5 \cdot 10^4$ ^{87}Rb atoms has been achieved.
Moreover Bose-Fermi mixtures of bosonic rubidium and fermionic potassium atoms in a magneto-optical trap have been realised. The individual ensembles contained $N_{Rb} = 1.3 \cdot 10^9$ rubidium and $N_K = 1.4 \cdot 10^6$ potassium atoms. For the production of the Bose-Einstein condensate the initial atomic ensembles have been laser cooled with divergent beams. The atomic cloud is successfully transported in a magnetic quadrupole trap and loaded into a astigmatic dipole trap where the trap frequencies have been measured.

In the context of this thesis the entire setup including a compact 2D-3D MOT vacuum complex, a robust, miniaturised dual species laser system and a compact coil design for magnetic transport has been setup and characterised.
Further improvements, extensions and upgrades are still in progress like the implementation of a high resolution imaging system for detection and manipulation with microscope objectives, an optical lattice confining the atoms in two dimensions and a spatial light modulator (SLM) for the application of arbitrary light fields.
With a tighter confinement in the disk shaped dipole trap and the SLM the behaviour of solitons will be soon investigated. Overall the setup reaches the quantum gas regime necessary for quantum simulations.

Appendix A

Level scheme for ^{87}Rb, ^{39}K and ^{40}K

	^{87}Rb	^{39}K	^{40}K
δ_1 [MHz]	-4271.7	-288.6	-571.5
δ_2 [MHz]	2563.0	+173.1	+714.3
δ_0' [MHz]	-302.1	-19.4	-46.6
δ_1' [MHz]	-229.9	-16.1	-2.3
δ_2' [MHz]	-72.9	-6.7	31.0
δ_3' [MHz]	+193.7	+14.4	+55.2
δ_{tot} [GHz]	6834.7	461.7	1285.8
δ_{tot}' [GHz]	495.8	33.8	101.6

Table A.1: *Hyperfine splitting of the D_2-line for ^{87}Rb, ^{39}K and ^{40}K:* The level scheme itself is very similar in between the species given that they are all alkali atoms. The values were taken from [77, 78] and are presented in a table in order to emphasize the nearly identical term scheme, only the energy scales vary going from one species to the other (compare δ_{tot} and δ_{tot}'). The larger HFS splitting are found in ^{87}Rb, followed by ^{40}K and ^{39}K showing the smallest splitting in the HFS structure. The values are given in comparison to the unsplit level $^2S_{1/2}$ respectively $^2P_{3/2}$. Remarkably there is only an addtional shift of 126 MHz in between the two excited states ($^2P_{3/2}$) of ^{39}K and ^{40}K. The point of reference for the ground state is for both isotopes identical.
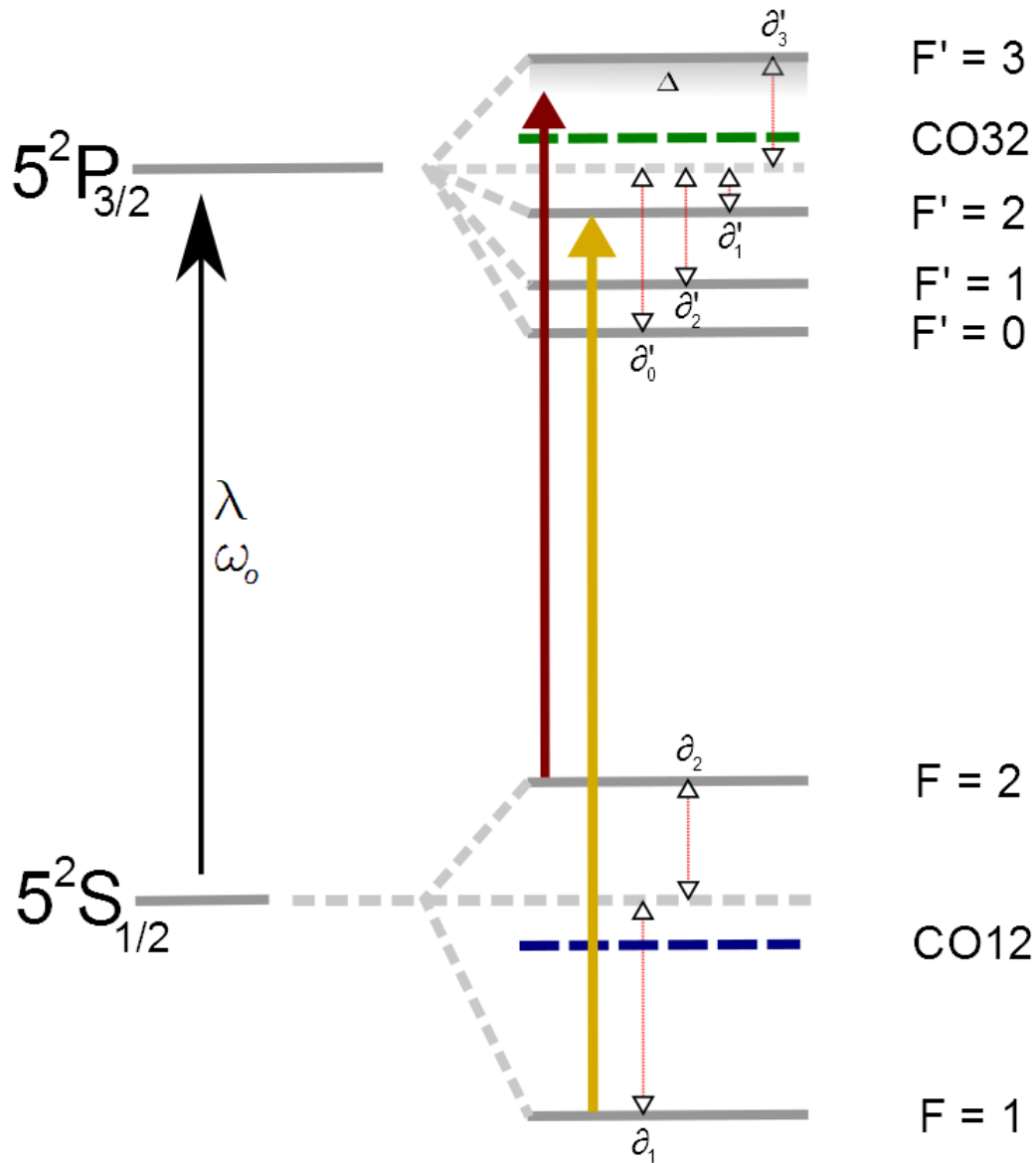
Figure A.1: *Level scheme of the D_2-line for the bosonic ^{87}Rb and ^{39}K:* It points out that both elements show the identical level structure with the same number of levels within the manifold structure due to the fact that they both are alkali atoms and share the same nuclear spin of 3/2. Only the magnitude of the splitting of the HFS manifold are different and can be found in table A.1. The numbers for the wavelength λ and the transition frequency ω_0 can be found in table 3.1. The red arrow indicates the cooling transition, the yellow one the repumper. Additional frequency shifting by the AOM is neglected. The detuning Δ of the cooling transition is controlled by the VCO frequency in the offset lock. The green dotted line indicates the position of the crossover transition in ^{87}Rb. The blue line shows the same for ^{39}K. In both cases is the master laser locked to this crossover transition.
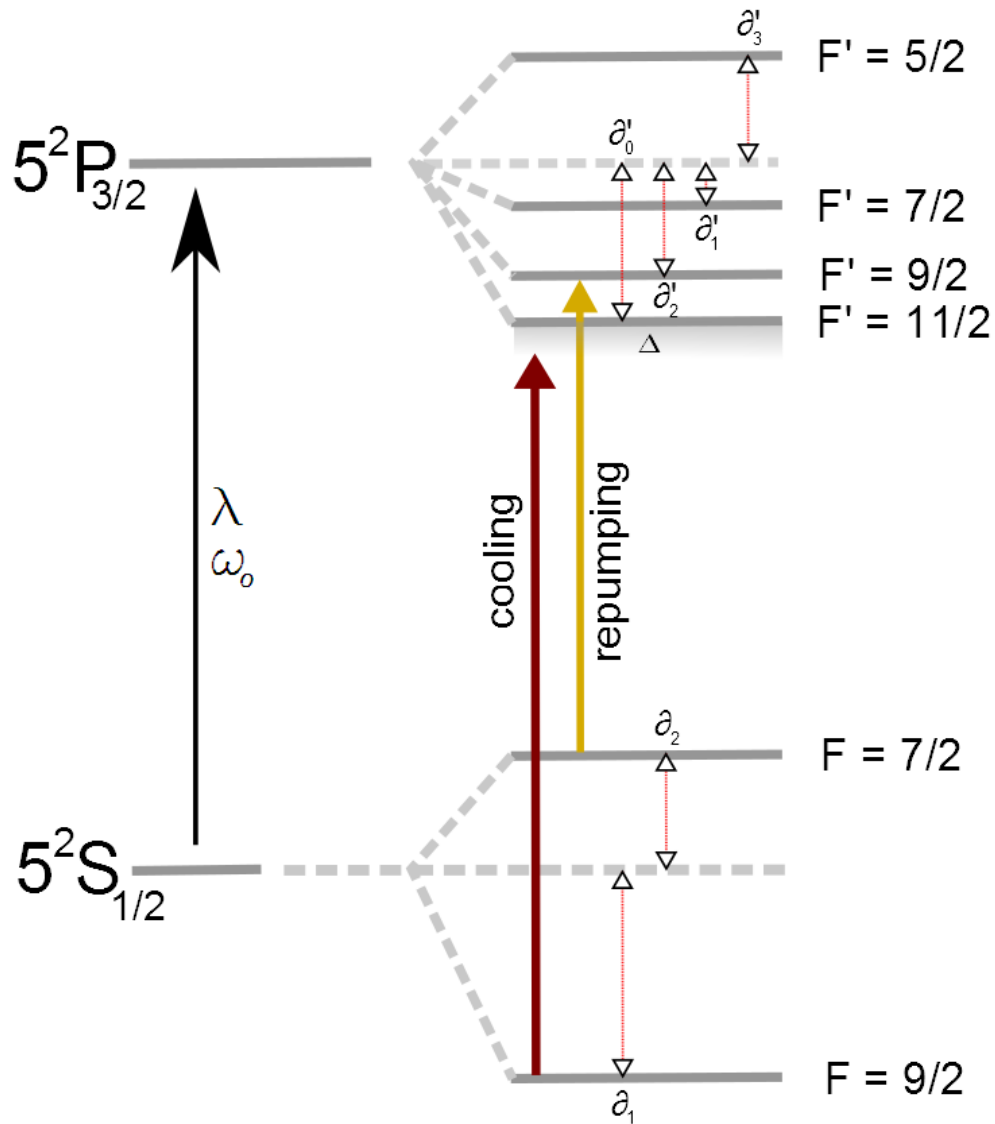
Figure A.2: *Level scheme of the D_2-line for the fermionic ^{40}K:* The level structure shows the same number of levels within the HFS manifolds like the bosonic ^{87}Rb and ^{39}K due to alkali atom nature. Only the nuclear spin of $I = 4$ inverts the hyperfine level structure. The values for the splitting of the HFS manifold can be found in table A.1. The numbers for the wavelength λ and the transition frequency ω_0 can be found in table 3.1. The red arrow indicates the cooling transition, the yellow one the repumper. Additional frequency shifting by the AOM is neglected. The detuning Δ of the cooling transition is controlled by the VCO frequency in the offset lock. Only 126 MHz separates the D_2-line transition in ^{40}K from ^{39}K

Appendix B

Validating the approximation for determination of the magnetic field gradient

Equation 4.7 in section 4.4 assumes an infinitely small winding which is a non-physical assumption but as it will be shown it is as expected a good approximation for wire sizes smaller than the distance of the coils.

For the coils realised in the context of this experiment flat wire is used with a width of $11mm$, a height of $0.254mm$ and a Kapton isolation of $25.4\mu m$ on one side of the wire. The width is much larger than the height. Therefore the considerations are only done for the width since the deviations are expected to be larger than for the width but the procedure for the height shall be analogue to the following. Replacing one winding by two windings carrying half the current I and being displaced by $\pm d$ further apart or closer to the centre of the coils equation 4.7 can be rewritten as

$$b_{1\,for\,2} = 3\mu_0 \frac{I}{2} R^2 \cdot \left(\frac{(A-d)}{(R^2 + (A-d)^2)^{(5/2)}} + \frac{(A+d)}{(R^2 + (A+d)^2)^{(5/2)}} \right) \quad \text{(B.1)}$$

If we divide equation B.1 by equation 4.7 it yields

$$\frac{b_{1\,for\,2}}{b_1} = \frac{1}{2} \cdot \frac{\frac{(A-d)}{(R^2+(A-d)^2)^{(5/2)}} + \frac{(A+d)}{(R^2+(A+d)^2)^{(5/2)}}}{\frac{A}{(R^2+A^2)^{(5/2)}}} \quad \text{(B.2)}$$

Expressing the radius in terms of the α parameter with $R = 2\alpha A$ and simplifying the equation gives the ratio in percent as

$$\frac{b_{1\,for\,2}}{b_1} = \frac{100}{2} \cdot \left[(1 - \frac{d}{A}) \cdot \left(\frac{A^2(4\alpha^2 + 1)}{(2\alpha A)^2 + (A-d)^2} \right)^{5/2} + (1 + \frac{d}{A}) \cdot \left(\frac{A^2(4\alpha^2 + 1)}{(2\alpha A)^2 + (A+d)^2} \right)^{5/2} \right]$$

APPENDIX B. VALIDATING THE APPROXIMATION FOR DETERMINATION OF THE MAGNETIC FIELD GRADIENT
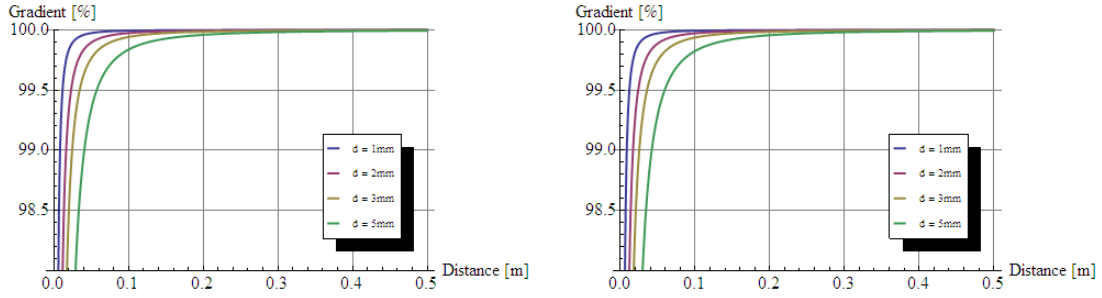
Figure B.1

The ratio is depicted in figure B.1 for α equal to 0.75 on the left and 1.25 on the right. The graphs within each plot are for different displacements d. A value of 100% indicates no deviation in between the two scenarios. It can be seen that for larger displacement d and smaller distances the deviation increases rapidly for distances smaller than $10cm$ because the displacement becomes more comparable to the distance. But in all cases relevant here with distances larger than $0.05m$ the deviation is smaller than 2% and the approximation is in good agreement.

For the specific case of the flat wire the maximum displacement is $d = \pm 5.5mm$. If the wire is interpreted as an infinite number of infinite small wires being displaced from $0mm$ to $5.5mm$ they will fulfil the approximation within a few %.

The approximation for distances larger than $10cm$ over a wide range of values for α is better than 1%.

161

Appendix C

Determination of parameters for magneto-optical trapping

The variables are used as the following. T is the temperature and P is the pressure of the gas, m is the mass and d is the diameter of the atom, k_B is the Boltzmann constant.

Maxwell-Boltzmann distribution The velocity probability distribution $p(v)$ of particles in a gas in thermal equilibrium with a temperature T and only interacting in two body elastic collisions is given by the Maxwell-Boltzmann distribution. The velocity of a particle is given by $v = \sqrt{v_x^2 + v_y^2 + v_z^2}$.

$$p(v) = 4\pi \sqrt{\left(\frac{m}{2\pi k_B T}\right)^3 v^2 \, exp\left(-\frac{mv^2}{2k_B T}\right)} \tag{C.1}$$

The root mean square speed is $v_{rms} = \sqrt{\frac{3k_B T}{m}}$.

Mean free path The mean free path l in between collisions in a gas that follows a Maxwell-Boltzmann distribution is

$$l = \frac{k_B T}{\sqrt{2}\pi d^2 P} \tag{C.2}$$

Recoil velocity and temperature The recoil velocity v_{rec} and temperature T_{rec} are gained or lost by an atom absorbing or emitting a resonant photon. With $|\vec{k}| = \frac{2\pi}{\lambda}$ being the wave vector of the light field the recoil velocity is given by

$$\vec{v}_{rec} = \frac{\hbar\vec{k}}{m} \tag{C.3}$$

162

And this relates to a temperature given by

$$T_{rec} = \frac{(\hbar \vec{k})^2}{m k_B} \tag{C.4}$$

Doppler temperature The Doppler temperature is reached in the magneto-optical trap if in the Doppler cooling picture of a two level atom the cooling rate is equal to the heating rate. It is given as

$$T_D = \frac{\hbar \Gamma}{2 k_B} \tag{C.5}$$

Gaussian beam The intensity profile of a Gaussian beam is given by

$$I(r, z) = I_0 \left(\frac{w_0}{w(z)} \right)^2 \exp \left(\frac{-2 r^2}{w^2(z)} \right) \tag{C.6}$$

where r is the radial coordinate and z the propagation direction of the beam. I_0 is the peak intensity, w_0 the smallest beam waist. The beam waist $w(z)$ evolves as

$$w(z) = w_0 \sqrt{1 + \left(\frac{z}{z_R} \right)^2} \tag{C.7}$$

where $z_R = \frac{\pi w_0^2}{\lambda}$ is the the so-called Rayleigh range. The power distribution $P(r, z)$ is given by

$$P(r, z) = P_0 \left[1 - \exp \left(\frac{-2 r^2}{w^2(z)} \right) \right] \tag{C.8}$$

$$P_0 = 1/2 \, \pi I_0 w_0^2 \tag{C.9}$$

with P_0 being the total power in the beam. With equation C.6 and C.9 the central intensity in a beam yields

$$I(0, z) = I_0 \left(\frac{w_0}{w(z)} \right)^2 \tag{C.10}$$

Appendix D

Constants

Speed of light	c	2.9979	$\cdot 10^8$	$\frac{m}{s}$
Planck constant	h	6.6261	$\cdot 10^{-24}$	Js
Permability of vacuum	μ_0	4π	$\cdot 10^{-7}$	$\frac{N}{A^2}$
Bohr magneton	μ_B	9.2740	$\cdot 10^{-24}$	$\frac{J}{T}$
Atomic mass unit	au	1.6605	$\cdot 10^{-27}$	kg
Boltzmann constant	k_B	1.3806	$\cdot 10^{-23}$	$\frac{J}{K}$
Bohr radius	a_0	5.2918	$\cdot 10^{-11}$	m
Gravitational constant	g	9.81		$\frac{m}{s^2}$
Electrical resistance (copper)	ρ	1.72	$\cdot 10^{-8}$	$\Omega \cdot m$

List of Figures

List of Tables

Bibliography

[1] R. P. Feynman. Simulating physics with computers. *International Journal of Theoretical Physics*, 21(6-7):467–488, 1982.

[2] J. Rudolph, N. Gaaloul, Y. Singh, H. Ahlers, W. Herr, T. A. Schulze, S. T. Seidel, C. Rode, V. Schkolnik, W. Ertmer, E. Rasel, H. Müntinga, T. Könemann, A. Resch, S. Herrmann, C. Lämmerzahl, T. van Zoest, H. Dittus, A. Vogel, A. Wenzlawski, K. Sengstock, N. Meyer, K. Bongs, M. Krutzik, W. Lewoczko-Adamczyk, M. Schiemangk, A. Peters, M. Eckart, E. Kajari, S. Arnold, G. Nandi, W. P. Schleich, R. Walser, T. Steinmetz, T. W. Hänsch, and J. Reichel. Degenerate Quantum Gases in Microgravity. *Microgravity Science and Technology*, 23(3):287–292, November 2010.

[3] H. Müntinga, H. Ahlers, M. Krutzik, A. Wenzlawski, S. Arnold, D. Becker, K. Bongs, H. Dittus, H. Duncker, N. Gaaloul, C. Gherasim, E. Giese, C. Grzeschik, T. W. Hänsch, O. Hellmig, W. Herr, S. Herrmann, E. Kajari, S. Kleinert, C. Lämmerzahl, W. Lewoczko-Adamczyk, J. Malcolm, N. Meyer, R. Nolte, A. Peters, M. Popp, J. Reichel, A. Roura, J. Rudolph, M. Schiemangk, M. Schneider, S. T. Seidel, K. Sengstock, V. Tamma, T. Valenzuela, A. Vogel, R. Walser, T. Wendrich, P. Windpassinger, W. Zeller, T. van Zoest, W. Ertmer, W. P. Schleich, and E. M. Rasel. Interferometry with Bose-Einstein Condensates in Microgravity. *Physical Review Letters*, 110(9):093602, February 2013.

[4] A.L. Schawlow and C. H. Townes. Infrared and Optical Masers. *Physical Review*, 112(6):1940, 1957.

[5] R. Frisch. Experimenteller Nachweis des Einsteinschen Strahlungsrückstoßes. *Zeitschrift für Physik*, 86(1-2):42–48, 1933.

[6] R. Grimm, J. Söding, and Y. B. Ovchinnikov. Coherent beam splitter for atoms based on a bichromatic standing light wave. *Optics letters*, 19(9):658–60, May 1994.

[7] R. Omori, T. Kobayashi, and A. Suzuki. Observation of a single-beam gradient-force optical trap for dielectric particles in air. *Optics letters*, 22(11):816–8, June 1997.

[8] D.E. Pritchard, E.L. Raab, V. Bagnato, C.E. Wieman, and R.N. Watts. Light traps using spontaneous forces. *Physical Review Letters*, 57(3):3–6, 1986.

[9] E.L. Raab, M. Prentiss, A. Cable, S. Chu, and D.E. Pritchard. Trapping of Neutral Sodium Atoms with Radiation Pressure. *Physical Review Letters*, 59(23):2631–2634, 1987.

[10] M.H. Anderson, J. R. Ensher, M. R. Matthews, C. E. Wieman, and E. A. Cornell. Observation of Bose-Einstein Condensation in a Dilute Atomic Vapor. *Science (New York, N.Y.)*, 269(5221):198–201, July 1995.

[11] K.B. Davis, M.-O. Mewes, M.R. Andrews, N.J. van Druten, D.S. Durfee, D.M. Kurn, and W. Ketterle. Bose-Einstein Condensation in a Gas of Sodium Atoms. *Physical Review Letters*, 75(22), 1995.

[12] A. Einstein. Quantentheorie des einatomigen idealen Gases Zweite Abhandlung. In *Sitzungsberichte der preussischen Akademie der Wissenschaften*, pages 3–10, 1925.

[13] S. Bose. Plancks Gesetz und Lichtquantenhypothese. *Zeitschrift für Physik*, 26:178, 1924.

[14] B. DeMarco. Onset of Fermi Degeneracy in a Trapped Atomic Gas. *Science*, 285(5434):1703–1706, September 1999.

[15] C. C. Bradley, C. A. Sackett, and R. G. Hulet. Bose-Einstein Condensation of Lithium: Observation of Limited Condensate Number. *Physical Review Letters*, 78(6):985–989, 1997.

[16] M.-S. Heo, J.-Y. Choi, and Y.-I Shin. Fast production of large ^{23}Na Bose-Einstein condensates in an optically plugged magnetic quadrupole trap. *Physical Review A*, 83(1):013622, January 2011.

[17] G. Roati, M. Zaccanti, C. D'Errico, J. Catani, M. Modugno, A. Simoni, M. Inguscio, and G. Modugno. ^{39} k bose-einstein condensate with tunable interactions. *Physical Review Letters*, 99(1):010403, July 2007.

[18] G. Modugno, G. Ferrari, G. Roati, R. J. Brecha, A. Simoni, and M. Inguscio. Bose-Einstein condensation of potassium atoms by sympathetic cooling. *Science (New York, N.Y.)*, 294(5545):1320–2, November 2001.

170

[19] S. L. Cornish, N. R. Claussen, J. L. Roberts, E. A. Cornell, and C. E. Wieman. Stable ^{85}Rb Bose-einstein condensates with widely tunable interactions. *Physical review letters*, 85(9):1795–8, August 2000.

[20] A. Griesmaier, J. Werner, S. Hensler, J. Stuhler, and T. Pfau. Bose-Einstein Condensation of Chromium. *Physical Review Letters*, 94(16):160401, April 2005.

[21] D. J. McCarron, H. W. Cho, D. L. Jenkin, M. P. Köppinger, and S. L. Cornish. Dual-species Bose-Einstein condensate of ^{87}Rb and ^{133}Cs. *Physical Review A*, 84(1):011603, July 2011.

[22] S. Kraft, F. Vogt, O. Appel, F. Riehle, and U. Sterr. Bose-Einstein Condensation of Alkaline Earth Atoms: ^{40}Ca. *Physical Review Letters*, 103(13):130401, September 2009.

[23] J. Goldwin, S. Papp, B. DeMarco, and D. Jin. Two-species magneto-optical trap with ^{40}K and ^{87}Rb. *Physical Review A*, 65(2):021402, January 2002.

[24] M. Greiner, C. A. Regal, and D. S. Jin. Emergence of a molecular Bose-Einstein condensate from a Fermi gas. *Nature*, 426(6966):537–40, December 2003.

[25] T. Stöferle, H. Moritz, K. Günter, M. Köhl, and T. Esslinger. Molecules of Fermionic Atoms in an Optical Lattice. *Physical Review Letters*, 96(3):030401, January 2006.

[26] S. Ospelkaus, C. Ospelkaus, R. Dinter, J. Fuchs, M. Nakat, K. Sengstock, and K. Bongs. Degenerate KRb Fermi Bose gas mixtures with large particle numbers. *Journal of Modern Optics*, 54(5):661–673, March 2007.

[27] I. Bloch, M. Greiner, O. Mandel, T. Esslinger, and T. W. Hänsch. Quantum phase transition from a superfluid to a Mott insulator in a gas of ultracold atoms. *Nature*, 415:39–44, 2002.

[28] Q. Chen, J. Stajic, S. Tan, and K. Levin. BCS-BEC crossover: From high temperature superconductors to ultracold superfluids. *Physics Reports*, 412(1):1–88, June 2005.

[29] J. K. Chin, D. E. Miller, Y. Liu, C. Stan, W. Setiawan, C. Sanner, K Xu, and W Ketterle. Evidence for superfluidity of ultracold fermions in an optical lattice. *Nature*, 443(7114):961–4, October 2006.

171

[30] M. Lewenstein, A. Sanpera, V. Ahufinger, B. Damski, A. Sen(De), and U. Sen. Ultracold atomic gases in optical lattices: mimicking condensed matter physics and beyond. *Advances in Physics*, 56(2):243–379, March 2007.

[31] D. Jaksch, C. Bruder, J. Cirac, C. Gardiner, and P. Zoller. Cold Bosonic Atoms in Optical Lattices. *Physical Review Letters*, 81(15):3108–3111, October 1998.

[32] I. Bloch. Ultracold quantum gases in optical lattices. *Nature Physics*, 1, 2005.

[33] L. Santos, M. Baranov, J. Cirac, H.-U. Everts, H. Fehrmann, and M. Lewenstein. Atomic Quantum Gases in Kagomé Lattices. *Physical Review Letters*, 93(3):030601, July 2004.

[34] S. Inouye, M. R. Andrews, J. Stenger, H. Miesner, and W. Ketterle. Observation of Feshbach resonances in a Bose Einstein condensate. *Nature*, 392:8–11, 1998.

[35] A. Simoni. Magnetic Control of the Interaction in Ultracold K-Rb Mixtures. *Physical Review Letters*, 90(16):1–4, April 2003.

[36] S. Inouye, J. Goldwin, M. Olsen, C. Ticknor, J. Bohn, and D. Jin. Observation of Heteronuclear Feshbach Resonances in a Mixture of Bosons and Fermions. *Physical Review Letters*, 93(18):183201, October 2004.

[37] P.-J. Wang, Z.-K. Fu, S.-J. Chai, and J. Zhang. Feshbach resonances in an ultracold mixture of ^{87}Rb and ^{40}K. *Chinese Physics B*, 20(10):103401, October 2011.

[38] C. A. Regal, M. Greiner, and D. S. Jin. Observation of Resonance Condensation of Fermionic Atom Pairs. *Physical Review Letters*, 92(4):040403, January 2004.

[39] A. N. Wenz, G. Zürn, S. Murmann, I. Brouzos, T. Lompe, and S. Jochim. From few to many: observing the formation of a Fermi sea one atom at a time. *Science (New York, N.Y.)*, 342(6157):457–60, October 2013.

[40] S. Hofferberth, I. Lesanovsky, B. Fischer, T. Schumm, and J. Schmiedmayer. Non-equilibrium coherence dynamics in one-dimensional Bose gases. *Nature*, 449(7160):324–7, September 2007.

[41] A. Polkovnikov, K. Sengupta, A. Silva, and M. Vengalattore. Colloquium: Nonequilibrium dynamics of closed interacting quantum systems. *Reviews of Modern Physics*, 83(3):863–883, August 2011.

[42] G. Wilpers, T. Binnewies, C. Degenhardt, U. Sterr, J. Helmcke, and F. Riehle. Optical Clock with Ultracold Neutral Atoms. *Physical Review Letters*, 89(23):230801, November 2002.

[43] M. Takamoto, F.-L. Hong, R. Higashi, and H. Katori. An optical lattice clock. *Nature*, 435(7040):321–4, May 2005.

[44] G.M. Tino, L. Cacciapuoti, K. Bongs, C. J. Bordé, P. Bouyer, H. Dittus, W. Ertmer, A. Görlitz, M. Inguscio, A. Landragin, P. Lemonde, C. Lammerzahl, A. Peters, E. Rasel, J. Reichel, C. Salomon, S. Schiller, W. Schleich, K. Sengstock, U. Sterr, and M. Wilkens. Atom interferometers and optical atomic clocks: New quantum sensors for fundamental physics experiments in space. *Nuclear Physics B - Proceedings Supplements*, 166:159–165, April 2007.

[45] S. Ospelkaus, K.-K. Ni, D. Wang, M. H. G. de Miranda, B. Neyenhuis, G. Quéméner, P. S. Julienne, J. L. Bohn, D. S. Jin, and J. Ye. Quantum-state controlled chemical reactions of ultracold potassium-rubidium molecules. *Science (New York, N.Y.)*, 327(5967):853–7, February 2010.

[46] D. DeMille. Quantum Computation with Trapped Polar Molecules. *Physical Review Letters*, 88(6):067901, January 2002.

[47] S. Diehl, A. Micheli, A. Kantian, B. Kraus, H. P. Büchler, and P. Zoller. Quantum states and phases in driven open quantum systems with cold atoms. *Nature Physics*, 4(11):878–883, September 2008.

[48] I. Buluta and F. Nori. Quantum simulators. *Science (New York, N.Y.)*, 326(5949):108–11, October 2009.

[49] J. Struck, C. Ölschläger, R. Le Targat, P. Soltan-Panahi, A. Eckardt, M. Lewenstein, P. Windpassinger, and K. Sengstock. Quantum simulation of frustrated classical magnetism in triangular optical lattices. *Science (New York, N.Y.)*, 333(6045):996–9, August 2011.

[50] I. Bloch, J. Dalibard, and S. Nascimbène. Quantum simulations with ultracold quantum gases. *Nature Physics*, 8(4):267–276, April 2012.

[51] G. Huang, V. Makarov, and M. Velarde. Two-dimensional solitons in Bose-Einstein condensates with a disk-shaped trap. *Physical Review A*, 67(2):023604, February 2003.

[52] U. Gavish and Y. Castin. Matter-Wave Localization in Disordered Cold Atom Lattices. *Physical Review Letters*, 95(2):1–4, July 2005.

173

[53] G. Roati, C. D'Errico, L. Fallani, M. Fattori, C. Fort, M. Zaccanti, G. Modugno, M. Modugno, and M. Inguscio. Anderson localization of a non-interacting Bose-Einstein condensate. *Nature*, 453(7197):895–8, June 2008.

[54] B. Damski, J. Zakrzewski, L. Santos, P. Zoller, and M. Lewenstein. Atomic Bose and Anderson Glasses in Optical Lattices. *Physical Review Letters*, 91(8):080403, August 2003.

[55] A. Schirotzek, C.-H. Wu, A. Sommer, and M. W. Zwierlein. Observation of Fermi Polarons in a Tunable Fermi Liquid of Ultracold Atoms. *Physical Review Letters*, 102(23):1–4, June 2009.

[56] K. B. Davis, M. O. Mewes, M. A. Joffe, M. R. Andrews, and W. Ketterle. Evaporative cooling of sodium atoms. *Physical review letters*, 74(26):5202–5205, June 1995.

[57] W. Petrich, M. H. Anderson, J. R. Ensher, and E. A. Cornell. Stable, Tightly Confining Magnetic Trap for Evaporative Cooling of Neutral Atoms. *Physical Review Letters*, 74(17), 1995.

[58] C. Myatt, E. Burt, R. Ghrist, E. Cornell, and C. Wieman. Production of Two Overlapping Bose-Einstein Condensates by Sympathetic Cooling. *Physical Review Letters*, 78(4):586–589, January 1997.

[59] A. G. Truscott, K. E. Strecker, W. I. McAlexander, G. B. Partridge, and R. G. Hulet. Observation of Fermi pressure in a gas of trapped atoms. *Science (New York, N.Y.)*, 291(5513):2570–2, March 2001.

[60] F. Schreck, L. Khaykovich, K. L. Corwin, G. Ferrari, T. Bourdel, J. Cubizolles, and C. Salomon. Quasipure Bose-Einstein Condensate Immersed in a Fermi Sea. *Physical Review Letters*, 87(8):080403, August 2001.

[61] S. Stellmer, B. Pasquiou, R. Grimm, and F. Schreck. Laser cooling to quantum degeneracy. *Phys. Rev. Lett. 110*, 110(263003):1–18, 2013.

[62] M. Holynski. *Creating a two dimensional cold mixture experiment*. PhD thesis, University of Birmingham, 2012.

[63] A. Vogel. *Bose-Einstein condensates for space applications and novel teaching concepts*. PhD thesis, University of Hamburg, 2009.

[64] M. Baumert. *Dipole traps and optical lattices for quantum simulations*. PhD thesis, University of Birmingham, 2012.

[65] B. O. Kock. *Magneto-Optical Trapping Of Strontium For Use As A Mobile Frequency Reference.* PhD thesis, University of Birmingham, 2013.

[66] K. Dieckmann, R. Spreeuw, M. Weidemüller, and J. Walraven. Two-dimensional magneto-optical trap as a source of slow atoms. *Physical Review A*, 58(5):3891–3895, November 1998.

[67] J. Schoser, A. Batär, R. Löw, V. Schweikhard, A. Grabowski, Y. Ovchinnikov, and T. Pfau. Intense source of cold Rb atoms from a pure two-dimensional magneto-optical trap. *Physical Review A*, 66(2):023410, August 2002.

[68] S. G. Cox, P. F. Griffin, C. S. Adams, D. DeMille, and E. Riis. Reusable ultra-high vacuum viewport bakeable to 240°C. *Review of Scientific Instruments*, 74(6):3185, 2003.

[69] NASA. Outgassing Data for Selecting Spacecraft Materials. `http://outgassing.nasa.gov/`, 2013.

[70] P. Hommelhoff. *Bose-Einstein-Kondensate in Mikrochip-Fallen.* PhD thesis, Ludwig-Maximilians-University Munich, 2002.

[71] H. A. Adam, S. Kaufman, and B. S. Liley. Indium seals for dismountable vacuum systems. *Journal of scientific instruments*, 34:123, 1957.

[72] H. Saeki, J. Ikeda, and H. Ishimaru. Optical window sealed with indium for ultrahigh vacuum. *Vacuum*, 39(6):563–564, 1989.

[73] WebElement: the periodic table on the web. `www.webelements.com/indium/physics.html`. Accessed 14-01-2014.

[74] WebElement: the periodic table on the web. `www.webelements.com/copper/physics.html`. Accessed 14-01-2014.

[75] B. Kaltenhäuser, H. Kübler, A. Chromik, J. Stuhler, and T. Pfau. Low retaining force optical viewport seal. *The Review of scientific instruments*, 78(046107), April 2007.

[76] T. van Zoest, N. Gaaloul, Y. Singh, H. Ahlers, W. Herr, S. T. Seidel, W. Ertmer, E. Rasel, M. Eckart, E. Kajari, S. Arnold, G. Nandi, W. P. Schleich, R. Walser, A. Vogel, K. Sengstock, K. Bongs, W. Lewoczko-Adamczyk, M. Schiemangk, T. Schuldt, A. Peters, T. Könemann, H. Müntinga, C. Lämmerzahl, H. Dittus, T. Steinmetz, T. W. Hänsch, and J. Reichel. Bose-Einstein condensation in microgravity. *Science (New York, N.Y.)*, 328(5985):1540–3, June 2010.

[77] D. A. Steck. Rubidium 87 D Line Data. `http://steck.us/alkalidata`, 2010.

[78] T. G. Tiecke. Properties of Potassium. `http://staff.science.uva.nl/~tgtiecke/PotassiumProperties.pdf`, 2010.

[79] G. C. Bjorklund, M. D. Levenson, W. Lenth, and C. Ortiz. Frequency modulation (FM) spectroscopy. *Applied Physics B Photophysics and Laser Chemistry*, 32(3):145–152, November 1983.

[80] L. Mudarikwa, K. Pahwa, and J. Goldwin. Sub-Doppler modulation spectroscopy of potassium for laser stabilization. *Journal of Physics B: Atomic, Molecular and Optical Physics*, 45:065002, 2012.

[81] P. Zorabedian and W. R. Trutna. Interference-filter-tuned, alignment-stabilized, semiconductor external-cavity laser. *Optics letters*, 13(10):826–828, 1988.

[82] X. Baillard, A. Gauguet, S. Bize, P. Lemonde, P. Laurent, A. Clairon, and P. Rosenbusch. Interference-filter-stabilized external-cavity diode lasers. *Optics Communications*, 266(2):609–613, October 2006.

[83] M. Gilowski, C. Schubert, M. Zaiser, W. Herr, T. Wübbena, T. Wendrich, T. Müller, E.M. Rasel, and W. Ertmer. Narrow bandwidth interference filter-stabilized diode laser systems for the manipulation of neutral atoms. *Optics Communications*, 280(2):443–447, December 2007.

[84] M. Hauth. Entwicklung eines Lasersystems für das Space-Atom-Interferometer. Diploma thesis,Universiy of Hamburg.

[85] T. W. Hänsch, M. D. Levenson, and A. L. Schawlow. Complete Hyperfine Structure of a molecular Iodine Line. *Physical Review Letters*, 26(16):946, 1971.

[86] T.W. Hänsch, I.S. Shahin, and A.L. Schawlow. High-Resolution Saturation Spectroscopy of the sodium D lines with a pulsed tunable dye laser. *Physical Review Letters*, 27(11):707–710, 1971.

[87] T.W. Hänsch, I.S. Shahin, and A.L. Schawlow. Optical Resolution of the Lamb Shift in Atomic Hydrogen by Laser saturation spectrsocopy. *Nature Physical Science*, 235:63–35, 1972.

[88] G. C. Bjorklund. Frequency-modulation spectroscopy: a new method measuring weak absorptions and dispersions. *Optics letters*, 5(1):15–17, 1980.

[89] J. L. Hall, L. Hollberg, T. Baer, and H.G. Robinson. Optical heterodyne saturation spectroscopy. *Applied Physics Letters*, 39(9):680, 1981.

[90] S. Kraft, A. Deninger, C. Trück, J. Fortágh, F. Lison, and C. Zimmermann. Rubidium spectroscopy at 778 to 780 nm with a distributed feedback laser diode. *Laser Physics Letters*, 2(2):71–76, February 2005.

[91] G. Ritt, G. Cennini, C. Geckeler, and M. Weitz. Laser frequency offset locking using a side of filter technique. *Applied Physics B*, 79(3):363–365, June 2004.

[92] R. Matthey, C. Affolderbach, and G. Mileti. Methods and evaluation of frequency aging in distributed-feedback laser diodes for rubidium atomic clocks. *Optics letters*, 36(17):3311–3, September 2011.

[93] R. W. Tkach and A. R. Chraplyvy. Regimes of Feedback Effects in 1.5 μm Distributed Feedback lasers. *Journal of Lightwave Technology*, LT-4(11), 1986.

[94] C. K. Laue, R. Knappe, K. J. Boller, and R. Wallenstein. Wavelength tuning and spectral properties of distributed feedback diode lasers with a short external optical cavity. *Applied optics*, 40(18):3051–9, June 2001.

[95] T. Okoshi, K. Kikuchi, and A. Nakayama. Novel method for high resolution measurement of laser output spectrum. *Electronics Letters*, 16(16):630–631, 1980.

[96] Wolfgang Demtröder. *Laserspectroscopy*. Springer, Heidelberg, 2010.

[97] G. Stéphan, T. Tam, S. Blin, P. Besnard, and M. Têtu. Laser line shape and spectral density of frequency noise. *Physical Review A*, 71(4):043809, April 2005.

[98] N. Y. Voo, P. Horak, M. Ibsen, and W. H. Loh. Linewidth and Phase Noise Characteristics of DFB Fibre Lasers. Technical report, Optoelectronics Research Centre, University of Southampton, Southampton.

[99] G. Santarelli, A. Clairon, S.N. Lea, and G.M. Tino. Heterodyne optical phase-locking of extended-cavity semiconductor lasers at 9 GHz. *Optics Communications*, 104(4-6):339–344, January 1994.

[100] A. C. Wilson, J. C. Sharpe, C. R. Mckenzie, P. J. Manson, and D. M. Warrington. Narrow-Linewidth master-oscillator power amplifier based on a semiconductor tapered amplifier. *Applied Optics*, 37(21):4871–4875, 1998.

[101] D. Voigt, E.C. Schilder, R.J.C. Spreeuw, and H.B. van Linden van den Heuvell. Characterization of a high-power tapered semiconductor amplifier system. *Applied Physics B*, 72(3):279–284, February 2001.

[102] Y. Xiong. Design and characteristics of a tapered amplifier diode system by seeding with continuous-wave and mode-locked external cavity diode laser. *Optical Engineering*, 45(12):124205, December 2006.

[103] John Malcolm. Isence project, university of birmingham. Personal communication, 2013.

[104] S. Ospelkaus-Schwarzer. *Quantum Degenerate Fermi-Bose Mixtures of ^{40}K and ^{87}Rb in 3D Optical Lattices.* PhD thesis, University of Hamburg, 2006.

[105] M. Perea. *To be published.* PhD thesis, University of Birmingham, 2014.

[106] W. Ketterle, S. Durfee, and M. Stamper. Making, probing and understanding Bose-Einstein condensates. *arXiv:cond-mat*, 9904034v2, 1999.

[107] H.J. Metcalf and P. van der Straten. *Laser cooling and trapping.* Springer, Heidelberg, 2001.

[108] M. Erhard. *Experimente mit mehrkomponentigen Bose-Einstein Kondensaten.* PhD thesis, University of Hamburg, 2004.

[109] C. G. Townsend, N.H. Edwards, C.J.Cooper, K.P. Zetie, C.J. Foot, A. M. Steane, P. Szriftgiser, H. Perrin, and J. Dalibard. Phase-space density in the magneto-optical trap. *Physical Review A*, 52(2), 1995.

[110] M. Greiner, I. Bloch, T. Hänsch, and T. Esslinger. Magnetic transport of trapped cold atoms over a large distance. *Physical Review A*, 63(3):1–4, February 2001.

[111] H. J. Lewandowski, D. M. Harber, D. L. Whitaker, and E. A. Cornell. Simplified System for Creating a Bose Einstein Condensate. *Journal of Low Temperature Physics*, 132(5-6), 2003.

[112] J. Goldwin, S. Inouye, M. Olsen, B. Newman, B. DePaola, and D. Jin. Measurement of the interaction strength in a Bose-Fermi mixture with ^{87}Rb and ^{40}K. *Physical Review A*, 70(2):021601, August 2004.

[113] K. Nakagawa, Y. Suzuki, M. Horikoshi, and J.B. Kim. Simple and efficient magnetic transport of cold atoms using moving coils for the production of Bose Einstein condensation. *Applied Physics B*, 81(6):791–794, September 2005.

[114] J. Bertelsen, H. Andersen, S. Mai, and M. Budde. Mixing of ultracold atomic clouds by merging of two magnetic traps. *Physical Review A*, 75(1):1–11, January 2007.

[115] S. Händel, T. Wiles, A. Marchant, S. Hopkins, C. Adams, and S. Cornish. Magnetic merging of ultracold atomic gases of ^{85}Rb and ^{87}Rb. *Physical Review A*, 83(5):053633, May 2011.

[116] T. Lahaye, G. Reinaudi, Z. Wang, A. Couvert, and D. Guéry-Odelin. Transport of atom packets in a train of Ioffe-Pritchard traps. *Physical Review A*, 74(3):033622, September 2006.

[117] D. Chen, H. Zhang, X. Xu, T. Li, and Y. Wang. Nonadiabatic transport of cold atoms in a magnetic quadrupole potential. *Applied Physics Letters*, 96(13), 2010.

[118] A. L. Migdall, J. V. Prodan, D. Phillips, and T. H. Bergeman. First Obsevation of Magnetically Trapped Neutral Atoms. *Physical Review Letters*, 54(24), 1985.

[119] W. H. Wing. On neutral particle trapping in quasistatic electromagnetic fields. *Progress in Quantum Electronics*, 8:181–199, January 1984.

[120] Y.-J. Lin, A. Perry, R. Compton, I. Spielman, and J. Porto. Rapid production of ^{87}Rb Bose-Einstein condensates in a combined magnetic and optical potential. *Physical Review A*, 79(6):1–8, June 2009.

[121] D. E. Pritchard. Cooling Neutral Atoms in a Trap for Precision Spectroscopy. *Physical Review Letters*, 51(15), 1983.

[122] T. Bergeman and H.J. Metcalf. Magnetostatic trapping field for neutral atoms. *Physical Review A*, 35(4), 1987.

[123] M. Mewes, M.R. Andrews, N. J. van Druten, D. M. Kurn, D.S. Durfee, and W. Ketterle. Bose-Einstein Condensation in a Tightly Confining dc Magnetic Trap. *Physical review letters*, 77(3):416–419, July 1996.

[124] T. Esslinger, I. Bloch, and T. W. Hänsch. Bose-Einstein condensation in a quadrupole-Ioffe-configuration trap. *Physical Review A*, 58(4):2664–2667, 1998.

[125] C. D'Errico, M. Zaccanti, M. Fattori, G. Roati, M. Inguscio, G. Modugno, and A. Simoni. Feshbach resonances in ultracold ^{39} K. *New Journal of Physics*, 9(7):223–223, July 2007.

[126] A. Marte, T. Volz, J. Schuster, S. Dürr, G. Rempe, E. van Kempen, and B. Verhaar. Feshbach Resonances in Rubidium 87: Precision Measurement and Analysis. *Physical Review Letters*, 89(28):283202, December 2002.

[127] J.D. Jackson. *Classical Electrodynamics*. 3rd edition, 1998.

[128] B. B. Pollock, D. H. Froula, P. F. Davis, J. S. Ross, S. Fulkerson, J. Bower, J. Satariano, D. Price, K. Krushelnick, and S. H. Glenzer. High magnetic field generation for laser-plasma experiments. *Review of Scientific Instruments*, 77(11):114703, 2006.

[129] D. O. Sabulsky, C. V. Parker, N. D. Gemelke, and C. Chin. Efficient Continuous-Duty Bitter-Type Electromagnets for Cold Atom Experiments for Cold Atom. *arXiv*, 1309.5330v, 2013.

[130] T. H. Lee. *Planar Microwave Engineering: A Practical Guide to Theory, Measurement, and Circuits*. Cambridge University Press, Cambridge, 2004.

[131] C. Bowick, C. Ajluni, and J. Blyler. *RF circuit design*. Newnes, 2nd edition, 2011.

[132] J. Welty, C. E. Wicks, R. E. Wilson, and G. L. Rorrer. *Fundamentals of Momentum, Heat, and Mass Transfer*. John Wiley & Sons, Inc, 4th edition, 2000.

[133] D.H. Bacon. *BASIC thermodynamics and heat transfer*. Butterworths, 1983.

[134] P. von Boeckh and T. Wetzel. *Heat Transfer*. Springer, Berlin Heidelberg, 2012.

[135] F. P. Incropera, D. P. DeWitt, T. L. Bergman, and A. S. Lavine. *Introduction to Heat Transfer*. John Wiley & Sons, Inc, 5th edition, 2007.

[136] Dynalene, inc. `http://http://www.dynalene.com/Heat-transfer-fluids-s/1477.htm`. Accessed: 2013-10-08.

[137] Paratherm corporation. `http://www.paratherm.com/heat-transfer-fluids/`. Accessed: 2013-10-08.

[138] C. F. Colebrook and C.M. White. Experiments with Fluid Friction in Roughened Pipes. *Proceedings of the Royal Society of London. Series A, Mathematical and Physical Sciences*, 161(906):367–381, 1937.

[139] L.F. Moody. Friction Factors for Pipe Flow. *Trans. ASME*, 66(8):671–684, 1944.

[140] E. Romeo, C. Royo, and A. Monzón. Improved explicit equations for estimation of the friction factor in rough and smooth pipes. *Chemical Engineering Journal*, 86(3):369–374, April 2002.

[141] L. Slătineanu, Ş. Potârniche, M. Coteaţă, I. G. Beşliu, L. Gherman, and F. Negoescu. Surface roughness at aluminium parts sand blasting. *Proceedings in Manufacturing Systems*, 6(2):4–9, 2011.

[142] C. O'Neale. *To be published*. PhD thesis, University of Birmingham.

[143] R. D. Adams and J. Comyn. Joining using adhesives. *Assembly Automation*, 20(2):109–117, 2000.

[144] W. D. Phillips. Laser cooling and trapping of neutral atoms. *Reviews of Modern Physics*, 70(3):721–741, 1998.

[145] C. Monroe, W. Swann, H. Robinson, and C. Wieman. Very cold trapped atoms in a vapor cell. *Physical Review Letters*, 6(13):1571–1575, 1990.

[146] K. E. Gibble, S. Kasapi, and S. Chu. Improved magneto-optic trapping in a vapor cell. *Optics letters*, 17(7):526–8, April 1992.

[147] E. Riis, D. S. Weiss, K. A. Moler, and S. Chu. Atom Funnel for the Productuin of a Slow, High-Density Atomic Beam. *Physical Review Letters*, 64(14):1658–1662, 1990.

[148] J. Nellessen, J. Werner, and W. Ertmer. Magneto-optical compression of a monoenergetic sodium atomic beam. *Optics Communications*, 78(3), 1990.

[149] W. Phillips and H. Metcalf. Laser Deceleration of an Atomic Beam. *Physical Review Letters*, 48(9):596–599, March 1982.

[150] WebElement: the periodic table on the web. `www.webelements.com/rubidium/atom_sizes.html`. Accessed 14-01-2014.

[151] S. Chu, L. Hollberg, J. E. Bjorkholm, A. Cable, and A. Ashkin. Three Dimensional Viscous Confinement and Cooling of Atoms by resonace Radiation Pressure. *Physical Review Letters*, 55(1):48–51, 1985.

[152] P.D. Lett, R.N. Watts, C.I. Westbrook, and W. D. Phillips. Observation of Atoms Laser Cooled below the Doppler Limit. *Physical Review Letters*, 61(2), 1988.

[153] J. Dalibard and C. Cohen-Tannoudji. Laser cooling below the Doppler limit by polarization gradients: simple theoretical models. *Journal of the Optical Society of America B*, 6(11):2023, November 1989.

[154] P. D. Lett, W. D. Phillips, S. L. Rolston, C. E. Tanner, R. N. Watts, and C. I. Westbrook. Optical molasses. *Journal of the Optical Society of America B*, 6(11):2084, November 1989.

[155] J. Catani, P. Maioli, L. De Sarlo, F. Minardi, and M. Inguscio. Intense slow beams of bosonic potassium isotopes. *Physical Review A*, 73(3):1–9, March 2006.

[156] C. Ospelkaus, S. Ospelkaus, K. Sengstock, and K. Bongs. Interaction-Driven Dynamics of $^{40}K -^{87}Rb$ Fermion-Boson Gas Mixtures in the Large-Particle-Number Limit. *Physical Review Letters*, 96(2):020401, January 2006.

[157] D. Sesko, T. Walker, C. Monroe, A. Gallagher, and C. Wieman. Collisional losses from a light-force atom trap. *Physical review letters*, 63(9):961–964, August 1989.

[158] D. Wallace, T. P. Dinneen, K.-Y .N. Tan, T. T. Grove, and P. L. Gould. Isotopic Difference in Trap Loss Collisions of Laser Cooled Rubidium Atoms. *Physical Review Letters*, 69(6), 1992.

[159] P. Feng, D. Hoffmann, and T. Walker. Comparison of trap-loss collision spectra for ^{85}Rb and ^{87}Rb. *Physical Review A*, 47(5):3495–3498, 1993.

[160] M.H. Anderson, W. Petrich, J.R. Ensher, and E.A. Cornell. Reduction of light-assisted collisional loss rate from a low-pressure vapor-cell trap. *Physical Review A*, 50(5):3597–3600, 1994.

[161] R. S. Williamson III and T. Walker. Magneto-optical trapping and ultracold collisions of potassium atoms. *JOSA B*, 12(8):1393–1397, 1995.

[162] C. Fort, A. Bambini, L. Cacciapuoti, F. S. Cataliotti, M. Prevedelli, G. M. Tino, and M. Inguscio. Cooling mechanisms in potassium magneto optical traps. *Spectroscopy*, 118:113–118, 1998.

[163] V. Gokhroo, G. Rajalakshmi, R. Kollengode Easwaran, and C. S. Unnikrishnan. Sub-Doppler deep-cooled bosonic and fermionic isotopes of potassium in a compact 2D 3D MOT set-up. *Journal of Physics B: Atomic, Molecular and Optical Physics*, 44(11):115307, June 2011.

[164] M. Landini, S. Roy, L. Carcagní, D. Trypogeorgos, M. Fattori, M. Inguscio, and G. Modugno. Sub-Doppler laser cooling of potassium atoms. *Physical Review A*, 84(4):043432, October 2011.

[165] F. S. Cataliotti, E. A. Cornell, C. Fort, M. Inguscio, F. Marin, M. Prevedelli, L. Ricci, and G. M. Tino. Magneto-optical trapping of Fermionic potassium atoms. *Physical Review A*, 57(2):1136–1138, 1998.

[166] G. Modugno, C. Benkö, P. Hannaford, G. Roati, and M. Inguscio. Sub-Doppler laser cooling of fermionic ^{40}K atoms. *Physical Review A*, 60(5):R3373–R3376, November 1999.

[167] C. Klempt. *Wechselwirkung in Bose-Fermi-Quantengasen*. PhD thesis, University of Hanover, 2007.

[168] W. Ketterle, K. B. Davis, M. A. Joff, A. Martin, and D. E. Pritchard. High Densities of Cold Atoms in a Dark Spontaneous-Force Optical Trap. *Physical Review Letters*, 70(15):2253–2256, 1993.

[169] R. Folman, P. Krüger, D. Cassettari, B. Hessmo, T. Maier, and J. Schmiedmayer. Controlling cold atoms using nanofabricated surfaces: atom chips. *Physical review letters*, 84(20):4749–52, May 2000.

[170] K. I. Lee, J. A. Kim, H. R. Noh, and W. Jhe. Single-beam atom trap in a pyramidal and conical hollow mirror. *Optics letters*, 21(15):1177–9, August 1996.

[171] J. J. Arlt, O. Marago, S. Webster, S. Hopkins, and C. J. Foot. A pyramidal magneto-optical trap as a source of slow atoms. *Optics Communications*, 157:303–309, 1998.

[172] D.M. Harber, J.M. McGuirk, J.M. Obrecht, and E.A. Cornell. Thermally Induced Losses in Ultra-Cold Atoms Magnetically Trapped Near Room-Temperature Surfaces. *Journal of Low Temperature Physics*, 133:229–238, 2003.

[173] G. Reinaudi, T. Lahaye, A. Couvert, Z. Wang, and D. Guéry-Odelin. Evaporation of an atomic beam on a material surface. *Physical Review A*, 73(3):035402, March 2006.

[174] Bose-einstein condensation in atomic gases: Proceedings of the international school of physics "enrico fermi" course cxl. In C. Wieman M. Inguscio, S. Stringari, editor, *Bose-Einstein Condensation in Atomic Gases*, volume 140 of *International School of Physics*, Varenna, Italy, January 1999. IOS Press.

[175] G. Ferrari, M. Inguscio, W. Jastrzebski, G. Modugno, G. Roati, and A. Simoni. Collisional Properties of Ultracold K-Rb Mixtures. *Physical Review Letters*, 89(5):053202, July 2002.

[176] H. Hess. Evaporative cooling of magnetically trapped and compressed spin-polarized hydrogen. *Physical Review B*, 34(5), 1986.

[177] N. Masuhara, J. M. Doyle, J. C. Sandberg, D. Kleppner, H. F. Hess, and G. P. Kochanski. Evaporative Cooling of Spin Polarized Atomic Hydrogen. *Physical Review Letters*, 61(8):935–938, 1988.

[178] D.W. Snoke and J.P. Wolfe. Population Dynamics of a Bose gas near saturation. *Physical Review A*, 39(7):4030–4037, 1989.

[179] E. Majorana. Teoria dei tripletti P Incompleti. *Il Nuovo Cimento*, 8(1):107–113, 1931.

[180] R. Dubessy, K. Merloti, L. Longchambon, P.-E. Pottie, T. Liennard, A. Perrin, V. Lorent, and H. Perrin. Rubidium-87 Bose-Einstein condensate in an optically plugged quadrupole trap. *Physical Review A*, 85(1):1–12, January 2012.

[181] K. Bongs. *Atomoptische Experimente mit Bose-Einstein Kondensaten*. PhD thesis, University of Hanover, 1999.

[182] H. M. J. M. Boesten, C. C. Tsai, J. R. Gardner, D. J. Heinzen, and B. J. Verhaar. Observation of a shape resonance in the collision of two cold ^{87}Rb atoms. *Physical Review A*, 55(1):636–640, January 1997.

[183] E. Burt, R. Ghrist, C. Myatt, M. Holland, E. Cornell, and C. Wieman. Coherence, Correlations, and Collisions: What One Learns about Bose-Einstein Condensates from Their Decay. *Physical Review Letters*, 79(3):337–340, July 1997.

[184] M. Yamashita, M. Koashi, T. Mukai, M. Mitsunaga, and N. Imoto. Optimization of evaporative cooling towards a large number of Bose-Einstein-condensed atoms. *Physical Review A*, 67(2):023601, February 2003.

[185] H. M. J .M. Boesten, A. J. Moerdijk, and B. J. Verhaar. Dipolar decay in two recent Bose-Einstein condensation experiments. *Physical review. A*, 54(1):R29–R32, July 1996.

[186] K. B. Davis and W. Ketterle. An analytical model for evaporative cooling of atoms. *Applied Physics B*, 60:155–159, 1995.

[187] J. Klinner, M. Wolke, and A. Hemmerich. Increased efficiency of rf-induced evaporative cooling by utilizing gravity. *Physical Review A*, 81(4):043414, April 2010.

[188] S. Chu, J. E. Bjorkholm, A. Ashkin, and A. Cable. Experimental Observation of Optically Trapped Atoms. *Physical Review Letters*, 57(3), 1986.

[189] R. Grimm, M. Weidemüller, and Y. B. Ovchinnikov. Optical dipole traps for neutral atoms. *arXiv:physics*, 9902072v1, 1999.

[190] J.E. Bjorkholm, R.R. Freeman, A. Ashkin, and D.B. Pearson. Observation of Focusing of Neutral Atoms by Dipole Forces of Resonance Radiation Pressure. *Physical Review Letters*, 41(20):1361–1364, 1978.

[191] J.D. Miller, R.A. Cline, and D.J. Heinzen. Far-off-resonance optical trapping of atoms. *Physical Review A*, 47(6):4567–4570, 1993.

[192] T. Savard, K. O'Hara, and J. Thomas. Laser-noise-induced heating in far-off resonance optical traps. *Physical Review A*, 56(2):R1095–R1098, August 1997.

[193] P. Pinkse, A. Mosk, M. Weidemüller, M. Reynolds, T. Hijmans, and J. Walraven. Adiabatically Changing the Phase-Space Density of a Trapped Bose Gas. *Physical Review Letters*, 78(6):990–993, February 1997.

[194] D. Stamper-Kurn, M. Andrews, A. Chikkatur, S. Inouye, H.-J. Miesner, J. Stenger, and W. Ketterle. Optical Confinement of a Bose-Einstein Condensate. *Physical Review Letters*, 80(10):2027–2030, March 1998.

Acknowledgements

First of all I want to thank Prof. Dr. Klaus Sengstock and Prof. Dr. Kai Bongs for the opportunity and the support to perform the experiments as part of the Quantum matter group at the University of Birmingham, UK.
The work would have been impossible to accomplish without the help of the entire Quantum gases group in Hamburg and the Quantum matter group in Birmingham, both mechanical work shops, stores and other staff.
My first year of my PhD in Hamburg would not have been the same without Anika, Japser, Parvis, Julian, Matthias, Jasper, Ortwin and all the others. And I would have never thought I miss the canteen!

Special thanks goes to my project group: First Prof. Kai Bongs who always had an open ear for questions and discussions and sometimes also unusual ideas how to approach problems. Dr. Jochen Kronjäger who taught me so much during the last years. Without him I would not have gotten that far. My colleagues Mike, Mathis and Amy who shared the sometimes painful time to start everything from scratch and inventing the wheel for another time. But we managed with a smile on our faces and always a good prank at hand. Marisa who is a very special person and became a close friend to me. I owe you for endless support during the night shifts. And last but not least Charlotte and Harry who put a lot of effort and care in the project now.
The archetype office with Ole, Matt, Steve and newer members Mark, Ania, Wei and Daniel. And people form next door, Alex, Clemens, Jon, Chris and the entire PhD student army. It never gets boring with you.
Emanuele who always broadens my horizon and reminds me of all the big and small things out there in the physics world I forget when I get lost in my work.
The workshop with Steve, Tony, Jag, John and Dave that build so many things for me that they thought for a while the disorder project is the only project.

And most importantly the people who make my world: Mama, Papa and Nici, who all of them absolutely always supported me in everything even if it might not have been the best idea. Maurice and Emma, who are the centre of the family